New technologies for ^{211}At targeted α-therapy research using ^{211}Rn and ^{209}At

Jason Raymond Crawford

BSc, University of British Columbia, 2007
MSc, University of Victoria, 2010

A dissertation submitted in partial fulfilment
of the requirements for the degree of

Doctorate of Philosophy

in the Department of Physics and Astronomy

New technologies for ^{211}At targeted α-therapy research using ^{211}Rn and ^{209}At

by

Jason Raymond Crawford

BSc, University of British Columbia, 2007

MSc, University of Victoria, 2010

Supervisory Committee

Dr. Thomas J Ruth, *Co-Supervisor*
Department of Physics and Astronomy

Dr. Andrew Jirasek, *Co-Supervisor*
Department of Physics and Astronomy

Dr. Wayne Beckham, *Committee Member*
Department of Physics and Astronomy

Dr. Dean Karlen, *Committee Member*
Department of Physics and Astronomy

Dr. Julian Lum, *Outside Member*
Department of Biochemistry & Microbiology

Abstract

The most promising applications for targeted α-therapy with astatine-211 (^{211}At) include treatments of disseminated microscopic disease, the major medical problem for cancer treatment. The primary advantages of targeted α-therapy with ^{211}At are that the α-particle radiation is densely ionizing, translating to high relative biological effectiveness (RBE), and short-range, minimizing damage to surrounding healthy tissues. In addition, theranostic imaging with ^{123}I surrogates has shown promise for developing new therapies with ^{211}At and translating them to the clinic. Currently, Canada does not have a way of producing ^{211}At by conventional methods because it lacks α-particle accelerators with necessary beam energy and intensity. The work presented here was aimed at studying the ^{211}Rn/^{211}At generator system as an alternative production strategy by leveraging TRIUMF's ability to produce rare isotopes. Recognizing that TRIUMF provided production opportunities for a variety of astatine isotopes, this work also originally hypothesized and evaluated the use of ^{209}At as a novel isotope for preclinical Single Photon Emission Computed Tomography (SPECT) with applications to ^{211}At therapy research.

At TRIUMF's Isotope Separator and Accelerator (ISAC) facility, mass separated ion beams of short-lived francium isotopes were implanted into NaCl targets where ^{211}Rn or ^{209}At were produced by radioactive decay, *in situ*. This effort required methodological developments for safely relocating the implanted radioactivity to the radiochemistry laboratory for recovery in solution. For multiple production runs, ^{211}Rn was quantitatively transferred from solid NaCl to solution (dodecane) from which ^{211}At was efficiently extracted and evaluated for clinical applicability. This validated the use of dodecane for capturing ^{211}Rn as an elegant approach to storing and shipping ^{211}Rn/^{211}At in the future. ^{207}Po contamination (also produced by ^{211}Rn decay) was removed using a granular tellurium (Te) column before proceeding with biomolecule labelling. Although the produced quantities were small, the pure ^{211}At samples demonstrated these efforts to have a clear path of translation to animal studies.

For the first time in history, SPECT/CT was evaluated for measuring ^{209}At radioactivity distributions using high energy collimation. The spectrum detected for ^{209}At by the SPECT camera presented several photopeaks (energy windows) for reconstruction. The 77-90 Po X-ray photopeak reconstructions were found to provide the best images overall, in terms of resolution/contrast and uniformity. Collectively, these experiments helped establish guidelines for determining the optimal injected radioactivity, depending on scan parameters. Moreover, ^{209}At-based SPECT demonstrated potential for pursuing image-based dosimetry in mouse tumour models, in the future. Simultaneous SPECT imaging with ^{209}At and ^{123}I was demonstrated to be feasible, supporting the future evaluation of ^{209}At for studying/validating ^{123}I surrogates for clinical image-based ^{211}At dosimetry. This work also pursued a novel strategy for labelling cancer targeting peptides with ^{211}At,

using octreotate (TATE, a somatostatin analogue for targeting tumour cells, mostly neuroendocrine tumours) prepared with or without N-terminus PEGylation (PEG_2), followed by conjugation with a *closo*-decaborate linking moiety (B10) for attaching ^{211}At. Binding affinity and *in vivo* biodistributions for the modified peptides were determined using iodine surrogates. The results indicated that B10-PEG_2-TATE retained target binding affinity but that the labelling reaction with iodine degraded this binding affinity significantly, and although having high *in vivo* stability, no ^{123}I-B10-PEG_2-TATE tumour uptake was observed by SPECT in a mouse tumour model positive for the somatostatin receptor (sstr2a). This suggested that further improvements are required for labelling.

A new method for producing ^{211}At at TRIUMF is established, and ^{209}At-based SPECT imaging is now demonstrated as a new preclinical technology to measure astatine biodistributions *in vivo* for developing new radiopharmaceuticals with ^{211}At. Combined with the theranostic peptide labelling efforts with iodine, these efforts provide a foundation for future endeavours with ^{211}At-based α-therapy at TRIUMF. All procedures were performed safely and rapidly, suitable for preclinical evaluations. All animal studies received institutional ethics approval from the University of British Columbia (UBC).

Table of Contents

List of Tables

List of Figures

Nomenclature

α alpha-particle, alpha decay, helium nucleus

β beta-particle, beta decay, electron

γ gamma-ray, photon

A Atomic mass, activity

ASE Air Sampling Ensemble

B10 (B10-NCS) isothiocyanatophenethyl-uriedo-*closo*-decaborate(2-)

BCCA British Columbia Cancer Agency

BCCRC British Columbia Cancer Research Centre

Bq Becquerel (number of disintegrations per second)

CARRIER Conveying Apparatus for the Rapid Recovery of Implanted Emanating Radionuclides

CCM Centre for Comparative Medicine

CT Computed Tomography

DNA Deoxyribose Nucleic Acid

EOB End of Beam/Bombardment

FC Faraday Cup

FEBIAD Forced Electron Beam Induced Arc Discharge (ion source)

FWHM Full-Width Half Maximum

GATE Geant4 Application for Emission Tomography

HEUHR High Energy Ultra High Resolution (SPECT collimator)

HPGe High Purity Germanium (detector)

HPLC High Performance Liquid Chromatography

IIS ISAC Implantation Station

ISAC Isotope Separator and Accelerator (facility)

iTLC Instant Thin Layer Chromatography

IYS ISAC Yield Station

kDa Kilodalton (1 kDa = 1.66×10^{-21} grams)

MIRD Medical Internal Radiation Dose (committee, dose calculation formalism)

mAb Monoclonal Antibody

MeV Megaelectron Volt (1 MeV = 1.6×10^{-13} Joules)

MC Monte Carlo

MLEM Maximum Likelihood Expectation Maximization (algorithm)

OLINDA/EXM Organ Level INternal Dose Assessment/EXponential Modeling (dose calculation code)

OSEM Ordered Subset Expectation Maximization (algorithm)

PEG_2 Polyethylene Glycol (polymer chain, n=2)

PET Positron Emission Tomography

POSEM Pixel-based Ordered Subset Expectation Maximization (algorithm)

RBE Relative Biological Effectiveness

RIB Rare-Isotope Beam

RIC Radioimmunoconjugate

RIT Radioimmunotherapy

SA Specific Activity (activity per unit mass of biomolecule

SPECT Single Photon Emission Computed Tomography

SRIM Stopping and Range of Ions in Matter (software)

SS Stainless Steel

sstr2a Somatostatin Receptor Type 2 a

TAT Targeted Alpha Therapy

TATE Octreotate

TRIUMF TRI-University Meson Facility (Canada's national laboratory for particle and nuclear physics)

TRT Targeted Radionuclide Therapy

Acknowledgements

This work was funded in part by a Canadian Cancer Society Innovation Grant.

With sincere gratitude, I would like thank my primary supervisor, Dr. Thomas Ruth, for his constant instruction, guidance and support during the course of my doctoral work. His cross-disciplinary experience and career as a world-leading scientist has forever inspired me, and is something I will always aspire to. I also extend this appreciation to my co-supervisors Dr. Andrew Jirasek and Dr. Wayne Beckham, who, from day 1, encouraged me to follow the professional interests I was most passionate about and provided me with the flexibility to pursue my most ambitious goals. I would also like to express huge gratitude to Dr. Scott Wilbur and Dr. Paul Schaffer, who each offered me extensive support with respect to all aspects of this work, as well as my development and training as a scientist. I also recognize the much appreciated commitment to this work made by my committee members, Dr. Dean Karlen and Dr. Julian Lum.

This effort would not have been possible without the committed effort of Dr. Hua Yang. She assisted me greatly on nearly all aspects of the radiochemistry reported in this work and her dedication and expertise were critical for the successes achieved in this area. I would also like to thank Dr. Peter Kunz for sharing his expertise with rare isotope production and assisting with instrumentation design. Likewise, I also take this opportunity to acknowledge the many contributions made by the extended ISAC Group towards executing the experiments, as well as Dr. Stefan Zeisler, Vinder Jaggi, Stephan Chan, and Jaroslaw Zielinski, for preparing implantation targets, quite often a rush order. Special thanks to Dr. Joseph Mildenberger for countless conversations that guided all aspects of radiation safety for this project. In addition, thank you to those who assisted with the handling and measurement of radioactivity, Danka Krsmanovic, Mike Johnson, Andrew Robertson, Maxim Kinakin, and Roxana Ralea. I would also like to acknowledge the UBC PET Imaging Group who made the imaging studies possible, Dr. Vesna Sossi, Dr. Stephan Blinder, Cristina Rodriguez, Chenoah Mah, and Katie Dinelle. Thank you also to Pedro Luis Esquinas for performing Monte Carlo simulations of the SPECT imaging system and the corresponding analysis. I greatly appreciate the many contributions made by those at the BC Cancer Research Centre (BCCRC) that made this work possible, specifically Francois Bénard and Kuo-Shin Lin who were collaborating investigators for this work, Dr. Johnson Zhang for chemistry support,

and Iulia Dude for performing the peptide binding assays. In addition, I would like to thank and acknowledge colleagues from UW and FHCRC for supplying materials for biomolecule labelling: thanks to Dr. Don Hamlin for preparing the antibody (B10-BC8) used for labelling studies (BC8 was supplied to us by Dr. Oliver Press), and Dr. Ming-Kuan Chyan for preparing the closo-decaborate moiety (B10-NCS) required for preparing biomolecules for At/I labelling.

Thank you to my extended family, I am truly privileged to have such a strong support network. I am very fortunate to have such wonderful, loving, understanding and encouraging parents. Thank you to Alanna Roberts for keeping me on track with her constant love and support. Thanks also to my younger brothers, Brandon and Colby, for continually teaching me, through example, that the only way to do anything is to give it all you have. Finally, I would like to thank my older brother, Joe. Joe was a constant source of technical support throughout the entirety of my education so far, and he will certainly continue to be throughout my career (he has no choice in this). He was also the person originally responsible for showing me the enormous power of science and the incredible value of scientific discovery, instilling in me a passion for physics at a very early age and to always question the status quo.

Dedication

"Go do, you'll learn to." – jónsi

To my extended family, for their infinite encouragement, support, and love ♡

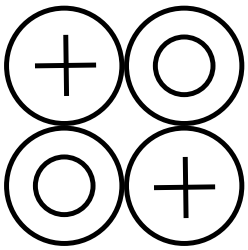

Chapter 1

Introduction

Destroying cancer with radiation

Innumerable triumphs in medicine have provided a deep understanding of cancer; new scientific discoveries are continually advancing diagnostic technologies for the detection and comprehensive assessment of cancer, as well as revealing new possible strategies for treatment. [1–3]. For example, becoming available in the 1970's, Computed Tomography (CT) revolutionized cancer treatment by precisely determining the size and location of solid tumours within the patient's anatomy, without the need for exploratory surgery [4, p. 312-314]. Medical imaging technologies such as CT have become indispensable for highly effective curative treatment strategies to eliminate tumours, namely surgery and radiation therapy (or *radiotherapy*), which both rely heavily on the ability to localize tumours within the body. While successful surgery that completely removes tumours can offer the best outcomes in terms of survival, it can also be highly invasive and carry an associated risk to the patient [5]. Additionally, microscopic disease can be missed during surgery and if left untreated, can result in tumour regrowth [6, 7]. As a complementary or alternative treatment modality, radiotherapy provides a widely available, non-invasive treatment option for many cancer patients.

Cell survival[1] probability decreases with the absorbed dose[2] of ionizing radiation [8, p. 377-378]. Radiation therapy attempts to distribute therapeutic doses to the tumour, while minimizing dose to the surrounding healthy tissues . This radiation is typically delivered from external sources; radionuclides or particle accelerators can be used to supply radiation that is carefully positioned at multiple angles and with variable intensities to selectively target and conform the dose to the tumour within the patient. In regards to the dose response, deoxyribose nucleic acid (DNA) has been identified as the primary target of ionizing radiation-induced damage[3] [9]. As an example of the probabilistic nature of

[1] In radiobiology, cell survival refers to a cell retaining its ability to reproduce (or divide).

[2] Absorbed dose is the energy imparted to matter per unit mass, measured in Gray (1 Gy = 1 Joule/Kilogram)

[3] This has been shown experimentally using microbeam irradiation experiments which have selectively

radiation-induced DNA damage, 1 Gy of sparsely ionizing radiation (eg. photons or electrons) produces approximately 2000 excitations in DNA leading to 1000 single stranded breaks. In turn, this produces an average 40 double stranded breaks, one chromosomal aberration, and finally 0.2-0.8 lethal events [10].

The stochastic physical processes leading to DNA damage and the complex and variable DNA repair mechanisms, make radiation-induced cell death probabilistic in nature. The consequences of DNA damage are very much determined by the physiological properties of the cell itself (including cell type and cell-cycle phase), the extent of damage, the rate at which the damage occurs, and the partly-random success or failure of repair mechanisms [11]. For photon/electron irradiation, the extent of damage is greatly influenced by the presence of oxygen which readily binds with the free radicals produced in DNA as a result of ionizing radiation, thereby sustaining the damage[4] [9, p. 94]. A depletion of oxygen in the tumour microenvironment, or *hypoxia*, is a typical characteristic of large solid cancers and often requires significantly more radiation dose to achieve the same therapeutic effect [8, p. 372],[12]. Additionally, if the damage occurs at a slow enough rate, repair enzymes may be able to correct the damage before lethal damage can accumulate, thus counteracting the effects of radiation [9, p. 74-79].

Therapeutic challenges of microscopic cancer

Radiation therapy relies on the availability of spatial information about the tumour. The dissemination of cancer cells from the primary site can result in microscopic clusters of tumour cells which do not always have a determinable position within the patient [13]. In these cases, any success radiotherapy has at destroying the primary tumour is jeopardized by the potential growth of small, pre-angiogenic[5] clusters of cancer cells that have relocated outside the primary tumour, called *micrometastases*, and recurrence is extremely common, if not inevitable [13].

When microscopic malignancies and micrometastases become distributed on body compartment surfaces, they become a highly irregularly-shaped target which cannot be precisely discerned from healthy tissue and are not treatable with surgery or conventional radiotherapy [14]. Analogously, following the surgical excision of macroscopic tumours, microscopic disease is often presumed to exist on the interior surface of the surgically created cavity and can cause recurrence. Some cancers do not produce macroscopic tumours and rather are termed monocellular malignancies [15], such as some cancers involving blood cells and lymphocytes. In these cases, the cancer cells can distribute

irradiated nuclear DNA, as opposed to the cell cytoplasm [9].

[4]Hydroxyl free radicals are produced by ionizing radiation which diffuse to and react with DNA, forming free radicals in the DNA. Molecular oxygen reacts with the free radicals and becomes chemically fixed, preventing reversion of the DNA molecule back to its undamaged condition [9, p. 94].

[5]micrometastases do not generally have a distinct blood supply

systemically throughout the body upon their onset and cannot be selectively targeted by conventional radiotherapy or surgery.

Additional challenges to treating cancer with conventional forms of radiation include the high levels of radioresistence observed for some cancers (e.g. glioma, melanoma), as well as, patient-specific variability in radiosensitivity and radioresistence related to hypoxia [16]. These conditions will often necessitate treatment protocols that deviate significantly from population-based radiation dose prescriptions [17]. Despite this, these factors are largely unknown and not typically considered by modern treatment planning but are expected to greatly influence cancer survival outcomes [18].

Following a diagnosis of disseminated disease, it is likely that there are widespread micrometastases, possibly distributed systemically throughout the patient [19]. These circumstances can necessitate the prescription of chemotherapy, often in the form of powerful pharmaceuticals that interfere with the biochemical processes of dividing cells [20]. These drugs can be administered alone or in combination with other therapeutic interventions, depending on the specific condition of the patient. Chemotherapy preferentially inactivates dividing cells and exploits the more rapid division of cancer cells compared to most normal healthy cells. Inevitably, chemotherapy results in systemic injury to dividing normal tissues, such as the regenerative tissue linings of the gastrointestinal tract, and chemotherapy recipients cope with severe, painful side-effects [21]. Consequently, the effectiveness of treatment is limited by normal tissue toxicity and dose limits are often surpassed before all cancer cells are inactivated [22]. Even so, these treatments can significantly reduce the tumour cell burden and can improve quality of life for the patient. Chemotherapy is currently the most effective and widely prescribed treatment for many metastatic cancers, while palliative radiation therapy with the intent of relieving localized symptoms is also a common practice in the management of cancer for these patients [20].

In contrast to systemically-acting chemotherapeutic pharmaceuticals, molecular targeted agents can be used to target cancer more specifically [23, 24]. Cancer-specific antigens, tumour-related gene expression and related mechanisms of tumour growth[6] can be targeted biochemically, possibly interfering with the processes of metastatic disease and thereby providing a desired therapeutic effect [24, 26]. There are a wealth of possible biochemical targets for treating cancer and presumably more that are yet unknown. However, molecular-targeted agents are generally not as cytotoxic as ionizing radiation or chemotherapy and, at the present time, are likely to be used most broadly for targeting cancer, not destroying it. Analogously to way that combining CT and radiation therapy has revolutionized cancer treatment, so too has the combination of molecular targeted

[6]One mechanism of tumour growth is *tumour angiogenesis*, whereby the tumour induces the formation of new blood vessels that supply oxygen and essential nutrients [25].

agents and sources of ionizing radiation in the form of therapeutic radionuclides, having applications to the treatment of diffuse microscopic disease.

Internal radionuclide therapy and theranostic isotopes

An emerging modality in radiotherapy is Targeted Radionuclide Therapy (TRT). This involves delivering therapeutic doses of radiation by administering radioactive substances (radionuclides attached to carrier molecules) that concentrate to the intended targets, internally[7] [27]. Three types of nuclear decay[8] provide distinct forms of radiation for TRT: β-particles, auger-electron cascades, and α-particles, each with its own applications in medicine [28]. β-particle emitters produce nuclear electrons with a relatively long range in tissue, from hundreds of microns up to a few centimetres. The ionization of tissue matter is sparsely distributed along the trajectory of a β-particle and at most results in easily repairable single stranded breaks in the targeted DNA. For betas to be effective for targeted radionuclide therapy, cellular damage must result from the crossfire of β-particles originating from adjacent targeted cells located within the macroscopic range of the radiation [29]. This requirement enables nearly homogeneous dose distributions to be delivered to macroscopic tumours by suitably targeted β-emitters, even when the biomolecular targeting of all tumour cells is not possible or not homogeneous. In contrast, the auger-electron cascades produced in the decay of some radionuclides are densely ionizing on the scale of nanometres and suitable for damaging single targeted molecules [30, p. 290]. α-particles [9] deposit their energy over tens of microns in tissue, and are extremely effective cell killers [31]. For this reason, α-particle emitters are considered the most suitable for treating microscopic disease, where the inactivation of single, possibly isolated cells is the intention of treatment. Nonetheless, an overwhelming majority of the research and clinical applications of TRT have been conducted with the more widely available β-emitters [32].

Modern medical imaging technologies of nuclear medicine provide a powerful tool set for determining the presence and patho-physiological processes of disease, by detecting, quantifying and geometrically determining the position of activity[10] distributions of radioactive substances administered to the body [2, 33]. There is a growing interest in *theranostic* isotopes, which can be used to deliver a therapeutic radiation dose, as well

[7] In some applications, chemical properties of the radionuclide can achieve the desired distribution internally, and a carrier molecule is not necessary. e.g. radioiodine

[8] Radionuclides have a time-dependent probability to spontaneously decay and emit radiation. The probability of nuclear decay to occur in time interval t is equal to $1-e^{-t\ln 2/t_{1/2}}$, where $t_{1/2}$ is an intrinsic property of the particular radionuclide, called *half-life*.

[9] α-particles are emitted with energies roughly between 2-9 MeV.

[10] The amount of a particular radioisotope can be reported in terms of the number of disintegrations per unit time, or *activity*. The units for activity are the *bequerel* (Bq), defined as 1 disintegration per second, and the *curie* (Ci), where 1 Ci is equivalent to 37 GBq, or 3.7×10^{10} disintegrations per second.

as, produce a detectable signal for imaging. Theranostic isotopes have major advantages in terms of monitoring treatment delivery and quantifying absorbed dose to the patient [2]. This information can be used to determine if a change in the course of treatment will be necessary, providing opportunities for improving therapeutic outcomes [34]. While some therapeutic radionuclides can be detected internally with medical imaging, others require a radioactive surrogate that has demonstrated identical or closely representative biodistribution patterns. Combined, a therapeutic isotope and its imaging surrogate are referred to as a *theranostic pair* [35].

Targeted Alpha Therapy (TAT)

Targeted Alpha Therapy (TAT) (or Targeted α-Therapy) is an experimental, internal conformal radiation treatment modality, specifically using biologically-targeted α-particle radiation[11] [36]. The two primary advantages of α-particle radiation are that they have a microscopic range in tissue and highly cytotoxic [37–39]. α-particles are densely ionizing, meaning they have a much higher Linear Energy Transfer[12] (LET), compared to more sparsely ionizing radiation such as β-particles or photons. For LET of 100 keV/μm, close to the mean LET of most α-particle emitters, the mean distance between ionization events[13] is close to the distance between complementary nucleotides of double-stranded DNA (2 nm) [3, 37]. The close proximity between successive ionizations increases the likelihood of double strand breaks, compared to photons or electrons depositing the same energy but with less correlation. This capacity for dense ionization by α-particles significantly reduces, if not eliminates, the dependence of cell inactivation on cell-cycle phase, oxygen concentration and dose rate [42]; cell survival has been shown to decrease mono-exponentially with the α-particle dose received by the cell nucleus, strongly indicating that the cellular repair mechanisms are not capable of repairing the extensive, correlated damage caused by α-particles [43].

The high cytotoxicity and short range of α-particles make them most suitable for therapies intended to inactivate single, isolated cells or small clusters. Experiments have shown that the passage of as little as 1 α-particle through the nucleus of a cell can cause cell inactivation [31]. On the contrary, β radiation would require tens of thousands of DNA crossings to have the same probability of cell inactivation. The inactivation of isolated cells is not feasible with β-emitters given even ideal targeting specificity and

[11] Instances of TAT which involve immunological targeting can be referred to as *α-immunotherapy*

[12] When an α-particle traverses a medium, it dissipates energy (E) while undergoing collisions (mainly with electrons), until coming to rest . The energy transferred to the local medium per unit distance (x) traversed by the particle, is called the Linear Energy Transfer (LET). It is related to the non-relativistic *stopping power* (dE/dx), with a suitable subtraction of energy lost to bremsstrahlung and highly energetic δ-rays that otherwise remove energy from the location of dose deposition [40].

[13] The mean energy transferred to secondary electrons by a 6 MeV α-particle in water is roughly 100 to 200 eV per collision, with a maximum energy transfer of 3 keV for a single collision [41, p.].

the adverse effects of the longer ranging β-particles at such high levels of activity on adjacent healthy tissue. As the energy of an α-particle is transferred to the cells, the relative amount of energy it expends per unit length increases to a maximum just before it comes to rest, called a *Bragg peak*, depositing all of the energy within 50-100 μm and spanning only a few cells [42]. To relate the physical absorbed dose and a measured or defined biological effect for a given source of radiation, Relative Biological Effectiveness (RBE) has been defined as the ratio of dose given by a reference radiation (typically sparsely ionizing radiation) and the radiation type of interest (in this case, α-particles), for a specific measurable effect, or *endpoint*. For therapeutic doses (roughly on the order of 1-10 Gy), typical RBE values for α-particle radiation are between 3 and 7 [42].[14] The most compelling reason for this high RBE is that the energy deposition of an α-particles is very tightly clustered, having a high degree of correlation along its track on a microscopic scale. In this way, the damage attributed to vital cellular structures (mainly DNA) is concentrated extremely efficiently and is so severe it is much less likely to be repairable, compared to more sparsely ionizing photon and electron/beta radiation. Based on these properties, the most promising applications for TAT include the treatment of micrometastatic disease, monocellular bloodborne malignancies and malignancy spread on body compartment surfaces [37].

Candidate α-emitters and clinical examples

The α-particle emitting radioisotopes which can be considered eligible candidates for current or future applications of TAT are listed in Table 1.1. None of these radioisotopes are widely available, and the development of TAT has been limited to a small number of institutions around the world [44, 45]. To date, a small number of other clinical trials have been conducted using one of ^{211}At, ^{213}Bi, and ^{225}Ac.

In December 2013, Health Canada issued a Notice of Compliance to Bayer Inc for radium-223 (^{223}Ra) dichloride (branded as "Xofigo" and previously as "alpharadin"). In doing so, ^{223}Ra became the first α-emitter to receive this designation in Canada, and to be used in the clinic. While not considered curative as a stand alone drug, [^{223}Ra]radium dichloride is now often described as a revolutionary pharmaceutical for palliative care, greatly improving the quality of life for these patients by eliminating or reducing painful bone metastases and delaying disease progression [39]. Radium shares some chemical characteristics with calcium and is targeted to areas of ossification, providing the basis for treating bone-metastasizing prostate and breast cancers with ^{223}Ra. The decay of ^{223}Ra and its daughters produces a total of four α-particle emissions which are theorized not only to destroy or damage the metastases, but also the micro-environments that

[14] At much lower doses, RBE can reach as high as 20, important when considering radiation safety standards in the context of occupational health.

support their growth. To date, only small number of other clinical trials have been conducted using one of ^{211}At, ^{213}Bi, and ^{225}Ac.

The selection of an optimal α-particle emitter for therapy is based on several factors, including availability and cost, half-life, α-particle energy, daughter nuclei, chemical compatibility with the targeting agent, and additional radiative processes which may extend the range of dose deposition (such as co-produced β-particle emissions) or be applicable to imaging (γ-rays or X-rays). In addition, the half-life of the α-particle must be well matched to the pharmacokinetics pertaining to the selected targeting molecule, for any therapeutic application. Optimal *in vivo* targeting can have a range from minutes to days, depending on the targeting strategy and the particular pathology of the targeted disease.

Fortunately, the small number of candidate α-emitters listed in Table 1.1 have half-lives that range between a fraction of an hour to several days. Half-life provides a major point of distinction between therapeutic α-emitters with respect to their potential applications in cancer treatment. Having a half-life of 7.2 hours, ^{211}At is well matched to many applications using immune-based targeting vectors (e.g. monoclonal antibodies or antibody fragments, see §2.3. In addition, 100% of ^{211}At decays produce α-particles for maximum therapeutic effect, while also not producing α-emitting daughter isotopes with long half-lives. These important attributes of ^{211}At strongly motivate its evaluation for cancer treatment.

The study of astatine-211 (^{211}At) and its use in therapy continues to be greatly hindered by the low availability of this isotope; the production of ^{211}At requires a medium

Table 1.1: α-particle emitting isotopes with potential for therapeutic applications.

α-emitter	Half-life (hr)	E_α (MeV)	Considerations	Production
^{149}Tb	4.15	4.0 (17%)	highest RBE, low % α-decay	heavy-particle accelerator, proton-spallation [46]
^{211}At	7.21	5.9, 7.5 (42%,58%)	thyroid-specific uptake, no long-lived isotopes	α-particle accelerator generator (^{211}Rn/^{211}At)
^{212}Pb/^{212}Bi	10.6 (^{212}Pb) 1.01 (^{212}Bi)	^{212}Bi:6.0,6.0,9.0 (26%,10%,64%)	*in vivo* generator, long-range betas,	generator (^{224}Ra/^{212}Pb/^{212}Bi)
^{213}Bi	0.76	6.0,8.5 (2%,98%)	short half-life, renal-specific uptake	generator (^{225}Ac/^{213}Bi)
^{223}Ra	273.6	5.6,6.7,7.4,6.6 (100%×4)	poor conjugation, localizes in bone 4 α-emissions (incl. daughters)	generator (^{227}Th/^{223}Ra)
^{225}Ac	240	5.9,6.0,6.4,7.2,8.5 (100%×4,combined)	4 α-emissions (incl. daughters)	generator (^{229}Th/^{225}Ra/^{225}Ac)

energy α-particle accelerator, of which there are only a small number in operation worldwide, and none are in Canada. Moreover, The short distribution range of ^{211}At from its site of production to potential researchers and hospitals is dictated by its short (7.2 hour) half-life. Despite limited global accessibility to ^{211}At, phase I clinical trials have been conducted for treatments of refractory ovarian cancer and recurrent brain cancer, and are in final stages of planning for leukaemia/lymphoma [47–49]. Initial clinical results for these studies have demonstrated great promise for ^{211}At and strongly support the continued development and clinical evaluation of these therapies.

In principle, ^{211}At is a theranostic isotope as it emits both α-particles that deliver therapeutic doses and X-rays which can be detected by external gamma cameras [50–52]. However, the capability of theranostic imaging with ^{211}At is inherently limited by the low intensity and low energy of the X-rays it emits, resulting in poor imaging potential for this isotope. While efforts to image ^{211}At are actively pursued in the clinical setting, more accurate quantification is expected to be achievable using other isotopes as surrogates with better imaging properties. Iodine-123 (^{123}I) is a strong candidate for clinical surrogate-based dosimetry of ^{211}At, having an established role as a diagnostic imaging isotope in the clinic and similar chemical properties to astatine. Establishing ^{123}I for ^{211}At surrogacy will require extensive validation in the preclinical and clinical settings.

Advancing targeted α-therapy at TRIUMF

TRIUMF, Canada's national laboratory for particle and nuclear physics, is a world leader in advancing novel techniques in medical isotope production. It operates a set of particle accelerators dedicated to research, including the world's largest proton cyclotron, providing unique opportunities for scientific discovery in a variety of fields. While TRIUMF's Life Sciences Division continues to focus primarily on developing technologies for diagnostic imaging with radioisotopes, efforts have been initiated to pursue innovative research for therapeutic α-emitters. Using state-of-the-art methods in accelerator-based isotope production, TRIUMF aims to address challenges related to isotope availability and theranostic procedures for advances in TAT. In principle, TRIUMF can produce all of the therapeutic α-emitters (listed in Table 1.1) as well as a multitude of related isotopes with potential applications for research.

Many research interests of TRIUMFs Life Sciences Division are closely aligned with those of the BC Cancer Agency (BCCA), which operates the BC Cancer Research Centre (BCCRC). Collaboration between these two institutions continually provides rapid transfer of technology from the laboratory to the clinical setting. BCCRC has a long standing research program that develops and evaluates radioactive tracers for diagnostic imaging. Moving forward together, TRIUMF and BCCRC aim to develop and study new methods in targeted α-therapy based on these promising cancer-targeting agents. Given

its strong partnership with BCCA and its access to additional resources and expertise in nuclear medicine at the University of British Columbia (UBC), TRIUMF has taken a prime position for pursuing impactful research in the field of targeted alpha therapy.

Developments for ^{211}At-related research

While not equipped with a medium energy α-particle accelerator, as is conventionally used to produce ^{211}At (via the ^{209}Bi(α,2n)nuclear reaction), TRIUMF can make advances toward ^{211}At by pursuing its production as the progeny resulting from the decay of radon-211 (^{211}Rn, $t_{1/2}$ = 14.6 hours), a strategy referred to as the ^{211}Rn/^{211}At *generator system* [44, 53, 54]. Since the ^{211}At is continually produced from a decaying supply of ^{211}Rn, the highest yields for ^{211}At recoverable up to one day after the initial ^{211}Rn production and isolation. This is in sharp contrast to the conventional production of ^{211}At where yields diminish at an exponential rate immediately after production. In this way, a ^{211}Rn/^{211}At generator could be shipped over large distances to remote institutions while the ^{211}At is produced in transit.

The ^{211}Rn/^{211}At generator system has been pursued by a small number of laboratories world-wide that have ^{211}Rn production capabilities. Despite widespread appeal of such a generator system, there has not yet been a clinical implementation and the concept still remains at an early stage of development [53, 55–58]. A major challenge to studying this generator system is the difficulty of producing ^{211}Rn, itself. Established technologies at TRIUMF for isotope production provides a method for producing ^{211}Rn from natural uranium using TRIUMF's high energy proton beams, motivating the continued development of the ^{211}Rn/^{211}At generator for supplying ^{211}At, in Canada.

Recognizing that TRIUMF has the capacity for producing a variety of astatine isotopes, those with detectable photon emissions were evaluated for their imaging prospects. In an original proposal of this work, astatine-209 (^{209}At; half-life = 5.41) was identified as a candidate for imaging, using Single Photon Emission Computed Tomography (SPECT), in particular. ^{209}At decays primarily by electron capture (95.9% ϵ, 4.1% α) and compared to ^{211}At, it is known to produce a higher abundance of X-rays and γ-rays per decay with sufficient energy for detection by modern imaging systems. The potential for producing ^{209}At at TRIUMF has created a new opportunity to evaluate its use in SPECT imaging for developing ^{211}At targeted α-therapies.

Thesis scope

Targeted α-therapy with ^{211}At is a vast subject for scientific discovery, with its continued development being highly motivated by its promise for the treatment of diffuse, microscopic cancer. In particular, the ^{211}Rn generator system and theranostic imaging for ^{211}At are broadly open areas of research. The approach taken by this doctoral thesis work was

to leverage TRIUMF's powerful facilities for isotope production to develop and study a small-scale ^{211}Rn generator system for preclinical evaluations. In parallel to this effort, preclinical SPECT imaging with ^{209}At was evaluated with pilot studies, in mice and phantoms. Both of these goals were enabled by developing novel production strategies for these isotopes. Further efforts were spent developing a novel approach to attaching ^{211}At to cancer-targeting peptides, with a focus on evaluating the effects of these modifications on cellular targeting efficacy.

In this thesis, background chapters offer context to research objectives described above: the foundations and current status for medical uses of ^{211}At are developed in Chapter 2, and topics in ^{211}At production are expanded on in Chapter 3, with an introduction to related facilities at TRIUMF. In the following chapters describing original research, methods and results with the ^{211}Rn generator system are summarized in Chapters 4 and 6, and SPECT imaging experiments with ^{209}At are presented in Chapters 5 and 7. The description of experimental work concludes with Chapter 8, providing a summary of peptide labelling experiments conducted in conjunction with the BCCRC. Finally, Chapter 9 summarizes this work and suggests future directions for research in these areas, with final thoughts on the perspectives formed by this PhD training.

Chapter 2

Targeted α-therapy with Astatine-211

This chapter provides context for this doctoral project in regards to the use of ^{211}At in medicine. The physics underlying the therapeutic advantage of targeted α-therapy with ^{211}At is detailed in §2.1, followed by considerations of its chemistry and biodistribution in §2.2. Practical aspects of targeting cancer cells with ^{211}At are discussed in §2.3, with the clinical applications discussed in §2.4. Finally, topics in dosimetry and imaging for ^{211}At are reviewed in §2.5.

The therapeutic advantage of ^{211}At

The motivation for ^{211}At-based targeted α-therapy is based primarily on decay properties. For ^{211}At, 100% of decays result in α-particles being emitted, according to the decay scheme presented in Figure 2.1. ^{211}At undergoes α-particle decay with 41.7% probability and produces ^{207}Bi. This product decays with a half-life of approximately 33 years to ^{207}Pb (stable). The 58.3% of ^{211}At decaying by electron capture produces ^{211}Po which rapidly decays by α-emission with a 0.5 second half-life to stable ^{207}Pb. The decay of ^{211}At to ^{211}Po is also promptly proceeded by the emission of 77-92 keV ^{211}Po X-rays, with energies (and intensity per ^{211}At decay) of 77 keV (13.2%), 79 keV (22.2%), 89 keV (2.6%), 90 keV (4.9%),and 92 keV (2.4%). In turn, theranostic imaging with ^{211}At is possible with clinical imaging systems (see §2.5).

These decay properties of ^{211}At are extremely favourable from a therapeutic perspective. The mean α-particle emission energy is 6.78 MeV and the mean LET is 100 keV/μm, corresponding to a range in tissue of 67.5 μm [37] and approximates the maximum possible RBE for any ionizing radiation (see §1.2 [59]. In addition, the fate of the daughter nuclides have little consequence in the body, in terms of dose or toxicity, for any therapeutically relevant quantity. In a landmark study published in *Science* in 1981, mice with intraperitoneal malignant ascites were shown to be cured with intraperitoneal injection of ^{211}At-tellurium colloid [60]. Treatment with ^{211}At was compared to Te colloid alone and a β-emitting radiocolloid, both of which failed to provide cure or improve median survival. The curative effects observed for ^{211}At-tellurium colloid were attributed directly to the

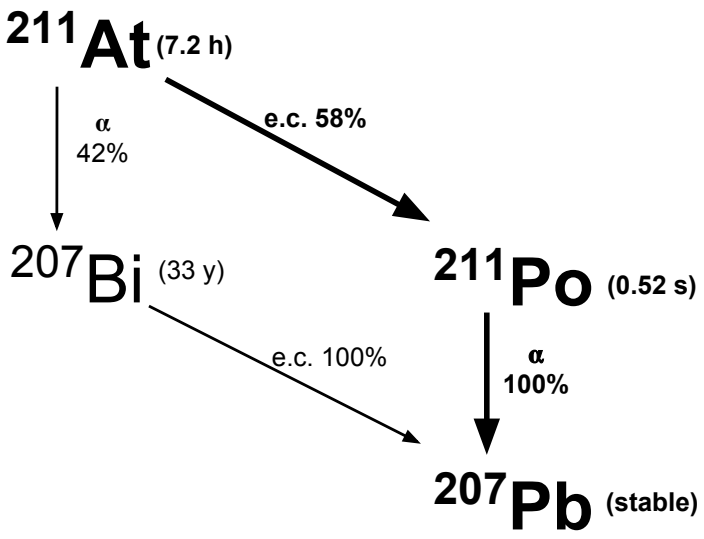

Figure 2.1: Simplified decay scheme for ^{211}At. e.c. = electron capture, α = α-decay

densely ionizing α-particle radiation for its capacity for producing irreparable damage to tumour cell DNA while simultaneously sparing healthy tissue out side of the range short-range α-particle tracks and avoiding morbidity [60].

Considerations of ^{211}At biodistributions

As an α-emitter, ^{211}At poses a potential health risk if it is in some way internalized. Even low doses could cause significant toxicity due to the high RBE of α-particles. Presently, the biodistribution of ^{211}At in humans remains largely unknown. Clinical applications have been scarce and too recent to have provided a measure of long-term effects in healthy tissues. Most of what is known about ^{211}At biodistributions and biokinetics is with respect to different mammal models. from which some general trends have been revealed and the human biodistribution can be partly predicted, especially from the studies conducted with more closely related species (e.g. monkeys and dogs) [61]. In this respect, ^{211}At shares chemical properties with iodine (I), the next-largest halogen. Iodine is necessary for physiological functions of the thyroid and is actively recruited from the blood to the thyroid by a membrane-crossing transport protein of the thyroid follicular cells, *the sodium-iodide symporter*. Experiments suggest that this protein also actively transports ^{211}At, and a large proportion of any free astatine that circulates in the blood is rapidly concentrated in the thyroid of all tested mammals [62]. In addition to the thyroid, there are several other organs that demonstrate appreciable uptake of astatine, including the stomach, lung, spleen, pituitary gland, adrenal gland, salivary glands, and ovaries [61, 63]. Uptake can be reduced with administration of suitable blocking agents (e.g. potassium iodide, sodium perchlorate, thiocyanate), with varying effectiveness, depending on the organ [64].

Biomolecular targeting with ^{211}At

Many cancer cells over-express specific membrane-bound molecules for which some natural or synthetic targeting biomolecule can have high affinity. Other biochemical pathways or growth mechanisms may provide molecular targets if they are associated with cancer. Targeting molecules can be used to transport the radionuclide to the therapeutically intended target within the body. The choice of vector can range in type from single amino acids to peptides, proteins, and colloids. Antibodies and their derivatives, called *antibody fragments*, can be among the most specific and well-suited targeting vectors for cancer therapy [30]. *Monoclonal Antibodies* (mAb) are naturally occurring biomolecules that are a primary component of the humoral response by the immune system of vertebrates. They are large proteins with complex tertiary and quaternary structure that includes a pair of identical *antigen-binding sites*, regions that have extremely high affinity for an immunologically-targeted molecule, or *antigen* [30]. The general form of a monoclonal antibody is shown in Figure 2.2.

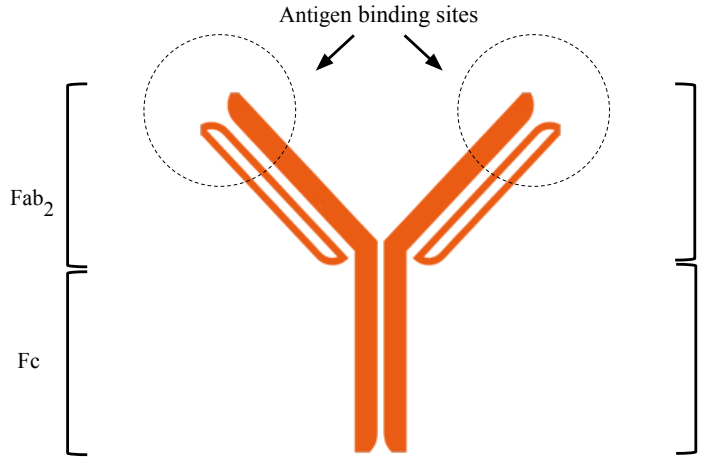

Figure 2.2: General components of monoclonal antibodies.

Typical *direct* labelling of proteins with iodine isotopes is completed by forming a covalent bond between the halogen and a carbon of an amino acid residue, most commonly tyrosine [30]. The astatine-carbon bond is less stable and ^{211}At-labelled antibodies constructed this way have low yields and undergo extensive *in vivo* deastintination [30, 61]. In general, astatine labelling therefore requires constructing a precursor molecule that provides stability astatinated molecules. Evaluations regarding the labelling stability of astatinated biomolecules was thoroughly reviewed by Wilbur (2008) [61]. Due to the electrophillic nature of At, labelling aryl carbon pendent groups can provide some stability ^{211}At-C bond. A standard approach was originally developed by Zalutsky (1988) [65]; using an N-succinimidyl tri-n-butylstannyl benzoate intermediate, where by ^{211}At electrophilic substitution with a tin compound on the phenyl group. The astatinated small

molecule is then conjugated to free amine groups (NH_2) of the targeting biomolecule (i.e. lysine residues of a protein).[1] Zalutsky's general approach has been adapted for direct labelling by conjugation of the linking moiety and antibody before astatination [66], and recently developed for automated production [67]. Also of interest to this approach, a recent animal study demonstrated brain tumour targeting of directly labelled ^{211}At-phenylalanine, where phenylalanine provides the aryl carbon pendent for labelling as well as a demonstrated capacity for targeting [68].

It has been shown that boron bonds more strongly to halogens than does carbon. This trend was presumed to extend to astatine; the highly neutrophilic boron cage-containing conjugates were hypothesized to provide the most suitable moiety precurser to astatination with respect to *in vivo* stability [69]. This was confirmed with a series of labelling experiments completed by Wilbur *et al.* (at the University of Washington *et al*), which compared *in vivo* deastatination of labelled antibodies relative to the same compounds labelled with iodine, for a variety of *closo*-decaborate(2-) and carborane moieties [70]. This thorough evaluation has identified $B_{10}H_9{-}NHCONH{-}CH_2CH_2{-}Ph{-}NCS$ (isothiocyanatophenethyl-uriedo-*closo*-decaborate(2-)), here referred to as B10-NCS, as the most suitable linking moiety for antibody labelling [49]. The acid-cleavable hydro-

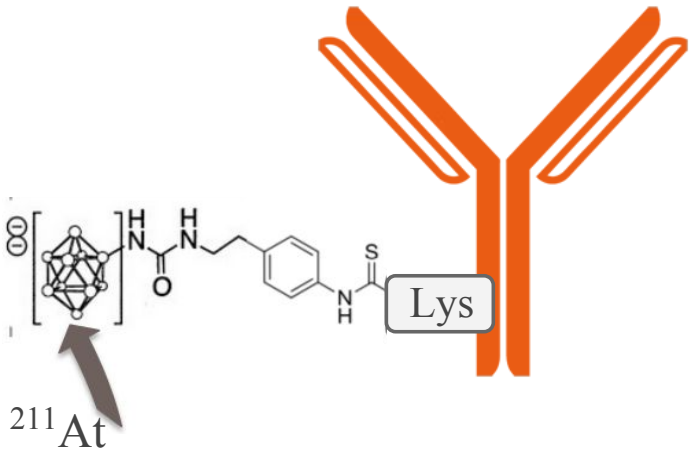

Figure 2.3: illustration of antibody preparation with *closo*-decaborate(2-) moiety for direct labelling of ^{211}At.

zone on the *closo*-decaborate(2-) provides susceptibility to hydrazone cleavage *in vivo*, found to provide faster clearance of the ^{211}At-labelled RICs from the kidney and other tissues, when a *closo*-decaborate(2-) linker is used [71]. Furthermore direct labelling of B10-immunoconjugates with either At and I results in very similar biodistributions for these RIC in animals. This demonstrates that direct labelling of tyrosine residuals by ^{211}At is not significant because it would lead to a significant differences in the biodis-

[1]The fraction of targeted molecule that becomes labelled is reported in terms of *specific activity*, the activity per unit mass of the RIC (e.g. MBq/mg or mCi/g).

tribution. This is evidence that *closo*-decaborate(2-) out-competes tyrosine residuals for direct labelling to the point where tyrosine labelling becomes completely negligible).

Clinical trials with ^{211}At

To date, two phase I clinical trials have been completed with ^{211}At:

Recurrent brain tumours: In 2008, Zalutsky *et al* published the results of a completed clinical trial for the adjuvent treatment of surgically resected recurrent brain tumours, mostly glioma [48]. Astatine-211 was conjugated to anti-tenascin monoclonal antibody ch81C6 targeting tenascin, an extracellular matrix glycoprotein upregulated by most glioma cells, and administered using a single dose via catheter to a resection cavity after surgery. In total, 18 patients received treatment with 14 of those patients receiving further chemotherapy (which varied, as prescribed by the neurooncologist). Survival time of the recipients who received TAT nearly doubled, compared to patients receiving surgery only, with a mean survival time of 54 weeks as opposed to 23 weeks. The authors of this study concluded that leakage of ^{211}At activity from the resection cavity was extremely low, resulting in no patients receiving dose-limiting toxicity (such as an high grade adverse neurological event). This provides the possibility of dose escalation in future clinical trials, taking advantage of the short range of the α-particles that spares surrounding healthy tissue.

Ovarian cancer: In 2009, Andersson *et al* published the results of a second Phase I clinical trial with ^{211}At for recurrent ovarian cancer [47]. Nine patients were treated with ^{211}At labelled to MX35 F(ab')2 antibody fragment, known to target the sodium-dependent phosphate transport protein 2b (NaPi2b) displayed by over 80% of ovarian cancers. Doses were administered to the intraperitoneal space following surgery and chemotherapy. All patients had refractory ovarian cancer and were in complete remission after salvage chemotherapy at the time of treatment with ^{211}At. For these patients, ovarian cancer cells form microscopic multicellular clusters on the lining of the abdominal cavity. Treatment resulted in acceptable normal tissue toxicities while also providing improvements in patient outcome, although noting that the sample size was low. For this treatment, the dose limiting organ was considered to be the peritoneum, for which the maximum allowable dose is unknown.

Several similarities can be identified between these completed clinical trials with ^{211}At: In each case, ^{211}At was administered directly to an anatomically defined region (i.e.the surgically-created resection cavity or the abdominal cavity/intra-peritoneal space). In both cases, low irradiation to bone marrow and/or other healthy tissues was attributable to the short half-life of ^{211}At, resulting in most of the dose deposited before the biological clearance from the cavity became significant [47, 48]. In addition, both trials used a

pharmaceutical agent to block thyroid uptake of ^{211}At (potassium iodide/liothyronine[48], potassium perchlorate[47]), given to the patient before, during and after treatment. Radiolabelling of immunoconjugates used in each of these trials were both done using the Zalutsky method.

More clinical trials with ^{211}At are poised to begin in 2016 at the Fred Hutchinson Cancer Research Center, in Seattle WA, for treatment of leukemia, lymphoma and some pediatric genetic diseases[2]. This study will employ ^{211}At-labelled BC8, an anti-CD45 murine monoclonal antibody that targets CD45 antigen expressed highly and exclusively in haematolymphoid cells and presents a suitable target for acute leukaemia [49, 72]. In contrast to the labelling of the completed clinical trials (described above), this will make use of the Wilbur method for mAb labelling with ^{211}At, followed by systemic injection. It should be noted that previous Phase I and I/II clinical trials have demonstrated antileukemic activity with ^{213}Bi and ^{225}Ac labelled antibodies [73].

Dosimetry and imaging with ^{211}At

Strategies for internal radionuclide dosimetry

Absorbed dose is a critical determinant for cancer cell survival and normal tissue toxicity [9]. The dosimetry of internally targeted radionuclides has been thoroughly evaluated by the Committee of Medical Internal Radiation Dose (MIRD) [1]. This committee has produced many recommendations and tools for dose calculations of internal radionuclides [33, 74–76]. Using the MIRD system, the absorbed dose (D_{r_k}) to a target region (r_k) is given as the sum of cumulative activity (A_{r_h}) in source regions (r_h) multiplied by a factor $S(r_k \leftarrow r_h)$, called the *S-value*, accounting for the type of emitted radiation, its energy, target mass (m_{r_k}), and source-target spatial configuration (as defined by the factor ϕ_i). In this way, dose to the target region (D_k) can be written as a sum of dose originating from all sources (h) given their *time-integrated activity*[3], as in (Equation 2.1),

$$D_{r_k} = \sum_h (\text{time-integrated activity}) \times S(r_k \leftarrow r_h) \tag{2.1}$$

where the dose where $S(r_k \leftarrow r_h)$, *the S-value*, is given by (Equation 2.2),

$$S(r_k \leftarrow r_k) = \frac{\sum_i n_i E_i \phi_i (r_k \leftarrow r_h)}{m_{r_k}} \tag{2.2}$$

[2]Treatment for these pediatric genetic diseases involves transplantation and gene therapy.

[3]Time-integrated activity is equal to the total number of disintegrations during the period of time considered by the dose calculation.

where n_i is the number of particles of type i with energy E_i emitted in the source region, ϕ_i is the fraction of particle energy emitted in the source which is absorbed in target, m_{r_t} is the mass of the target. It is important to note that the target can also be a source.

For organ-based dosimetry, MIRD have used an anatomically representative phantom called 'Reference Man' to precalculate S-values for a broad range of clinical dosimetry applications by simulating the transport of hundreds of particle types, energies and activity distributions using Monte Carlo. The OLINDA/EXM software expands on this methodology by enabling the user to evaluate a larger set of reference geometries, and include minor patient-specific adjustments of the reference patient geometry, using interpolation of a set of reference conditions [77]. A more advanced technique is voxel-based dosimetry, also operating within the framework of Equation 2.1 [74]. By this method, each voxel of an activity distribution acts as a source and a target. Dose is thus calculated by convolving the activity distributions with the kernel given by the S-value. The primary advantage of this method of dose calculation is its consideration of patient-specific geometry. A notable weakness is that the kernel does not take into account heterogeneity in the patient anatomy [74]. This limitation can be addressed by full Monte Carlo simulation of particle transport resulting from the given activity distribution, but is only beneficial in some circumstances [78]. In the context of pure α-emitters, the α-particles are non-penetrating on the macroscopic scale and thus organ-based dosimetry must only consider the case where the source is also the target. Although this greatly simplifies the problem of calculating absorbed dose on a macroscopic level, in general, it is completely inadequate for describing the microscopic dose deposition of α-emitters that define their biological impact.

An important aspect of the MIRD formalism is that it can be applied on both a macroscopic scale (e.g. where the source and target are whole organs) or a microscopic scale (e.g. where the source is cell cytoplasm and the target is the cell nucleus). The short-range of alpha emitters means that, on a macroscopic level, the energy of the alpha-particle is absorbed at the location of α-decay. For α-emitting radionuclides, the S-value is designed to give the average absorbed dose to cell nuclei, given some microscopic distribution of the alpha emitter. Calculation of the S-value as applied to α-decay defines the target as the cell nucleus and the source as an assumed microscopic distribution of the radionuclide. S-values have been calculated from Monte Carlo simulations of α-particle energy deposition; these have been repeated for a set of standard cell and nucleus size combinations, with multiple generic geometries (e.g. homogeneous distribution, membrane-bound distributions, etc.). Dose calculations based on these S-values provide the approximate mean absorbed dose to cell nuclei for representative conditions. The application of these methods to ^{211}At dosimetry requires imput with respect to the cumulative activity distribution, as well as, a knowledge regarding the microscopic distribution with respect to

critical structures.

Image-based activity measurements

For dose calculations using Equation 2.1, the measured quantities in the MIRD formalism are activity and its physical distribution, both spatially and temporally. In the context of ^{211}At (or any α-emitter), knowledge about the microscopic (or cell-level) distributions are often required to properly understand the biological outcome of the dose distributions. The according measurements are not generally possible in humans but information can be gained from theoretical modelling/calculations, cell studies, and *ex vivo* animal measurements. Inferences regarding the clinical situation can be made, in turn, by extrapolating those findings. By combining the information gained by these exercises with patient-specific factors and theranostic imaging (or other diagnostic tools), a better understanding of dose response can emerge and provide a basis for optimizing therapeutic efficacy on a patient-specific basis.

α-particle dedicated *ex vivo* autoradiography

Due to the short range of the α-particle radiation, the cell-level (oligo-cellular) activity distributions are determines the biological damage. Activity distributions can be imaged with high resolution using an *α-camera*, a technology that was pioneered relatively recently and originally assessed for ^{211}At-TAT [79]. The α-camera measures the activity distributions in tissue samples imaged *ex vivo* to provide α-particle dosimetry for animal experiments and is of great interest to quantitative TAT dosimetry. Briefly, the procedure for α-camera imaging is as follows: The sample containing ^{211}At –for example, an organ harvested from a treated animal subject– is frozen and cut extremely thin ($\sim$14 μm) using a cryostat microtome, into *cryosections*. These cryosections are then placed on top of a 60 micron thin layer of activated zinc sulfide phosphor, a scintilator, which is thick enough to completely stop all traversing α-particles. The scintillator emits light isotropically and proportional to α-particle dose deposition coming from the decay of ^{211}At in the sample. Some of the light is projected back through the cryosection to a Charge-Coupled Device (CCD) for detection. The spatial resolution of the resulting ^{211}At distribution image is approximately 35$\pm$11 μm determined experimentally, and linearity and uniformity for these detectors have been experimentally confirmed [79]. For an α-camera image, histological staining of the next cryosection sliced from the sample can provide a detailed image of the underlying microscopic anatomy . This technique has been expanded upon with the iQID camera, which uses optical intensifiers to increase energy resolution. A benefit of this is that isotope can be identified by the energy of the emitted α-particles, useful for isotopes with multiple α-emitting daughter [80]. In this way, α-cameras and related technologies can provide valuable activity distributions required for quantitative,

meaningful cell-level dosimetry.

SPECT imaging with ^{211}At

With complement from cell-level dosimetry, SPECT provides necessary input for clinical dosimetry based on the MIRD formalism by determining activity distributions on a macroscopic scale [76]. Activity distributions can be measured with SPECT scanners that detect penetrating, ionizing photons originating from a radioactive source distribution, in 2-dimensions, and from multiple angles, in order to geometrically determine the source geometry and quantify the activity [4, p. 706]. For conventional SPECT scanners, photons are detected as 2-dimensional projections from the radioactive source using a flat-panel (planar) thallium-doped Sodium Iodide (NaI(Tl)) scintillation detector. This provides a planar *image* (or 2-D array) where pixel values depend on the amount and spatial distribution of the activity. Since photons produced by radioactive decay are produced *isotropically*, meaning in any direction with equal probability, a collimator is required in order to establish the direction of detected photons for which their source of origin can be inferred. These collimators (most commonly as holes arranged in parallel) are typically made of metal (such as tungsten (W) or lead (Pb)) that block photons (by attenuation) which do not originate from a particular direction. While still effective, the use of collimation does not permit differentiation between *primary* photons, coming from the direction of the source, from *scattered* photons, which have undergone a change in direction from that of the primary photon, mainly by Compton scattering (as well as coherent scattering). In addition, photons can occasionally penetrate the collimator and are counted as originating from the wrong location. These factors amount to blurring and noise in the detected images.

The 3-D activity distribution is reconstructed from the set of planar images (measured from multiple angles). The task of reconstruction is accomplished using the Maximum Likelihood Expectation Maximization (MLEM) or a closely related algorithm ([81]. The principle behind the MLEM approach is to make a prediction of the activity distribution, determine the projections that would result from that prediction, and make iterative changes to the predicted activity distribution until the measured and predicted projections converge [82, 83]. Based on this method, Ordered-Subset Expectation Maximization (OSEM) performs this task with greater computational efficiency by first dividing the total number of projections considered by each iteration into smaller subsets of projections for preliminary MLEM optimization before performing the operation with the complete data set [83, 84]. For translation from activity to time-integrated activity (cummulated activity) for dose calculations (as according to Equation 2.1), *time-activity curves* must be determined that describe changes in the activity with respect to time, made possible by interpolating between a serial SPECT measurements or one SPECT measurement and

a set of planar images [74].

SPECT was first evaluated for measuring ^{211}At activity distributions in the early 1990's at Duke University (Durham, NC) [50, 51]. For multiple collimator designs, 3-dimensional activity distributions were reconstructed using filtered backprojection based on images acquired by NaI gamma cameras. This study found quantitative measurements could be accomplished for simple phantom geometries with approximately 10% error, provided that attenuation and scatter was accounted for during reconstruction. Phantom measurements indicated that the achievable resolution for this system was 19.5 mm (FWHM)[4] [50]. These studies were performed over 20 years ago and modern SPECT imaging can be expected to perform better. SPECT scanning was utilized for the clinical trial completed with ^{211}At for ovarian cancer. These measurements were effective at determining the extent of perfusion for ^{211}At abdominal cavity after injection to the intraperitoneal space, and that no uptake was observable in the lungs, liver and kidney [47]. Both clinical trials measured thyroid uptake with 2-D imaging acquired by γ-scintigraphy (planar γ-camera imaging) determining that uptake of ^{211}At in the thyroid was absent or close to background (not significant), when the blocking agent was used.

To date, experience with ^{211}At-based SPECT imaging is relatively low and this technology appears to be an understudied area of research. Given the low intensity of low energy Po X-rays produced from ^{211}At decay, the possible applications of theranostic SPECT imaging with ^{211}At will perhaps be few in number, as well. The labelling of TAT targeting molecules with higher energy photon-emitters (e.g. ^{123}I) and positron emitters (e.g. ^{124}I) could provide surrogate activity distributions for ^{211}At-TAT dosimetry calculations. This would benefit from highly stable labelling for the radio-immunoconjugates to prevent errors arising from the differences in biodistribution of astatide and iodide. Additionally, the targeted surrogate would only be valid if its *in vivo* distribution did not deviate significantly from the astatinated analog. Given the chemical similarity of iodine and astatine, as well as, the highly stable labelling provided be decaborate-derived compounds, it is quite likely that certain iodine isotopes, specifically ^{123}I (SPECT) and ^{124}I (PET[5]) will be used for ^{211}At dosimetry. The application of these surrogates could certainly have impact for ^{211}At dosimetry but remain to be validated.

Chapter summary

Expanding on the concepts originally introduced in chapter 1, this chapter presented background material regarding the use of ^{211}At in medicine. Topics included the thera-

[4]For a function $y(x)$, Full width half-maximum (FWHM) is given by the difference in values of x (an independent variable, in this case distance) which spans the maximum value of y (a dependent variable, in this case voxel intensity), for which the values of y are equal to half its maximum value.

[5]Positron Emission Tomography, medical imaging system which uses coincidence detection of annihilation photon pairs produced by positron-emitting isotopes, such as ^{124}I.

peutic advantages of ^{211}At as well as its biodistribution, labelling chemistry, clinical trials, and dosimetry. Two important concepts were the high *in vivo* stability of biomolecular labelling with *closo*-decaborate(2-) moieties, and the potential role of SPECT-based theranostic dosimetry, particularly with the use of iodine imaging surrogates.

Chapter 3

^{211}At Production and the ISAC Facility

Astatine (named for the Greek word *astatos*, meaning unstable) has atomic number (Z) 85 and has no stable isotopes. The longest-lived isotopes of astatine are ^{210}At ($t_{1/2}$ = 8.1 h), ^{211}At ($t_{1/2}$ = 7.2 h), and ^{209}At ($t_{1/2}$ = 5.4 h). It is the rarest naturally occurring element that is found on Earth, with minute quantities produced at a steady rate as short-lived components of the natural actinide decay chains. Even still, astatine was first discovered in 1940 at the University of California, Berkeley, by producing the ^{211}At isotope artificially using an α-particle accelerator driven nuclear reaction (further discussed in §3.1) [85]. Almost immediately after its discovery, ^{211}At was hypothesized to have medical applications, specifically for the treatment of cancer [86]. Modern clinical applications with ^{211}At are estimated to require activities of up to approximately 2 GBq per patient, while preclinical studies in mice can be performed using activity of roughly 0.1-1 MBq per mouse [49, 63, 87, 88]. The current limit to the supply of ^{211}At is one of the most significant impediments to the clinical application with this radionuclide. This fact is not the result of difficulties in production and isolation technologies, but instead is determined by the limited availability of α-particle accelerators with appropriate beam characteristics required for conventional methods of producing ^{211}At [45]. The methods of ^{211}At production and their implications are discussed in the following sections. Conventional production and isolation routes for ^{211}At are discussed in §3.1. Next, experimental production via the the ^{211}Rn/^{211}At generator system is presented as an alternative production strategy in §3.2, along with current challenges in this area. This discussion is expanded in the context of TRIUMF's infrastructure for producing rare isotopes in §3.3, with considerations for ^{211}Rn and ^{209}At production.

^{211}At production via the ^{209}Bi(α,2n)^{211}At reaction

Currently, the production of clinically-significant ^{211}At activity (roughly between 3 and 7 GBq) is accomplished by bombarding a bismuth-209 (^{209}Bi) target with 28-29 MeV α-particles [45]. As an α-particle approaches the nucleus of the ^{209}Bi atom, it is slowed by the coulomb potential. If the α-particle has sufficient energy, called the *threshold energy*,

it can overcome the coulomb barrier and be incorporated into the nucleus [41, p. 59-64]. Upon receiving the residual energy of the α-particle, the nucleus is left in an excited state and lowers its energy by altering its nuclear structure, sometimes with the emittance of neutrons (a process called *neutron evaporation*) [41, p. 62]. For the compound nuclear formation of single α-particles and ^{209}Bi nuclei, the excited nuclei enter lower energy states by ejecting neutrons that occupy the highest energy nuclear orbitals.

The energy dependence of the cross-section[1] ($\sigma(E)$) for ^{211}At production regarding ^{209}Bi target bombardment with α-particle beams has been empirically determined . In general, the production rate with respect to time t, for reaction cross-section and initial particle energy E_0, can be calculated with Equation 3.1 [54, 89],

$$-\frac{dn}{dt} = \text{production rate} = nI\left(1 - e^{-\lambda t}\right)\int_{E_O}^{E_f} \frac{\sigma(E)}{dE/dx} dE \tag{3.1}$$

where n is the number of target nuclei per cm^2, I is the incident particle flux per unit time, λ is the decay constant[2] of the product, dE/dx is the stopping power, and E_f is the particles energy at the end of its range.

For bismuth targeted with α-particles, ^{211}At is produced with a threshold energy of 21 MeV and the subsequent evaporation of 2 neutrons, identified as an (α,2n) reaction [41, p. 64]. The cross-section for this reaction reaches a maximum of 0.8 Barns (8×10^{-25} cm^2) when the α-particle energy is approximately 31 MeV. The theoretical α-particle energy threshold for the ^{209}Bi(α,3n)^{210}At reaction is 28.6 MeV, and the cross-section of this reaction increases sharply above 30 MeV ([89]). ^{210}At cannot be chemically separated from ^{211}At and decays to polonium-210 (^{210}Po, $t_{1/2} = 138$ days), which is highly toxic and can jeopardize clinical applications, even in minute quantities; the recommended annual limit of ^{210}Po is 10 kBq for workers, as determined by the International Commission on Radiation Protection (ICRP) [90]. To prevent the production of ^{210}At via the (α,3n) reaction, α-particles are typically accelerated to a maximum of 28-29 MeV for ^{211}At production.

The α-particles are accelerated to 28-29 MeV by an α-particle cyclotron and made incident to a natural bismuth target. Natural bismuth is composed of only the ^{209}Bi isotope and the targets for ^{211}At are fairly inexpensive to manufacture. Bismuth target designs can be made in a variety of forms, from simple cuboidal shapes supported by aluminium frames [91], to more complex designs such as targets inside of the cyclotron with curved surfaces that form to the path of orbiting α-particles [92, 93].

Only a handful of cyclotrons are currently being used to produce ^{211}At. The production of ^{211}At via the ^{209}Bi(α,2n)^{211}At reaction is currently limited to the following institu-

[1] The probability of nuclear reaction as a function of particle energy, in units of area.

[2] By the definition of half-life, the decay constant (λ) of a radionuclide is equal to $ln(2)/t_{1/2}$.

tions: University of Washington Medical Center (The University of Washington, *Seattle, WA, US*), Rigshospitalet (National hospital of Denmark, *Copenhagen, Denmark*), Duke University Medical Center (Duke University, *Durham, NC, US*), The National Cancer Institute (National Institutes of Haelth, *Bethesda, MD, US*), The Heavy Ion Laboratory of the University of Warsaw (*Warsaw, Poland*), The Istitute for Transuranium Elements-Joint Research Centre-European Commission (*Karlsruhe, Germany*), and most recently at The University of Nantes (*Nantes, France*).

^{211}At can be isolated from the bismuth target using at least three different methods: dry-distillation[94], two-stage dry-distillation [95], and wet-chemistry [87, 96]. A reasonably high efficiency in isolated yield of 67%±16% has been reported for either dry-distillation procedure[3] [64, 93]. In comparison, the chemistry approach has been shown to provide 85%±11% isolation yield efficiency [71, 87].

Dry-distillation

With the *dry-distillation* procedure [94], isolation begins by heating the ^{211}At-containing bismuth to approximately 670 °C. At this temperature, some of the ^{211}At evaporates and can be evacuated by a pressure gradient and trapped as condensation in capillary tubes, roughly held at -77 °C. Chloroform can be used to rinse ^{211}At condensate from the capillary tubes into a vial suitable for beginning radiolabelling procedures, after the chloroform is removed by evaporation.

Two-stage distillation

Another distillation procedure takes advantage of disposable targets, and is referred to as *two-stage distillation* [95]. In the first stage, the bismuth is heated to over 800 °C. At this temperature, astatine can be vacuum pumped through a glass column and adsorbed to a silver wire held at negative potential, for collection. The glass column is then filled with a small amount of methanol. In the second step, the astatine is desorbed in the methanol by heating the silver wire to 500 °C, while keeping the methanol relatively cool.

Wet-chemistry

Alternative to dry-distallation and two-step distillation for ^{211}At isolation, *wet-chemistry* has been shown to provide better consistency with respect to activity yield efficiency [71]. The technique begins by dissolving the bismuth target with concentrated HNO_3, which is then removed (with the bulk mass of ^{209}Bi by distillation before the remaining residue is dissolved in 8 M HCl. The challenge is to remove the ^{211}At from such a highly acidic solution (and separate it from any residual bismuth). This is done by mixing the aqueous solution with di-isopropyl ether, an organic solvent, in which the ^{211}At is efficiently

[3] reported yield efficiency for two-stage distillation was 68% [95].

extracted, leaving behind the bismuth target material. The aqueous layer is discarded and the ^{211}At can then be extracted from the organic phase with 1-2 N NaOH, in the form of astatide (At^-).

The ^{211}Rn/^{211}At generator system

The rarity of α-particle cyclotrons, the low beam currents provided by these accelerators, and the short half-life of ^{211}At collectively limit the availability of ^{211}At for clinical evaluation. Moreover, this method of production can only provide ^{211}At for relatively local and immediate use. For these reasons, novel approaches to ^{211}At production should be considered. An alternative method for producing ^{211}At is via the decay of its parent isotope ^{211}Rn ($t_{1/2} = 14.6$ hours), which decays by electron capture to ^{211}At in 73% of radioactive decays; The remaining 27% of ^{211}Rn decays proceed by alpha decay to produce polonium-207 (^{207}Po; $t_{1/2} = 5.8$ hours) [44]. The decay of ^{211}Rn and subsequent grow-in of ^{211}At and ^{207}Po is quantitatively described in Figure 3.1.

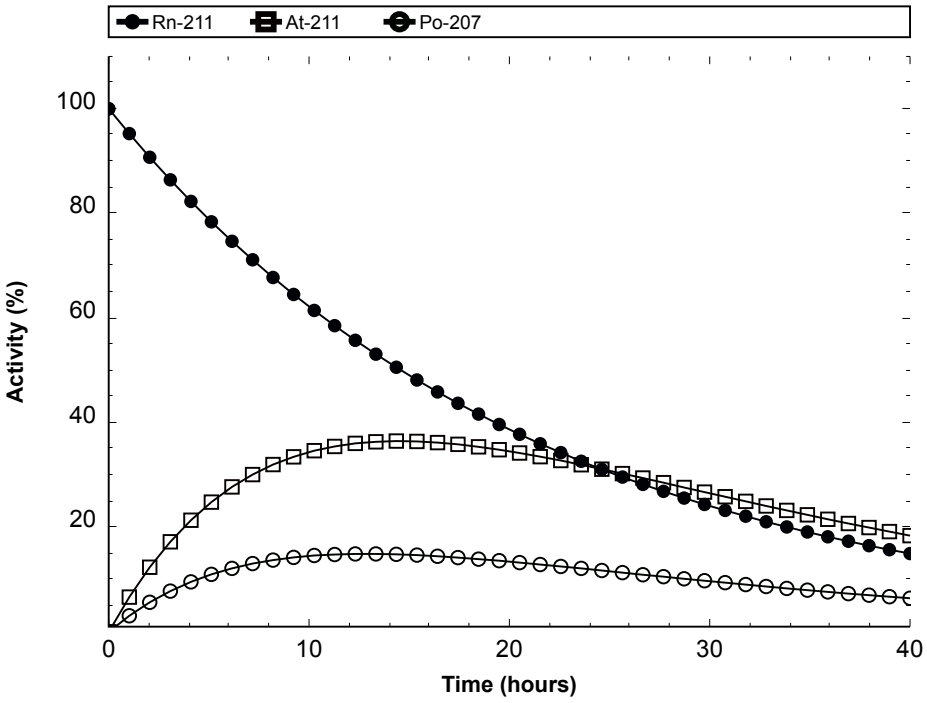

Figure 3.1: The decay of ^{211}Rn and grow-in of ^{211}At and ^{207}Po progeny.

Generator systems for medical isotope production can be highly advantageous for the wider distribution of short-lived isotopes. For a given generator system, the longer-lived parent activity decays in containment and the concentration of shorter-lived daughter

activity grows in over time, according to Equation 3.2 [54]:

$$A_d(t) = A_p(0)b_d\left[\frac{(\lambda_d)(e^{-\lambda_p t} - e^{-\lambda_d t})}{\lambda_d - \lambda_p}\right], \ (\lambda_p < \lambda_d, \text{ for generators}) \tag{3.2}$$

where $A_d(t)$ is the amount of the daughter isotope at time t, $A_p(0)$ is the initial amount of the parent isotope, b_d is the decay branching ratio for producing the daughter, and where λ_p and λ_d are the decay constants of the parent and daughter, respectively [54]. After a period of time, the daughter activity decreases with the same half-life as the parent, a condition called *transient equilibrium* [97].

Compared to conventional ^{211}At production, the ^{211}Rn/^{211}At generator is met with distinct challenges, namely the manipulation of ^{211}Rn gas and its isolation from nuclear reaction by-products and target materials, as well as addressing the contamination of ^{211}At daughters with the ^{207}Po also produced in the decay of ^{211}Rn. Radon is a noble gas and is chemically inert, while having a very low boiling point at -62°C. This makes the containment and separation of trace amounts of radon difficult in the standard laboratory setting, with associated implications for radiation safety. Still, the generator principle could make ^{211}At more available by widening its physical distribution to more distant users, and ^{211}Rn production is actively pursued in a limited capacity by a handful of laboratories world-wide.

Two primary methods for producing ^{211}Rn have been pursued, either by lithium ion beams (either by ^{209}Bi(^{7}Li,5n)^{211}Rn [55, 57] or ^{209}Bi(^{7}Li,5n)^{211}Rn [58]), or by the spallation of actinide targets [53, 56]. The production of ^{211}Rn is extremely limited due to the necessity of either a means of lithium ion acceleration to 40-60 MeV or high energy proton accelerators (100-1000 MeV). As a result, any construction of a clinical ^{211}Rn/^{211}At generator system, at this time, is still very much in early stages of development. Continued evaluation of ^{211}Rn production and purification remains highly motivated by the strong clinical potential of ^{211}At.

^{211}Rn production with lithium ion beams

^{211}Rn can be produced directly by the nuclear reaction of ^{209}Bi targets with lithium ion beams, with either ^{6}Li (42 MeV) or ^{7}Li (60 MeV) [57, 58]. In both instances, the beam energy is low enough to prevent the co-production of ^{210}Rn/^{210}At/^{210}Po. Incorporation of the ^{6}Li (or ^{7}Li) nucleus by ^{209}Bi is followed by the evaporation of 4 (or 5) neutrons, producing ^{211}Rn *in situ* that is presumably held in the solid bismuth target by van der Walls interaction. Radon isolation from a bismuth target has been performed by recent studies in two distinct ways: In the first method, ^{211}Rn was isolated from the ^{209}Bi target and radioactive contamination by dissolving the bismuth in 6-8 M HNO_3 and extracting the radon into dodecane ($C_{12}H_{26}$) by simple mixing [57]. The organic solvent was shown

to efficiently trap the radon gas, which nearly completely vacated the aqueous solution. The contaminants (including Bi, Po, and At isotopes) were then extracted by washing with aqueous solutions. In the second method, ^{211}Rn gas that diffused from Bi targets was collected into charcoal traps during continuous lithium beam delivery [58]. Using a low pressure flow of inert gas, the radon was directed through a column of activated charcoal where it was observed it could be stopped completely (trapped). Efficient recovery of the radon by diffusion proved to be problematic, requiring that the bismuth target be heated to near melting temperature, destroying the target and interrupting continuous operation. Although the ^{209}Bi(^{6}Li,4n)^{211}Rn and ^{209}Bi(^{7}Li,5n)^{211}Rn reactions have proven to be effective routes for producing ^{211}Rn with relatively low radioactive contamination, the medium energy lithium accelerators required for this reaction are even more rare than α-particle accelerators, limited to only three institutions world-wide: The Heavy Ion Medical Accelerator in Chiba (HIMAC, Chiba, Japan), The Universal Linear Accelerator (GSI, Darmstadt, Germany), and The ATLAS Accelerator (ANL, Chicago, USA).

^{211}Rn production by the spallation of actinide targets

The spallation of actinide targets (either uranium or thorium) with high energy protons (on the order of $10^2 - 10^3$ MeV) is an attractive means of producing ^{211}Rn. In spallation, protons collide with target nuclei with enough energy to eject many numbers of protons and neutrons, in multiple combinations [41, p. 65]. The bombardment of natural uranium with high energy protons results in the production of a wide range of isotopes by spallation, as well as, subsequent nuclear fission and multiple types of lower energy nuclear reactions. The production rate for radionuclides produced in the bombardment of [^{238}U]uranium (at 0.05 mol/cm^2, equal to approximately 12 grams of uranium) with 480 MeV protons is shown in Figure 3.2 (Geant4[4] target simulation (unpublished), courtesy of TRIUMF).

Due to the high yields for ^{211}Rn, the spallation of actinide targets is an attractive production route for enabling a clinical ^{211}Rn/^{211}At generator. The greatest challenge to this endeavour is the handling and discarding of the numerous and abundant radioactive by-products. In most cases, it is possible to separate elements on a chemical basis; however, chemical properties are indistinguishable for isotopes of the same atomic number. Isotope separation is possible with the use of mass separators, which use the mass dependence of a charged-particle's trajectory through a magnetic field to spatially separate the isotopes with different atomic mass (A). The combination of isotope production by spallation and immediately consecutive extraction and mass separation of the radioactive products is known as the Isotope Separator On-Line (ISOL) technique [99]. This state-of-the-art technology is used to produce Rare-Isotope Beams (RIB) at TRIUMF's

[4]Geant4 is a powerful tool kit for performing Monte Carlo simulations for particle physics [98].

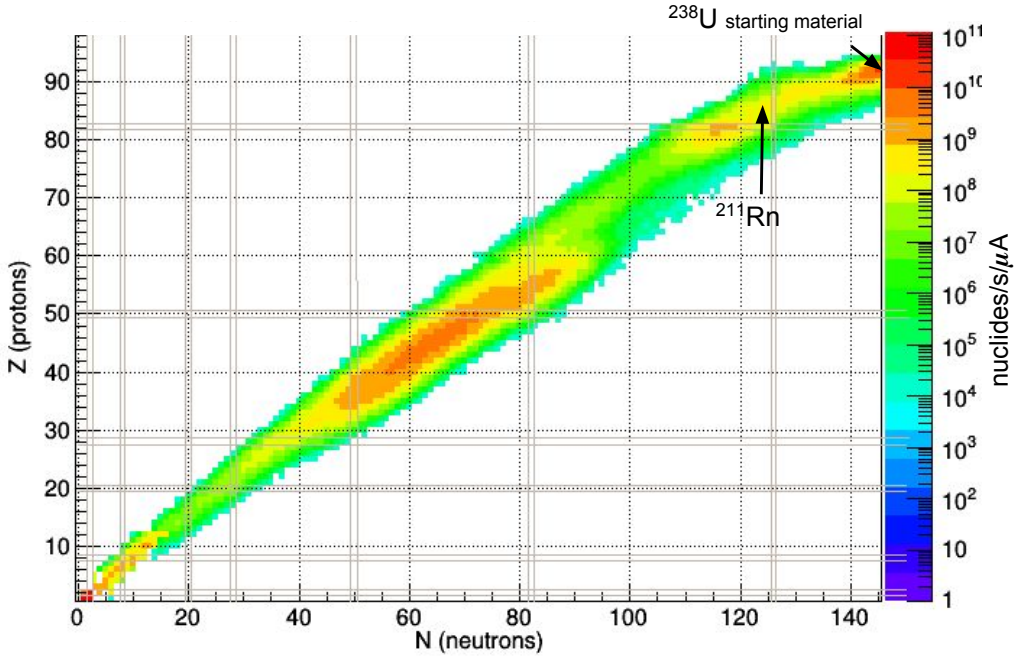

Figure 3.2: Calculated nuclide yields (in nuclides/s/μA) for 480 MeV protons on a 0.05 mol/cm^2 [^{238}U]uranium target. Monte Carlo calculated yields were performed with a Geant target simulation, courtesy of TRIUMF (unpublished).

Isotope Separator and Accelerator (ISAC) facility [100, 101].[5] ISAC can be used to produce radioactive ion beams composed of (or decaying to) a variety of radon and astatine isotopes.

The ISAC facility for RIB production

The main cyclotron at TRIUMF accelerates hydrogen ions (H^-) up to 520 MeV and is capable of supplying the high energy proton beams required for the production of ^{211}Rn by the spallation of actinide targets (uranium or thorium). The production, mass separation, yield measurement, acceleration and delivery of RIB is accomplished routinely at the ISAC facility, described in Figure 3.3 (major components of which are discussed in the following sections). Briefly, proton beams up to 480 MeV are stripped from TRIUMF's Main Cyclotron and delivered continuously at up to 100 μA to target materials at the ISAC target station. The targets are heated to temperatures up to 2200 °C, permitting the diffusion of radioactive products away from the bulk target material [100, 101, 103]. The radionuclides that escape are selectively ionized (depending on the mechanism of ionization) and accelerated across an electric potential of up to 60 kV, electrostatically directed further downstream [103]. The resulting RIB of mixed mass numbers is then directed through the high resolution mass separator, with mass resolution of 2500:1 (ions of selected mass mumber:ions of any other mass numbers) [103]. The strong magnet of

[5]ISAC is the predecessor of TISOL (Test On-Line Isotope Separator), TRIUMF's original implementation of the ISOL-technique established in the 1980's [102].

the separator bends the beam to select the particular path of the desired atomic mass number. The resulting RIB is then delivered to a number of locations, including the ISAC Yield Station (IYS), the ISAC Implantation Station (IIS), or a number of physics experiments with or without further linear acceleration. The IYS is equipped with the infrastructure for remote yield quantification and beam composition analysis, while IIS can be used to implant the radioactive material for manual recovery. RIB production, mass separation and beam transport take place continuously during target spallation (*on-line isotope separation*).

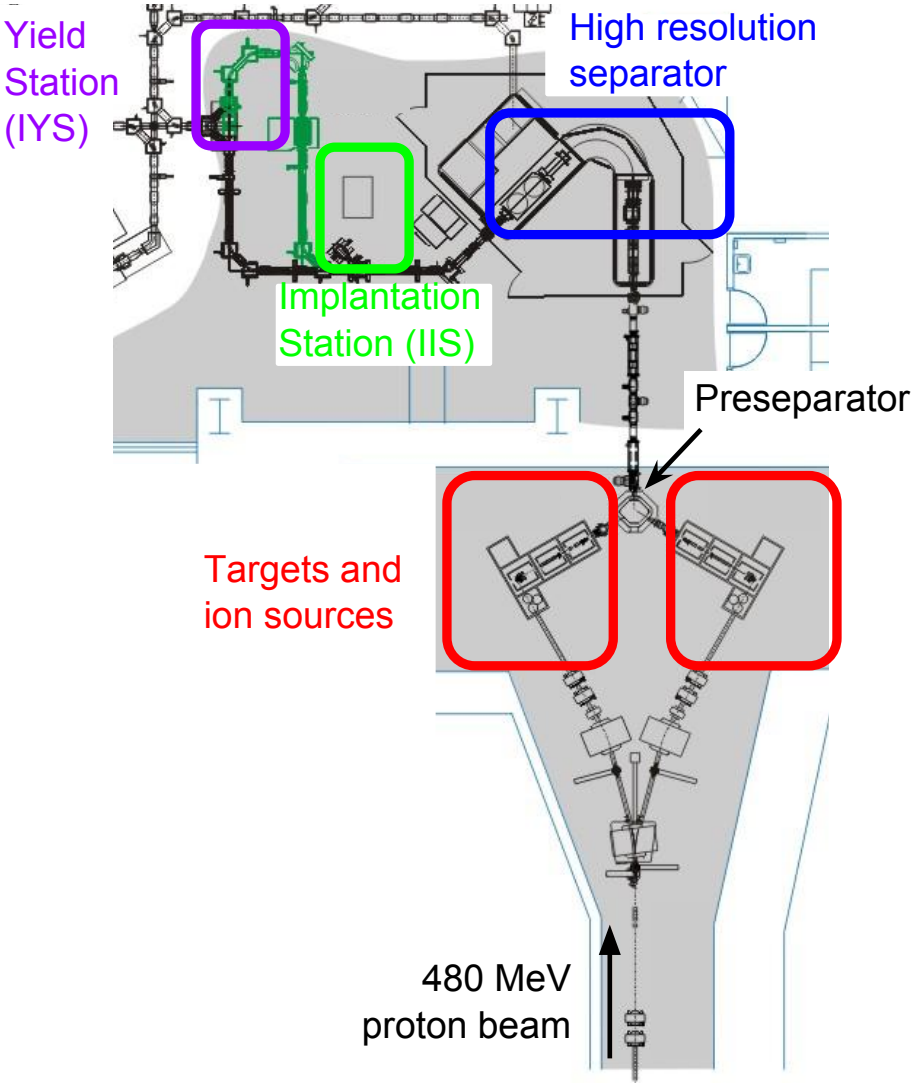

Figure 3.3: Beamline diagram for the target and separator of ISAC, the radioactive ion beam facility at TRIUMF.

ISAC target design

ISAC operates with several target materials, depending on the required RIB for a given application. For example, tantalum (Ta) provides a suitable target material for producing lanthanide isotopes, while thorium and uranium are required to generate RIB of higher

atomic mass, including isotopes of radon and astatine. ISAC uranium carbide target material is contained within a tantalum (Ta) tube (length = 19 cm, outer diameter =1.9 cm, wall thickness 0.4 mm), welded (or crimped) shut with tantalum end caps [104]. The only point of escape for material is a second narrow Ta tube orthogonally intersecting the target tube, provides a conduit for escaping radioisotopes that can form the RIB. Tantalum provides a container with very high melting point above 3000 °C, and is relatively unreactive with respect to most elements. Resistive heating can be supplied to the tantalum target tube (shown in Figure 3.4a) to increase the temperature above what is supplied by the proton beam, increasing diffusion and effusion of the spallation products away from the target material. The target is mounted to electrically insulating material and surrounded by a water-cooled copper heat shield (Figure 8.2b).

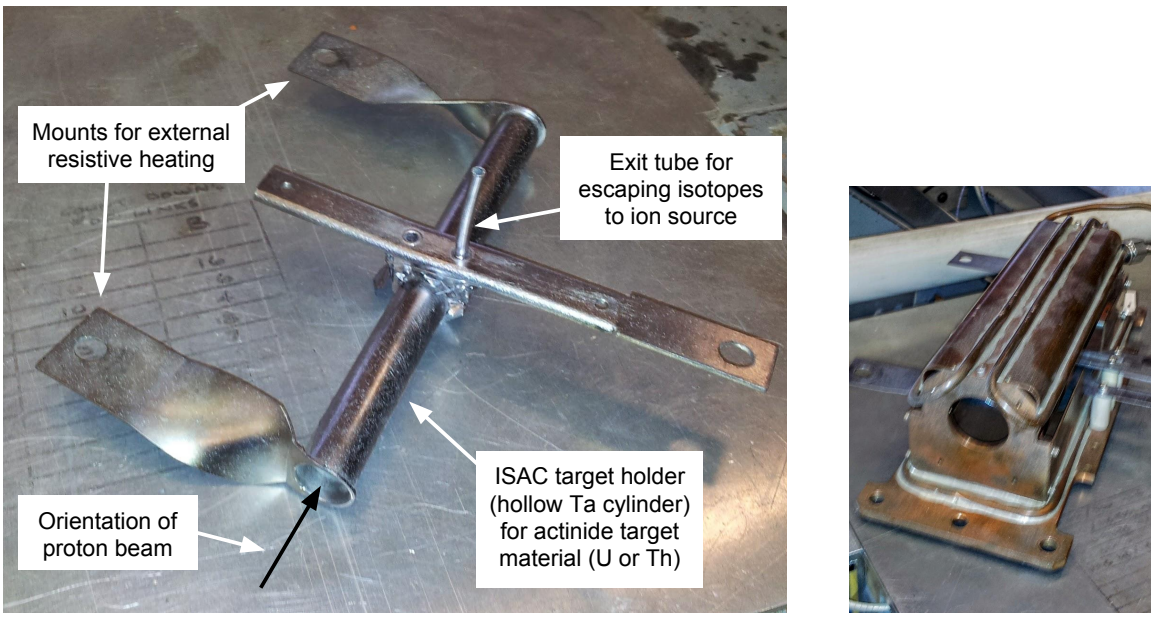

Figure 3.4: **(a)** Tantalum target holder for containing actinide targets during proton irradiation, and **(b)** the water-cooled copper heat shield with the target holder inside.

ISAC ion sources

Isotopes that diffuse from the spallation targets must be ionized before electromagnetic acceleration and steering can be used form and propel the beam downstream, away from the target and towards an experiment, requiring an *ion source*. The subject of ion sources is an immense topic and the discussion presented here is only a brief (and narrow) introduction to some of the concepts that are important to consider when requesting RIB of Rn and At isotopes, at ISAC. Several types of ion sources exist, categorized by the physical mechanism of ionization they employ. These include surface ionization, laser resonance, and different types of electron beam sources such as electron cyclotron resonance (ECR) and Forced Electron Beam Induced Arc Discharge (FEBIAD), all of which have

been used for RIB production at ISAC. Each have distinct advantages and disadvantages to be carefully considered for RIB production. The rhenium (Re) surface ionizing ion source has the simplest design: isotopes that randomly collide with the hot Re surface (up to 2200 °C) have a certain probability to be ionized, and this probability decreases exponentially with increasing 1^{st} ionization energy[6] of the particular isotope [104]. Surface ionizing ion sources are typically reasonably efficient for ionization energies below 6 eV. While this limits the possible RIB to those with low ionization energy, this can serve as a means of selection and greatly reduce the number of elements that compose a given RIB. Francium has the lowest ionization energy of any element and ionization of francium isotopes with this type of ion source is approximately 100% efficient, at ISAC. The FEBIAD uses a brute force method whereby the diffusing spallation products are ionized directly by an electron beam, creating a plasma from which the radioactive ions are electrostatically accelerated [105]. The ionization efficiency is much less dependent on ionization energy. Although the FEBIAD ion source provides a means of generating RIB of isotopes with high ionization energy, the resulting RIB are prone to suffer from high isobaric[7] contamination because of the lack of discrimination in ionization for different elements. The resonant laser ion source provides the most ideal means of isotope selection, providing the possibility of only ionizing isotopes of a particular element [106]. Laser ion sources are used for isotopes with ionization energies roughly between 6-9 eV, including those of Astatine [107]. Although the achievable beam purities are excellent, laser ion sources are not as efficient as other ion sources and result in RIB beam intensities that are 2-4 orders of magnitude lower, compared to the RIB produced by either Re surface ionizing or FEBIAD ion sources.

ISAC mass separators

Mass separators are used to enhance the composition of the RIB to single mass number, eliminating all but one isotope of a given element. This is accomplished by passing the RIB through a uniform magnetic field perpendicular to there motion, producing a mass-dependent curvature in trajectory. One single mass number is selected by collimating the split beam so that only one trajectory is preserved and steered further down the beamline. At ISAC, the range of mass numbers composing an RIB is initially reduced by the ISAC pre-separator to eliminate most of the radioactive contamination, and then passed through the ISAC high resolution separator to select a mass number, with an estimated resolution in mass discrimination of 2500:1 (selected mass:all other masses).

[6]Ionization energy is the energy required to free an electron bound to an atom with neutral charge, thereby ionizing it to the (1+) chemical oxidation state.

[7]Isotopes with the same atomic mass (A) but different atomic number (Z) are called *isobars*.

ISAC Yield Station (IYS)

The ISAC Yield Station is a fully remote-controlled facility for measuring the beam intensities and radioactive composition of RIB, following mass separation[107]. Briefly, ion beams are implanted into aluminized Mylar tape for short periods of time and measured *in situ* by γ- and α-spectroscopy, independently. Consecutive cycles of the procedure can be completed to improve statistics. The α-particle energy spectrum is measured with a pin diode (Hamamatsu S3590-9, Hamamatsu Photonics, Hamamatsu City, Shizuoka, Japan) remotely positioned in front of the tape after implantation. A High Purity Germanium (HPGe) detector (Ortec GMX40, Ortec®, Oak Ridge, TN) is used for measuring the γ energy spectra, and is normally positioned at 50 cm from the implantation point (The distance can be adjusted by a linear actuator to increase sensitivity.) β-particle radiation can also be detected by a set of 4 scintillation detectors. Using γ-spectroscopy and α-spectroscopy, the cumulative counts (Δn) for a particular emission energy can be used to calculate the RIB beam intensity (in terms of ions/s) for the corresponding radionuclide with decay constant λ, according to the following derivation [107]:

Calculation of RIB yield (ions/s) at IYS

For the implantation of radionuclide i at constant implantation rate (r_i) for a total time t_{EOB} (where subscript EOB, refers to End of Beam/Bombardment), the total number of atoms N_i at time t ($0 \leq t \leq t_{EOB}$) is given by the differential equation (Equation 3.3):

$$\frac{dN_i}{dt} = r_i - \lambda_i N_i, \qquad 0 \leq t \leq t_{EOB} \tag{3.3}$$

Solving for N_i as a function of t,

$$N_i = \frac{r_i}{\lambda_i}\left(1 - e^{-\lambda_i t}\right) \tag{3.4}$$

As shown in Figure 3.5, the amount of radionuclide $N(t)$ implanted at rate (r) would build-up to $N(0)$ according to Equation 3.4 for a total time $t_{collect}$ (time at end of collection), after which time it would simply decay exponentially:

$$N(0) = \frac{r}{\lambda}\left(1 - e^{-\lambda t_{collect}}\right) \tag{3.5}$$

At $t = t_{count}$, the difference in the number of atoms at $t = 0$ and $t = t_{count}$ is proportional to the total number of detected counts (Δn) during that time, and inversely proportional to the detector efficiency (ϵ_{det}) and branching ratio b, for the decay emission that was counted (γ-ray or α-particle):

$$N(0) - N(t_{count}) = N(0)(1 - e^{-\lambda t_{count}}) = \frac{\Delta n}{\epsilon_{det} b} \tag{3.6}$$

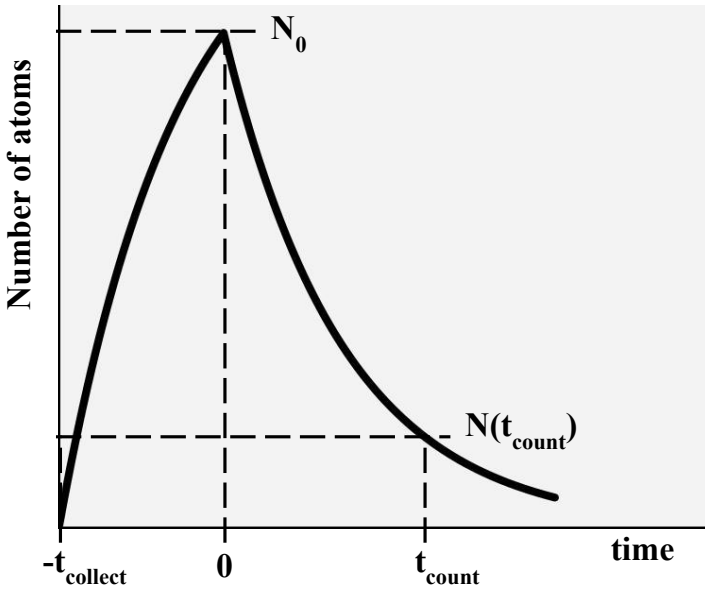

Figure 3.5: Theoretical RIB implantation (number of atoms as a function of time) for describing RIB intensity calculations.

Substituting $N(0)$ of Equation 3.5 into Equation 3.6,

$$\frac{r}{\lambda}(1 - e^{-\lambda t_{collect}})(1 - e^{-\lambda t_{count}}) = \frac{\Delta n}{\epsilon_{det} b} \tag{3.7}$$

Solving for production rate r,

$$r = \frac{\lambda}{1 - e^{-\lambda t_{collect}}} \times \frac{1}{1 - e^{-\lambda t_{decay}}} \frac{\Delta n}{\epsilon_{det} b} \tag{3.8}$$

ISAC implantation station

The ISAC implantation station (IIS) is the terminal end of a short section of beamline that originates very close to the high resolution separator beam exit point. The beamline is equipped with its own vacuum system and can be isolated from the vacuum of the main beamline with a gate valve, operated remotely. The IIS Faraday cup[8] (FC) can be inserted into the beam path upstream from the gate valve to measure beam current, relative to FCs positioned upstream or at other locations, such as the IYS.

Production of ^{211}Rn and ^{209}At with Rare-Isotope Beams (RIBs)

ISAC is capable of producing intense beams of short-lived radionuclides with high isotopic purity, while isobaric contamination can be minimized by the choice of ion source. ISAC is capable of producing RIB containing either ^{211}Rn/^{211}At or ^{209}At directly; however,

[8] A Faraday cup is an electrically conducting metal beam block designed to catch charges particles in a vacuum. The rate at which electric charges are collected (as deposited by the ions) provides a current measurement (charge per unit time).

efficient radon and astatine ionization requires the FEBIAD ion source in combination with actinide targets[9]. In recent years, uranium carbide targets have been more often combined with Re surface ionizing ion sources, which provide intense beams of francium isotopes that can serve as indirect pathways to the production of ^{211}Rn or ^{209}At.[10] Francium has the lowest ionization energy of any element and is ionized with nearly 100% efficiency. In Table 3.1, ISAC RIB intensity yields of ^{211}Rn or ^{209}At are compared to the intensity of their short-lived parent francium isotopes, ^{211}Fr or ^{213}Fr, respectively. ISAC Yield Station measurements for RIB produced under these conditions have consistently shown radium to be the only source of isobaric contamination. Typical ^{211}Fr beams have been measured to contain approximately 1% ^{211}Ra contamination, while ^{213}Fr beams were contaminated with roughly 30% of ^{213}Ra (see Table 3.1).

Table 3.1: RIB production rates at ISAC for various configurations relevant to the production of ^{211}Rn/^{211}At and ^{211}At. All yields were measured at the ISAC Yield Station, For RIB produced by spallation of uranium with 480 MeV protons at 9.8 μA. See Figures 4.1 and 4.3 for the decay schemes related to these RIB isotopes

Application	Ion	half-life (min)	1^{st} ionization energy (eV)	Yield (ions/s)	^{211}Rn or ^{209}At per ion	ISAC ion source	RIB (A)
^{211}Rn production:	^{211}Rn	876	11.18	1x10^8	1	FEBIAD	211
	^{211}Fr	3.1	3.94	1x10^9	0.2	Re Surface	211
	^{211}Ra	0.22	5.28	1x10^7	0.014	Re Surface	211
^{209}At production:	^{209}At	324.6	9.54	6x10^7	1	FEBIAD	209
	^{213}Fr	0.58	3.94	1x10^9	0.99	Re Surface	213
	^{213}Ra	2.7	5.28	3x10^8	0.66	Re Surface	213

Chapter summary

In this chapter, conventional practices for ^{211}At production were compared to production by the ^{211}Rn/^{211}At generator system, still in the early phases of development. Various options for pursuing the ^{211}Rn/^{211}At generator system were presented, with special consideration to high energy proton spallation of actinide targets. The ISAC facility was introduced, discussing the methods for producing mass separated ion beams, with examples of ^{211}Rn and ^{209}At production.

[9] Astatine ion beams were measured to be $10^2 - 10^3$ times lower using the laser ion source, compared to the FEBIAD ion source at ISAC.

[10] Note that beams requiring the FEBIAD ion source can be requested at ISAC, and availability will depend on scheduling decisions involving multiple beam requests, determined by the TRIUMF's Physical Science Division.

Chapter 4

Methods for ^{211}Rn/^{211}At and ^{209}At Recovery at ISAC

The ^{211}Rn/^{211}At generator system has been proposed as an alternative production method for ^{211}At (Meyer *et al*, 1980 [55]). At the present time, this generator is still in the early stages of development due in part to the severely limited production of ^{211}Rn (see §3.2). TRIUMF's implementation of the ISOL-technique at the ISAC facility provided the opportunity to produce significant amounts of ^{211}Rn, as well as study astatine isotopes rarely produced by more conventional production strategies. Specifically, ISAC RIB provided a means of producing ^{209}At for enabling its evaluation as a novel isotope for preclinical SPECT imaging for ^{211}At-based therapies. The primary aim of this study was the production of ^{211}Rn/^{211}At and ^{209}At collected from the decay chains of ^{211}Fr and ^{213}Fr, respectively, based on the ISAC yield data in Table 3.1. The approach taken was to collect the francium ions by implantation, safely monitor and transport the resulting radioactive inventory, and finally recover ^{211}Rn/^{211}At or ^{209}At in solution, suitably prepared for applications in ^{211}At-based therapy research.

This chapter discusses the methods used for producing, recovering, and isolating, ^{211}Rn/^{211}At and ^{209}At isotopes at TRIUMF. Critical aspects of producing these isotopes using mass separated francium and radium ion beams are presented in §4.1. §4.2 highlights methods related to the delivery of RIB to IIS with considerations to α-decay processes. The various designs of equipment and instruments for recovering the radioactive inventory are reviewed in §4.3. This is followed by a description of the methods used for target processing and isolation chemistry, provided in §4.4. Some small procedures for antibody labelling with the astatine isotopes in §4.5, followed by a brief description of the methods and equipment used for quantifying the process with activity measurements in §2.5.2. Finally, these sections are summarized in §4.7.

Production by mass separated beams of francium and radium

^{211}Rn production via ^{211}Fr and ^{211}Ra decay

^{211}Rn was produced via the electron capture decay of ^{211}Fr ions collected at the ISAC Implantation station. RIB composed of ^{211}Fr and ^{211}Ra decay to produce a variety of isotopes, including ^{211}Rn as well as a large amount of contaminating radioactive inventory. The decay diagram for the combination of ^{211}Fr and ^{211}Ra is shown in Figure 4.1 and an abbreviated list of radiations for each radionuclide is given in Table 4.1. The branching ratios for ^{211}Fr decay modes (electron capture vs α-decay) were not well known; Nuclear Data Sheets for A=211 (2013) report the branching ratios of ^{211}Fr as $b_\alpha > 0.80$ (α-decay) and $b_{ec} < 0.2$ (electron capture) [108].

Importantly, the decay chains of ^{211}Fr and ^{211}Ra demonstrated that the only radon isotopes that could be produced by these isotopes included ^{211}Rn and ^{207}Rn. Given the relatively short 9.2 minute half-life of ^{207}Rn compared to ^{211}Rn, the amount of ^{207}Rn would be negligible after a 2-3 hours (representing 10 half-lives of ^{207}Rn). This permitted the isolation of ^{211}Rn as the only Rn isotope, once the ^{207}Rn had decayed away. It was also noted that the longest lived isotopes in these decay chains were ^{207}Bi ($t_{1/2}$ = 33 years) and ^{203}Pb ($t_{1/2}$ = 2.16 days), both of which decay exclusively by electron capture to stable daughters. No α-decaying inventory had half-lives that exceeded that of ^{211}Rn.

The evolution of radionuclidic yields with respect to time following ^{211}Fr decay was calculated with the *Nucleonica Decay Engine* [109], and plotted in Figure 4.2. The rapid decay of ^{211}Fr (using $b_\alpha = 0.8$ and $b_{ec} = 0.2$) resulted in almost 98% of the initial activity being in the form of ^{207}At. After ten hours, the activity of faster decaying ^{207}At would drop below that of ^{211}Rn, while ^{211}At would grow-in and become nearly equal to that of ^{211}Rn between 20-30 hours. The largest source of contamination for the ^{211}Rn/^{211}At at that time would be ^{207}Po, as the dominant decay product of the large initial amount of ^{207}At. The slower and less significant grow-in of ^{203}Pb and ^{203}Bi would have amounted to additional contamination (in low relative proportion). Given that the branching ratios of ^{211}Fr were not known exactly, this calculation was only able to provide the expected trends in the evolution of radionuclidic inventory, not the actual activities of each radioisotope.

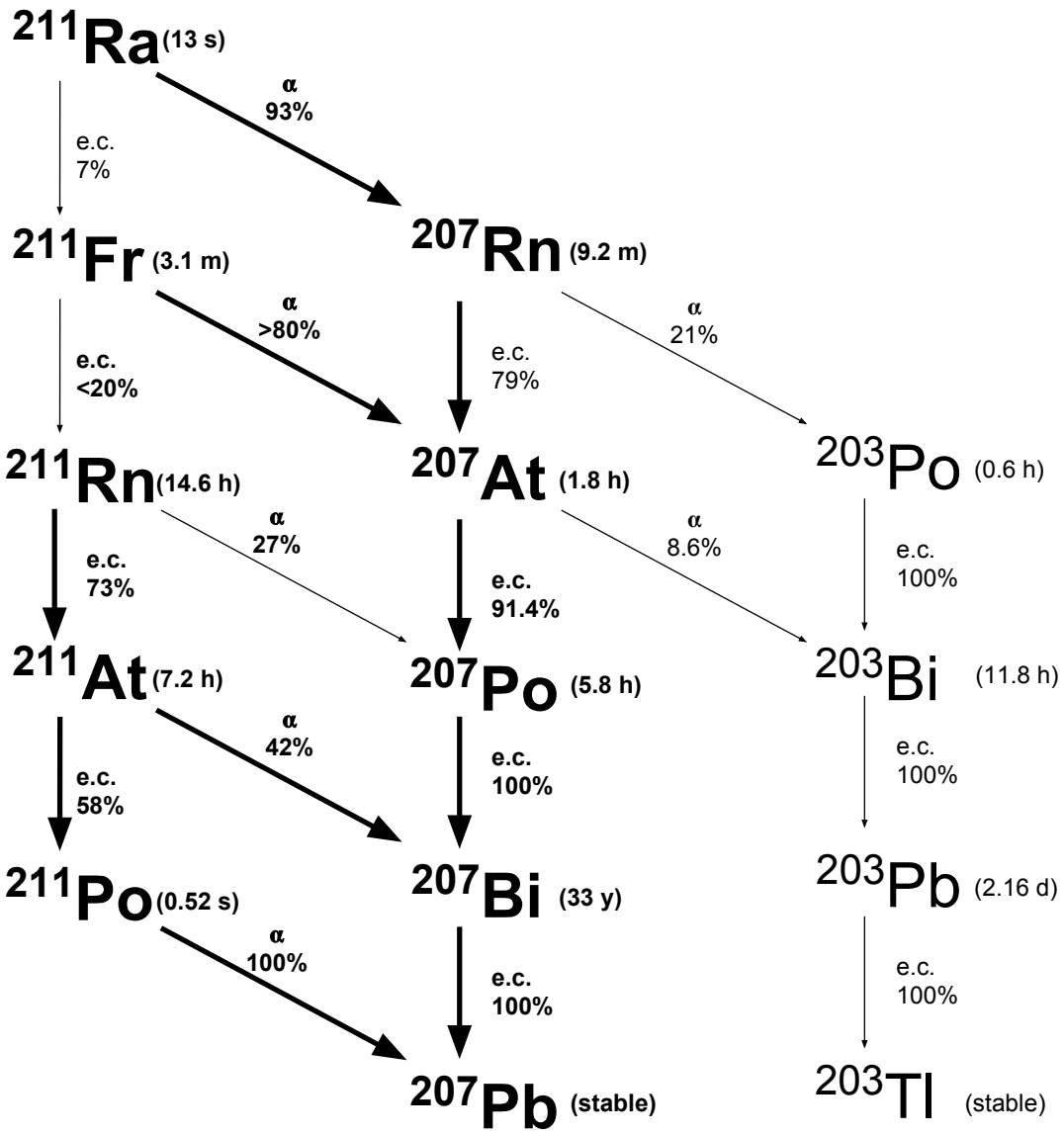

Figure 4.1: The combined decay chains of ^{211}Fr and ^{211}Ra leading to ^{211}Rn/^{211}At. Note that α = α-decay, e.c. = electron capture. β+-decays had very low probability in this mass range and were included in the e.c. probabilities.

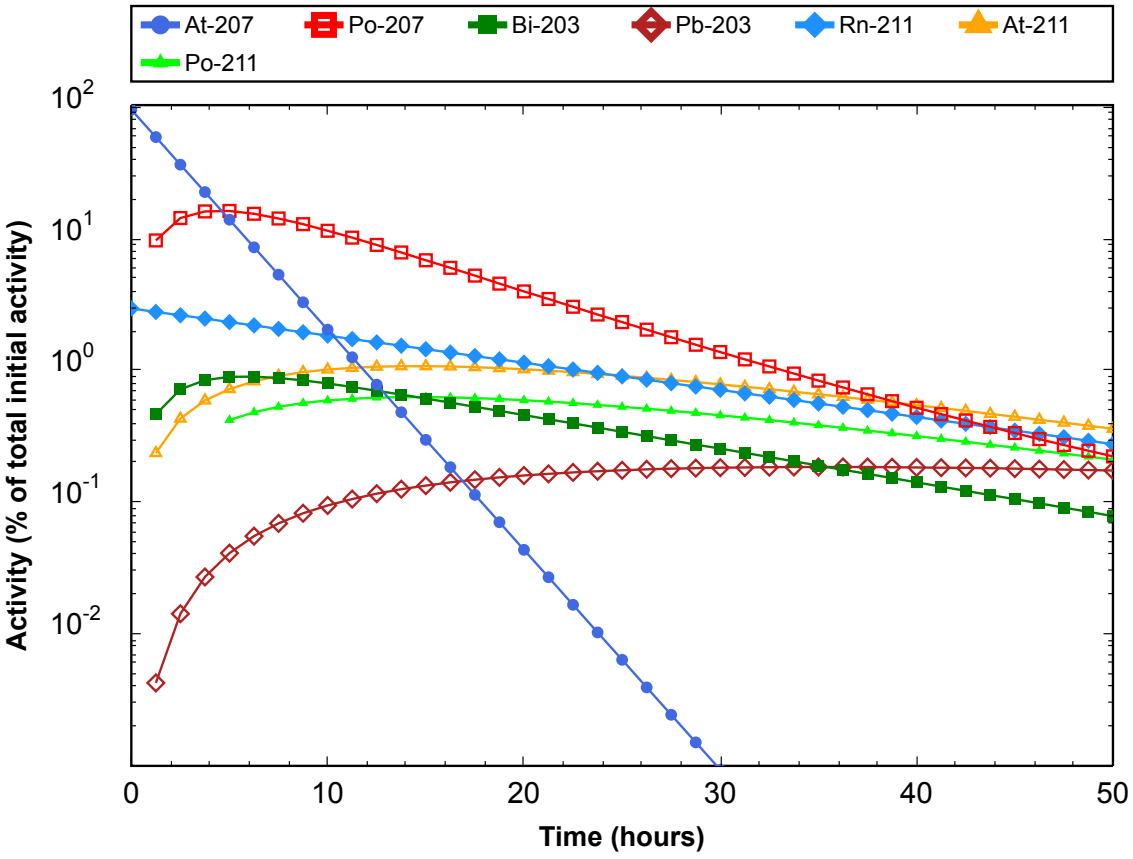

Figure 4.2: Radionuclidic yields with respect to time following ^{211}Fr decay chain.

Table 4.1: Radiations from the ^{211}Ra decay chain leading to ^{211}Rn/^{211}At. Only γ-rays and X-rays with emission intensity above 3% were listed. Data was extracted from the *National Nuclear Data Center, NuDat 2.6 database, http://www.nndc.bnl.gov/nudat2/*, based on Nuclear Data Sheets (NDS), A = 211 [108], A = 207 [110], A = 203 [111].

^{211}Ra 13 s	Emission type	Energy (keV)	Intensity (%/decay)
	α	6909 4	92.7 % 3

^{211}Fr 186 s)	Emission type	Energy (keV)	Intensity (%/decay)
	α	6660 5	100×b_α %
	γ-rays:		
		281	34×b_{ec} %
		440	20×b_{ec} %
		539.9 2	100×b_{ec} %
		918.3 2	55×b_{ec} %
		983	20×b_{ec} %

^{211}At 7.21 h	Emission type	Energy (keV)	Intensity (%/decay)
	α	5869.5 22	41.80 %
	γ/X-rays:		
	X-ray	11.1	18.6 % 7
	X-ray	76.863	12.4 % 3
	X-ray	79.29	20.7 % 4
	X-ray	89.256	2.50 % 5
	X-ray	89.807	4.79 % 9
	X-ray	92.317	1.77 % 4
		687.0 1	0.261 % 12

^{211}Rn 14.6 h	Emission type	Energy (keV)	Intensity (%/decay)
	α	5783.9 17	17.3 % 11
	α	5852.2 24	9.3 % 6
	γ/X-rays:		
	X-ray	11.4	31.5 % 19
	X-ray	78.948	18.8 % 12
	X-ray	81.517	31.0 % 19
	X-ray	91.73	3.76 % 23
	X-ray	92.315	7.2 % 4
		168.7 1	6.8 % 5
		250.2 1	6.0 % 4
		416.4 1	3.49 % 23
		442.2 1	23.1 % 16
		674.1 1	45.4 %
		678.4 1	29.0 % 18
		853.4 1	4.6 % 3
		866.0 1	7.9 % 5
		934.7 1	3.68 % 23
		946.7 1	5.0 % 14
		947.4 1	16.3 % 19
		1126.7 1	22.2 % 16
		1362.9 1	32.7 % 22
		1538.8 2	4.7 % 5

*Continued from previous page (Table 4.1)

^{211}Po 0.52 s	Emission type	Energy (keV)	Intensity (%/decay)
	α	6568.3 9	0.537 % 19
	α	6891.5 8	0.546 % 19
	α	7450.3 5	98.916 %
	γ-rays:		
		569	0.297 %
		897	0.310 %

^{207}Rn 0.15 h	Emission type	Energy (keV)	Intensity (%/decay)
	α	6131 4	21 % 3
	γ/X-rays:		
	X-ray	11.4	21.9 % 12
	X-ray	78.948	14.6 % 8
	X-ray	81.517	24.1 % 12
	X-ray	92.315	5.6 % 3
		329.45 5	3.0 % 4
		344.53 5	45.8 %
		402.68 5	11.9 % 13
		674.00 5	8.2 % 9
		674.00 5	4.1 % 5
		747.15 7	14.2 % 16

^{207}At 1.81 h	Emission type	Energy (keV)	Intensity (%/decay)
	α	5758 3	8.6 %
	γ/X-rays:		
	X-ray	11.1	38.3 % 18
	X-ray	76.863	24.6 % 9
	X-ray	79.29	41.0 % 15
	X-ray	89.256	4.96 % 18
	X-ray	89.807	9.5 % 3
	X-ray	92.317	3.51 % 13
		300.648 13	12.9 % 8
		467.116 13	7.2 % 5
		529.790 25	3.5 % 3
		588.333 23	19.5 % 12
		648.095 20	4.3 % 3
		658.40 15	6.5 % 8
		670.41 7	3.8 % 4
		675.154 23	6.8 % 5
		721.14 4	6.1 % 5
		814.41 3	45 % 3
		907.08 3	6.7 % 5
		1115.196 24	4.9 % 3
		1676.50 10	3.06 % 21
		1730.76 6	3.8 % 3

*Continued from previous page (Table 4.1)

^{207}Bi 33 y	Emission type	Energy (keV)	Intensity (%/decay)
	γ/X-rays:		
	X-ray	10.6	33.2 % 13
	X-ray	72.805	21.4 % 5
	X-ray	74.969	35.7 % 7
	X-ray	84.45	4.31 % 9
	X-ray	84.938	8.27 % 18
	X-ray	87.3	3.02 % 7
		569.698 2	97.75 % 3
		1063.656 3	74.5 % 3
		1770.228 9	6.87 % 3

^{207}Po 5.83 h	Emission type	Energy (keV)	Intensity (%/decay)
	α	5115.4 24	0.021 %
	γ/X-rays:		
	X-ray	10.8	34.1 % 15
	X-ray	74.815	24.0 % 6
	X-ray	77.107	40.1 % 10
	X-ray	86.83	4.85 % 12
	X-ray	87.349	9.28 % 23
	X-ray	89.784	3.41 % 9
		405.78 8	9.70 %
		742.72 15	28.4 % 7
		911.77 23	17.0 % 4
		992.39 20	59.2 % 13
		1148.47 21	5.81 % 13

^{203}Po 0.612 h	Emission type	Energy (keV)	Intensity (%/decay)
	α	5383 3	0.110 %
	γ/X-rays:		
	X-ray	10.8	40.6 % 24
	X-ray	74.815	24.1 % 14
	X-ray	77.107	40.2 % 24
	X-ray	86.83	4.9 % 3
	X-ray	87.349	9.3 % 5
	X-ray	89.784	3.42 % 20
		189.5 1	3.8 % 4
		214.8 1	14.3 % 13
		893.5 1	18.7 % 15
		908.6 1	55 %
		1090.9 1	19.2 % 15
		1242.4 1	4.6 % 4

^{203}Pb 2.16 d	Emission type	Energy (keV)	Intensity (%/decay)
	γ/X-rays:		
	X-ray	10.3	36.4 % 15
	X-ray	70.832	26.4 % 6
	X-ray	72.873	44.2 % 9
	X-ray	82.115	5.34 % 11
	X-ray	82.574	10.22 % 21
	X-ray	84.865	3.73 % 8
		279.1952 10	80.9 %
		401.320 3	3.35 % 10

*Continued from previous page (Table 4.1)

^{203}Bi 11.8 h	Emission type	Energy (keV)	Intensity (%/decay)
	γ/X-rays:		
	X-rays	10.6	36.4 % 18
	X-ray	72.805	24.6 % 10
	X-ray	74.969	41.1 % 17
	X-ray	84.45	4.96 % 20
	X-ray	84.938	9.5 % 4
	X-ray	87.3	3.48 % 14
		186.6 5	3.2 % 3
		264.2 5	5.3 % 4
		722.4 5	4.8 % 4
		816.3 5	4.1 % 3
		820.2 5	30.0 % 25
		825.2 5	14.8 % 12
		847.2 5	8.6 % 7
		896.9 5	13.2 % 11
		1033.7 5	8.9 % 7
		1506.7 5	3.7 % 3
		1536.5 5	7.7 % 6
		1679.6 5	8.9 % 7
		1719.7 5	3.5 % 3
		1847.3 5	11.6 % 10
		1893.0 5	8.3 % 7

^{209}At production via ^{213}Fr and ^{213}Ra decay

^{209}At was recovered from the decay of ^{213}Fr ($t_{1/2}$=34.6 s), for which over 99% of decays produce ^{209}At. Figure 4.3 provides the decay diagram for the combination of ^{213}Fr and ^{213}Ra, with the corresponding radiations for each isotope listed in Table 4.2 (where X-rays/γ-rays with intensity below 3% have been omitted). For A=213, the only significant isobar was ^{213}Ra, which decayed to ^{213}Fr (20%) and ^{209}Rn (80%), making ^{213}Ra an *in situ* source of ^{209}At.[1]

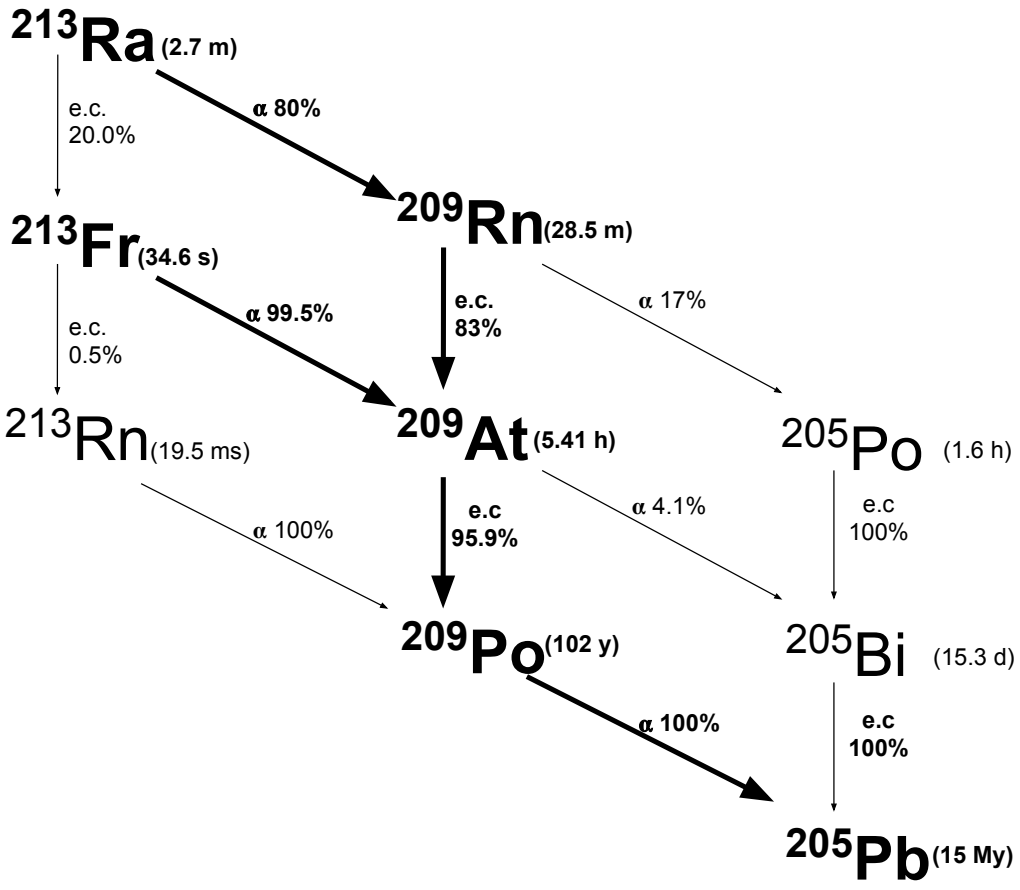

Figure 4.3: Combined decay chains for ^{213}Ra and ^{213}Fr leading to ^{209}At.Note that α = α-decay, e.c. = electron capture. β+-decays had very low probability in this mass range and were included in the e.c. probabilities.

The production rate of ^{213}Ra was previously measured to be 1/3 that of ^{213}Fr, and was expected to result in a net increase in ^{209}At of roughly 15%. A small amount of ^{205}Po ($t_{1/2}$=1.6 h) coming from the decay of ^{209}Rn was the only additional contaminating radionuclide from ^{213}Ra decay with a significant half-life. Longer-lived isotopes in the decay chain of ^{213}Fr build-up over several hours. Compared to the initial starting activity

[1]Although ^{213}Ra was considered a source of contamination to an otherwise pure ^{213}Fr beam, 86% of ^{213}Ra decays led to additional ^{209}At activity (via either ^{213}Fr or ^{209}Rn daughter intermediates). This contributed significantly to the final inventory of ^{209}At.

of ^{209}At, ^{209}Po and ^{205}Bi activity were calculated to reach maximums of $10^{-6} - 10^{-5}$ and $10^{-4} - 10^{-3}$ times less, respectively. The activities for ^{209}At, ^{209}Po and ^{205}Bi were calculated as a function of time using Nucleonica Decay Engine[109], plotted in Figure 4.4. In terms of relative activity, the decay of ^{213}Fr thus provided a relatively pure source of ^{209}At.

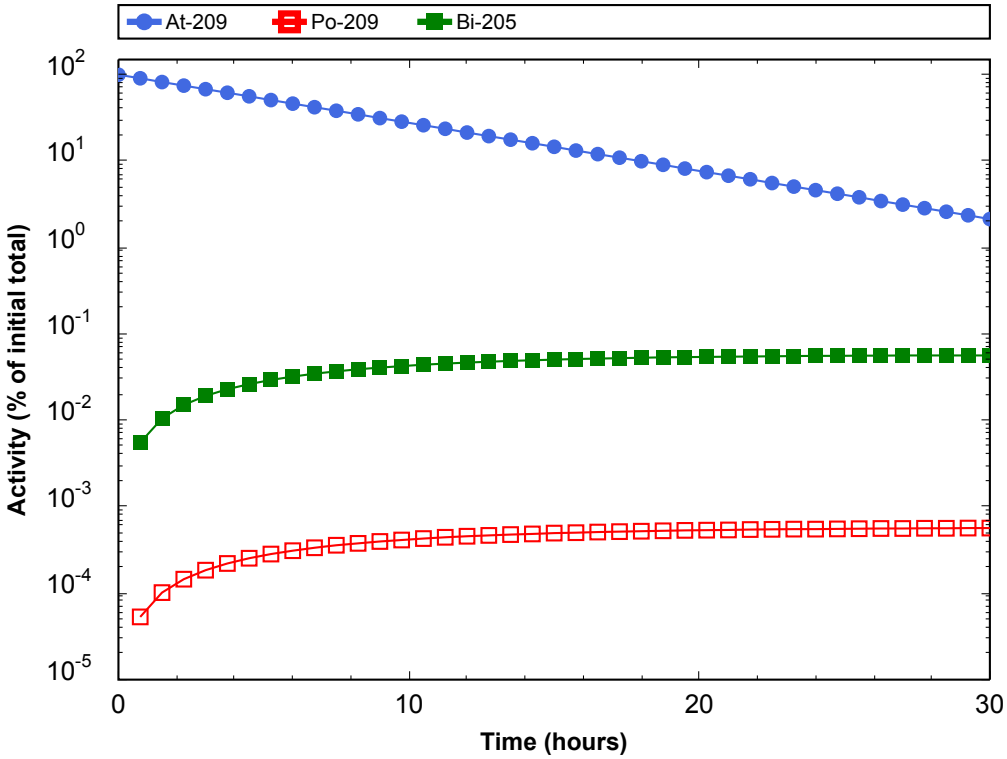

Figure 4.4: Calculated activity of ^{209}At (and daughters) as a function of time. Values were calculated relative to the initial ^{209}At activity, using the Nucleonica Decay Engine application [109].

Table 4.2: Radiations from the ^{213}Ra decay chain leading to ^{209}At. Only γ-rays and X-rays with emission intensity above 3% were listed. Data was extracted from the *National Nuclear Data Center, NuDat 2.6 database, http://www.nndc.bnl.gov/nudat2/*, based on Nuclear Data Sheets (NDS), A = 213 [112], A = 209 [113], A = 205 [114]

^{213}Ra (162 s)	Emission type	Energy (keV)	Intensity (%/decay)
	α	6521.9 23	4.6 % 6
	α	6624.7 23	39 % 3
	α	6732.3 23	36 % 3
	γ/X-rays:		
	X-ray	11.7	11.6 % 9
		110.3	6.0 % 4

^{213}Fr (34.6 s)	Emission type	Energy (keV)	Intensity (%/decay)
	α	6211 5	0.10 % 3
	α	6378 5	0.12 % 3
	α	6775 2	99.23 % 17

^{213}Rn (19.5 ms)	Emission type	Energy (keV)	Intensity (%/decay)
	α	7252 4	1.04 % 12
	α	7554 4	0.71 % 10
	α	8089 3	98.20 % 20

^{209}Rn (0.475 h)	Emission type	Energy (keV)	Intensity (%/decay)
	α	6039 3	16.9 % 20
	γ/X-rays:		
	X-ray	11.426	12.7 % 3
	X-ray	13.694	3.23 % 17
	X-ray	13.875	8.0 % 5
	X-ray	78.948	21.1 % 7
	X-ray	81.517	35.1 % 11
	X-ray	91.730	4.19 % 13
	X-ray	92.315	7.99 % 25
		337.45	14.5 % 4
		408.32 4	50.3 % 15
		672.82 4	3.27 % 11
		689.26 5	9.7 % 3
		745.78 4	22.8 % 6
		794.72 7	3.36 % 23
		855.76 5	4.9 % 3
		1037.93 6	4.16 % 21

*Continued from previous page (Table 4.2)

^{209}At (5.41h)	Emission type	Energy (keV)	Intensity (%/decay)
	α	5647 2	4.1 % 5
	γ/X-rays:		
	X-ray	11.1	60 % 3
	X-ray	76.863	36.3 % 21
	X-ray	79.29	60 % 3
	X-ray	89.256	7.3 % 4
	X-ray	89.807	14.0 % 8
	X-ray	92.317	5.2 % 3
		195.0 1	23.5 % 11
		239.190 18	12.5 % 5
		545.0 1	90.9 %
		551.0 1	4.91 % 18
		781.9 1	83.3 % 24
		790.2 1	63.5 % 19
		903.0 1	3.67 % 11
		1103.4 1	5.39 % 18
		1170.6 1	3.00 % 9

^{209}Po (102 y)	Emission type	Energy (keV)	Intensity (%/decay)
	α	4622 5	0.551 % 6
	α	4883 2	79 % 8
	α	4885 2	19.7 % 20

^{205}Bi (15.3d)	Emission type	Energy (keV)	Intensity (%/decay)
	γ/X-rays:		
	X-ray	10.6	35.9 % 16
	X-ray	72.805	21.5 % 7
	X-ray	74.969	35.9 % 12
	X-ray	84.45	4.33 % 15
	X-ray	84.938	8.3 % 3
	X-ray	87.3	3.04 % 10
		570.60 5	4.34 % 8
		579.80 10	5.44 % 9
		703.45 5	31.1 %
		987.66 5	16.1 % 3
		1043.75 5	7.51 % 13
		1764.30 10	32.5 % 7
		1775.80 10	3.99 % 9
		1861.70 10	6.17 % 12

^{205}Po (1.6h)	Emission type	Energy (keV)	Intensity (%/decay)
	γ/X-rays:		
	X-ray	10.8	36.3 % 18
	X-ray	74.815	25.6 % 11
	X-ray	77.107	42.7 % 17
	X-ray	86.83	5.16 % 21
	X-ray	87.349	9.9 % 4
	X-ray	89.784	3.63 % 15
		212.0 1	3.6 % 3
		261.0 1	4.0 % 3
		836.8	19.2 % 15
		849.8 1	25.5 % 20
		872.4 1	37.0 %
		1001.2 1	28.8 % 21
		1239.1 1	4.6 % 4

RIB production and delivery

Radioactive ion beams of mass number A=211 or A=213 were created using the ISOL-technique by the spallation of uranium carbide targets (target density = 10 g/cm^3) with 480 MeV protons delivered at 9.8 μA and a rhenium surface ionizing ion source. Ions were accelerated across an electric potential of 20 or 28 kV, and passed through the ISAC preseparator.[2] The resulting singly-charged ion beams of mixed francium and radium isotopes were then directed through the high resolution mass separator to select mass numbers A=211 or A=213, with RIB delivery to the IIS at 20 or 28 keV, for 3 minutes to 9.5 hours, depending on the particular run.

RIB production rate measurements

All RIB production for these experiments was performed at ISAC using uranium carbide targets with Re surface ionizing ion sources. Before implantation, ion beam intensity and composition was measured at the ISAC yield station. Briefly, ion beams were implanted into aluminized Mylar tape for a collection time $t_{collect}$ of 0.1 s and counted for 4 seconds (t_{count}) *in situ* by γ- and α-spectroscopy, independently. Three consecutive cycles of the procedure were completed for each measurement to reduce statistical uncertainty. All production rates (in terms of ions/s) at IYS for francium and radium isotopes were calculated using Equation 3.1.

There was a known difference between the RIB beam intensity that was delivered to IYS and IIS. This difference was attributable to the fact that these stations are physically located at different positions within the ISAC facility. The RIB beam path was several metres longer for deliveries to IYS, compared to deliveries to the IIS. The longer path length and the additional beam steering that was required for delivery to IYS amounts to a decrease in beam intensity. This difference in beam intensity was accounted for by calculating a transmission factor ($\epsilon_{\mathrm{IIS/IYS}}$) using the relative beam currents measured by independent Faraday cups located slightly upstream from each station, as shown in Equation 4.1.

$$\text{Transmission Factor, } \epsilon_{\mathrm{IIS/IYS}} = \frac{\text{current at IIS}}{\text{current at ISAC Yield Station}}, \tag{4.1}$$

where the rate of ion implantation at IIS (r_{IIS}) is given by the rate measured at the IYS (r_{IYS}) multiplied by ($\epsilon_{\mathrm{IIS/IYS}}$), (Equation 4.2),

$$r_{IIS} = r_{IYS} \times \epsilon_{\mathrm{IIS/IYS}} \tag{4.2}$$

[2]Beam property requests always indicated a preference of 28 keV or higher but this was not always available at ISAC due to unrelated issues in RIB production. Most commonly, RIB were delivered at 20 keV.

α-recoil of daughters produced by α-decay

When radionuclides α-decay, momentum is conserved by the recoil of the daughter isotopes. The recoil energy is given simply by the energy of the emitted α-particle multiplied by the ratio of the α-particles mass to that of the daughter radionuclide, as in Equation 4.3:

$$E_{\text{recoil}} = E_{\alpha}\frac{m_{\alpha}}{m_{\text{daughter}}} \tag{4.3}$$

$$\text{Example } (^{213}\text{Fr } \alpha\text{-decay}): \quad E_{^{209}\text{At}} = (6775 \text{ keV})\frac{4}{209} = 130 \text{ keV} \tag{4.4}$$

Given that the energy of recoiling daughter isotopes produced by α-decay was higher than the implantation energy (≤ 28 keV), a significant fraction of the activity was ejected from the implantation target and back into the vacuum of the chamber. With reference to Figure 4.5, the probability of a recoiling daughter nucleus to escape implantation (P_{esc}) was estimated by the solid angle resulting in ejection, relative to the full solid angle of a sphere (4π):

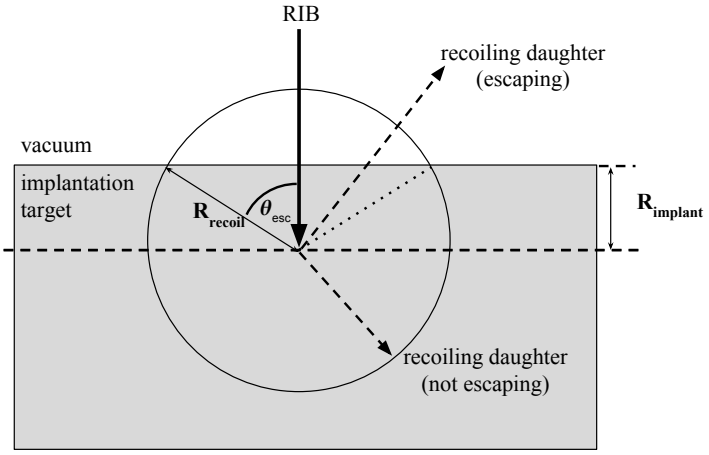

Figure 4.5: Diagram for α-decay daughter recoil calculation.

$$P_{esc} = \frac{\Omega_{esc}}{\Omega_{sphere}} = \frac{1}{4\pi}\int_{\phi=0}^{\phi=2\pi}\int_{0}^{\theta_{esc}} sin(\theta)d\theta d\phi \tag{4.5}$$

This approximation assumed that the direction of recoil was isotropic (isotopes came to rest and then decayed) and daughters recoiled with straight trajectories. Integrating over the limits of θ,

$$P_{esc} = -\frac{1}{2}\Big(cos(0) - cos(\theta_{esc})\Big) \tag{4.6}$$

As shown in Figure 4.5, $cos(\theta_{esc})$ is equal to the mean implantation depth ($R_{implant}$) divided by the mean recoil distance (R_{recoil}), for a given material. distance recoiled, so that P_{esc} can be written as

$$P_{esc} = \frac{1}{2}\left(1 - \frac{R_{implant}}{R_{recoil}}\right), \qquad R_{implant} \leq R_{recoil} \tag{4.7}$$

The geometrical efficiency for retaining recoiling daughter nuclei following *alpha*-decay ($\epsilon_{\mathrm{geo},\alpha}$) was thereby given as

$$\epsilon_{\mathrm{geo},\alpha} = 1 - P_{esc} = \frac{1}{2}\left(1 + \frac{R_{implant}}{R_{recoil}}\right), \qquad R_{implant} \leq R_{recoil} \tag{4.8}$$

The factor ϵ_{geo} was then defined as

$$\epsilon_{geo} = \begin{cases} \epsilon_{\mathrm{geo},\alpha}, & \text{if daughter produced by } \alpha\text{-decay} \\ \\ 1, & \text{if daughter produced by e.c.} \end{cases} \tag{4.9}$$

Theoretical activity calculations

As described in the derivation below, the IYS spectroscopy measurements were used to calculate the theoretical activity of ^{211}Rn and ^{209}At daughters resulting from the decay of ^{211}Fr and ^{213}Fr RIB, respectively, implanted at a constant rate (r_p).[3] In accordance with Equation 3.4, activity of the initial parent isotope ($A_p = N_p\lambda_p$) was given by Equation 4.10:

$$A_p(t) = \begin{cases} r_p\left(1 - e^{-\lambda_p t}\right), & 0 < t \leq t_{\mathrm{EOB}} \\ \\ r_p\left(1 - e^{-\lambda_p t_{\mathrm{EOB}}}\right)e^{-\lambda_p(t - t_{\mathrm{EOB}})}, & t > t_{\mathrm{EOB}} \end{cases} \tag{4.10}$$

With similarity to Equation 3.3, the amount of daughter atoms N_d was described with respect to time by the differential equation in Equation 4.11, where the production rate of the daughter isotopes (subscripted d) that did not escape the implantation target due to α-recoil was given by the activity of the parent isotope ($A_p(t)$) multiplied by the

[3]for an implantation rate r, the subscript p refers to the fact that ^{211}Fr and ^{213}Fr are parent isotopes of there respective overlapping decay chains.

branching ratio for producing the daughter (b_d) and ϵ_{geo} from Equation 4.9.

$$\frac{dN_d}{dt} = -\lambda_d N_d + A_p(t) b_d \tag{4.11}$$

Substitution of $A_p(t)$ from Equation 4.10 gave the conditional differential equation:

$$\frac{dN_d}{dt} = \begin{cases} -\lambda_d N_d + b_d r_p \epsilon_{geo}\left(1 - e^{-\lambda_p t}\right), & 0 \leq t \leq t_{\text{EOB}} \\ -\lambda_d N_d + b_d r_p \epsilon_{geo}\left(1 - e^{-\lambda_p t_{\text{EOB}}}\right) e^{-\lambda(t - t_{\text{EOB}})}, & t > t_{\text{EOB}} \end{cases} \tag{4.12}$$

Equation 4.12 could be solved exactly and gave the daughter activity A_d as a function of time, according to Equation 4.13.

$$A_d(t) = \begin{cases} r_p b_d \epsilon_{geo}\left(1 + \dfrac{\lambda_d}{\lambda_d - \lambda_p} e^{-\lambda_p t} - \dfrac{\lambda_p}{\lambda_d - \lambda_p} e^{-\lambda_d t}\right), & 0 \leq t \leq t_{\text{EOB}} \\ r_p b_d \epsilon_{geo}(1 - e^{-\lambda_p t_{\text{EOB}}}) \dfrac{\lambda_d}{\lambda_d - \lambda_p}\left(e^{-\lambda_p (t - t_{\text{EOB}})} - e^{-\lambda_d (t - t_{\text{EOB}})}\right) & \\ \qquad + A_d(t_{\text{EOB}}) e^{-\lambda_d (t - t_{\text{EOB}})}, & t > t_{\text{EOB}} \end{cases} \tag{4.13}$$

Since the γ-ray emissions were known relative to the branching ratio for electron capture decay (see Table 4.1), the rate of ^{211}Fr production could only be expressed as the ions/s divided by the branching ratio for electron capture (b_{ec}). As a result, the b_{ec} cancelled in Equation 4.13 and the theoretical activity of ^{211}Rn could be calculated independently of the probability of ^{211}Fr electron capture. It was noted that the independent γ-spectroscopy and α-spectroscopy measurements provided an experimental measure of the branching ratios for ^{211}Fr. For further details, see §6.5.1.

Instrumentation for RIB implantation

Implantation targets

RIB were directed to the ISAC implantation station (IIS) and implanted into thin sodium chloride targets (solid crystal). The cuboid crystal lattice of the salt provided a matrix to trap incoming radionuclides that could prevent migration or diffusion of the implanted activity. NaCl had been previously shown to effectively trap radon at beam energies similar to those achieved at ISAC (≈30 keV) [115]. Other advantages of NaCl as target material include its high solubility in aqueous solution (360 g/L in water [116]). ^{213}Fr ions implanted in solid crystal NaCl targets were calculated to have a mean range of 20

nm ± 4 nm, based on Monte Carlo simulation using the *Stopping and Range of Ions in Matter* (SRIM) software package (Figure 4.6).[117]

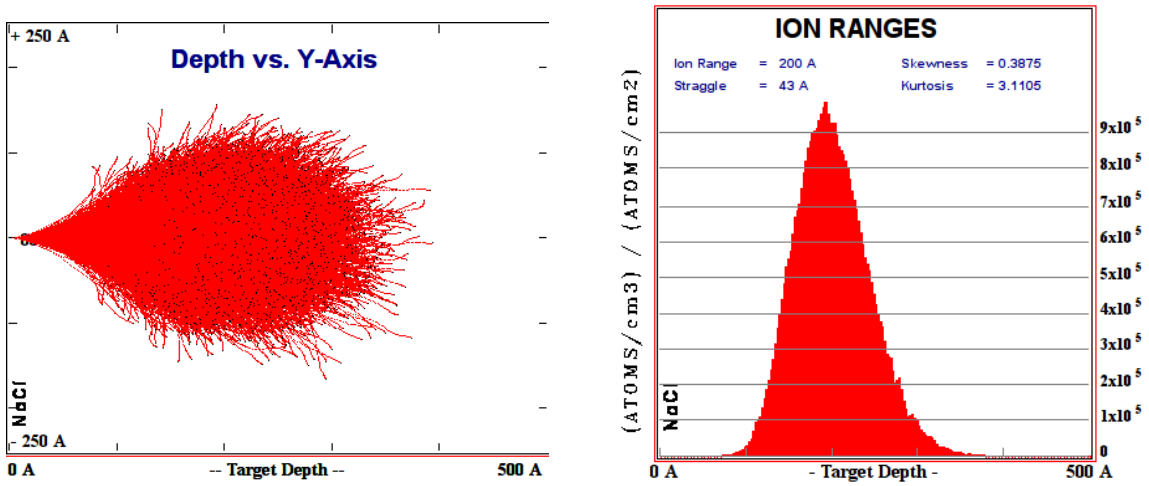

Figure 4.6: SRIM simulation of ^{213}Fr implantation in NaCl: **(a)** 2D projection of ^{213}Fr ion trajectories during implantation, and **(b)** a histogram showing the distribution and straggle of ^{213}Fr atoms along the axis of implantation. The implantation was simulated with 40000 incident ^{213}Fr ions at 20 keV.

NaCl targets were prepared on-site by Micromatter™ by evaporating NaCl onto the front surface of 18 mm diameter circular target backings, as shown in Figure 4.7.[4] Standard scanning electron microscope (SEM) pin-stub specimen mounts (Ted Pella, Inc.) were originally used as backings but the aluminum was found to be incompatible with optimal conditions for target processing. Instead, stainless steel target backings were machined at TRIUMF to the same dimensions as the SEM sample holders. The NaCl target thickness was roughly 230 nm, corresponding to an NaCl coating of 50 μg/cm^2.

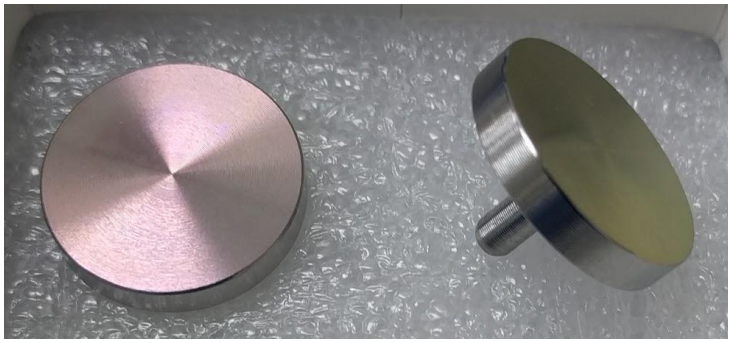

Figure 4.7: NaCl coated stainless steel targets for RIB implantations.

Calculation of $\epsilon_{\mathrm{geo},\alpha}$ for RIB implanted into NaCl

In order to calculate the probability of retaining daughters accounting for α-recoil ($\epsilon_{\mathrm{geo},\alpha}$), SRIM range tables were generated to determine mean $R_{implant}$ and R_{recoil} in NaCl. Using

[4]Originally based on-site at TRIUMF, Micromatter™ is now based in Surrey, BC.

Equation 4.8, $\epsilon_{\text{geo},\alpha}$ was calculated to be 0.65 (35% loss due to α-decay recoil) at 20 keV ion beam implantation energy, and 0.69 (31% loss) at 28 keV implantation energy.

Chamber design for RIB implantation and transport

Sodium chloride targets were positioned at the terminal end of the IIS beam line, housed by a custom-built vacuum chamber, named by this work as a CARRIER (or Conveying Apparatus for the Rapid Recovery of Implanted Emanating Radionuclides), shown in Figure 4.8. The CARRIER was designed to be a chamber that could hold the NaCl target foils in vacuum during collection and facilitate rapid transfer of the collected radioactivity from the ISAC implantation station to an appropriate laboratory fume hood, with considerations to radiation safety.

The CARRIER was constructed from a stainless steel 6-way cross KF40 chamber (MDC Vacuum Products Corporation, Hayward, CA), described by Figures 4.8a and 4.8d. The NaCl target was supported by an electrical feed-through (outside Coax BNC to inside single-pin, MDC Vacuum Products Corporation, Hayward, CA), which could be used for beam tuning and current readout during beam delivery (Figure 4.8c). A passive collimator (Collimator A, 12 mm inner diameter) was positioned at the entrance of the chamber, immediately downstream from a manual gate valve (Kurt J. lesker Inc., Concord, ON) that could be sealed following implantation to maintain a high vacuum inside the CARRIER even after disconnection from the IIS beamline. Another round orifice beam collimator (collimator B) with an inner diameter of 8 mm was positioned at the centre of the chamber on the beam axis, connected to second electrical feed-through. Both Collimators were made of stainless steal and made on site at TRIUMF (Figure 4.8b). Together, the target and collimator B could be used to focus the RIB onto the NaCl target by fine adjustment of beamline magnets to maximize the target current while minimizing the current measured at collimator B. Two connection points for venting and air sampling were each equipped with vent valves fitted with downstream quick connect adaptors (Swagelok Company, Solon, OH), for rapid connection and venting with air sampling equipment (described in §4.3.5).

The CARRIER was attached to the existing beamline with a quick-releasing spring-loaded manual clamp and vitan o-ring gasket, taking only a few seconds to take on or off, and not requiring tools. Following ion implantation, the CARRIERs gate valve was manually closed to completely separate the CARRIERs radioactive contents from the IIS beamline. IIS was isolated from the ISAC beamline further upstream by a remotely operated gate valve and then vented to atmosphere. The CARRIER, still under high vacuum, was then disconnected from the IIS immediately upstream of the manual gate valve. Blank offs were used to close the IIS beam-pipe and the exposed portion of the gate-valve. The CARRIER was then bagged and transported by hand to an appropriate

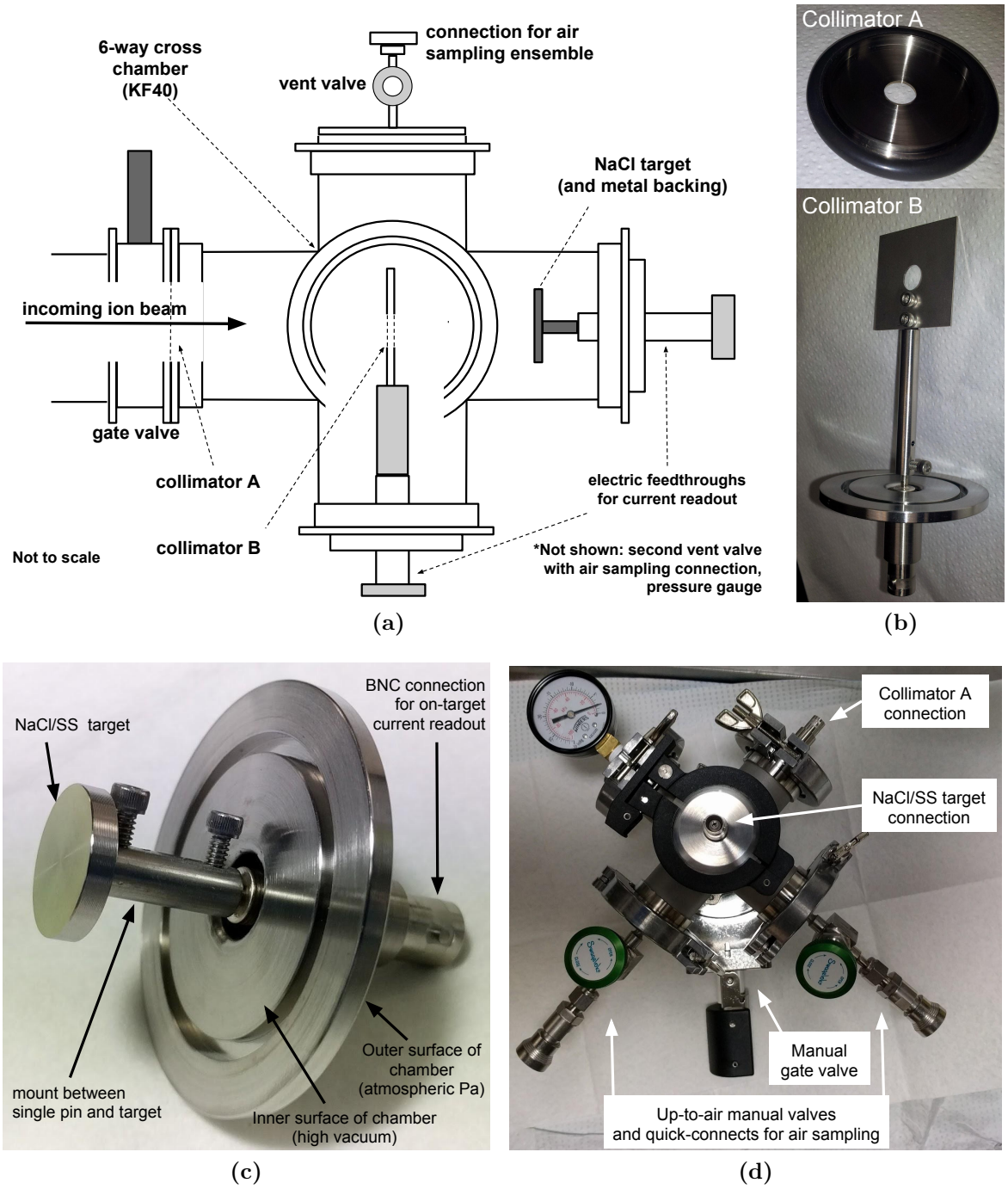

Figure 4.8: Chamber for ion implantation (CARRIER) with collimators and target with current readout. **(a)** schematic diagram, **(b)** passive collimators A (at gate-valve) and B (at center of cross), **(c)** NaCl/SS target mounted to a single-pin electrical feedthrough with current readout, and **(d)** photograph of CARRIER.

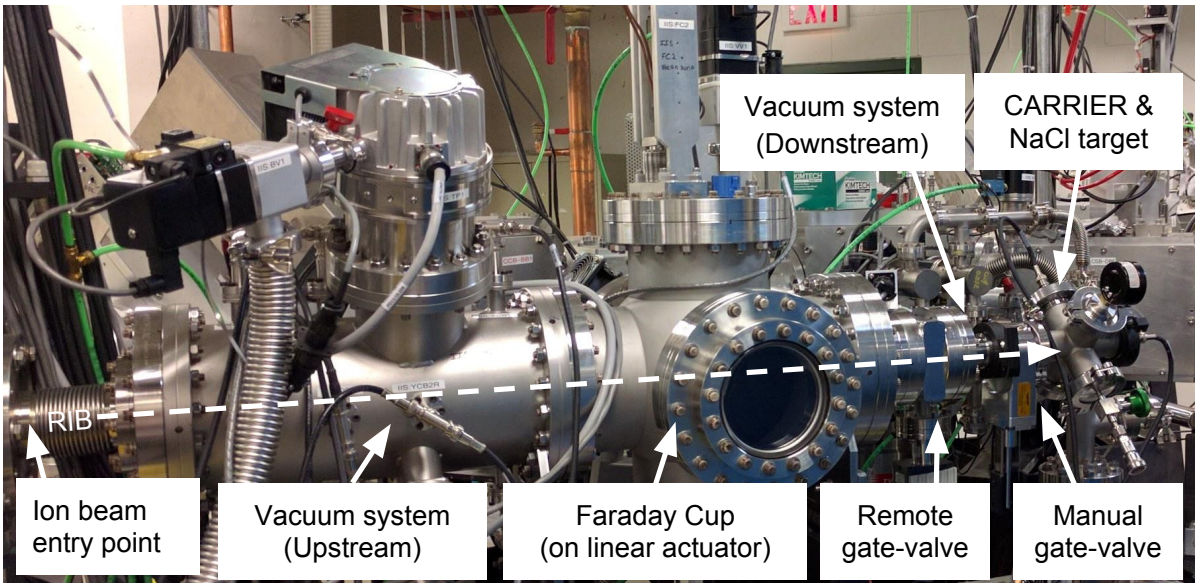

Figure 4.9: Photographs of the IIS beamline with the CARRIER mounted.

location for foil processing. With the CARRIER installed at the ISAC implantation station and brought to high vacuum (10^{-6} torr), beam tuning to the target was performed with stable uranium to avoid contamination of the chamber before beginning implantation. Fine beam positioning for aligning with the location of implantation target was accomplished with the upstream steering magnets by manually searching for the position of maximum current as measured by the current monitor. Beams of stable uranium were generated without the use of proton bombardment by externally heating the uranium target.

Following each RIB implantation (described in § 4.2), the gate valve on the CARRIER was manually closed to completely separate the radioactive contents inside the CARRIER from the IIS beamline. IIS was isolated from the ISAC beamline further upstream by a remotely operated gate valve and then vented to atmosphere. The CARRIER, still under high vacuum, was then disconnected from the IIS immediately upstream of the manual gate valve. The IIS beampipe and the exposed portion of the gate-valve on the CARRIER were then quickly closed with KF40 flange covers (blankoffs). The CARRIER was immediately bagged and transported by hand to an appropriate location for target processing.

Prior target and CARRIER designs for initial ^{209}At production runs

The first set of implantations for ^{209}At production (A=213) were completed with a simpler version of the CARRIER and NaCl target design, described in Figure 4.10a. The original CARRIER had a side-mounted bracket to support NaCl target disks at the centre of the chamber (Figure 4.10b). The target did not have an electrical connection for on-target current readout. Instead, a 18 mm diameter disk-shaped copper faraday cup

was positioned at the back of the chamber, connected to the inside connector of an electrical feed-through that also provided support and alignment (Figure 4.10c).[5] This initial CARRIER did not have any collimators. Insertion of the target foil prevented electrical readout of any kind during beam delivery.

Circular 18 mm diameter NaCl implantation targets were constructed for RIB implantations using two distinct designs, made for order by Micromatter™ (Surrey, BC). The first target type (NaCl/Mylar) was constructed with electrically-insulating adhesive, a plastic outer support ring, and omitted the silver layer. Such a design contained any electrically-insulating components that may have created a *space-charge* during implantation. Although NaCl is itself an insulator, it was not considered thick enough to cause space-charge on its own; however having it positioned between Mylar and plastic could have resulted this effect. The second target type (NaCl/Ag) was similar but was constructed by stacking NaCl at 50 μg/cm^2(250 nm thick) and silver at 100 μg/cm^2 on a mylar backing for structural support, with stainless steel clamping ring mounted with electrically-conducting (silver conductive epoxy) adhesive to the outer perimeter of the target surface. Unlike the targets described in §4.3.3, neither of these target types had current readout and could not be used for beam tuning or monitoring during RIB implantation. Implantations for ^{209}At production were performed using the earlier version of the CARRIER with both target types, as well as, the final version of the CARRIER and NaCl targets (as described in §4.3.1 and §4.3.3.

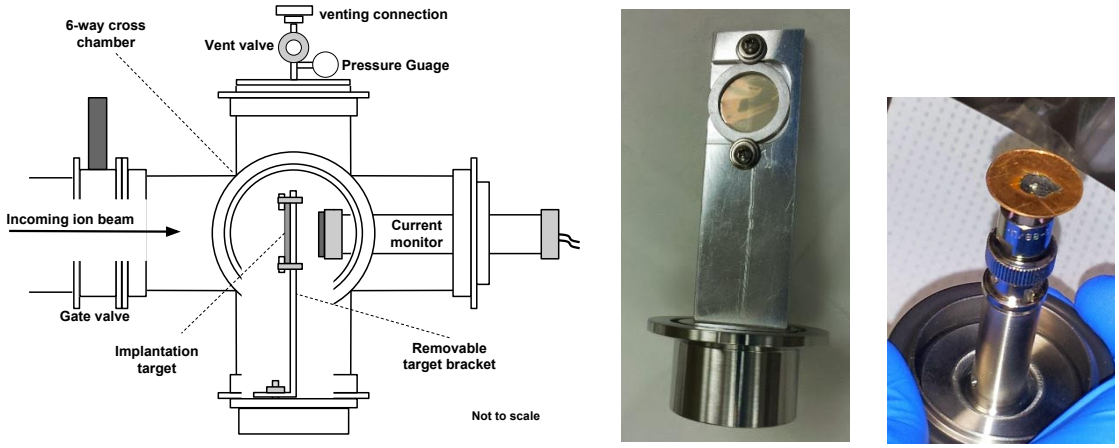

Figure 4.10: Early CARRIER design used for first set of ^{209}At production runs. **(a)** Schematic diagram of the CARRIER, **(b)** the target bracket for positioning disk-shaped NaCl targets at the center of the chamber during implantation, and **(c)** the small Faraday cup used for beam tuning/setup before implantation, mounted on a KF40 BNC-to-BNC electrical feed-through and requiring the target bracket to be uninstalled for current measurement.

[5]The electrical feedthrough was purchased stock from MDC Vacuum Products Corporation (Hayward, CA), while the Faraday cup was custom made at TRIUMF.

Internal air sampling of chamber after implantation

Before opening the CARRIER and retrieving the active targets, the relative amount of volatile α-emitting radioactivity escaping the target within the chamber (presumed to be composed of radon and astatine isotopes) was measured with the Actinide Sampling Ensemble (ASE), an airtight series of connected components including an air reservoir, charcoal filter, air pump, and a well-type alpha-particle detector called a *Lucas cell*. The Lucas Cell has essentially a cylindrical reservoir lined on the inside (top and sides) with zinc sulfide (ZnS), a well known scintillator for response to α-particles. A photomultiplier tube was coupled to the bottom, from wich counts were recorded by a Pylon Model AB6A portable radiation monitor (Pylon Electronics, Ottawa, ON). Readout from the Lucas cell. A schematic diagram of the ASE is shown in Figure 4.11. A vacuum tight closed-loop air circuit was made by connecting the ASE input and output lines to the CARRIER vent-valves via the quick connect adaptors. With the CARRIER and ASE connected in a closed circuit, the two vent valves were slowly opened over roughly 5 minutes, filling the chamber with the air already inside the ASE (originally at atmosphere) to a pressure of ~ -5 mm Hg. The air was circulated at 1 litre/minute (using the pump) through the the CARRIER-ASE assembly for approximately 10 minutes to record counts per minute detected by the Lucas cell, read out in real-time. Upon shutting off the pump, the Lucas cell was disconnected (isolated) from the ASE and left to record count rate as a function of time for several hours.

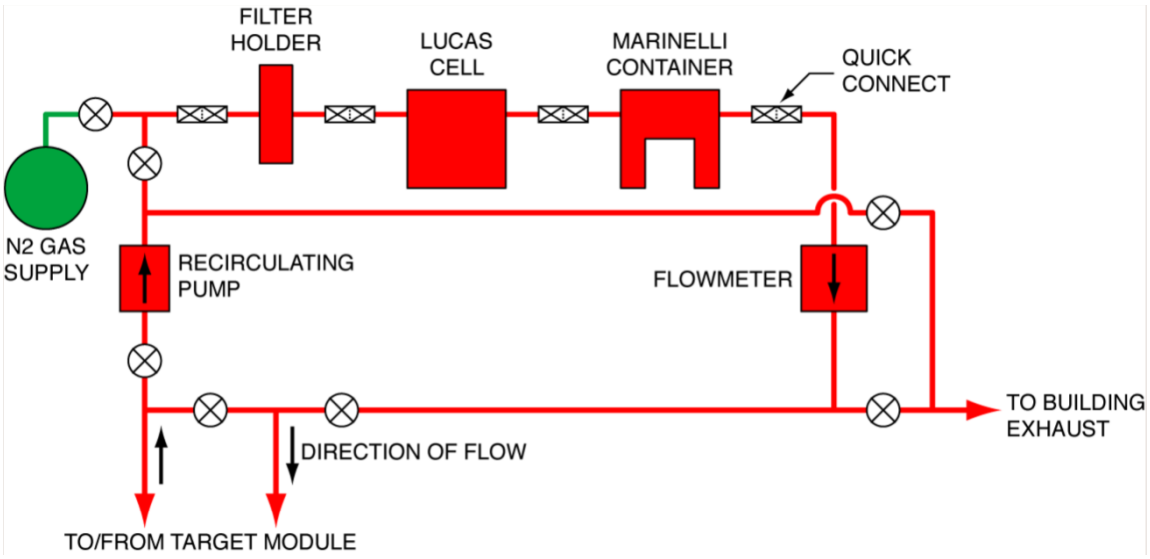

Figure 4.11: Schematic diagram of air sampling ensemble. $\otimes$ = valve (open/close), and target module refers to connection to the two vent valves on the CARRIER. Note: N_2 gas supply was not open during connection to the CARRIER

Target processing

The use of NaCl implantation targets enabled simple and rapid target dissolving with small amounts of aqueous solution to recover the contained activity. All targets were dissolved with dilute (0.01-2 N) NaOH, in order to chemically reduce astatine, thereby significantly limiting the volatility of astatine.

^{211}Rn/^{211}At recovery from A=211 implantations

While radon has been shown to be trapped in the matrix of NaCl, its behaviour in solvents is less well studied. While multiple approaches to radon gas trapping were possible, including cryogenic traps, charcoal traps, and liquid alkane hydrocarbons, this last option was considered to be the most elegant approach to isolation as it would contain the radon isotopes in solution which could be easily manipulated in the standard chemistry laboratory. Given the low amount of published research regarding radon gas trapping in dodecane (or decane), it was important that the radon be released into a container where liquids could be manipulated without creating pressure differences that might require venting to atmosphere. Based on these factors, the apparatus shown in Figure 4.12 was configured for processing the targets containing ^{211}Rn.

Briefly, for A=211 implantations, the NaCl targets and metal backing (made of either either stainless steel or aluminum) was placed in a 30 mL syringe before the plunger was inserted. Dodecane (6 or 8 mL) was drawn into the syringe through a 3-way valve. The NaCl target was insoluble in dodecane and presumably continued to hold the activity *in situ*. With the NaCl target facing up, 2 mL NaOH (0.01 N for Aluminum backing, 2 N for stainless steel backing) was added to the syringe from below to create a bottom layer of aqueous solution and top layer of dodecane. The 3-way valve was closed and the target was inverted, exposing it to the aqueous layer immediately and completely dissolving it. The two solvents were then mixed vigorously by shaking the apparatus by manually.

Keeping the apparatus vertical (aqueous solution on bottom), the dodecane and aqueous solution was allowed to separate and the aqueous solution was completely removed. A minimal amount of solution constituting the inferace of the aqueous/dodecane layers (containing both solvents) was discarded, and a relatively small sample of the dodecane layer (up to 0.5 mL) was collected for analysis. Each liquid was collected into vials through septa. A 3 mL syringe attached to the 3-way valve (the "Vacating syinge" shown in Figure 4.12) was filled with air and used to clean out (or vacate) any residual active liquid remaining within the small volumes of the syringe. The vacating syringe continuously connected to the 3-way valve throughout target processing to maintain the closed system.

The dodecane (containing the recovered ^{211}Rn activity) was left in the 30 mL syringe undisturbed for approximately 22 hours to allow for the grow-in of ^{211}At and establishing

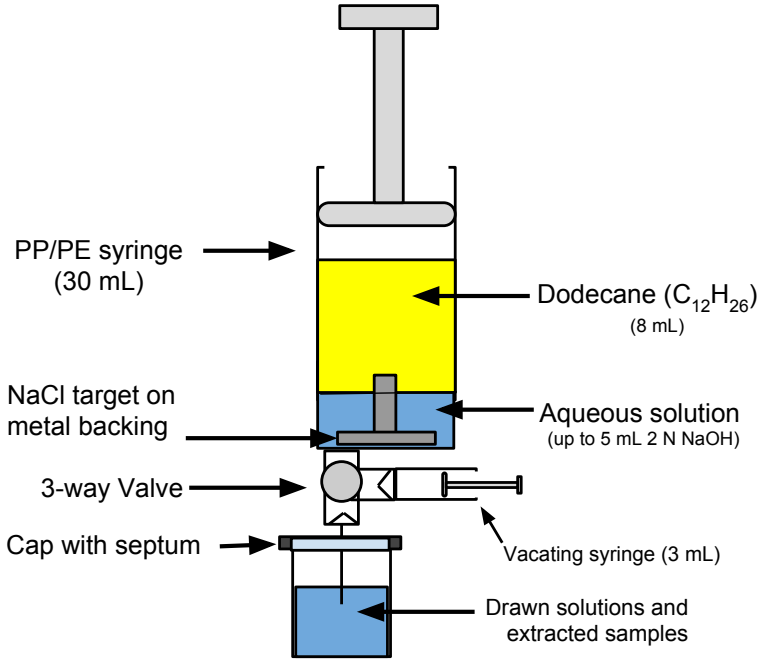

Figure 4.12: Apparatus for ^{211}Rn isolation and ^{211}At extraction. The syringe permitted the manipulation of solution volumes (dodecane and aqueous solution) while maintaining a counstant pressure as to not require venting that could otherwise release radon gas and other volatile activity. The "vacating syringe" was used to flush the needle after each use with air to minimize contamination of the extracted solutions.

transient equilibrium. 2-5 mL of 0.01-2 N NaOH was drawn into the syringe/generator, shaken vigorously with the dodecane, and withdrawn several minutes after the two liquids had separated. Aqueous solutions containing ^{211}At and ^{207}Po were prepared from the generator for further purification or used directly for preliminary antibody labelling experiments (see §4.4.2-4.5 for details).

^{211}At purification using tellurium columns

A general method for chemically isolating astatine from polonium was followed, originally described by Bochvarova *et. al.* in 1972 [118]: For each extraction from the generator, the basic solution containing ^{211}At and ^{207}Po was added to 8 mL of 6 M HCl and 0.1 M $SnCl_2$ and loaded on to a custom 8 mm diameter tellurium column (column length = 10 mm or 2 mm, Te: 200 mesh), pre-equilibrated with 6 M HCl and 0.1 M $SnCl_2$. The $SnCl_2$ was used to convert the astatine to astatide. The column was washed, in order, with 10 mL of 6 M HCl and 0.1 M $SnCl_2$, 10 mL 6 M HCl, and 10 mL distilled water. The ^{211}At was eluted in three 0.2 mL fractions of 2 N NaOH. In principle, polonium can remain strongly bound to tellurium even under such basic conditions, while the astatide readily releases from tellurium as an eluent in the strong base [118].

^{209}At recovery from A=213 implantations

For NaCl/Mylar and NaCl/Ag targets, the target bracket was removed from the CARRIER and then the target was ejected from the bracket and placed in an flat, shallow glass dish, with the NaCl side facing up. Using a micropipette, the NaCl surface was dissolved in 100-300 μL of 0.1 N NaOH. With such a small volume of dissolving liquid, the clamping ring kept all solution on the inside surface of the target, which was recovered into a dry glass vial. NaCl/SS targets were simply put into a glass beaker and dissolved by applying droplets of 0.1 N NaOH to the NaCl surface (for 0.5 mL total solution). Additional washes of the targets surface were collected using the same method to recover any residual activity that had not been initially transferred, with each wash collected in a separate vial. Each vial was measured by Capintec dose calibrator using the ^{18}F setting to determine the relative amount of activity in each vial relative to the total amount recovered. The response of the dose calibrator to ^{209}At was unknown, but could be cross-calibrated at a later time with comparison with quantitative γ-spectroscopy measurements of the same samples (see §4.6.2).

Antibody labelling with ^{211}At and ^{209}At

The early clinical use of antibodies for targeting ^{211}At dose deposition to cancer cells emphasizes the important role these biomolecules will have in future therapies. The general methods for antibody (or large protein) labelling are immediately transferable to an increasing number of targeting molecules with potential clinical applications, without damaging to the targeting efficacy of these large biomolecules. Given the important role antibodies continue to have in ^{211}At-based targeted α-therapy, it was imperative to demonstrate that samples of ^{211}At and ^{209}At prepared at TRIUMF (using the methods described in Chapters 4-6) were suitable for antibody labelling. Regarding ^{211}At, an unknown implication of the ^{211}Rn/^{211}At generator system was the effect of ^{207}Po contamination on the labelling process and end product. In addition, biomolecule labelling with ^{209}At had never been attempted and presented a unique opportunity for preparing ^{209}At-labelled radioimmunoconjugates in advance of ^{209}At-based imaging studies (fully described in Chapters 5-7).

For this preliminary evaluation of antibody labelling with ^{211}At and ^{209}At, BC8 was selected as suitable antibody given its imminent clinical evaluation (see §2.4). BC8 was supplied by Dr. Oliver Press (Fred Hutchinson Cancer Research Center, Seattle, WA). The *closo*-decaborate moiety optimized for astatine labelling (isothiocyanatophenethyluriedo-*closo*-decaborate(2-)), here referred to as B10-NCS (see §2.3, was conjugated to lysine residues of the BC8 antibody courtesy of Dr. Scott Wilbur (Department of Radiation Oncology, University of Washington, Seattle, WA). The B10-BC8 in phosphate buffer solution (PBS) was shipped to TRIUMF and stored at 4°C. Labelling was com-

pleted combining roughly 200 μg of B10-BC8 in up to 40-60 μL of phosphate buffer (0.5 M, pH 6.8) with 15% volume equivalent of chloramine-T (1 mg/mL) and one of (i)the Tellurium-purified ^{211}At, (ii) a mixture of ^{211}At and ^{207}Po, or (iii) ^{209}At (in H_2O, pH 7). The role of chloramine-T (an oxidizing agent) was to oxidize astatine to its (1+) oxidation state for bonding to *closo*-decaborate(2-). After 2 minutes of gentle mixing, the reaction was stopped by the addition of sodium metabisulfite ($Na_2S_2O_5$) (1 mg/ml, 15% volume equivalent). The product was loaded onto a disposable PD-10 desalting column (GE Healthcare Life Sciences), packed with Sephadex G-25 Medium for removal of low molecular weight compounds ($\leq$5 kDa). High molecular weight reaction products were eluted in 0.5-1.0 mL fractions[6] of PBS with fractions collected individually (up to 10 fractions).

The percentage of activity in the eluent that was bound to the antibody was determined by Instant Thin Layer Chromatography (iTLC). Silica on glass fibre (iTLC paper) was spotted with a small fraction of the column eluent, allowed to dry, and then run with 10% trichloroacetic acid (Cl_3CCOOH) in H_2O. For these conditions, the large antibody BC8 remained stationary on the paper while free ions move with the solvent line. Once the solvent line had moved sufficiently (5-7 cm), the paper was cut in equal halves both pieces were measured with HPGe γ-spectroscopy[7]. Specific activity (SA, activity per unit mass of biomolecule) of the labelled product was not determined directly. Instead, a 25% loss of the antibody was assumed based on experience with ^{211}At labelling in Seattle (measured directly by UV absorbance), from which it was estimated that the procedure resulted in 150 ug of labelled product. Exact quantification of SA was not necessary for these initial studies but it should be noted that SA is expected to be an important parameter for specific antigen targeting.

Activity measurements

Gamma spectroscopy

Quantification of the activity recovered after target processing and isolation chemistry was performed by γ-spectroscopy, using a high purity germanium (HPGe) detector with the GENIE-2000 software package (Canberra Industries, Meriden, CT), for acquisition and analysis. This set-up consisted of a high purity germanium (HPGe) detector (semiconductor, cooled with liquid nitrogen), positioned within a lead (Pb) well for shielding, and fitted with a 0.5 mm beryllium window for minimal attenuation of sample emissions.

[6]PD-10 elutions for ^{211}At-B10-BC8 were done with 1.0 mL fractions, where as ^{211}At-B10-BC8 was eluted in 0.5 mL fractions, in order to yield fractions with higher concentration that are advantageous for animal studies.

[7]At the time of γ-spectroscopy, the radioactivity (initially a small amount to begin with) had mostly decayed, meaning iTLC simply indicated whether the astatine was bound to protein or free (as opposed to showing how much was bound).

Detector efficiency was determined by the TRIUMF Radiation Protection Group (RPG) as a function of energy using a europium-152 (^{152}Eu) calibration source with standard geometry (e.g. 20 mL glass vial filled with solution) and uncertainty of 3.4% (representing the minimum uncertainty for activity measurements). All measurements in this experiment used the efficiency calibrated with the 20 mL glass vial, except for iTLC papers[8]. Calibration of this detector was done on a weekly basis for background activity and efficiency calibration. An example of these measurements is shown in Figure 4.13 (TRIUMF data, figure courtesy of Andrew Robertson, UBC/TRIUMF). Detection efficiency was a strong function of energy between 10 keV and 200 keV, with a peak in efficiency at approximately 100 keV, producing a larger measurement uncertainty in this energy range. Note that ^{152}Eu did not have many emissions of low energy (50-100 keV) for calibration, also contributing to the uncertainty for these measurements.

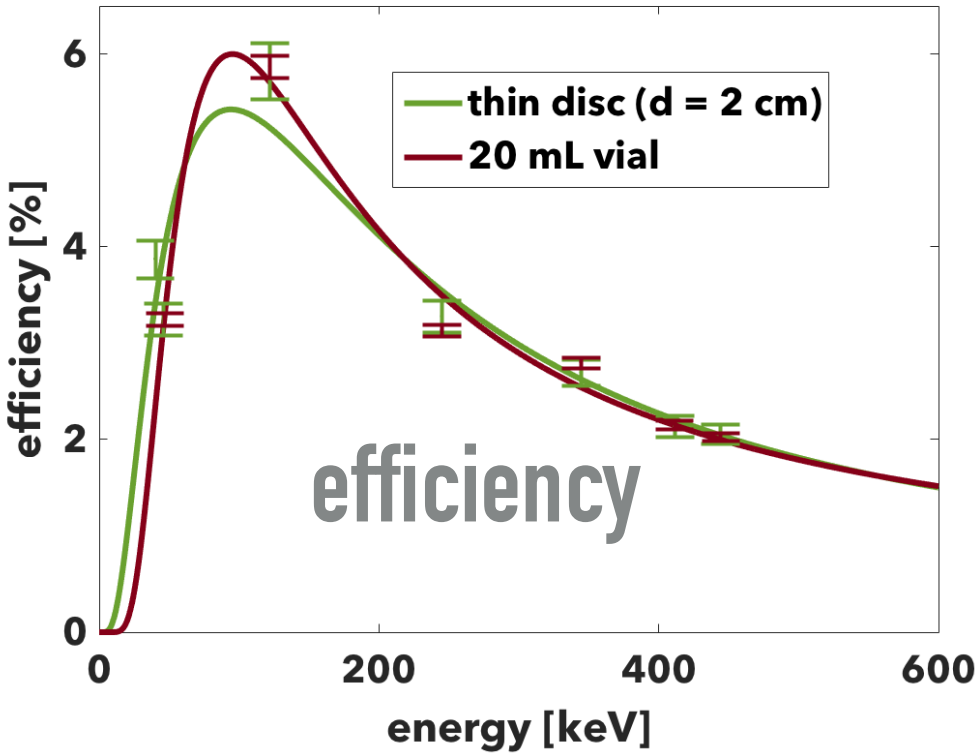

Figure 4.13: HPGe detector efficiency calibration as a function of energy. Detector efficiency was a strong function of energy between 10 keV and 200 keV, with a peak in efficiency at approximately 100 keV. All measurements for these experiments used the efficiency calibrated with the 20 mL vial. Data measured by TRIUMF RPG, figure courtesy of Andrew Robertson (UBC/TRIUMF graduate student).

Small aliquots (1-300 μL) of each solution were added to 20 mL glass vials filled with the same solvent. For quantitative analysis using the Genie 2000 software package,

[8]iTLC papers were measured with an efficiency calibration used for contamination swipes (because both objects have similar size and geometry).

libraries of radionuclide decay properties were constructed using the data listed in Tables 4.1 (for A=211 implantations) or 4.2 (for A=213 implantations). Integral counts for each peak were corrected for efficiency followed by radionuclide identification (based on the library). Detector dead time was kept below a maximum of 10%, but was typically less than 1%. Post-processing by this software included decay correction and interference correction (for when peaks overlapped).

Activity measurements of ^{211}Rn, ^{211}At, ^{207}At, ^{207}Po, and ^{209}At were quantified based only on emissions above 200 keV to avoid unnecessary uncertainties arising from the low energy efficiency calibration (as described above). With the exception of ^{211}At, all of these isotopes provided high intensity γ-rays; a 7% measurement uncertainty was attributed to these activity measurements, corresponding to the uncertainty in the calibration source (3.4%), aliquot measurement uncertainty (5%), and uncertainty in efficiency calibration function determined by the Genie 2000 software (1%), added in quadrature. ^{211}At activity was estimated in the same manner, although branching ratios for ^{211}At γ-rays were relatively low (687.0 keV; 0.261%), and overlapped with emissions by ^{211}Rn (684.7 keV; 0.59%), ^{207}At (686.0 keV; 2.03%), and ^{207}Po (687.5 keV, 1.81%). Interference corrections by the Genie 2000 were enabled to determine the proportion of counts originating from ^{211}At. As the short-lived daughter ^{211}At, ^{211}Po also provided low intensity γ-rays for quantification (569 keV, 897 keV; 0.535%, 0.551%), which provided an indirect measure of ^{211}At activity (in proportion to the branching ratio for ^{211}At $\leftarrow$ ^{211}Po decay (58%). The ^{211}Po γ-rays did not significantly overlap with emissions from other significant isotopes in these samples. Relatively low number of counts available for ^{211}At was incorporated into the measurement uncertainty determined by the Genie 2000 analysis, amounting to the higher total uncertainty in ^{211}At measurements reported by this work (ranging between 7%-18%).

Decay correction of ^{211}At γ-ray counts was also a non-trivial consideration for solutions containing both ^{211}At and ^{211}Rn (given that ^{211}Rn provided an additional source of ^{211}At throughout measurement. In order to properly decay correct the number of counts for ^{211}At, samples containing ^{211}At and ^{211}Rn were measured while the isotopes were in transient equilibrium, at which point the effective half-life of ^{211}At (for the purpose of decay correction) was approximately equal to that of ^{211}Rn (14.6 hours). Likewise, the effective half-life of short-lived ^{211}Po was considered equal to that of ^{211}At (7.21 hours), since ^{211}Po and ^{211}At were always in equilibrium during the HPGe detector measurements.

Dose calibrator measurements

A Capintec CRC-25R dose calibrator (Capintec Inc, Ramsey, NJ) was used to measure relative At-209 activity, enabling the rapid determination of activity while preparing sam-

ples for animal studies, for which prompt quantification was a necessity[9]. This detector is a well-shaped, thin-wall argon gas ionization chamber. The dose calibrator measurements made using the precalibrated ^{18}F setting were cross-calibrated with ^{209}At activity measurements determined by γ-spectroscopy, by measuring the same sample by each detector. The calibration factor (CF) was defined as,

$$\mathrm{CF} = \frac{(\text{MBq } ^{209}\text{At determined by } \gamma\text{-spectroscopy})}{(\text{MBq determined by dose calibrator using F-18 setting})}, \tag{4.14}$$

where activity determined by γ-spectroscopy was decay-corrected to the time of the dose calibrator measurement. In this way, it was possible to measure absolute ^{209}At activity with the dose calibrator, for any sample.

Chapter summary

This chapter described the set of methods and instrumentation that were developed for studying ^{211}Rn and ^{209}At production and recovery from ISAC, as well as construct ^{211}Rn/^{211}At generators for isolation and labelling studies. The results of these experiments are discussed in Chapter 6.

[9]Several ^{209}At samples were used within a few hours after preparation for time-sensitive SPECT imaging studies involving animals.

Chapter 5

Methods for SPECT Imaging with ^{209}At

SPECT (described in §2.5.2) is a powerful tool for determining the targeting efficacy for many radionuclide therapies [1, 119]; Compared to single point *ex vivo* measurements, the primary theoretical advantages of measuring activity distributions with SPECT are two-fold: (i) ^{209}At distributions can be measured *in vivo*, for multiple time points of a single animal, while ^{211}At measurements typically require multiple animals for *ex vivo* measurements at each time point; (ii) activity is recorded in 3-dimensions, required for voxel-based dose calculations (*ex vivo* activity is typically measured with whole-organ activity counting).

The study of ^{211}At-based therapies with *in vivo* SPECT imaging is, however, limited by the low energy of emissions (77-92 keV Po X-rays) and low intensity of these, both factors contributing to a weak signal compared to common SPECT isotopes. In addition, doses of ^{211}At are low compared to β-emitters with lower RBE, reducing the total number of emissions available for imaging. Meaningful image-based ^{211}At studies may use inferences from surrogate isotopes with better imaging properties. In contrast to ^{211}At, the decay of ^{209}At ($t_{1/2}$=5.41 h) is accompanied by a greater abundance of X-rays and an additional set of higher energy photons of high intensity. The most intense X-rays and γ-rays for ^{211}At and ^{209}At are summarized in Table 5.1. In addition to this larger set of emissions, roughly 20 times more ^{209}At activity can be administered before the same whole-body α-particle dose is reached, compared to ^{211}At, since the α-decay branching ratio of ^{209}At is only 4.1%. This means that more activity can be administered per injection to increase statistics, thereby strengthening the signal for imaging. For these reasons, ^{209}At presents a novel and motivated opportunity to image astatine activity distributions, with SPECT.

The decay of ^{209}At by electron capture produces a long-lived polonium isotope, ^{209}Po ($t_{1/2}$ = 102 years), a pure α-emitter. This might present the most significant limitation for ^{209}At SPECT imaging. Although the *in vivo* properties and toxicity of ^{209}Po had never been studied experimentally, it can be assumed to be biochemically equivalent to ^{210}Po ($t_{1/2}$ = 138 days), and as such, both have the same biological half-life (roughly 50

Table 5.1: Energy and intensity of photon emissions from ^{211}At and ^{209}At.

X-ray energy (keV)	γ-ray energy (keV)	^{211}At intensity (% per decay)	^{209}At intensity (% per decay)
77		13.2	36.4
79		22.2	61.0
89		2.6	-
90		4.9	41.6
92		2.4	-
	195	-	22.6
	239	-	12.4
	545	-	91.0
	782	-	83.5
	790	-	63.5

days in humans) and both sequester to the same locations, *in vivo* [120]. The potential for high toxicity of ^{210}Po is well known as it is naturally targeted to the bone marrow in mammals [120]. Other disadvantages for clinical use include the higher equivalent dose rate for ^{209}At compared to ^{211}At, and the limited availability of this isotope. For these reason, ^{209}At would not be considered suitable for clinical SPECT imaging, and should be reserved for animal studies. These properties of ^{209}At limit its use to animal studies and clinical use of this isotope is not suggested by this work.

The ^{209}At/^{211}At theranostic pair is an acceptable approach for preclinical studies in animals, and a potential application of ^{209}At-based SPECT might be in establishing the biodistribution equivalence of ^{123}I/^{209}At labelled biomolecules, with respect to theranostic pairing of At and I. The readily available ^{123}I is already used clinically as a SPECT tracer and provides the possibility of surrogate dosimetry for ^{211}At-based targeted α-therapy in humans. Motivated by this prospect, dual-isotope SPECT for simultaneous imaging of ^{209}At/^{123}I activity distributions provided a novel approach for determining the equivalence of cancer targeting efficacy with these isotopes. Although this endeavour exceeded the scope of this work, the core component of this technology was tested by evaluating the independence of images reconstructed for each isotope after simultaneous SPECT scanning.

The production of ^{209}At at ISAC, still in development, enabled the first assessment of this isotope for measuring astatine activity distributions with high energy SPECT. This chapter summarizes methods or the set of preliminary experiments that amount to a pioneering pilot study of small animal SPECT imaging with ^{209}At, demonstrating the feasibility of imaging with this isotope and examining practical aspects of the process.

General methods for image acquisition and image reconstruction are described in §5.1 and §5.2, respectively. §5.3 outlines the methods for imaging with phantoms and presents the various approaches used for analysis. Finally, methods for *in vivo* imaging are presented in §5.4

Image acquisition

High energy SPECT imaging was performed with VECTor/CT, a small animal imaging system installed at the UBC Centre for Comparative Medicine. The VECTor/CT had three large flat-panel thallium-doped sodium iodide scintillation detectors of thickness 9.5 mm, positioned parallel and equidistant to a central axis and surrounding a cylindrical focused pinhole collimator, positioned along central axis. A variety of collimators were available and could be manually interchanged between scans. Physical collimation for this experiment utilized the High Energy Ultra High Resolution (HEUHR) collimator, a hollow cylinder of tungsten (W) with a bore radius of 4.8 cm and W wall thickness of roughly 4-4.5 cm, as measured from the inner diameter to the outer diameter.[1] The HEUHR collimator had 162 pinholes, focused on a volume of 0.5 mL. For each detector, counts were recorded in list mode (meaning on an event-by-event basis).

The VECTor/CT system used an automated, robotic arm to precisely position the *bed*[2], as defined indirectly by the user by selecting the volume of interest for imaging. The helical scanning focus method was used whereby the focused volume (as geometrically determined by the pin-hole collimator) was scanned through a series of stationary bed positions in a helical pattern in order to measure entire field of view (user-defined). Each set of spatially distinct, consecutively acquired bed positions, called a *frame*, could be repeated multiple times throughout the duration of a single scans. Before or after each SPECT scan, a CT scan of the specimen was acquired using the on-board CT scanner, positioned in series with the SPECT system (directly adjacent). The CT data was used to determine the field of view for SPECT imaging, and to record a measure of attenuation for estimating the attenuation correction after image reconstruction. The CT image was also used to compare imaged activity distributions to physical and anatomical structures.

Monte Carlo simulation of VECTor measurements for ^{209}At

Data from a Monte Carlo simulation of the detected energy spectrum for VECTor with ^{209}At was provided by UBC, courtesey of Pedro Luis Esquinas (Department of Physics and Astronomy, UBC). The detector simulation was performed with GATE (Geant4 Application for Emission Tomography) [121], and general components of the simulation were originally prepared for a related study of ^{188}Re, for which the simulation had been previously validated. Several simplifications were made for the simulation compared to

[1] The exact dimensions of the collimator have not yet been published by the manufacturer.

[2] The support for the animal or phantom during imaging is called the *bed*.

the actual physical geometry. Briefly, the focussed pin-hole collimator was approximated as a cylindrical tungsten collimator (thickness = 4.3 cm), with 15 pinholes arranged in a ring. The pinhole geometry (diameter = 0.7 mm and opening angle = 16 deg) was obtained from Goorden *et al.* 2013 [122]. The ^{209}At source was modelled as a small spherical water source with a radius of 1 mm and homogeneous ^{209}At distribution. While not physically accurate, the simplifications of the simulation geometry were considered sufficient for explaining general features of the measured spectrum for ^{209}At. It should be noted that performing this Monte Carlo simulation was not a component of this body of work, but provided valuable information for interpreting the experimental measurements of ^{209}At with VECTor/CT.

Image reconstruction

SPECT image reconstruction was performed with proprietary software provided by the manufacturer MILabs (Utrecht, The Netherlands), described as Pixel-based Ordered Subset Expectation Maximization (POSEM). Based on the traditional Maximum-Likelihood Expectation-Maximization (MLEM) image reconstruction method, POSEM is an iterative numerical optimization algorithm that searches for the most probable distribution of activity based on the spatial distribution of counts detected, as quantified by the energy selected for reconstruction. The parameters for reconstruction that were used for this experiment matched the standard mode of operation by UBC CCM: list-mode data acquisition was used to select an energy window for the counts used in reconstruction, with window width (defined as a percentage of the energy) set to 25% of the counts in the window energy, and triple window scatter correction[3] was performed by setting energy windows (of width 20%) on either side of the primary energy window to define the background. Linear interpolation between the background windows was used to estimate the background counts, which were then subtracted from the counts before reconstruction. For all SPECT image reconstructions, 10-15 iterations were performed with 16 subsets (user-defined parameters of the POSEM reconstruction method, consistent with the standard mode of operation at UBC CCM).

Reconstructed SPECT and CT data sets were spatially co-registered with the CT image for combined (fused) SPECT/CT viewing. This procedure resampled the SPECT data (voxel size = 0.4x0.4x0.4 mm) to CT voxel-size (0.16mmx0.16mmx0.16mm) by trilinear interpolation. All images were smoothed with a 3-D Gaussian smoothing filter[4] (1 mm FWHM, kernel size 7) to reduce noise while preserving spatial resolution, also consis-

[3]Using triple window scatter correction, the background counts in the primary energy window is interpolated by the mean counts in adjacent energy windows.

[4]For each spatial direction of the 3-D activity distribution, guassian smoothing was applied by convolving the raw activity distribution images with an array of discrete values mapped by a 1D Guassian ditribution (as defined by FWHM), truncated to the array length given by the kernel size).

tent with UBC CCM practices. In some cases where uptake of activity was relatively low (resulting in lower number of counts, statistically), heavier Gaussian filtering was performed (2 mm FWHM, kernel size 31). All image analysis was performed using AMIDE 1.0.5 (AMIDE's a Medical Image Data Examiner [123]) except for generating line profiles, with extent Vinci 4.61.1. (Volume Imaging in Neurological Research, Co-Registration and ROIs included) [124].

Phantom imaging

Description of phantoms

Phantoms were used to evaluate the measured activity distribution of ^{209}At as measured by SPECT, in comparison with the physical distribution ^{209}At in solution as defined by the internal volume of the phantom. Phantoms were made of plastic and filled with ^{209}At in aqueous solution (0.1 N NaOH) for which the activity and activity concentrations had been previously measured. Multiple phantom types were used, including the μ-Jaszczak and Jaszczak phantoms used for evaluating contrast and resolution, also known as 'hot-rod phantoms, and a 20 mL syringe for evaluating image uniformity. The details for each of these phantoms and there respective scan parameters are listed in Table 5.2. The Jaszczak phantoms (described schematically by Figure 5.1 were had a complex physical design, composing of single plastic cylinder with six sets of hollowed out cylinders (rods) positioned symmetrically about its axis. Each set of rods were defined by a different rod diameter, with the space between rod centres being 2 times the rod diameter. The rod diameters and number of rods in a set were as listed in Table 5.2. In contrast, the uniformity phantom (20 mL syringe) was much simpler, giving a physically uniform ^{209}At activity distribution over a wide, symmetrical volume.

Table 5.2: Description of phantom imaging experiments.

Phantom	**Description**	**^{209}At**	**Scan parameters**
μ-Jaszczak (μ-hotrod)	plastic cylinder with 6 sets of fillable rods rod diam. (mm): 0.45, 0.50, 0.55, 0.75, 0.80, 0.85, rods/set: 6, 6, 6, 10, 10, and 15, respectively	5.0 MBq	11 hr scan, 22 30 min frames
Jaszczak (hotrod)	plastic cylinder with 6 sets of fillable rods rod diam. (mm): 0.85, 0.95, 1.1, 1.3, 1.5, and 1.7, rods/set: 3, 3, 3, 3, 6, and 6, respectively	2.9 MBq	3 hr scan 15 12 min frames
Uniformity (20 mL syringe)	cylindrical shape, internal diameter = 20 mm, filled to 7.2 mL , (length of internal volume = 21 mm)	9.8 MBq	3 hr scan 1 frame of 3 hrs

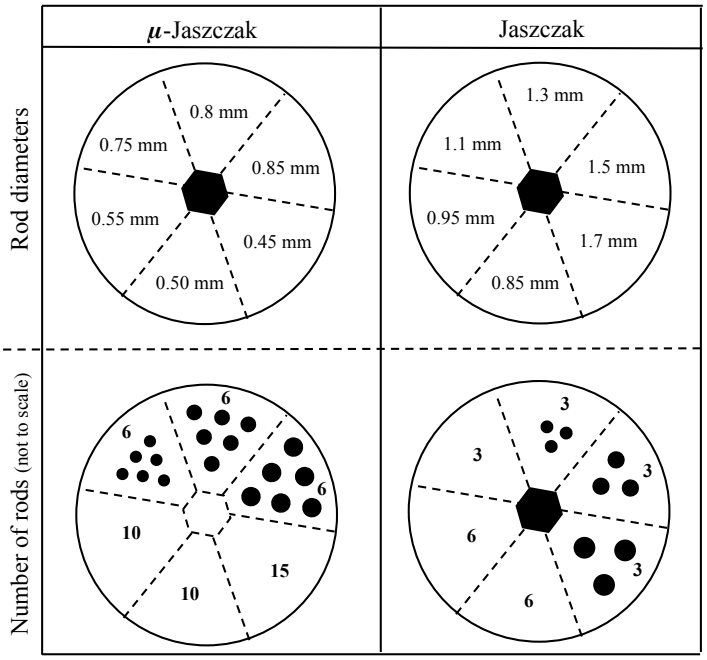

Figure 5.1: Physical description of μ-Jaszczak and Jaszczak phantoms. Not to scale.

Phantom image analysis

SPECT images produced for the μ-Jaszczak phantom were analyzed qualitatively, and suggested that a more thorough quantitative assessment of image resolution and contrast should be done with the larger Jaszczak phantom. The Jaszczak phantom was used to evaluate contrast and contrast-to-noise ratios as a function of rod diameter, for image reconstructions using various energy windows of the spectrum, representative of the most abundant emissions. For transverse cross-sections of the SPECT image, contrast and noise were quantified by defining a set of circular ROIs for each set of rods, with diameter 0.9 times the rod diameter. *Hot* ROIs were positioned concentric with the hotrods, and *cold* ROIs were evenly distributed in the space between a given set of rods. (For a picture of ROI positioning with respect to rod position, see Figure 7.5). ROIs were repeated on ten consecutive 0.4 mm slices within the central section of the phantom[5]. For a given set of rods (of equal diameter), the mean and standard deviation over hot and cold ROIs were calculated separately in order to compute quantitative measures of contrast and noise, defined by Equations 5.1 and 5.2:

$$\text{contrast} = \frac{\overline{hot} - \overline{cold}}{\overline{hot}} \,, \tag{5.1}$$

$$\text{noise} = \sqrt{\sigma^2_{hot} + \sigma^2_{cold}} \,, \tag{5.2}$$

[5]Rod filling was homogeneous over this volume (or set of slices), determined visually by the CT data.

where $\overline{hot}$ and $\overline{cold}$ were the mean relative activities of hot and cold ROIs, respectively, σ_{hot} and σ_{cold} were the corresponding standard deviations of the mean ROI values. This analysis was performed with Matlab 7.9.0 ((MathWorks; Natick, MA, USA), with scripts primarily written by Dr. Matthew Walker during post-doctoral work with the UBC PET Imaging Group (*related 2014 publication, [125]*).

The uniformity phantom physically provided a large activity distribution of uniform concentration. SPECT image uniformity was evaluated in terms of the amount of variation in the resulting SPECT image. Uniformity was quantified with three metrics that could be compared to established criteria for quantitative SPECT imaging with ^{18}F, as previously determined at UBC CCM: the root mean square noise (rms-noise), the integral uniformity, and the coefficient of variation ($COV(\%)$). For calculating rms-noise and integral uniformity, analysis was performed with ImageJ 1.50g: 7 adjacent transverse slices of the phantom image were summed to give a 2D cross section of the phantom with thickness of 1.12 mm diameter (7 slices x 0.16 mm slice thickness). A 2D circular ROI with diameter 15 mm was positioned concentric with area of activity within the syringe.

With respect to pixels in this ROI, rms-noise (%) was defined as:

$$\text{rms-noise } (\%) = \frac{\text{standard deviation in pixel value}}{\text{mean pixel value}} \times 100\%, \tag{5.3}$$

and integral uniformity (%) was calculated as

$$\text{integral uniformity } (\%) = \frac{\text{max pixel value - min pixel value}}{\text{max pixel value + min pixel value}} \times 100\%, \tag{5.4}$$

These metrics were defined this way by the American association of Physicists in Medicine, AAPM Report NO. 52, "Quantitation of SPECT Performance", (1995) [126].

$COV(\%)$ was calculated for a well defined set of ROI (described below) using Equation 5.5,

$$COV(\%) = \frac{\sigma_{\overline{p}}}{\overline{p}} \times 100\%, \tag{5.5}$$

where $\overline{p}$ was the average voxel value over all ROI, and $\sigma_{\overline{p}}$ was the standard deviation between mean values of each ROI. 28 evenly spaced spherical ROI (radius -0.9 mm) were defined throughout the volume of the syringe, as shown in Figure 5.2. This positioning of ROI was comparable to previous measures of $COV(\%)$ for ^{18}F at UBC, and provided the opportunity to compare to published values (from [127]). Accepted values for quantitative SPECT measurement at UBC CCM were previously determined as: rms noise (%) $< 8\%$, integral uniformity (%) $< 20\%$, and $COV(\%) < 5\%$.

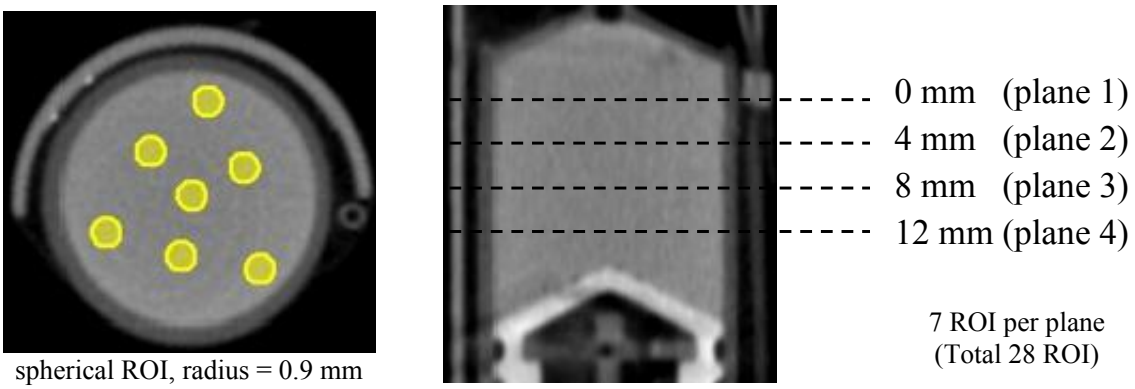

Figure 5.2: ROI defined for ^{209}At SPECT images of the uniformity phantom (20 mL syringe filled to 7.2 mL). Each ROI was cylindrical with radius 1.5 mm and length 2mm. Seven ROI were defined for each of 4 parallel planes, with adjacent planes 3 mm apart, totalling 28 individual ROI for determining the uniformity as defined by the coefficient of variation.

Mouse imaging

The availability of ^{209}At presented an opportunity to perform the first pilot study of small animal SPECT imaging with ^{209}At, in mice. The production of ^{209}At was still in development and had major uncertainties in terms of both the quantities produced and the timing of production; it was considered not suitable to test ^{209}At in animal models of disease that may otherwise be left unused in the event of ^{209}At production failure. Instead, mouse imaging was performed with male C57BL/6 mice, an inbred strain of laboratory mouse characterized as normal (or healthy), and routinely used at UBC CCM. In all cases, radioactivity was administered to the blood stream by tail-vein injection, with the mouse anaesthetized. This use of animals by this experiment adhered to the approved ethics and operating protocols (UBC animal care certificate number A12-0172, years 2014-2015), reviewed by the UBC animal care committee.

Description of in vivo imaging of ^{209}At (in mice)

Three types of ^{209}At scans were completed, with the scanning parameters for each listed in Table 5.3. First, free ^{209}At^{-} was delivered to normal mice to establish the SPECT imaging as capable of measuring the well-known biodistribution of unbound astatide in normal mice, where astatine normally sequesters, most significantly, in the the thyroid, stomach, lungs, salivary glands, and urine. This provided a baseline for the second type of scan, which imaged the biodistribution of the ^{209}At-labelled protein (prepared as described in §4.5 and §6.4.2). Two mice were injected with different amounts of activity, with the second mouse receiving only 40% of the injected activity administered to the first mouse. The variable quantity of injected activity was used to compare the effect on image quality arising between these two injected quantities. The third type of scan was a simultaneous, dual-isotope scan with the ^{209}At-labelled protein and free ^{123}I ($t_{1/2}$),

with its most intense γ-ray emission at 159 keV (83%). This simultaneous measurement was used to determine if the activity distribution of each isotope could be measured independently, based on the distinct photon energies emitted by each isotope. This was considered a critical step in determining if ^{209}At would be suitable for evaluating ^{123}I as a surrogate for determining the activity distributions of clinical applications of ^{211}At-based therapies. For each type of scan, mice were anaesthetized and full body SPECT imaging was performed for 40 to 45 minutes followed immediately by CT scan. One additional SPECT scan was performed by repeating imaging of free ^{209}At but using the standard high resolution SPECT collimator (1.5 cm W, 75 focussed pinholes), in order to assess if high energy collimation was actually required for ^{209}At.

Table 5.3: Description of mouse imaging experiments with ^{209}At. p.i.=post-injection (of activity into blood stream via tail-vein)

Scan type	Details	Injected activity	Scanning parameters
Free [^{209}At^{-}]astatide	included *ex vivo* biodistribution, scanned at 30 min p.i.	11.6 MBq ^{209}At	45 min scan 9 frames of 5 minutes
^{209}At-labelled BC8	n=2, scanned at 1, 3, and 24 hrs p.i.	1: 6.2 MBq ^{209}At 2: 2.5 MBq ^{209}At	40 min scan 8 5 min frames
^{209}At-labelled protein + free [^{123}I^{-}]iodide	^{123}I injected 10 min after ^{209}At, scanned at 1 hour p.i. (of ^{209}At)	4.1 MBq ^{209}At 48.1 MBq ^{123}I	42 min scan 6 7 min frames

Ex vivo biodistribution measurements of free ^{209}At

The biodistribution of a mouse imaged with free ^{209}At was performed. Immediately after SPECT/CT scanning was complete, the mouse was sacrificed and some selected tissues were harvested and weighed. These specimens included the thyroid (including an attached segment of the trachea), the stomach (contents included), the heart, the liver, the lungs, and 5 mL of blood. The activity in each specimen was counted by a gamma counter (Packard Cobra II Gamma Counter, Packard Instrument Company Inc, Meriden, CT, USA), for which background counts were determined by measuring a blank sample of water. The tail was also measured to determine the amount of residual activity in the tail following administration by tail-vein injection. Absolute quantification of the activity in each sample was accomplished by also measuring samples of ^{209}At in water that had been diluted by 100 and 1000 times from concentrated stock solution of ^{209}At in 0.1 N NaOH, previously measured by dose calibrator. This provided the means to calibrate the gamma counter in terms of activity in Bq per count, allowing for activity in each organ/sample to be determined absolutely. This cross calibration between dose calibrator actually represented a 3-step cross calibration between the initial quantification by γ-spectroscopy,

the dose calibrator used for measuring ^{209}At standards, and the gamma counter at CCM. The uncertainties for each step were approximately between 5% and resulted in a net uncertainty of nearly 10% in the calibration of the gamma counter for ^{209}At activity measurements (adding the uncertainties of each measurement in quadrature). This was considered sufficient for comparison to published biodistribution measurements and the activity distribution measured by SPECT. The weight of specimen was measured and used to calculate the percent of injected activity in each organ at the time of specimen collection.

Chapter summary

This chapter presented the methods that were used to conduct the first-ever imaging study with ^{209}At. Specifically, details were provided regarding image acquisition, image reconstruction, phantom studies and *in vivo* (mice) studies, using a small animal SPECT scanner with high energy collimation. The results for these experiments are presented in Chapter 7.

Chapter 6

Results of ^{211}Rn/^{211}At and ^{209}At Recovery at ISAC

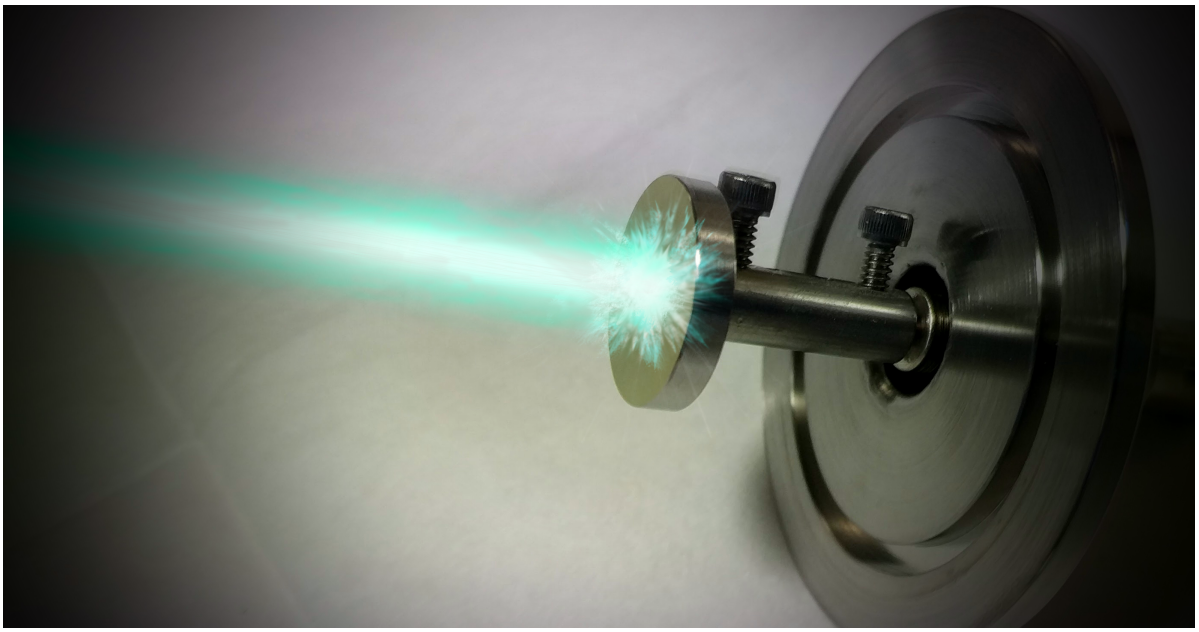

Figure 6.1: Artistic rendition of ion beam implantation.

The sections of this chapter summarize the results for production and isolation experiments, performed according to the procedures detailed in chapter 4. Each step of the production procedures are analyzed sequentially in §6.1-6.4, before addressing some further observations in §6.5. The chapter concludes with an extended discussion of these results and their implications for future work in §6.6.

Summary of RIB implantations

RIB implantations were performed four times for A=211 (^{211}Fr and ^{211}Ra) and seven times for RIB of A=213 (^{213}Fr and ^{213}Ra). Two of the seven A=213 implantations had a significant loss of beam intensity attributable to loss of proton beam during implantation, or some kind of target failure. In these cases, the recovery efficiency calculations for these

runs were excluded from the analysis because the theoretical activity was not deemed accurate; however, these production runs still produced significant quantities of ^{209}At that were used for the imaging experiments discussed in Chapter 5. The ISAC RIB production and implantation parameters for each run are summarized in Table 6.1, along with the corresponding IYS measured RIB yields. Before each RIB implantation, the α-spectrum and γ-spectrum of the RIB was measured at the IYS to determine beam intensity (in ions/s for each isotope composing the beam, as described in §3.3.4). The transmission factor accounting for the relative difference between beam intensity delivered to IIS and IYS ($\epsilon_{\mathrm{IIS/IYS}}$, defined by Equation 4.1) was measured to be 1.25 (a 25% increase in beam intensity at the IIS, relative to the IYS yield measurement). A representative sample of the spectra measured at the IYS by this experiment is shown in Figure 6.2, where peaks for the major beam components have been identified.

Table 6.1: RIB production run parameters and calculated ion yield from IYS measurements.

	Run#	A	specifications	RIB ions/s (α-spec)	RIB ions/s (γ-spec)
^{211}Rn/^{211}At production:	1	211	3 min @ 20 keV NaCl/Al target	^{211}Fr=$1.2 \times 10^9/b_\alpha \pm 11\%$ ^{211}Ra=$1.0 \times 10^7 \pm 15\%$	^{211}Fr=$8.8 \times 10^7/b_{ec} \pm 5\%$ N/A
	2	211	40 min @ 20 keV NaCl/Al target	^{211}Fr=$1.0 \times 10^9/b_\alpha \pm 11\%$ ^{211}Ra=$4.0 \times 10^7 \pm 15\%$	^{211}Fr=$1.72 \times 10^8/b_{ec} \pm 5\%$ N/A
	3	211	210 min @ 20 keV NaCl/Al target	^{211}Fr=$2.5 \times 10^7/b_\alpha \pm 11\%$ ^{211}Ra=$1.0 \times 10^7 \pm 15\%$	^{211}Fr=$3.2 \times 10^6/b_{ec} \pm 12\%$ N/A
	4	211	200 min @ 20 keV NaCl/SS target	^{211}Fr=$8.7 \times 10^7/b_\alpha \pm 11\%$ ^{211}Ra=$1.3 \times 10^7 \pm 15\%$	^{211}Fr=$8.6 \times 10^6/b_{ec} \pm 8\%$ N/A
^{209}At production:	5	213	490 min @ 20 keV NaCl/Mylar target	^{213}Fr=$7.7 \times 10^8 \pm 10\%$ ^{213}Ra=$1.6 \times 10^8 \pm 10\%$	N/A N/A
	6	213	300 min @ 20 keV NaCl/Mylar	^{213}Fr=$7.1 \times 10^8 \pm 10\%$ ^{213}Ra=$1.0 \times 10^8 \pm 10\%$	N/A N/A
	7	213	561 min @ 28 keV NaCl/Ag target	^{213}Fr=$1.1 \times 10^9 \pm 10\%$ ^{213}Ra=$3.9 \times 10^8 \pm 10\%$	N/A N/A
	8	213	551 min @ 28 keV NaCl/Ag target	^{213}Fr=$8.7 \times 10^8 \pm 10\%$ ^{213}Ra=$1.6 \times 10^8 \pm 10\%$	N/A N/A
	9	213	390 min @ 20 keV NaCl/SS target	^{213}Fr=$8.6 \times 10^8 \pm 11\%$ ^{213}Ra=$1.6 \times 10^8 \pm 13\%$	N/A N/A

As shown in the Figure 6.2a, α-particle emissions for ^{211}Fr and ^{211}Ra were the dominant peaks of the α-spectrum for RIB with mass separation at mass A=211. ^{207}Rn produced in the decay of ^{211}Ra was also detected in low relative abundance, as expected.

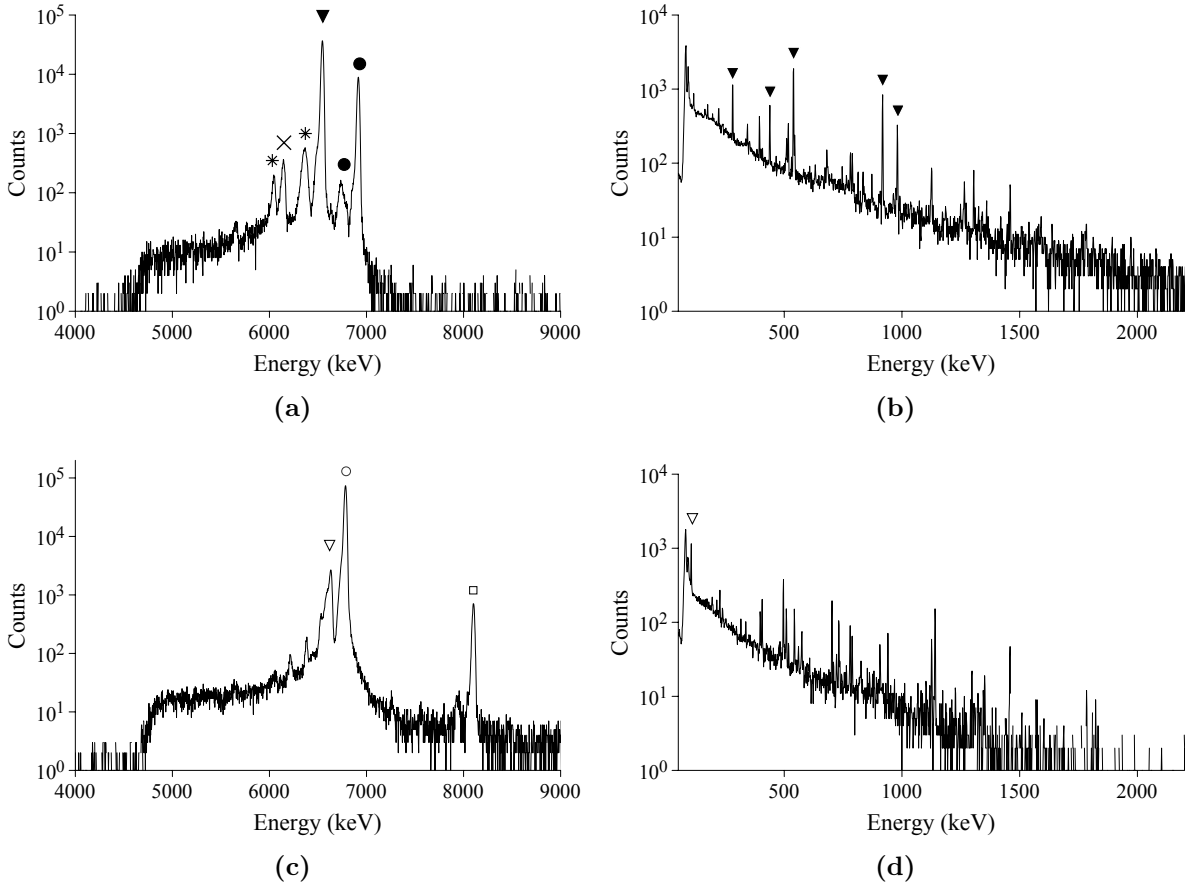

Figure 6.2: α- and γ energy spectra measured at the ISAC Yield Station for RIB delivered to the ISAC yield station: **(a)** α-energy spectrum for A=211, **(b)** γ-energy spectrum for A=211, **(c)** α-energy spectrum for A=213, and **(d)** γ-energy spectrum for A=213. The summed number of counts for peaks corresponding to ^{211}Fr, ^{211}Ra, ^{213}Fr, or ^{213}Ra were used to calculate the RIB yields in ions/s, according to Equation 3.8. (20 keV or 28 keV RIB produced by 480 MeV protons, UCx target, Re surface ionizing ion source. Legend: ▼ = ^{211}Fr, •= ^{211}Ra, ▽ = ^{213}Ra, ○ = ^{213}Fr, □ = ^{213}Rn, x = ^{207}Rn, $*$ = Energies match some ^{212}Fr emissions ($t_{1/2}$=20 min), possibly the result of minor contamination at IYS. This was not expected to be a component of the RIB delivered to IIS.

For two of these four RIB deliveries, the yields for ^{211}Fr were much lower than expected, increasing the relative proportion (and significance) of ^{211}Ra in the beam. The reason for the variable ratio in ^{211}Fr and ^{211}Ra was unclear; one explanation for this discrepancy in RIB composition was that the ionization of Fr and Ra by the Re surface ionizing ion source was very temperature dependent, with a variable dependence for each element. ^{211}Fr yield was also independently quantified with γ-ray counts (Figure 6.2b). Interestingly, the α-sprectroscopy and γ-spectroscopy measurements could be used together to determine branching ratio of ^{211}Fr decay, for which the analysis is provided as supplementary observations in §6.5. ^{209}At production was completed using RIB of mass A=213 (Runs 5-9 in Table 6.1). ^{213}Fr and ^{213}Ra were identified as the major contributors to these beams, for which peaks were easily identified by the α-spectra (shown in Figure 6.2c). The measured IYS γ-spectrum for these RIB were not used to calculate RIB yields for these

isotopes; ^{213}Fr and ^{213}Ra did not have sufficiently intense γ-ray emissions for accurate quantification[1].

Air sampling measurements

Following each implantation and relocation of the CARRIER to the radiochemistry laboratory, venting and air sampling was conducted according to the methods described in §4.3.5. Volatile α-emitting activity was expected to be present within the CARRIER following implantation due to α-decay recoil and diffusion. For the most part, the air sampling procedure acted as a fail safe for the CARRIER, indicating if a major release of volatile activity had occurred within the chamber, before it was opened. Quantitative measurements were carried out as supplementary analysis and are reported in §6.5.2. That analysis showed that the α-particle activity could be attributable to volatility of Rn and At isotopes. In all cases, the amount of volatile activity of α-emitters was below 0.1% of the total predicted activity. These levels of volatile activity indicated that the CARRIER could be opened inside of the open-door hotcell (equipped with 150 CFM[2] high flow-rate ventilation) without posing a significant radiation safety hazard. In practice, an internal TRIUMF safety review established 100,000 counts per minute (measured by the Lucas cell) to be a suitable "hold point" to consider the possible implications before opening the chamber. The exact magnitude of the limit was not critical for safety, but grossly surpassing this limit could be used to identify if the implantation had somehow failed, resulting in a major release of volatile activity (which did not occur during these experiments).

Recovery yields following target processing

Recovery of ^{211}Rn (and comparison to recovered ^{207}At)

The implantation of ^{211}Fr in NaCl resulted in the build-up of its immediate daughters ^{211}Rn and ^{207}At, *in situ*, as well as the inventory produced by their decay. Following the procedure outlined in §4.4.1, the NaCl target was rapidly dissolved, releasing the ^{211}Rn and other radioactive inventory into one of three volumes: the aqueous solution (0.1 N NaOH), the dodecane, and the airspace of the 30 mL syringe. Aliquots of each solution were measured by gamma spectroscopy and the total recovered activity of ^{211}Rn. The γ-spectra for samples of aqueous solution and dodecane collected immediately after target dissolving (Run 1) are shown in Figure 6.3. None of the aqueous solutions tested by this experiment were found to contain ^{211}Rn (or any radon isotope). In contrast, the dodecane was found to contain all of the recoverable ^{211}Rn. ^{207}At and ^{207}Po were observed to be present in significant quantities for both the aqueous solution and dodecane. Measure-

[1]The most intense ^{213}Ra emission was 6% at 110 keV, which can be identified in Figure 6.2d.
[2]CFM stands for cubic feet per minute.

ment details and recovery efficiency for each ^{211}Rn production run are summarized in Table 6.2.

The total recovered yields were calculated based on γ-spectroscopy assay measurements for ^{211}Rn. Additionally, the total activity of ^{207}At recovered in solution was determined for comparison. Measurement uncertainty was estimated to be 10% by ISAC, based on previous measurements during commissioning [107]. These values were compared to the theoretical for each run (and given set of production rates for ^{211}Fr and ^{211}Ra, theoretical (or predicted) yields for ^{211}Rn and ^{207}At were calculated using Equation 4.13. Recovery efficiency was defined as $\frac{\text{measured } A}{\text{predicted } A} \times 100\%$. These results are summarized in Table 6.2. The mean recovery efficiency for ^{211}Rn was 26%±2%. This was similar to recovery efficiencies of 21%-23% determined for ^{211}At (excluding the outlying recovery efficiency listed for run 4, where a measurement error was assumed to have occured for the aqueous sample).

Recovery of ^{209}At

Following each implantation with ^{213}Fr and ^{213}Ra, the NaCl target was rapidly dissolved in a minimal amount 0.1 N NaOH, between 1-3 hours after EOB. γ-spectroscopy of the resulting solutions confirmed that the activity was composed predominantly of ^{209}At. The ^{209}At in these samples was easily detected by its prominent γ-rays, with the most intense being at 545 keV (91%),782 keV (83.3%), 790 keV (63.5%), 195 keV (23.5%), 239 keV (12.5%). Figure 6.4 shows the resulting spectrum measured for the ^{209}At sample recovered from Run# 9. All other samples of recovered ^{209}At produced nearly identical spectra. These results demonstrated that mass separation of the RIB had resulted in high isotopic purity of the astatine, preventing contamination with other astatine isotopes such as ^{210}At.

The measured yields for ^{209}At were compared to predicted yields (from Equation 4.13) to determine recovery efficiency for each production run. This analysis is summarized in Table 6.3. For these five runs, the mean recovery efficiency for ^{209}At was $25\% \pm 2\%$ (mean + std). No significant difference was found between the various CARRIER configurations (insulating versus conducting, or collimators versus no collimators).

.

Further discussion of recovery efficiencies

The close agreement between ^{211}Rn, ^{207}At, and ^{209}At recovery efficiencies indicated that, for these implantation energies, radon was trapped as efficiently as astatine in the NaCl target. The most important conclusion that can be drawn from this observation is that the radon was transferred from the solid NaCl target to the dodecane with nearly 100% efficiency. Furthermore, the recovery efficiency of ^{209}At was also in agreement with that of ^{207}At and ^{211}Rn. Together, runs 1 through 9 represent a wide range of implantation

conditions. It can be concluded that the overall efficiency of production/recovery of roughly 25% is not a strong function of implantation rate, α-decay rate, dose, dose rate, duration of implantation, time of measurement after EOB, composition of RIB, etc.

The low recovery efficiency could possibly be attributable to two independent factors: (i) inaccurate estimation of RIB production rates (ion/s) at IIS, or (ii) some intrinsic property of the NaCl target. Regarding the former (i), the RIB rate was never actually measured at IIS directly and loss of RIB intensity between the IYS and IIS could not be ruled out. Still, even large uncertainties of 15% could not account for the observed recovery efficiencies. For the latter (ii), one possible explanation is that space-charge build-up on the surface of NaCl could have partially deflected incoming ions, although space-charge was expected to be a function of the rate of implanted and recoiled charge, which both varied greatly over the nine production runs of this analysis. Ultimately, the analysis could not explain the low recovery efficiency observed by this experiment.

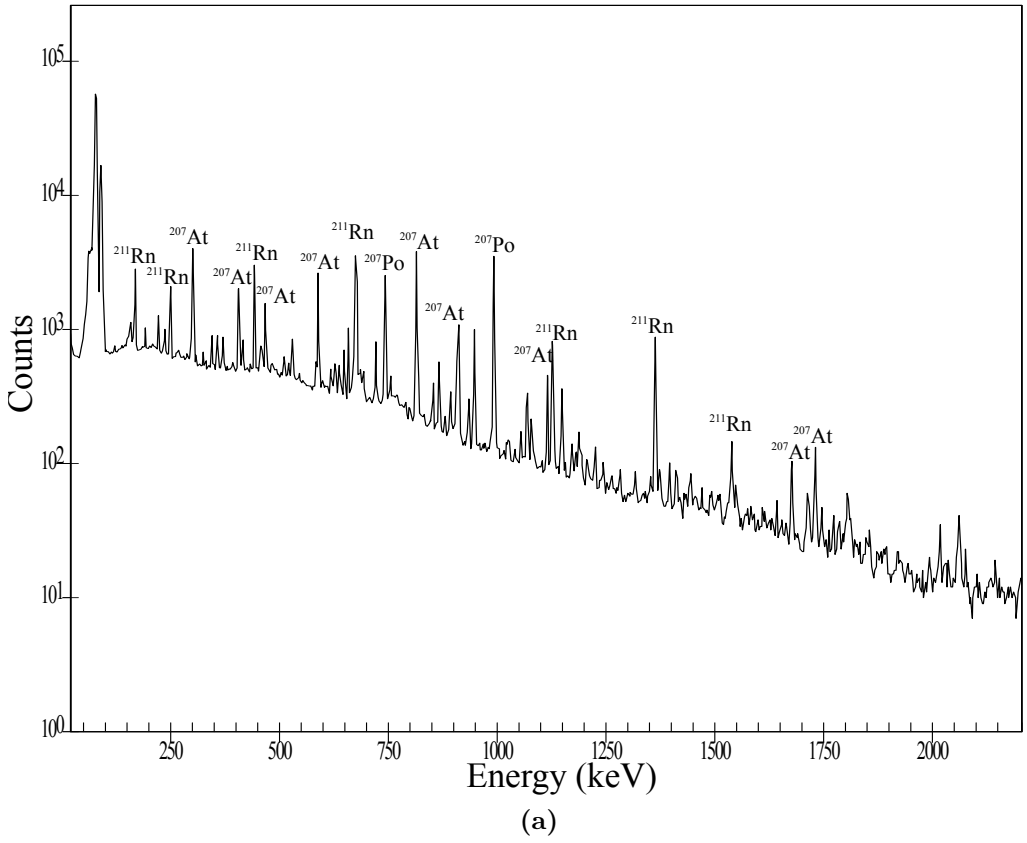

(a)

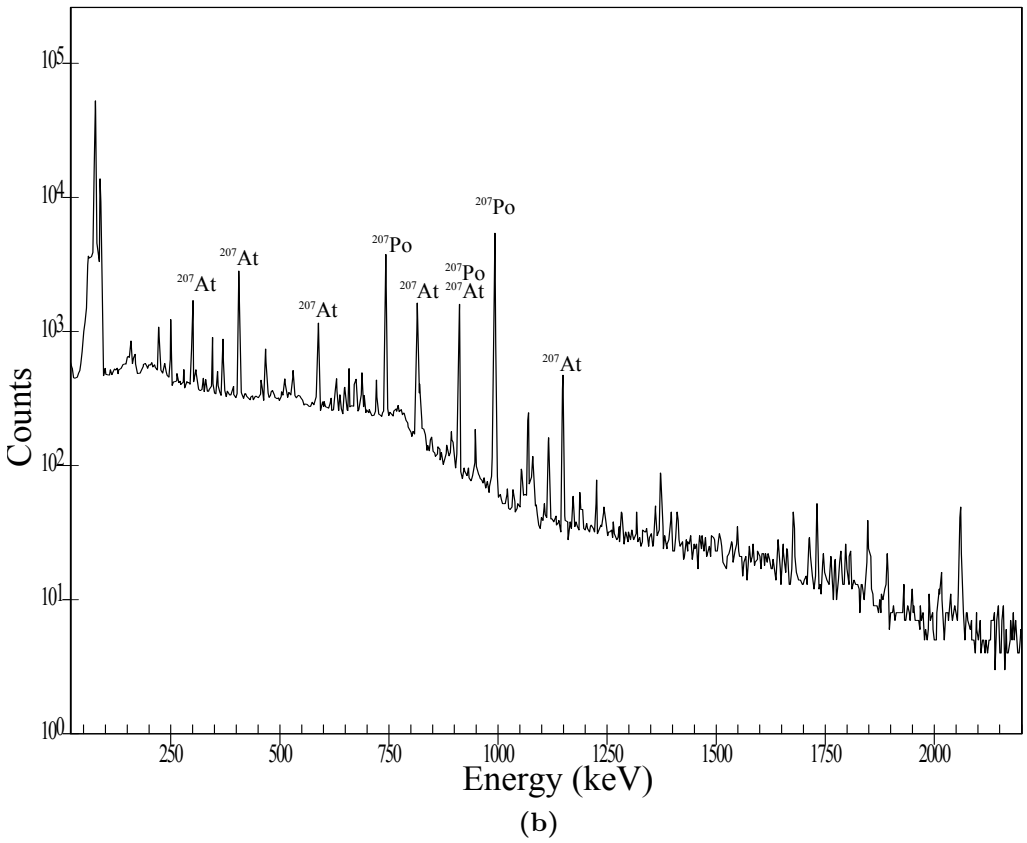

(b)

Figure 6.3: HPGe γ-spectra of solutions assayed after dissolving from NaCl targets following implantated with ^{211}Fr (Run 1) with dodecane and aqueous solution (0.01 N NaOH): **(a)** dodecane and **(b)** 0.01 N NaOH aqueous solution.

Table 6.2: Yields of ^{211}Rn recovered from ISAC, for runs $\#1-4$ (RIB A = 211). Assay time refers to the time between EOB and HPGe detector (γ-spectroscopy) measurement. For Run #2, ^{207}At recovery could not be determined because this isotope had decayed away by the assay time. For Run #4, the amount of ^{207}At was significantly less. This was presumed to be an outlier in the data, possibly the result of an error in estimating the amount of solution transferred to the 20 mL vial used for γ-spectroscopy.

		^{211}Rn			^{207}At		
Run#	Assay time (h)	Predicted Bq±15%	Measured Bq±7%	Recovery eff. ($\pm\sim5\%$)	Predicted Bq±15%	Measured Bq±7%	Recovery eff. ($\pm\sim5\%$)
1	9.2	1.69×10^5	4.64×10^4	27%	5.65×10^5	1.33×10^5	23%
2	31.3	7.15×10^5	1.89×10^5	26%	1.29×10^3	–	–
3	2.9	5.59×10^5	1.38×10^5	25%	6.67×10^6	1.39×10^6	21%
4	6.9	1.15×10^6	2.77×10^5	24%	4.19×10^6	2.86×10^5	7%*

Further details:

Run#	Isotope (solvent)	Activity measured (γ-spec) in assay sample (Bq ±5%)†	Fraction of total in aliquot (±5%)
1	^{211}Rn (dodecane)	1.16×10^3	1/40
	^{211}Rn (0.01 N NaOH)	(none detected)	1/40
	^{207}At (dodecane)	2.21×10^3	1/40
	^{207}At (0.01 N NaOH)	1.12×10^3	1/40
2	^{211}Rn (dodecane)	7.57×10^3	1/25
3	^{211}Rn (dodecane)	5.51×10^3	1/25
	^{211}Rn (0.01 N NaOH)	(none detected)	1/50
	^{207}At (dodecane)	1.67×10^4	1/25
	^{207}At (0.01 N NaOH)	1.95×10^4	1/50
4	^{211}Rn (dodecane)	3.77×10^3	1/80
	^{211}Rn (1 N NaOH)	(none detected)	1/40
	^{207}At (dodecane)	3.39×10^3	1/80
	^{207}At (1 N NaOH)	3.68×10^2	1/40

∗: Declared as outlier, after comparison to ^{209}At yields (Table 6.3).
†: Reported activities for samples of dodecane were overestimated; calibration standard of active solution was water.

Theoretical (predicted) activities (using Equation 4.13):

^{211}Rn (d) from ^{211}Fr (p): $r_p = \epsilon_{IIS/IYS}\times(r_{211Fr}+0.07\times r_{211Ra}),\quad \epsilon_{geo}=1$

^{207}At (d) from ^{211}Fr (p): $r_p = \epsilon_{IIS/IYS}\times(r_{211Fr}+0.07\times r_{211Ra}),\quad \epsilon_{geo}=\epsilon_{\alpha,geo}=0.65$
^{207}At (d) from ^{207}Rn (p): $r_p = \epsilon_{IIS/IYS}\times(0.93\times r_{211Ra}),\quad \epsilon_{geo}=\epsilon_{\alpha,geo}=0.65$

Total ^{207}At = (^{207}At from ^{211}Fr) + (^{207}At from ^{207}Rn)

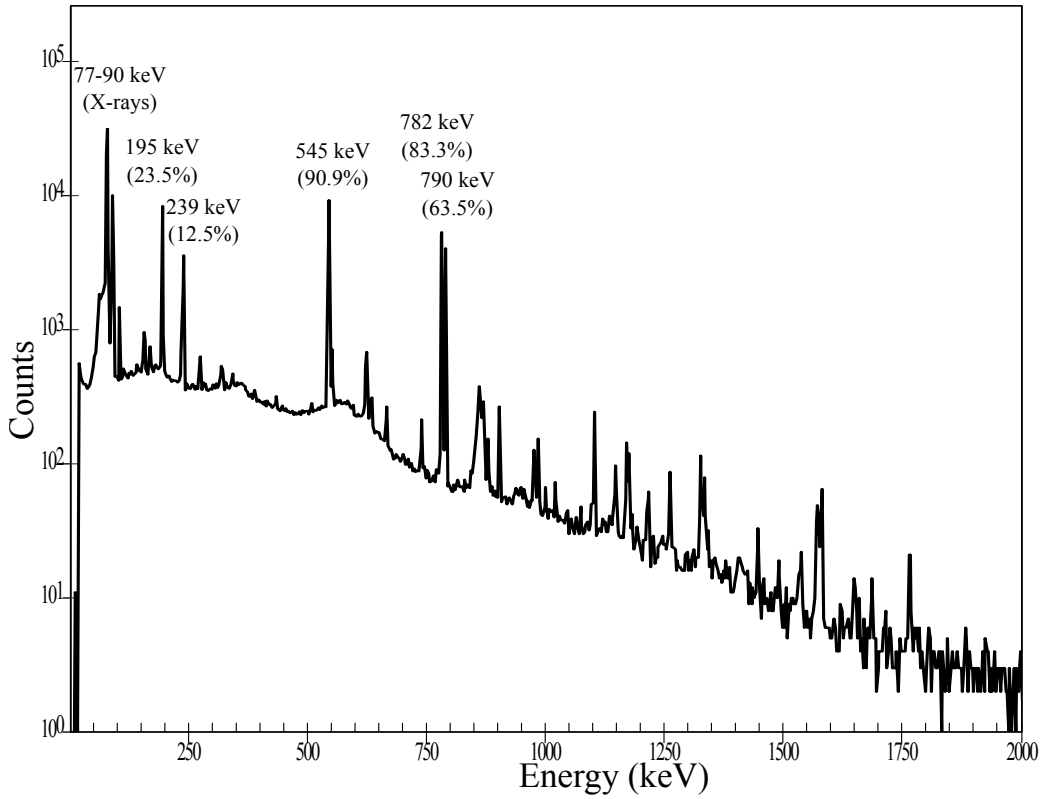

Figure 6.4: HPGe detected energy spectrum (γ-spectroscopy) of a ^{209}At sample prepared from a NaCl target dissolved in aqueous solution, following co-implantation of ^{213}Fr and ^{213}Ra (Run #9). Measured within 1 hour of ^{209}At target processing (recovery into solution). The broad peak centred at approximately 860 keV was identified as low activity of ^{205}Po, which had a short half-life (1.6 hours) and did not represent a significant contaminant. All other small peaks could be attributed to lower intensity ^{209}At emissions.

Table 6.3: Yields of ^{209}At recovered from ISAC, for runs #5 – 9 (RIB A = 213). Measured activities were decay-corrected to the time at which RIB implantation ended (t_{EOB}).

Run#	Target type	^{209}At		
		Predicted (at t_{EOB}) (Bq±15%)	Measured (Bq±7%)	Recovery eff. (± ∼ 5%)
5	(NaCl/Mylar)	4.96×10^8	1.27×10^8	26%
6	(NaCl/Mylar)	3.15×10^8	8.32×10^7	25%
7	(NaCl/Ag)	8.54×10^8	2.13×10^8	25%
8	(NaCl/Ag)	6.10×10^8	1.32×10^8	22%
9	(NaCl/SS)	4.81×10^8	1.32×10^8	27%

Further details:
Theoretical (predicted) activities (using Equation 4.13):

^{209}At (d) from ^{213}Fr (p): $r_p = \epsilon_{IIS/IYS} \times (r_{213Fr} + 0.2 \times r_{213Ra})$, $\epsilon_{geo} = \epsilon_{\alpha,geo} = 0.65$
^{209}At (d) from ^{209}Rn (p): $r_p = \epsilon_{IIS/IYS} \times (0.8 \times r_{213Ra})$, $\epsilon_{geo} = \epsilon_{\alpha,geo} = 0.65$
Total ^{209}At = (^{209}At from ^{213}Fr) + (^{209}At from ^{209}Rn)

^{211}At isolation

^{211}At separation from ^{211}Rn (extraction from dodecane)

^{211}Rn/^{211}At generators were constructed using the ^{211}Rn recovered from Runs 2-4. The ^{211}Rn (contained in dodecane, inside of the 30 mL syringe) was left for approximately 24-32 hours, during which time the ^{207}At decayed to negligible levels and ^{207}Po substantially increased. These changes can be identified in the γ-spectrum for the dodecane after 24 hours, shown in Figure 6.5a (sampled immediately before extraction of ^{211}At). Regarding Runs 2 and 3, ^{211}At was extracted with 2 mL of 0.01 N NaOH after mixing for 5 minutes with the dodecane in the generator. It was found that ^{211}At was partially extracted from the dodecane with this aqueous solution, albeit rather inefficiently; using this method, only about 10% of the ^{211}At was extracted. In addition, a significant proportion of the ^{207}Po tracked with the ^{211}At into the aqueous solution. The aqueous extract from the generator for Run 2 is shown in Figure 6.5b.

The NaOH concentration and volume of extracting solution were increased in an attempt to increase the extraction efficiency of ^{211}At from the dodecane. An increase of NaOH concentration to 1 N was shown to begin dissolving the aluminum target backing that was also inside of the syringe (as expected), creating bubbles and prohibiting extraction. To overcome this, Run 4 was performed using a stainless steel backing for the NaCl target that would not react in higher concentrations of NaOH. For run 4, 5 mL of 2 N NaOH were used for the extraction which improved extraction efficiency to approximately 90% $\pm$ 22%.

^{211}At purification (^{207}Po elimination) with tellurium column

The aqueous extractions from the ^{211}Rn/^{211}At generator contained a mixture of ^{211}At and ^{207}Po. The polonium was eliminated from the extracted solutions with small volume tellurium (Te) packed columns, using the methods described in §4.4.2. Two 8 mm diameter column lengths were used: 10 mm and 2 mm). After loading the column with the mixture of ^{211}At and ^{207}Po, ^{211}At was eluted with 2 N NaOH, collected in up to 8 200 μL fractions. The elution of ^{211}At was up to 74% efficient for the 10 mm Te column (63% for the 2 mm Te column), summing the first 600 μL eluted. As shown in Figure 6.6, nearly all of the ^{211}At was eluted in the first 3 fractions (or 600 μL). This concentration of the ^{211}At was considered advantageous for downstream chemistry applications, such as antibody labelling, which required reactions to be completed at high concentrations.

The Te column was shown to be highly effective at eliminating the ^{207}Po contamination. Table 6.4 lists the ^{207}Po activities in elution fractions collected from Te columns (10 mm or 2 mm long, 8 mm diameter). The best result of ^{207}Po elimination was accomplished with the 10 mm column, which was found to remove over 99.98% of the polonium. This result was consistent with those published in the literature [118].

The HPGe energy (γ) spectrum for the Te column elution (after purification) is shown in Figure 6.7. The most striking feature of this spectrum was how much it is dominated by the X-ray energy range (< 100 keV), compared to the very minor contribution from ^{207}Po, expected for high purity samples ^{211}At. Another point of interest is identification of small amounts of ^{207}At. Although these levels of ^{207}At was not very significant to this overall process, its appearance in the energy spectrum is an artifact of the production of ^{211}At via ^{211}Fr decay (also producing ^{207}At, along with ^{211}Ra). Even after 30+ hours, ^{207}At was still detectable. In turn, ^{207}At would have been eluted from the Te column with ^{211}At and provided a source for small amounts of ^{207}Po after ^{211}At purification. This offers one explanation for the differences in efficiency observed between column types. the difference in efficiency for these columns may not have been determined by there design, but instead by different amounts of ^{207}At in the sample at the time of purification (performed with two different generators). This was not evaluated further and is simply left as a topic for further evaluation in the future.

Table 6.4: ^{211}At recovery and ^{207}Po elimination with tellurium columns.

	10mm, 8mm diam.		2mm column, 8mm diam.	
	(Bq ± 7%)	(%)	(Bq ± 7%)	(%)
^{207}Po Loaded on Te column:	4.52×10^5		1.65×10^4	
2 N NaOH elutions (200μL):				
Fraction 1	6.5×10^1	0.01%	8.2×10^1	0.5%
Fraction 2	2.1×10^1	0.005%	2.1×10^2	1.2%
Fraction 3	1.3×10^0	<0.001%	1.5×10^1	1.2%
Fraction 4	1.3×10^0	<0.001%		
Fraction 5	1.1×10^1	0.002 %		
Fraction 6	1.5×10^1	0.003 %		
Fraction 7	2.6×10^1	0.006 %		
Fraction 8	1.6×10^1	0.004 %		
	^{207}Po removed >99.98%		**^{207}Po removed = 98%**	
	^{211}At (first 600 μL) =74%		**^{211}At (first 600 μL) =63%**	

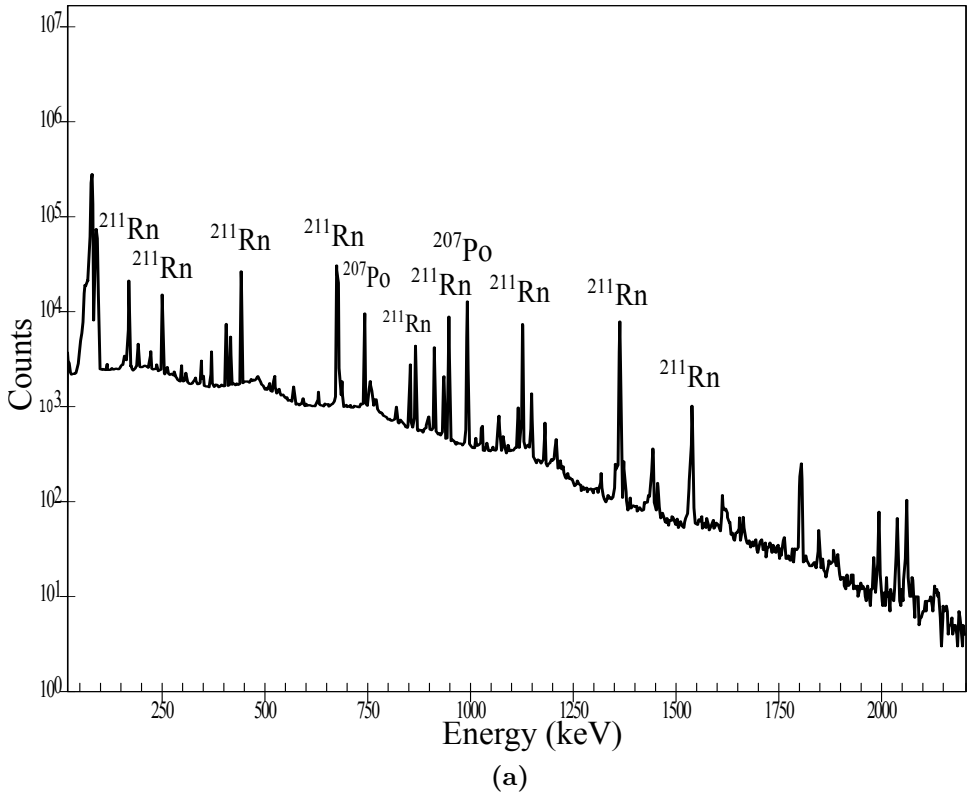

Figure 6.5: HPGe γ-spectra for **(a)** the ^{211}Rn/^{211}At generator system in transient equilibrium (in dodecane), and **(b)** the aqueous solution after ^{211}At extraction with 0.01 N NaOH.

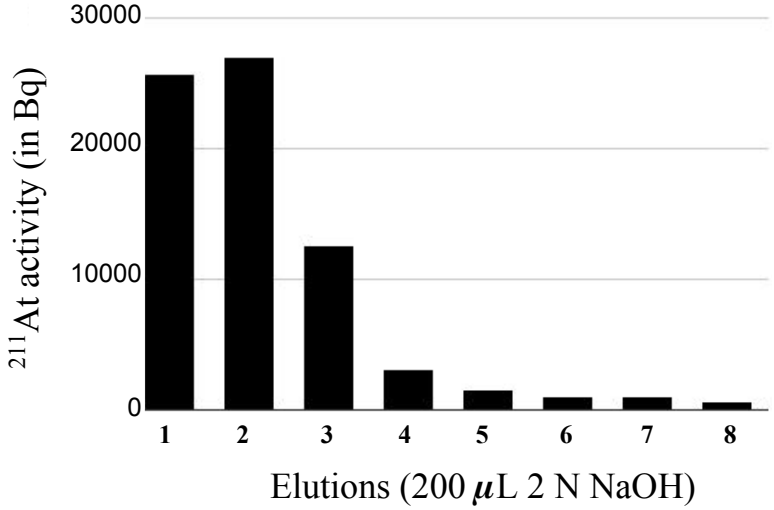

Figure 6.6: ^{211}At activity in 8 consecutive elution fractions from a Te column loaded with a mixture of ^{211}At and ^{207}Po. Uncertainty was estimated at 7%.

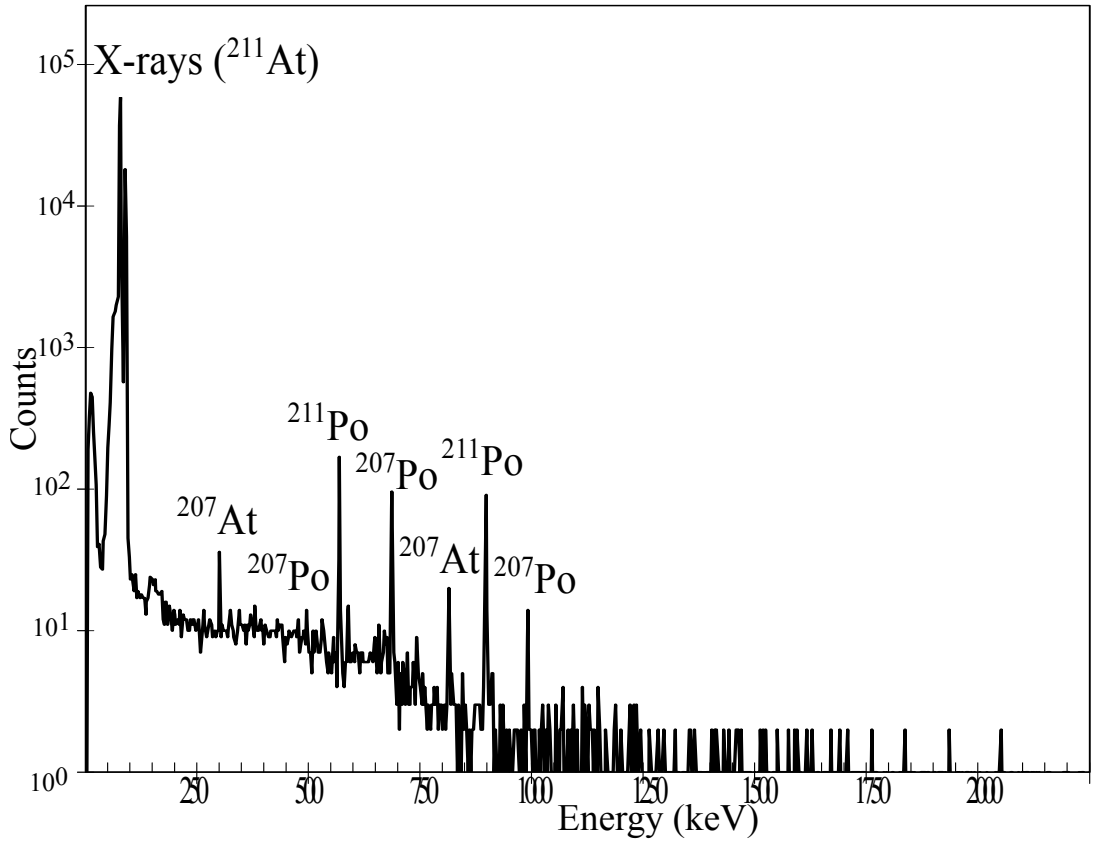

Figure 6.7: HPGe gamma spectra demonstrating elimination of ^{207}Po from a mixed ^{211}At/^{207}Po solution using a tellurium column (8 mm x 10 mm granular Te column). The initial concentration of ^{211}At was roughly 50% of the initial ^{207}Po concentration (in terms of activity).

Antibody labelling results

The antibody labelling experiments were carried out primarily as demonstrations of applicability of the ^{211}At and ^{209}At produced by these methods to the preparation of clinically relevant radioimmunoconjugates, using standard methods. Results for the preparation of ^{211}At-B10-BC8 and ^{209}At-B10-BC8 are described below.

^{211}At-B10-BC8

The preparation of ^{211}At-B10-BC8 was performed using ^{211}At samples recovered from the ^{211}Rn generator, in accordance to the methods described in §4.5. Table 6.5 summarizes the labelling reactions, with comparison between Te column purified ^{211}At versus an unpurified sample used directly after extraction from the ^{211}Rn (thus having a much higher level of ^{207}Po contamination). Using either condition, decay corrected labelling efficiency was 74-75% (calculated as the fraction of ^{211}At activity (Bq) eluted from the PD-10 column (fractions 4-6) and the total amount of ^{211}At used for the reaction). Importantly, for both reaction conditions, roughly half of the initial ^{207}Po activity tracked with the astatinated antibody, thereby contaminating the collected product. Since the initial amount of ^{207}Po was very low in the reaction preceded by Te column purification, the final sample of ^{211}At-B10-BC8 was extremely pure in this case. This product purity was most apparent in the measured energy spectrum of the labelled product, shown in Figure 6.8a. In contrast, the extent of ^{207}Po contaminating the ^{211}At-B10-BC8 PD-10 column elutions were considered catastrophic to the labelling process. The extent of ^{207}Po was easily identified and quantified by the detected energy spectrum, shown in Figure 6.8b.

Table 6.5: Analysis of antibody labelling reactions with ^{211}At, with comparison to the labelling reaction with high-levels of ^{207}Po contamination. Activities reported for collected fractions are reported in terms of decay corrected percentage of the initial activity loaded onto the PD-10 column.

	Activity with Te column		Activity without Te column	
	^{211}At	^{207}Po	^{211}At	^{207}Po
Added to labelling reaction (in Bq):	1.5×10^3	2.1×10^1	9.0×10^4	3.3×10^4
PD-10 column elutions (1.0 mL):				
Combined fractions 1-3	0%	4%	2%	2%
Combined fractions 4-6	75%	31%	74%	56%
Combined fractions 7-9	0%	0%	1%	3%

The previously described iTLC procedure provided a method to test if the isotopes were bound to the antibody. The amount of activity at the time of counting the iTLC

papers were very low, allowing only for qualitative assessment. iTLC confirmed that the ^{211}At was bound to the antibody. The basis of this conclusion was that ^{211}At did not move with the solvent on the iTLC paper, where as free ^{211}At did. Furthermore, iTLC demonstrated that the majority of the ^{207}Po was also bound to the antibody (most ^{207}Po did not move with the solvent, but all ionic ^{207}Po did move with the solvent). The binding of Po to an antibody had not been reported for this way labelling reaction and demonstrated the importance of properly isolating the ^{211}At from contaminating Po isotopes before proceeding with labelling.

^{209}At-B10-BC8

Before beginning the reaction experiments, the the ^{18}F setting of the dose calibrator was cross-calibrated with the HPGe detector γ-spec measurements. The calibration factor (CF), defined by Equation 4.14, was calculated to be 0.30 $\pm$ 0.01 in units of (MBq ^{209}At)/(MBq ^{209}At on ^{18}F-setting), based on independent measurements (i.e. 3 separate samples were collected and measured with each instrument separately). The high purity of ^{209}At samples recovered from ISAC contributed to the low variability in this calibration factor. Recovered ^{209}At was used for the astatination of B10-BC8, according to the methods described in §4.5. The labelling was performed three times and the results are provided in Table 6.6. The mean labelling efficiency for the preparation of ^{209}At-B10-BC8 was 86% $\pm$ 7% (decay corrected to the reaction start-time). ^{209}At was confirmed to be bound to the antibody by iTLC as in the case of ^{211}At labelling studies above. As a result of this positive outcome, ^{209}At-B10-BC8 was considered suitable for evaluation by SPECT imaging *in vivo*, and used accordingly as described in §5.4.

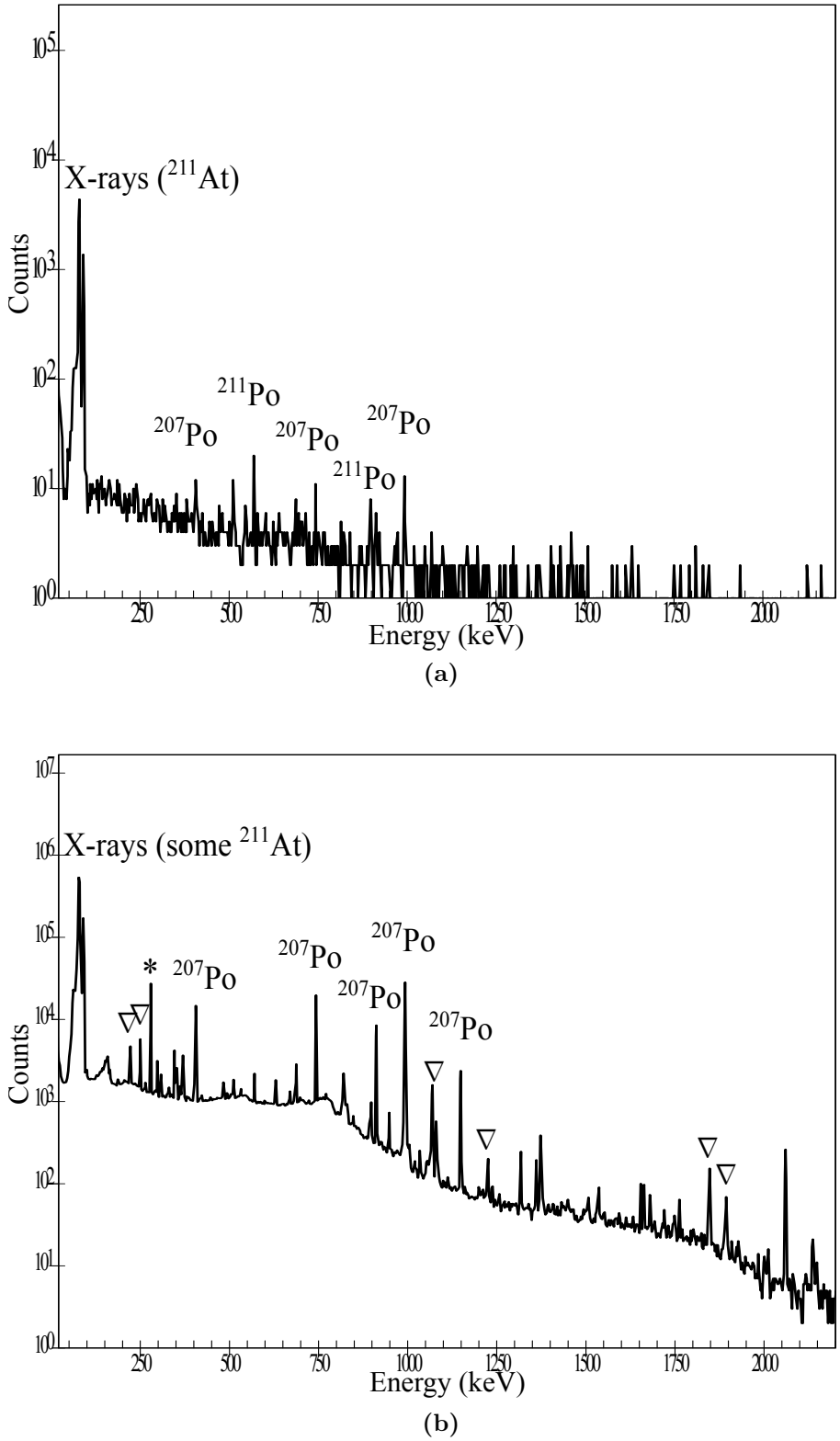

Figure 6.8: HPGe gamma spectra of B10-BC8 labelled with ^{211}At: **(a)** using ^{207}Po elimination with a tellurium column prior to the labelling reaction, and **(b)** without the use of a tellurium column (no ^{207}Po elimination prior to labelling). Peaks identified with the ∇ symbol were possibly produced by small quantities of ^{203}Bi or ^{203}Po.

Table 6.6: Analysis of antibody labelling reactions with ^{209}At. All reported activities were decay corrected to the start time of the labelling reaction. Uncertainty in absolute activity was estimated to be 7%.

	^{209}At (MBq)	^{209}At (MBq)	^{209}At (MBq)
Added to labelling reaction	33.19	27.51	4.41
PD-10 column elutions (0.5 mL):			
Fractions 0 through 5	0.00	0.00	0.00
Fraction 6	0.57	0.93	0.19
Fraction 7	14.22	13.21	1.38
Fraction 8	9.70	6.88	0.63
Fraction 9	0.88	1.05	0.20
Remaining in vial	3.44	4.08	1.42
Remaining on column	2.81	1.87	0.49
Labelling efficiency (ϵ_L)	85%	94 %	80 %
$\epsilon_L = \frac{\sum(\text{fractions})}{(^{209}\text{At added} - {}^{209}\text{At in vial})}$			
Mean labelling efficiency (^{209}At-B10-BC8) = 86% ± 7%			

Further observations

Determination of ^{211}Fr branching ratios (this work)

Branching ratios for ^{211}Fr could be calculated based on the production rate measurements at IYS.

As stated in §4.1.1, branching ratios ^{211}Fr were recorded in the literature in terms of bounded intervals ($b_\alpha > 0.8$, $b_{ec} < 0.2$). By assuming that $b_\alpha = 1 - b_{ec}$, the IYS measurements of Fr-211 intensity (r_α from α-spec, r_γ from γ-spec were used to calculate the branching ratio for which r_α and r_γ were equal. in this way, IYS yield measurements were shown to be consistent with the ^{211}Fr α-decay branching ratio b_α equal to 0.89 ± 0.06 ($\overline{b_\alpha} \pm \overline{\sigma}$, see Table 6.7).

Table 6.7: Calculated branching ratios for ^{211}Fr electron capture and α-decay.

Run #	Calculated b_{ec} $1/(1+r_\alpha/r_{ec})$	Calculated b_α $(1-b_{ec})$	σ_i
1	0.07	0.93	12%
2	0.14	0.86	12%
3	0.11	0.89	16%
4	0.09	0.91	14%

$$\overline{b_\alpha} \pm \overline{\sigma} = 0.89 \pm 0.06$$

$$\overline{b_\alpha} = \frac{\sum_i \frac{b_{\alpha,i}}{\sigma_i^2}}{\sum_i \frac{1}{\sigma_i^2}}, \qquad \overline{\sigma}^2 = \frac{1}{\sum_i \frac{1}{\sigma_i^2}}$$

Air sample Lucas cell measurements

In addition to real-time readout of total α-particle activity, the Lucas cell data provided a means of quantifying the composition of the activity, with respect to particular α-decaying isotopes. The radionuclidic composition and absolute activity was of interest because of the differences in volatility between radon and astatine. For the co-implantation of ^{211}Fr and ^{211}Ra, significant α-emissions were attributable to ^{211}Rn, ^{211}At, ^{207}Rn, and ^{207}At.

The total alpha activity (measured directly by the Lucas cell) was the sum of Rn and At activity multiplied by there respective α-decay branching ratios. With initial activities at the time of starting measurement, the Rn activity decreased exponentially with time according to its half-life, while At activity depended on exponential decay and production by the decay of the Rn parent. Lucas cell count rate as a function of time for air samples collected at roughly the time of opening the CARRIER are shown in Figure 6.9 The volume of the Lucas cell (V) was 0.151 L and its detection efficiency (ϵ_{lc}) was previously determined to be (0.749). Using this information, a least squares

method fit was performed for Lucas cell count rate as a function of time, with a multi-term exponential function to describe the decaying source of α-emitters, described in the following derivation: the total rate of α-decay (measured) for the air sample was described by Equation 6.1,

$$\text{Total rate of } \alpha\text{-decay} = \frac{\text{Lucus cell count rate (211)}}{\epsilon_{lc}},$$

$$= \alpha\text{-decay rate from initial } ^{211}\text{At} + \alpha\text{-decay rate from intial } ^{211}\text{Rn and } ^{211}\text{At daughters}$$
$$+ \alpha\text{-decay rate from initial } ^{207}\text{At} + \alpha\text{-decay rate from intial } ^{207}\text{Rn and } ^{207}\text{At daughters} \quad (6.1)$$

By defining the initial airborne activities per litre of circulating air of each isotope as A_1 (^{211}At), A_2 (^{211}Rn), A_3 (^{207}At), and A_4 (^{207}Rn), Equation 6.1 was rewritten as,

$$\text{Lucus cell count rate (211)} = \Big(A_1 \times F_1 + A_2 \times F_2 + A_3 \times F_3 + A_4 \times F_4\Big) \times \frac{V}{\epsilon_{lc}}, \quad (6.2)$$

where F_1, F_2, F_3,and F_4 were given by,

$$F_1 = e^{-\lambda_{211At}t} b^{\alpha}_{211At},$$

$$\mathrm{F}_2 = e^{-\lambda_{211Rn}t} b^{\alpha}_{Rn211} + \frac{\lambda_{211At}}{\lambda_{211At} - \lambda_{211Rn}}(e^{-\lambda_{211Rn}t} - e^{-\lambda_{211At}t}) b^{\alpha}_{211At}(1 - b^{\alpha}_{211Rn}),$$

$$\mathrm{F}_3 = e^{-\lambda_{207At}t} b^{\alpha}_{207At},$$

$$\mathrm{F}_4 = e^{-\lambda_{207Rn}t} b^{\alpha}_{207Rn} + \frac{\lambda_{207At}}{\lambda_{207At} - \lambda_{207Rn}}(e^{-\lambda_{207Rn}t} - e^{-\lambda_{207At}t}) b^{\alpha}_{207At}(1 - b^{\alpha}_{207Rn}), \quad (6.3)$$

where t was time, and the α-decay branching ratios for these isotopes (indicated by subscript) were b^{α}_{211At} (1, including ^{211}Po decay), b^{α}_{211Rn} (0.27), b^{α}_{207At} (0.086), and b^{α}_{207Rn} (0.21). The second terms in F_2 and F_4 accounted for the grow-in of the astatine daughters produced by radon isotopes, described by Equation 3.2 (see §3.2). The fitted parameters were thus A_1 and A_2, A_3, and A_4 (the unknown initial airborne activities per litre of circulating air of ^{207}At, ^{207}Rn, ^{207}At, and ^{207}Rn, respectively). In this way, Equation 6.2 accounted for the independent α-decay of initial astatine and radon inventory, as well as the additional astatine from radon electron capture decay by these isotopes (^{207}Rn and ^{211}Rn).

The same fitting procedure was done for Lucas cell measurements (213) in regards to the co-implantation of ^{213}Fr and ^{213}Ra (see Figure 6.10. In this case, only two fit parameters needed to be defined because there were only two significant sources of α-decaying airborne activity (^{209}At and ^{209}Rn).

$$\text{Lucus cell count rate (213)} = \Big(A_1 \times F_1 + A_2 \times F_2\Big) \times \frac{V}{\epsilon_{lc}} \tag{6.4}$$

where F_1 and F_2 were given by,

$$F_1 = e^{-\lambda_{209At} t} b^{\alpha}_{209At},$$

$$\mathrm{F}_2 = e^{-\lambda_{209Rn} t} b^{\alpha}_{209Rn} + \frac{\lambda_{At}}{\lambda_{209At} - \lambda_{209Rn}} (e^{-\lambda_{209Rn} t} - e^{-\lambda_{209At} t}) b^{\alpha}_{209At} (1 - b^{\alpha}_{209Rn}), \tag{6.5}$$

where A_1 and A_2 were the initial airborne activities per litre of circulating air of ^{209}At and ^{209}Rn, respectively, and b^{α}_{At} (0.041) and b^{α}_{Rn} (0.17) were the respective α-decay branching ratios of ^{209}At and ^{209}Rn. The measured Lucas cell count rates for CARRIER air samples were fit with Equations 6.2 and 6.4 for implantations of A = 211 (Figure 6.9) and A = 213 (Figure 6.10), respectively. The initial airborne activities of radon and astatine isotopes were defined by the parameters of fit functions provided the initial activities of radon and astatine isotopes, at the time of air sampling.

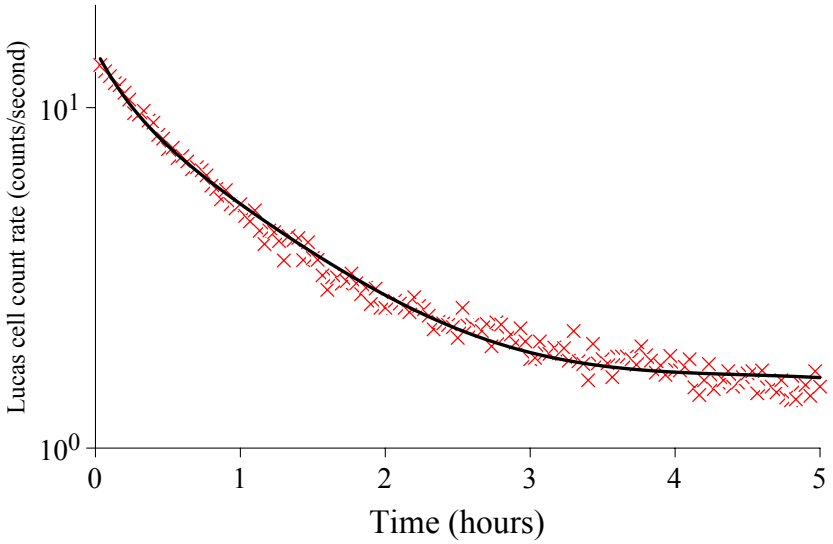

Figure 6.9: Lucas cell counts (α) from air sample following the co-implantation of ^{211}Fr and ^{211}Ra (Run 4) ("×" = Lucas cell raw data points, "–"= fit function (Equation 6.2).

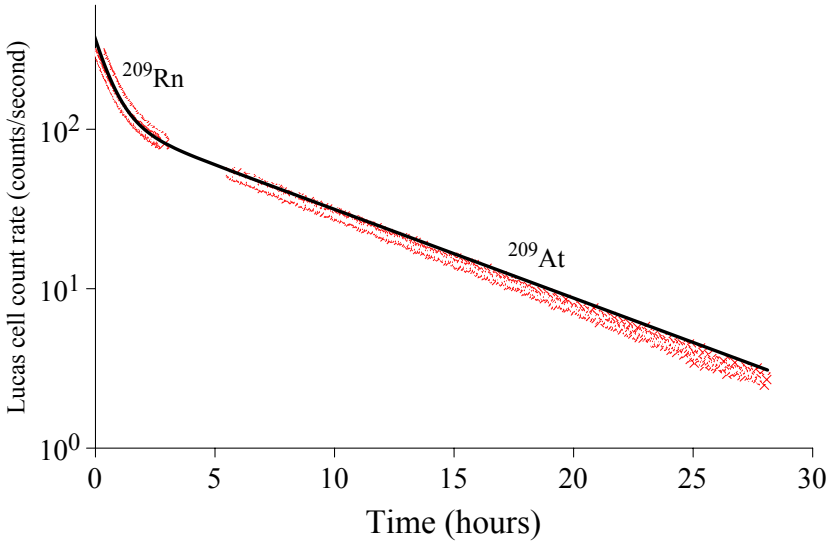

Figure 6.10: Lucas cell counts (α) from air sample following the co-implantation of ^{213}Fr and ^{213}Ra (Run 5). Data collection was interrupted for over 2 hours during the counting period and produced the gap in raw data. ("×" = Lucas cell raw data points, "−"= fit function (Equation 6.4).

By this fitting procedure, initial activities of each isotope in the air samples were determined as the parameters of the fitted functions for Lucas cell count rate, and are listed in Table 6.8. Based on these values, the amount of airborne α-emitting activity was considerably lower than the implanted inventory. This demonstrated that almost all of collected activity was firmly implanted and not significantly volatile. For example, the initial activity of ^{209}At (A_1) was 2.332×10^4 Bq/L ($\pm$80 Bq/L), and the initial activity of ^{209}Rn (A_2) was 1.342×10^4 ($\pm$60 Bq/L)[3]. The internal volume of the CARRIER was estimated to be approximately 1 L, meaning that it only contained roughly 36 kBq of airborne α-emitters at the time it was opened (^{209}At and ^{209}Rn activity, combined). Combining the volumes of Lucas cell of the CARRIER (1 L), the Lucas cell (0.151 L), the merrinelli can (1 L) and other connecting hoses ($\sim$0.2 L), and accounting for the activity measured on the charcoal filter, we can determine that the total airborne activity originating from the CARRIER $\sim$100 kBq, or only 0.1% of the recovered activity.

Discussion

As seen in Table 6.1, the production rates of ^{211}Fr varied by over two orders of magnitude between production runs of this experiment. The loss reported for Run 3 was likely the result of a break in the tungsten mounts used for resistive heating, (see Figure 3.4a). As a result, diffusion of isotopes from the uranium carbide target was much slower. The loss reported in Run 4 was attributable to a malfunctioning of the extraction electrode on the ion source. Longer implantation times were used to make up for the loss of RIB intensity,

[3]Bounds in brackets define the 95% confidence bounds, determined by the fit (R-square value = 0.9992).

Table 6.8: Activities of airborne α-emitters determined by air sample measurements.

Airborne activity from fit (for Run 4, A=211)		Airborne activity from fit (for Run 5, A=213)	
Isotope	Bq/L	Isotope	Bq/L
^{211}At (A_1)	$2.90 \times 10^2 \pm 13\%$	^{209}At (A_1)	$2.332 \times 10^4 \pm 0.4\%$
^{211}Rn (A_2)	$1.34 \times 10^3 \pm 11\%$	^{209}Rn (A_2)	$1.342 \times 10^4 \pm 0.5\%$
^{207}At (A_3)	$2.50 \times 10^3 \pm 10\%$		
^{207}Rn (A_4)	$1.11 \times 10^2 \pm 10\%$		

and recovered yields of ^{211}Rn/^{211}At were still sufficient for conducting the planned experiments. However, these inconsistencies in beam delivery would be severely damaging to experiments that require maximum attainable yields, such as preclinical studies with small animals. The production of RIB with actinide targets at TRIUMF is still in active development and must be considered a cutting-edge technology for which inconsistencies should be expected. As further developments are made in this area, improvements in consistency and quality should be achievable.

Radon-211 was successfully recovered from ^{211}Fr ion beams produced at ISAC. ^{211}Rn was transferred from solid NaCl to liquid hydrocarbon (dodecane) with high efficiency ($\sim$100% recovery compared to ^{207}At). The presented methods for the separation of ^{211}At from ^{211}Rn and ^{207}Po provided suitable samples for chemistry applications of ^{211}At (including mAb labelling), without significant contamination by other astatine isotopes.

Several important conclusions can be drawn from the reported extraction and purification of ^{211}At. First, the 90% efficiency for extracting ^{211}At from dodecane implies that two consecutive extractions could be made to recover 99% of the ^{211}At. The second observation is that the total volume of aqueous solution used for ^{211}At extraction (from dodecane) could be made larger without increasing the volume of Te column purified ^{211}At. In this case, the loading volume for the column would increase, but the ^{211}At would still be eluted in 600 μL. Since radon was not detected in any of the aqueous solution extraction, this also implies that the dodecane (containing ^{211}Rn) could be washed repeatedly immediately after the NaCl target is dissolved to remove nearly all of the contamination. Most importantly, this ^{211}Rn isolation procedure would remove ^{207}At completely and permit extraction of ^{211}At at an earlier time point ($\sim$16 hours, instead of $\sim$30 hours). Future experiments are planned for testing this procedure.

A major distinction of the generator, compared to conventionally produced ^{211}At (by ^{209}Bi(α,2n) reactions), in general, is the co-production of ^{207}Po. Isolation from Po was demonstrated as a critical step in the preparation of pure astatinated antibodies using these methods. This conclusion is of particular importance to the ^{211}Rn/^{211}At generator system and contributes to forward progression of research in this area. Also, since the time

of the labelling experiment, the ^{211}At isolation step (referring to purification using the Te column) was improved upon. Using the longer column (more Te mass), the ratio of ^{211}At to ^{207}Po was greatly increased, and in turn, is expected to significantly increase the purity of ^{211}At-B10-BC8 produced by these methods. This demonstration in labelling chemistry was the first of its kind to be done with pure samples of ^{209}At, thereby validating and supporting the novel ISOL-based production strategy for ^{209}At developed by this work.

These protocols for ^{211}Rn production were not developed to maximize the net amount of recovered activity. The amounts of ^{211}Rn/^{211}At recovered by these experiments were considered ideal for a preliminary evaluation of the ^{211}Rn/^{211}At generator system based on ISAC RIB collection; however, these yields were 2-3 orders of magnitude lower than what would be required for small scale *in vivo* studies with mice, which would require a minimum of roughly 10 MBq to 100 MBq of ^{211}At. Clinical applications would require at least 50 times more ^{211}At activity. Even if recovery and isolation efficiencies for ^{211}At were 100%, the maximum ^{211}At that could be recovered from a long (24 hour) implantation of ^{211}Rn would be roughly 40 MBq (assuming a maximum RIB implantation rate of 1.5e8 ions/s)[4]. This would be sufficient for small scale mouse studies and labelling research. If the implantation recovery efficiency is assumed to be ∼25% and recovery from Te column purification is 74%, the net maximum ^{211}At would be lower than 6 MBq. This amount of ^{211}At would not be enough for preclinical small animal studies, but still appreciable for ^{211}At chemistry and in vitro studies. In principle, small animal biodistribution studies may still be possible with such low activity, but not the evaluation of in vivo therapeutic efficacy, where the absolute absorbed dose would be the determining factor.

For ^{211}Rn production times of 24 hours or less, the amount of recoverable ^{211}At activity is roughly proportional to the implantation rate at ISAC IIS; increasing the implantation rate by a factor of ten would be highly advantageous for the practical implementation of this ^{211}Rn/^{211}At generator for preclinical studies with small animals. Increasing production rate would require increasing the rate of spallation, necessitating a larger target (uranium) mass and/or higher primary proton current at ISAC. Neither of these options is currently possible due to radiation license restrictions at TRIUMF.

ISAC RIB composed directly of ^{211}Rn were not available during the course of this experiment. In the absence of direct ^{211}Rn beams, ^{211}Fr beams provided a suitable source for ^{211}Rn for small scale evaluations of the ^{211}Rn/^{211}At generator system. Directly produced ^{211}Rn RIB (at 1×10^8 ions/s, FEBIAD ion source) or indirectly via the decay of ^{211}Fr (10% of 1×10^9 ions/s, Re surface ion source) provide equivalent production rates of ^{211}Rn, while the difference between these RIB would be the resulting contamination. For direct production of ^{211}Rn RIB with the FEBIAD ion source, previous yield station

[4]Increasing implantation time would not produce proportionately more ^{211}At because the ^{211}Rn activity gets closer to saturation with increasing implantation time.

measurements at ISAC determined that the only significant contaminant in the RIB was ^{211}At, which would only serve to increase the net yield of ^{211}At that could be extracted from the Rn-211 source. In contrast, the production of ^{211}Rn via ^{211}Fr decay produced several contaminants, including high levels of ^{207}At/^{207}Po. One major limitation of this additional inventory was an increase in dose rate compared to the amount of recovered ^{211}Rn. While longer implantation times could be used to increase the amount of ^{211}Rn produced by these methods, the increase in dose rate from ^{207}At/^{207}Po could become a limiting factor. For these reasons, scaling up these production methods for obtaining higher ^{211}Rn and ^{211}At activity should be pursued with ^{211}Rn RIB directly.

ISAC Yields for ^{211}Rn and ^{211}At are about equal using the FEBIAD ion source. This suggests that if these RIB were co-implanted, the initial ^{211}At activity that built up in the target during implantation could be recovered immediately, while a second yield could be recovered from the grow-in produced by ^{211}Rn 16 hours later. From a practical perspective, the ability to harness ^{211}At on two consecutive days from the same production run would be extremely useful. This is another major advantage for using ^{211}Rn RIB produced with the FEBIAD rather than ^{211}Fr RIB produced with the Re surface ionizing ion source. These factors strongly support the increased availability of actinide targets in combination with FEBIAD ion sources at ISAC, in the future.

At the onset of this experiment, the removal and recovery of radioactive samples from ISAC RIB deliveries was not commonly performed, and only rarely performed at very low levels long-lived activity. This novel approach to the production of astatine isotopes ultimately provided an opportunity to establish a general procedure for collecting other medical isotopes from RIB at ISAC. To date, TRIUMF has already applied these general methods to produce small quantities of other therapeutic α-emitters, namely ^{225}At and ^{213}Bi (unpublished).

Chapter 7

Results of SPECT Imaging with ^{209}At

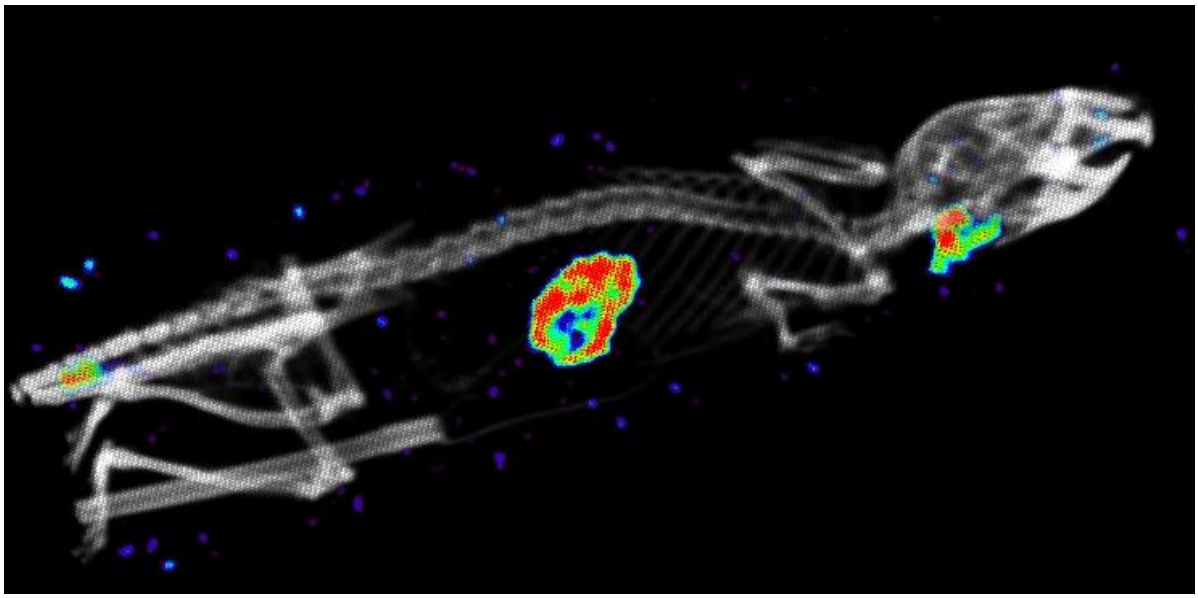

Figure 7.1: 3D render of SPECT/CT images (fused), showing free $^{209}At^{-}$ uptake in a mouse.

This chapter provides an analysis of ^{209}At-based imaging studies chapter, for which the methods were described in Chapter 5. An evaluation of detector response is first presented in §7.1, followed by results for phantom imaging and *in vivo* imaging in §7.2 and §7.2, respectively. These individual elements are discussed in a broader context in §7.4.

Description of detected energy spectra for ^{209}At SPECT measurements

Photon detection by VECTor/CT was recorded on an event-by-event basis, also known as *list-mode*, recording the energy, direction, and time of each detection. The rate of individual events were binned according to energy to give the total number of counts per second as a function of bin energy, thus providing the energy spectrum of detected counts for the detector. The energy spectrum from the Jaszczak phantom is shown in Figure 7.2. It should be noted that the energy calibration of the spectrum was inaccurate at energies

above 400 keV, by a systematic error of as much as 10% below the actual energy. The spectrum was interpreted with respect to the known ^{209}At γ-rays, and all subsequent analysis refers to the actual γ-ray energies rather than the systematically shifted energies reported by the detector. A correction to the detector calibration will likely be done in the future[1].

Several features of the detected energy spectrum were observed: *Photopeaks*[2] could be attributed to the most abundant γ-rays produced in ^{209}At decay, at 545 keV (91%), 782 keV (83%), 790 keV (64%) and 195 keV (24%). The spectrum showed a sharp, intense photopeak below 100 keV which was consistent with the high amount of X-rays promptly emitted by ^{209}Po following ^{209}At electron capture decay. Photopeaks broadened with increasing energy, reflecting the 10% energy resolution of the detector. Additionally, photopeaks at 545 keV and 782/790 keV were symmetrical, rising above an apparent background that fell smoothly as energy increased. The background appeared to be much higher at lower energies between 100-300 keV, from which the detected 240 keV (13%) ^{209}At γ-rays were not differentiable as a distinct photopeak. The dominant component of this background was suspected to be scattering radiation originating from the interaction of high energy γ-rays interacting with the tungsten collimator and other components of the system (Compton scattering). The background signal appeared to have significantly interfered with the detection of 195 keV and 240 keV γ-rays.

Additional details of the spectrum were evaluated by a GATE Monte Carlo simulation of the detector, with simplification to the detector geometry (as described in §5.1.1). As shown in Figure 7.3a, the simulated spectrum closely matched the experimentally measured spectrum, taking into account the erroneous energy calibration of the detector at high energies. Collectively, the overall similarity between the measured and simulated spectra provided confidence that the simulation accurately quantified the relative contributions of the spectra for ^{209}At. The simulated spectrum was decomposed to its various components, shown in Figure 7.3b, including primary emissions (^{209}At γ-rays), promptly emitted ^{209}Po X-rays, scatter, and tungsten X-rays originating from the collimator. Importantly, this analysis showed that the impact of the tungsten X-rays was almost negligible compared to the high abundance of X-rays resulting from ^{209}At decay, supporting the pursuit of X-ray-based image reconstruction. The scatter component was further decomposed into various sources, defined by the ^{209}A gamma-ray energy (or X-ray energy) from which it originated (Figure 7.3c). Viewed in this way, the simulation implied that scatter (below 790 kEV) was composed almost entirely of roughly equal amounts of scatter originating from the 782/790 keV γ-rays and the numerous, low intensity gamma-rays emitted at higher energies (>800 keV). Even with an abundance of photon emissions

[1]The responsibility for detector calibration is handled by the CCM staff and was not a component of this experiment.

[2]A distinguishable, relatively abrupt rise and fall in the energy spectrum is called a *photopeak*.

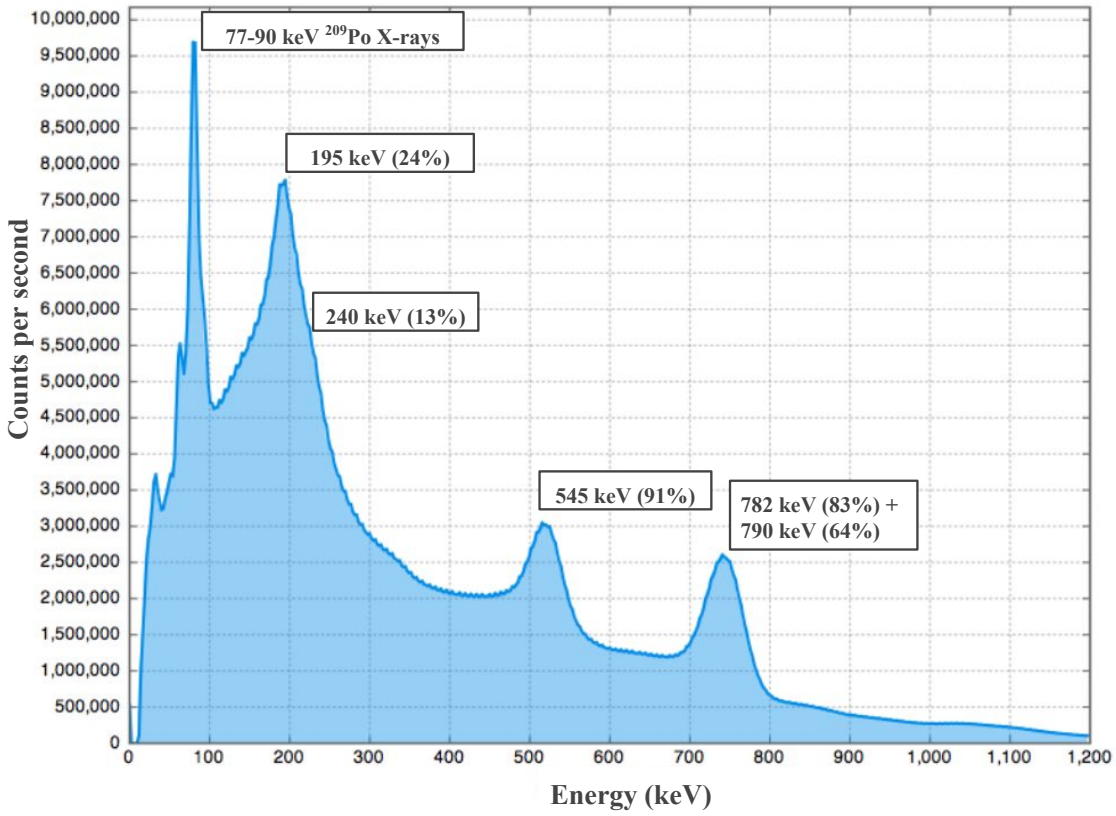

Figure 7.2: Energy spectrum of ^{209}At acquired by the VECTor/CT imaging system. The spectrum is a histogram of the detected counts per energy bin, with energy bin width of 2.3438 keV (512 bins). Energy resolution of the scanner was known to be approximately 10%, as evidenced by the peak broadening at higher energies.

well-suited for SPECT imaging with VECTor, this analysis implied that the potential of ^{209}At as a high energy SPECT isotope was inherently limited by the high energy γ-rays that scatter in the system and cumulatively interfere with the detection of the primary signal.

Phantom imaging studies with ^{209}At

μ-Jaszczak (μ-hotrod) phantom

The SPECT measurement of ^{209}At in a μ-Jaszczak (μ-hotrod) phantom produced the first-ever image of an ^{209}At activity distribution. Four individual images were produced by selecting four different photopeak energies for reconstruction, which included 77-90 keV (X-rays), 195 keV, 545 keV or 790 keV, according to the methods described in §5.2. (It should be noted that in this work, the term "X-ray image" refers to the 77-90 keV Po X-ray reconstructed SPECT image, and is completely distinct from the CT image, acquired with an externel X-ray source). Transverse cross-sections of each image are shown in Figure 7.4. The image reconstructed with X-rays showed enough contrast between rods to differentiate rods that were separated by as little as 0.75 mm (an estimate

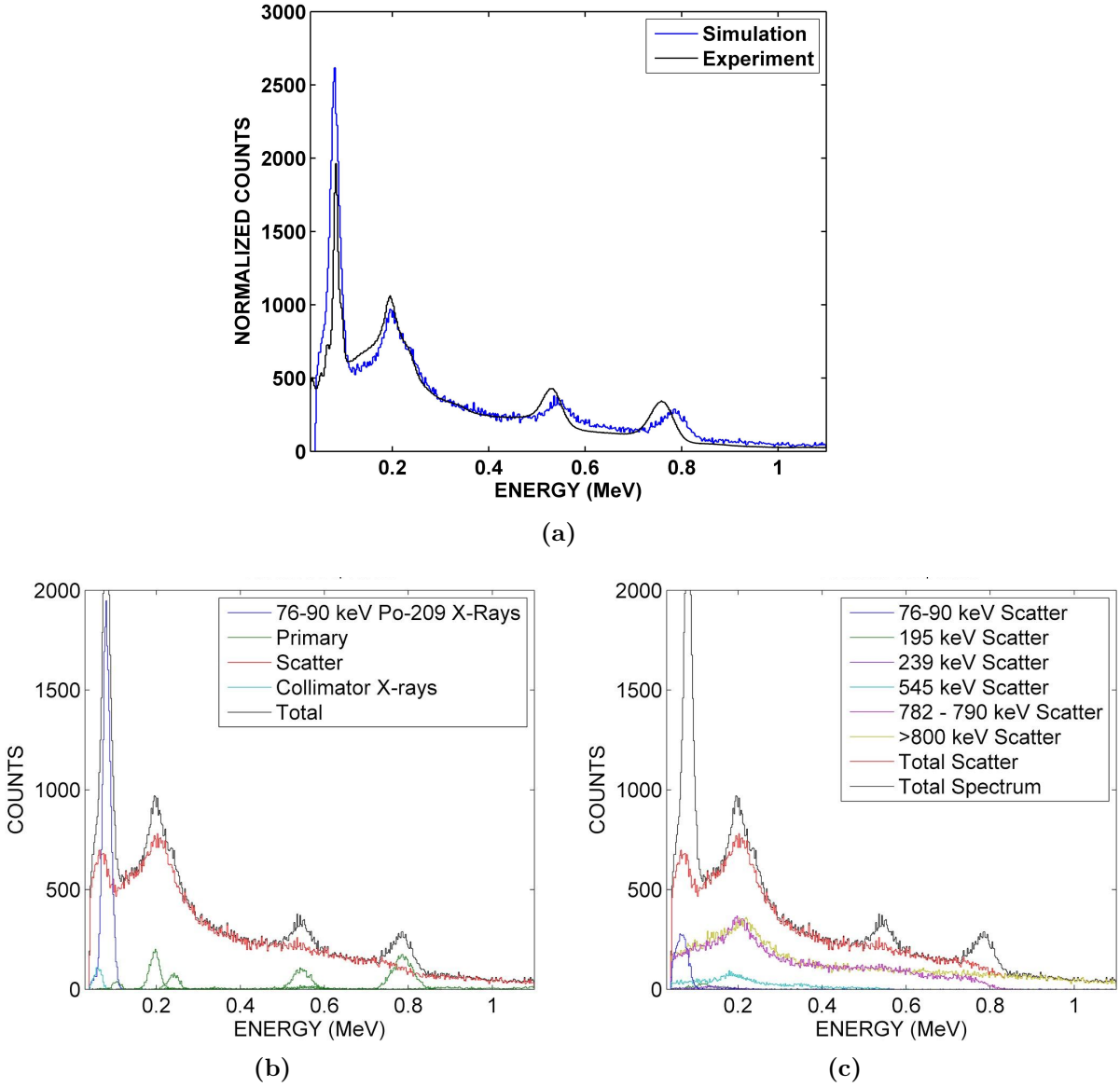

Figure 7.3: Monte Carlo simulated energy spectrum detected for ^{209}At by the VECTor SPECT system: **(a)** The MC simulated energy spectrum compared to measurement, **(b)** components of the MC simulated energy spectrum, and **(c)** the dependence of scatter on γ-ray energy, as determined by the MC simulation. Energy bin width was 2.3438 keV (512 bins).

of resolution); however, the activity distribution was not physically accurate and suffered from some fairly major image artifacts. Activity distributions did not follow the rod dimensions, appearing as smaller rod diameters in the image. In addition, rod shape was morphed to appear slightly triangular. The misshaping of the image was possibly related to the triangular arrangement of the flat panel NaI detectors for this system, but the exact cause of this artifact was not further explored. The 195 keV image suffered from the most noise and rods were not resolvable. The image noise was presumably the effect of the large amount of scatter in this region of the energy spectrum (downscatter from higher energy γ-rays) which interfered with the detected primary signal. The 545 keV image had much less noise, but even the 0.85 mm diameter rods were barely distinguishable. Despite the decreased resolution in this image, the contrast observed between each set of rods and the background suggested that 545 keV images could be useful despite a compromise in image resolution. Rods were not distinguishable for the 782/790 keV image, confirming our expectations that sub-mm resolution would not be possible at such high energies. These preliminary images motivated a more thorough evaluation of the ^{209}At-based SPECT imaging, and was basis for choosing to complete a more thorough study of contrast and resolution using the larger version of the Jaszczak phantom.

Jaszczak (hotrod phantom):

SPECT measurements of the Jaszczak phantom resulted in perhaps the most meaningful images of ^{209}At-activity for the series of phantom imaging studies. Figure 7.5 shows a set of images produced by a single acquisition, again where each individual image was reconstructed using one of the same four most-prominent photopeaks. For this phantom, the highest resolution is observed for the 77-90 keV X-rays at $\geq$ 0.85 mm. All energies provided resolution at equal to or above 1.3 mm, while the 195 keV reconstruction suffered from extensive amounts of noise.

Metrics of contrast and the contrast-to-noise ratio pertaining to each set of rod dimensions were evaluated quantitatively, as described in §5.3.2. Calculated values of contrast were plotted as a function of rod diameter, shown in Figure 7.8a. For assessment of resolution, a value for contrast above 0.2 within a given set of rods was considered sufficient for resolving image detail[3] at the resolution of the rod diameter (d). Reconstructions with all four energies produced contrast above the threshold for resolution (0.2) for $d \geq$ 1.3 mm diameter or greater, while X-ray-based reconstructions surpassed this threshold for $d \geq$ 0.95 mm. Contrast as a function of rod diameter was shown to behave very similarly for 545 keV and 782/790 keV reconstructed images. This was also true for the contrast-to-noise ratio with respect to rod diameter for those energies, which were roughly 2-4 times lower than the contrast-to-noise ratio determined for the X-ray image over the

[3]This criteria had been previously used by UBC for the same image analysis, only with ^{18}F [125].

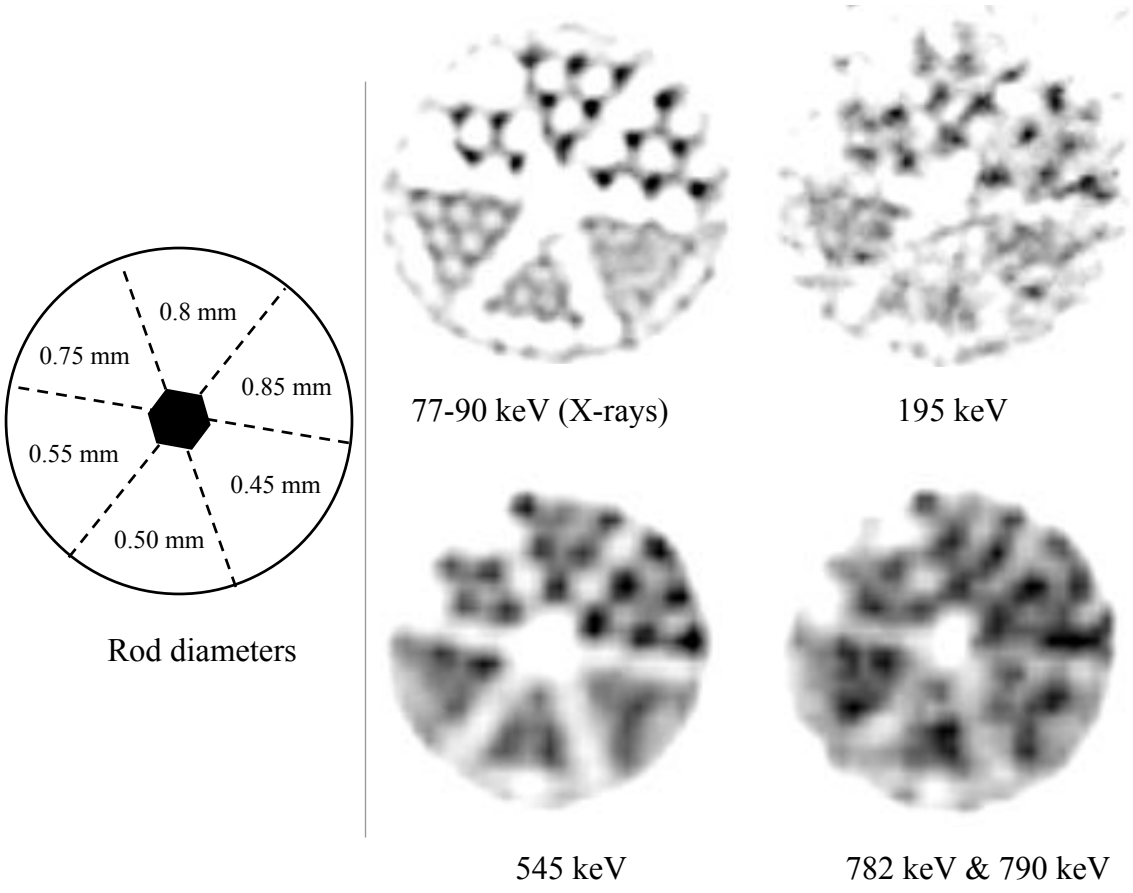

Figure 7.4: First set of SPECT images of ^{209}At completed using the μ-Jaszczak phantom, as reconstructed with one of 4 different energy photopeaks: 77-90 keV (X-rays), 195 keV, 545 keV, or 790 keV. Rods of a given set had an equal diameter (d) of (in mm) 0.45, 0.50, 0.55, 0.75, 0.80, or 0.85. The distance between rod centres was $2 \times d$.

entire range of d. These results are plotted in Figure 7.8b The 195 keV image had a contrast value slightly above 0.2 for d=0, but the image was very noisy, and difficult to interpret from a practical perspective. Images reconstructed with the 195 keV photopeak were considered inferior in both quality and utility, compared with the images of other energies, and no further reconstructions with this energy were completed.

In an extension of this analysis, two more images were produced, by reconstruction with multiple photopeaks (X-rays+545 keV or X-rays+545 keV + 782/790 keV). These were compared to the corresponding linear combinations (sum) of images reconstructed with single photopeaks (as given above). This set of images is provided in Figure 7.7. For both combinations of photopeaks, better resolution was achieved by the summed images compared to the images produced by multipeak reconstruction. This was also quantified in terms of contrast and contrast-to noise (Figure 7.8): summed images provided contrast values above (or very close to) the 0.2 threshold at rod diameters as low as 1.1 mm, while the multipeak reconstructions did not. Collectively, these results indicated

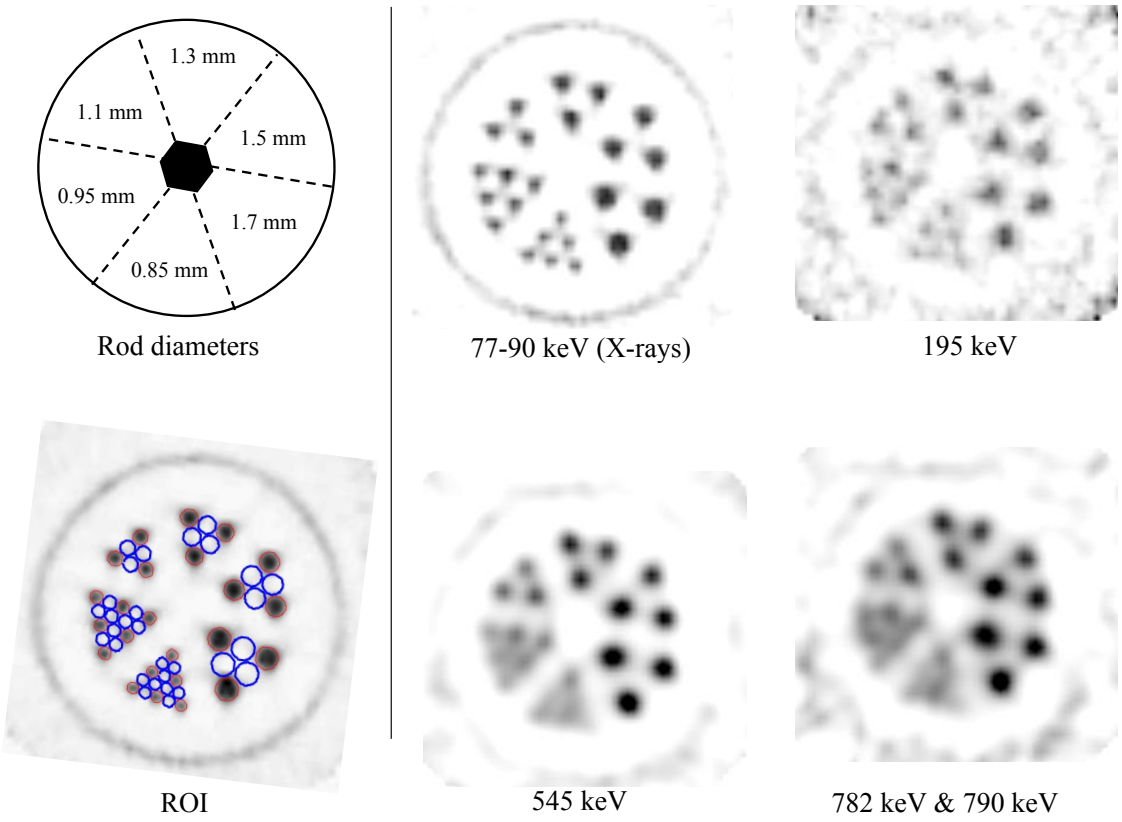

Figure 7.5: SPECT images of ^{209}At, completed using the Jaszczak phantom, as reconstructed with one of 4 different energy photopeaks: 77-90 keV (X-rays), 195 keV, 545 keV, or 782/790 keV. Rods of a given set had an equal diameter (d) of (in mm) 0.85, 0.95, 1.1, 1.3, 1.5, or 1.7. The distance between rod centres was $2 \times d$.

that summing single peak reconstructions provided image equality that was equivalent or superior to multipeak reconstructions. This provided confidence that the summing procedure was valid, which was important because attenuation corrections could not be applied to multipeak image reconstructions. Attenuation corrections could be made to single photopeak images before performing linear combination, permitting the evaluation of attenuation corrected summed images pertaining to *in vivo* studies (§7.3).

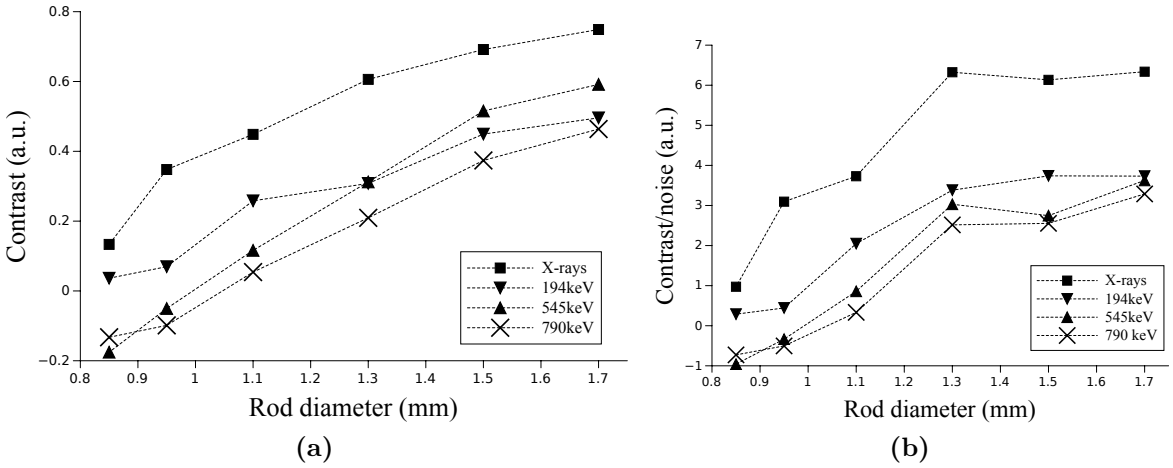

Figure 7.6: Comparison of Contrast and contrast-to-noise ratio as functions of rod-diameter, for reconstructions using single energy photopeaks of the ^{209}At spectrum. Photopeaks corresponded to X-rays (77-90 keV), or individual γ-rays (195 keV, 545 keV, or 782/790 keV).

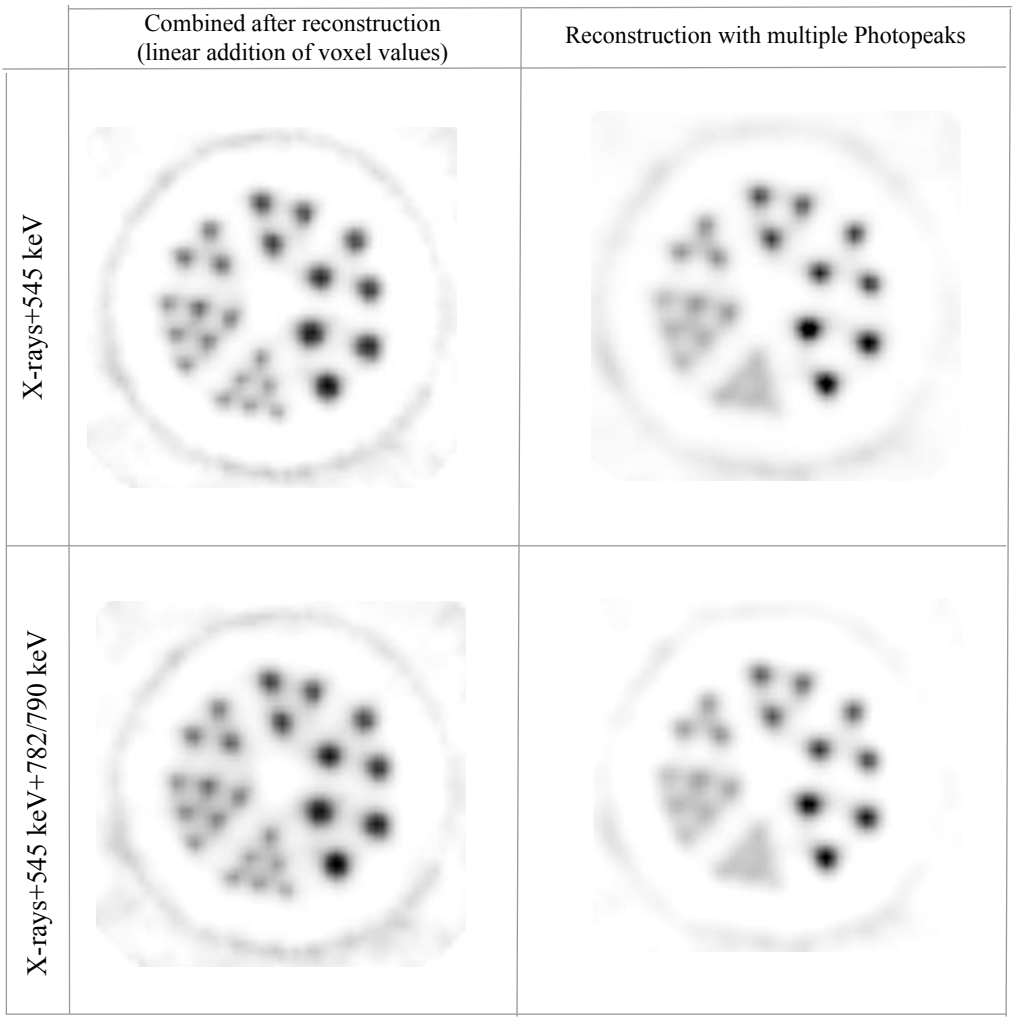

Figure 7.7: ^{209}At SPECT images produced by summing single energy compared to reconstructions using multiple photo-peaks of the same energies (jaszczak phantom). Analysis was performed for the combination of 77-90 keV (X-rays) and 545 keV photopeaks, alone or also in combination with the 782/790 keV photo-peak.

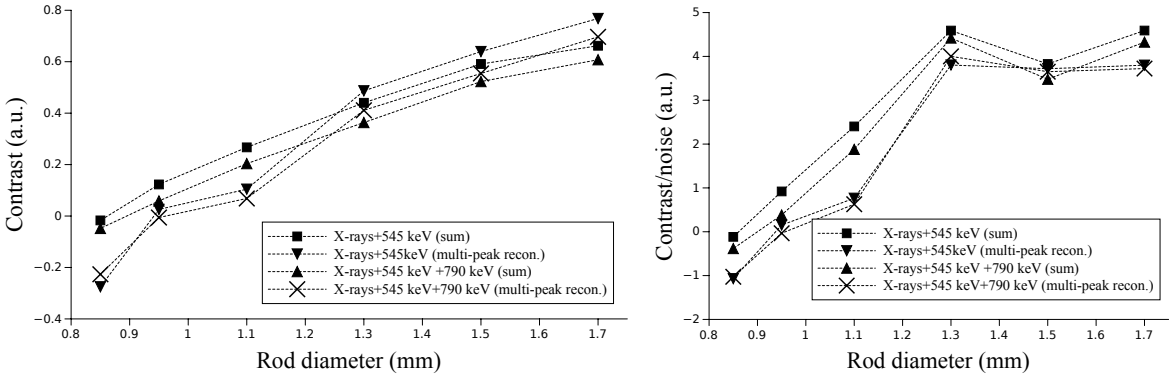

(a) **(b)**

Figure 7.8: Comparison of contrast and contrast-to-noise ratio as functions of rod-diameter, from images produced with multiple photopeaks of the ^{209}At spectrum (combined single energy photopeak reconstructions vs multiple photopeak reconstructions). In particular, analysis was performed for the combination of 77-90 keV (X-rays) and 545 keV photopeaks, alone or also in combination with the 782/790 keV photo-peak.

Uniformity phantom (20 mL syringe)

Uniformity of ^{209}At SPECT imaging with VECTor was assessed with the uniformity phantom, a 20 mL syringe filled with [^{209}At^{-}]astatide in 7.2 mL of aqueous solution (0.1 N NaOH) to provide a physically uniform distribution of ^{209}At. Unfortunately, it was determined that the detector count rate for this SPECT scan exceeded manufacturer specifications for maximum count rate by a factor of 1.75 (max count rate = 80,000 counts/second, per panel detector). As a result, the images were expected to demonstrate artifacts related to detector dead-time (or saturation), and the results reported here should be interpreted as a worst case scenario for image uniformity. Attempts to repeat these syringe phantom measurements with lower activity were made, but limitations with respect to ISAC yields and beam availability ultimately foiled these attempts. The result of these circumstances is that the assessment of uniformity is incomplete. The data is currently in adequate for a proper quantitative assessment requiring the experiment to be repeated at some point in the future. Nonetheless, the analysis was still performed according to the methods described in §5.3.2. Values for the quantitative metrics of uniformity determined by this work therefore present values to which future measurements can be compared.

Images were reconstructed for the 77-90 keV (X-rays) and 545 keV (γ-ray) photopeak and corrected for attenuation. A summed (linear combination) of the resulting X-ray and 545 keV images was also computed. Figure 7.9 shows central transverse and coronal planes of the fused SPECT/CT images for each energy. Qualitatively, uniformity was much better for the X-ray image, compared to the 545 keV and summed images. For images of the latter, discrepancies in uniformity were observed to dramatically increase (worsen) with distance from the central axis.

Line profiles of image intensity were generated for each image, matched to the same physical location. Figure 7.9 also shows the line profiles in the transverse plane (perpendicular to the central axis of the cylindrical syringe), as well as, profiles parallel to the centre axis, both at the central axis and with a 3 mm off-set (coronal plane). Line profiles off-set from the central axis showed major discrepancies in uniformity for the 545 keV image (and accordingly the summed image). The X-ray image was much more uniform, where better uniformity was also observed for off-axis positions in the activity distribution (also in the coronal plane).

The uniformity of these images were quantified in terms of the rms-noise, integral uniformity, and %COV metrics, as described in §5.3.2. These metrics were also computed for the summed (linearly combination) of the X-rays image and the 545 keV image. The metrics are compared to accepted values in Table 7.1. With the exception of $\%COV$ and rms-noise for the 77-90 keV X-rays image, all metrics calculated for this image set failed to meet the criteria regarding uniformity for quantitative SPECT imaging. These

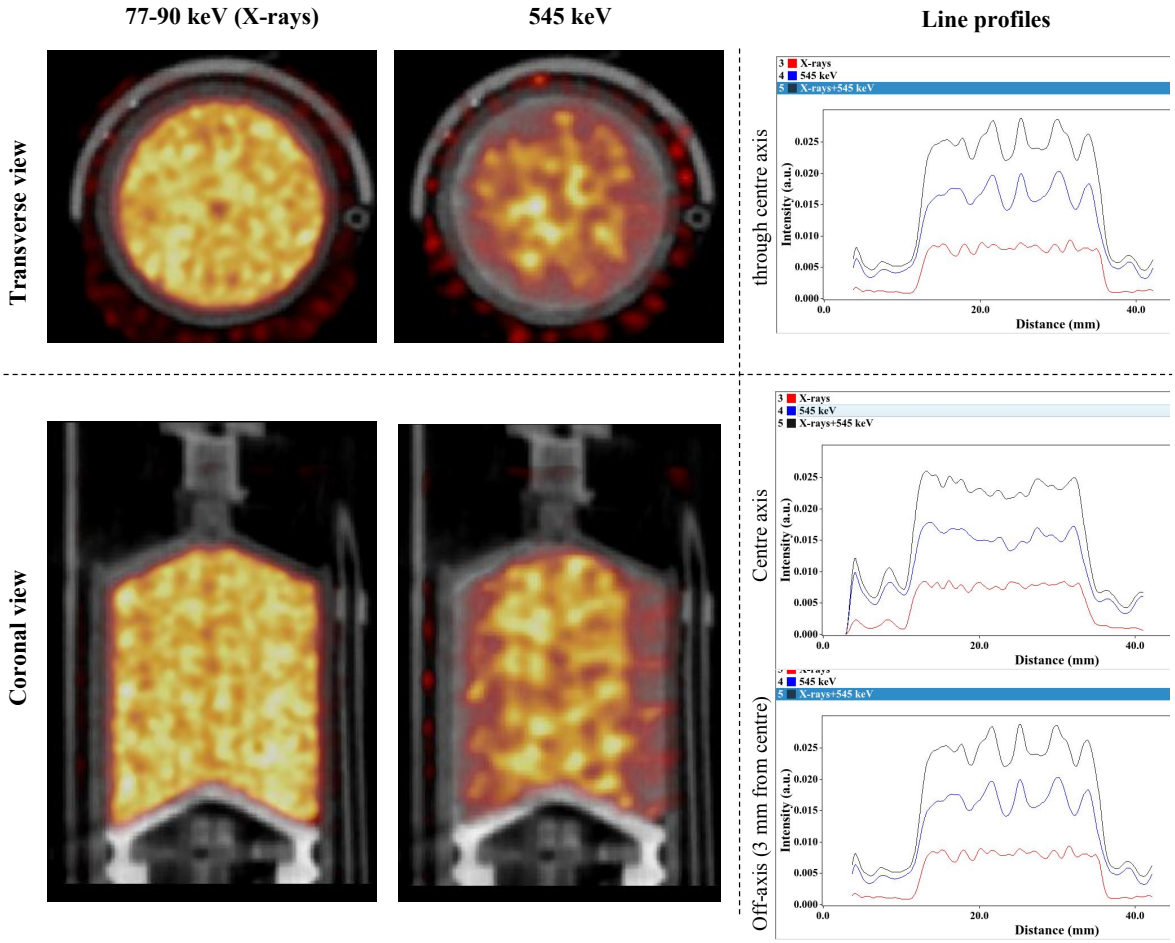

Figure 7.9: Fused SPECT/CT images with ^{209}At for the uniformity phantom (20 mL syringe filled to 7.2 mL), reconstructed with 77-90 keV X-rays and 545 keV γ-rays, and related line profiles. The CT image is shown greyscale and the SPECT image is shown in a hot metal colour scheme. Line profiles of ^{209}At-based SPECT image of uniform distribution, for images reconstructed with 77-90 keV X-rays and 545 keV γ-rays (as well as the linear combination of the images).

were likely a worst-case scenario for the determination of uniformity because of the high detector count rate (deadtime). It is expected that the uniformity would be improved by lowering the amount of activity used for this measurement by approximately 50% (given by the count-rate of 1.75 times the recommended maximum used for these measurements, as indicated above).

Based on these preliminary phantom studies, and with greater consideration to the Jaszczak phantom measurements, it was determined that 77-90 keV X-rays provided the best photopeak for image reconstruction for assessments of the activity distributions. This conclusion was very much consistent with the Monte Carlo results fpr the detected energy spectrum, which showed that for the X-ray photopeak, the primary signal was much higher than the signal produced from the scatter, compared to scatter the high energy photopeaks.

Table 7.1: Metrics of uniformity calculated for ^{209}At-based SPECT images of the uniformity phantom, in comparison to accepted values. Images were reconstructed with single energy photopeaks (77-90 keV or 545 keV photopeaks), as well as, the combination of two resulting images (summed image). *: recommended limit from UBC-CCM. †: recommended limit from AAPM (1995) [126], (UBC-CCM limit not known).

Photopeak energy	**integral uniformity**	**rms-noise**	**%*COV***
Acceptable values	$< 20\%^*$	$< 7.2\%^\dagger$	$\leq 5\%^*$
image:			
77-90 keV (X-rays)	28%	7.2%	4.1%
545 keV (γ-rays)	32%	11.2%	8.5%
77-90 keV + 545 keV	22 %	8.5%	6.2%

Mouse imaging studies with ^{209}At

The *in vivo* SPECT imaging of ^{209}At, in normal mice, was performed as described in §5.4. These studies produced the first-ever images of ^{209}At in a living specimen. Imaging was performed for three distinct injection types, including free [^{209}At$^-$]astatide, ^{209}At-labelled peptide, and the co-administration of ^{209}At-labelled peptide and free [^{123}I$^-$]iodide. Although very limited in scope, these variations were meant to demonstrate the feasibility of using ^{209}At as a novel isotope for measuring the activity distributions of astatine with small animal SPECT.

Free ^{209}At in normal mouse

A normal mouse (C57BL/6) was injected with 11.6 MBq of free ^{209}At$^-$ into the blood stream via tail vein. A significant fraction of the injected activity was observed to be injected subcutaneously and not distributed to the blood stream. SPECT scanning began at 30 minutes post-injection and continued for 45 minutes (9 frames of 5 minutes). Activity distributions of free ^{209}At measured at 30 minutes post-injection were reconstructed with the 77-90 keV (X-rays) and 545 keV (γ-ray) photopeaks, corrected for attenuation. The linear combination of voxels was also created calculated from both images (producing the X-rays + 545 keV summed image), the resulting set of images are shown in Figure 7.10. For either reconstruction energies, thyroid and stomach uptake were clearly observable and presented the organs of highest ^{209}At uptake. None of the images showed activity in the lungs or intestinal tract with high resolution/low sensitivity Gaussian smoothing (1 mm FWHM), demonstrating the importance of image filtering with stronger Gaussian smoothing (i.e. 2 mm FWHM, kernel=31) for identifying low activity uptake that may be present in some organs (e.g. lungs), which was subsequently performed. As shown in the Figure 7.11, activity was clearly distributed to organs that astatine normally sequesters [61], including the thyroid, stomach, salivary glands, lungs, liver, and bladder (in urine).

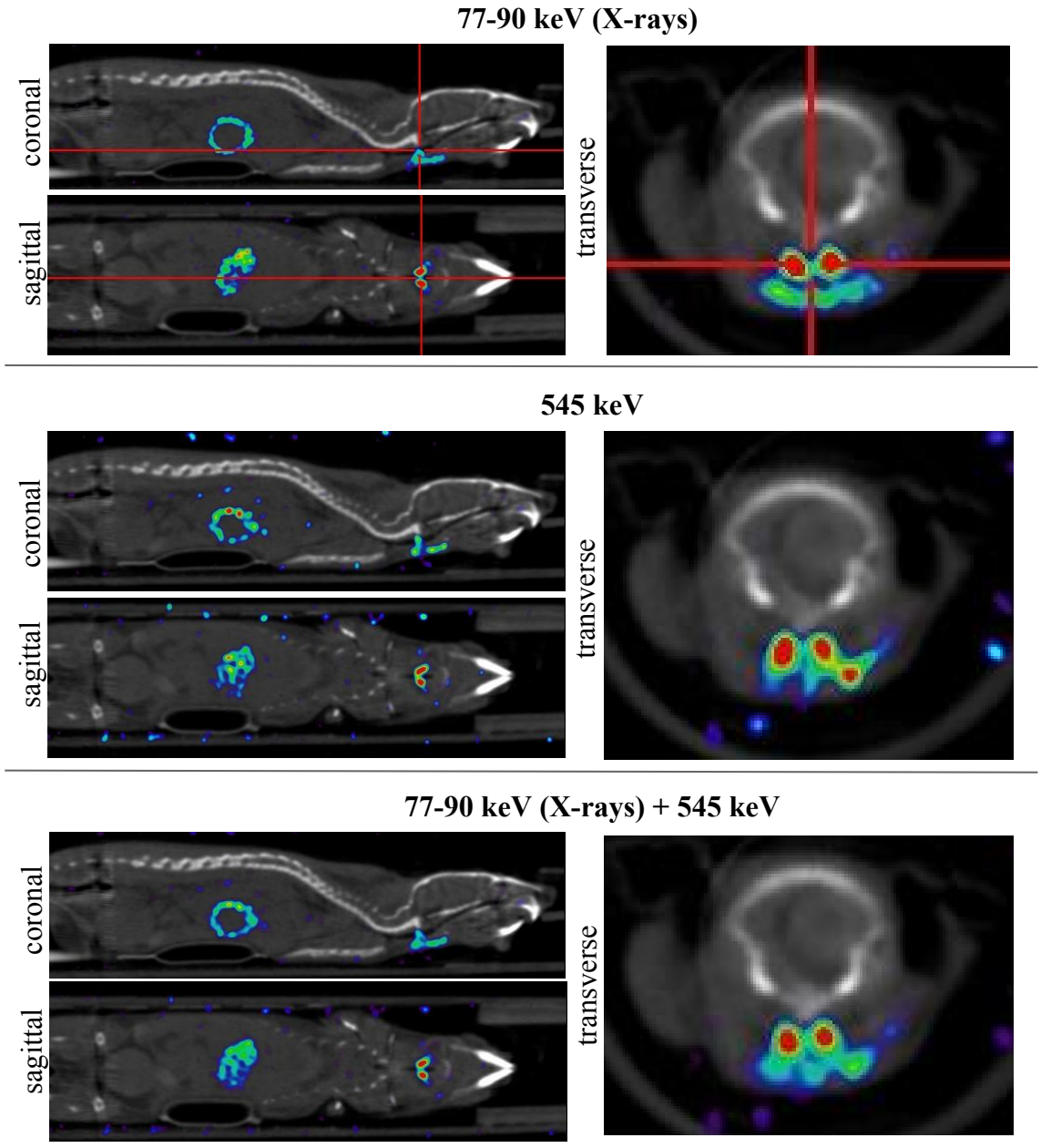

Figure 7.10: SPECT/CT (fused) of a mouse 30 minutes after intravenous injection with free ^{209}At (via tail vein). SPECT scanning duration was 45 minutes, taken in 9 frames of 5 minutes each. Independent SPECT image reconstruction were performed with the 77-90 keV (Po X-rays) and 545 keV photopeaks, alone, as well as in linear combination (summed single photopeak reconstructions).

With high resolution Gaussian smoothing (Figure 7.11a), uptake was clearly identified in the stomach lining and not the contents, presented as a void in the activity distribution. Low resolution (high sensitivity) was required to resolve activity in the lungs, bladder and liver, but was found to dramatically reduce image resolution.

In all SPECT images, each thyroid gland was clearly distinguishable, separated by the void created by the trachea. This provided a means of evaluating image resolution for this system, in the context of actual *in vivo* imaging. Transverse line profiles were

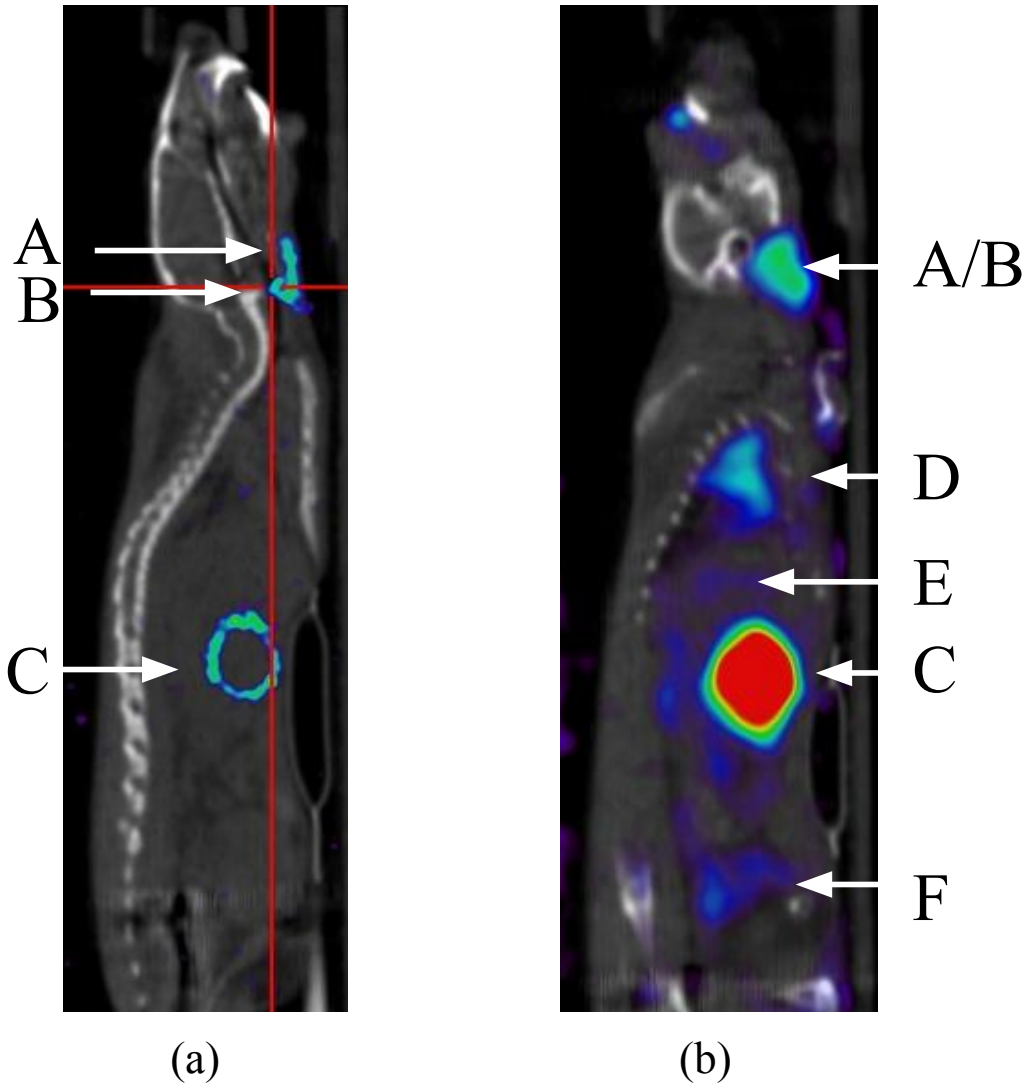

Figure 7.11: Fused SPECT/CT showing the activity distribution of free 209At- (astatide) in a normal mouse at 1 hour post-injection via tail vein. (a) Imaging High resolution/low sensitivity Gaussian smoothing (1 mm FWHM, kernel size = 7) where A=salivary glands, B=thyroid, C=stomach lining). (b) Low resolution/high sensitivity Gaussian smoothing (2 mm FWHM, kernel size = 31) where A=salivary glands, B=thyroid, C=stomach, D=lungs, E=liver, F=Bladder). Images were reconstructed using the 77-90 keV photopeak.

created through the thyroid gland of reconstructed ^{209}At activity distribution, as shown in Figure 7.12. Orientation of the profile was defined in the transverse view and intersected the centre of both thyroid lobes of the thyroid. The physical diameter of each lobe (as defined by average anatomy for healthy mice) was expected to be approximately 1 mm, separated by about 1 mm by the trachea. For all reconstructions evaluated, peak to peak separation in the intensity line profiles was 2 mm, and agreeing well with the average physical distance between lobe centres of the Thyoid in normal mice. The FWHM of each lobe was equal for each energy but differed between reconstructions, respectively, with the FWHM given by the summed image being between these two values. This

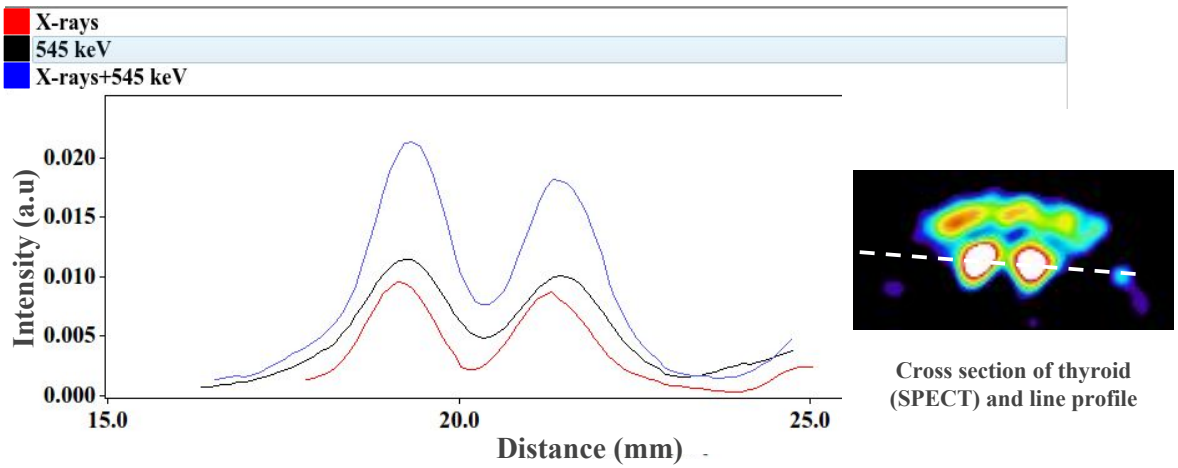

Figure 7.12: Line profiles through thyroid of SPECT image of free [^{209}At]astatide. Data sets were smoothed with a 1 mm gaussian filter.

analysis shows that all images could achieve sub mm resolution of uptake to the thyroid.

Immediately after scanning, the mouse was sacrificed by full body bleed and cervical dislocation, along with an overdose of isoflurane. Quantitative, whole-organ biodistribution measurements were completed, as described in §5.4.2. Figures 7.13a and 7.13b show the measured activity and percent injected dose per gram, respectively, for the selection of organs. As previously stated, a percentage of the injected dose was administered subcutaneously and did not enter the blood stream directly. For this reason, activity in the tail was also measured *ex vivo*. Tail vein activity was measured to be 16% of the injected dose and this was subtracted from the total injected activity when calculating the results given in Figure 7.13b.

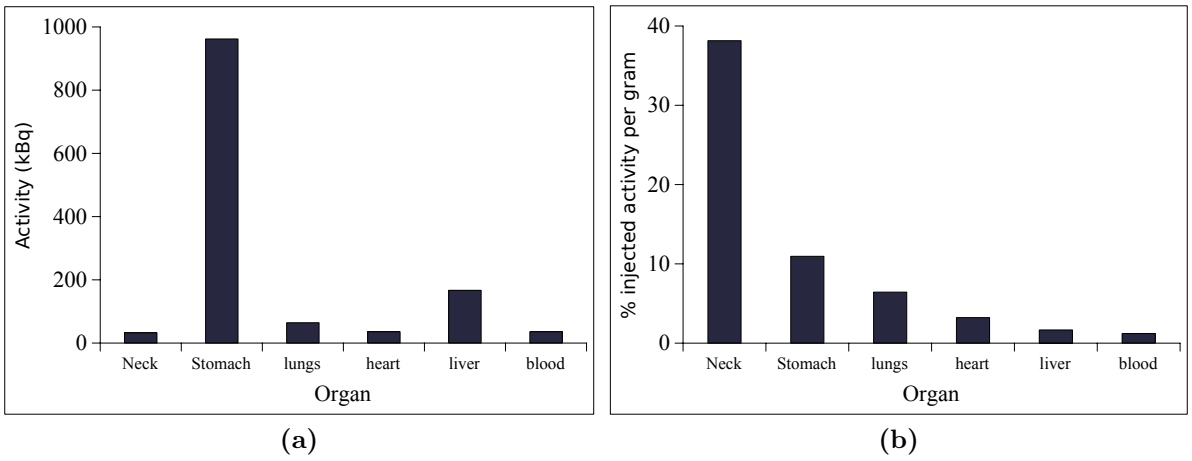

Figure 7.13: *Ex vivo* biodistribution of free [^{209}At^{-}]astatide in a normal mouse, 80 minutes after intravenous injection via tail vein. The measured organs included thyroid/trachea, stomach, lung, liver, heart and blood. **(a)** Absolute activity measured in each organ, and **(b)** % injected activity per gram measured in each organ. Each organ was measured separately by gamma counter, cross calibrated with the dose calibrator used to measure injected activity. Note: the organ identified as 'Neck' referred to the thyroid gland and a small segment of the trachea.

As a first assessment of SPECT image data quantification, the ratio of stomach to thyroid ^{209}At activity (as measured by the biodistribution) was compared to uptake quantified by SPECT imaging. Separate ROI were defined around each organ (stomach or thyroid) and the sum of all voxels within these ROI were calculated for images reconstructed with either the X-rays or the 545 keV photopeak. From the biodistribution, this ratio was given as 29:1 $\pm$ 15%, the values obtained by the SPECT image data were 19:1 (X-rays image) and 25:1 (545 keV image), differences[4] of 34% and 14%, respectively. Although this involved only one data point and not necessarily representative of how well each image type can quantify the actual activity distribution, in general, this analysis did provide the first assessment of activity quantification, *in vivo*, demonstrating how such measurements can be made. Even though the significance of this result could not be determined, it does motivate further evaluation in the future with more data points (i.e. sets of images and corresponding *ex vivo* biodistribution measurements). The better agreement between biodistribution and the 545 keV reconstructed image could be due to the fact that that the attenuation for X-rays is much more significant compared to the higher energy γ-rays and errors related to inaccuracies in attenuation correction might be exaggerated for the X-ray image.

SPECT imaging with free ^{209}At in a normal mouse was also attempted using the high resolution standard SPECT collimator (1.5 cm thick tungsten), otherwise repeating the experimental methods used for the high energy collimator (4-4.5 cm W). Inspection of the resulting SPECT image, shown in Figure 7.14, confirmed that the standard collimator was insufficient for meaningful SPECT imaging with ^{209}At. The primary signal from the 77-90 keV Po X-rays was negligible in comparison to the collimator penetration of higher energy scatter. Based on this single scan, it was concluded that the high energy collimator was a requirement for ^{209}At-based SPECT, and all subsequent scanning was performed with the high energy collimator.

^{209}At-labelled antibody (aggregated) in normal mice

Two normal mice also received tail vein injections of ^{209}At activity, in the form of ^{209}At-labelled antibody (BC8) and scanned at 1, 3 and 24 hours post-injection (40 minutes/scan), and further details for this sequence of scans listed Table 5.3.

As previously suggested, the BC8 mAb had most likely become aggregated and was no longer functional against the CD45 antigen. Based on the cellular expression of this antigen (exclusively by haematolymphoid cells) [128], ^{209}At would be expected to accumulate in the spleen, thymus, bone marrow, lymph nodes, and, to a lesser extent, the liver. In contrast, the SPECT images of the ^{209}At-labelled BC8 (aggregated) demonstrated that

[4]Percent difference was calculated as $\frac{real - image}{real} \times 100\%$, where 'real' was the ratio given by the biodistribution, and 'image' was the ratio determined by SPECT.

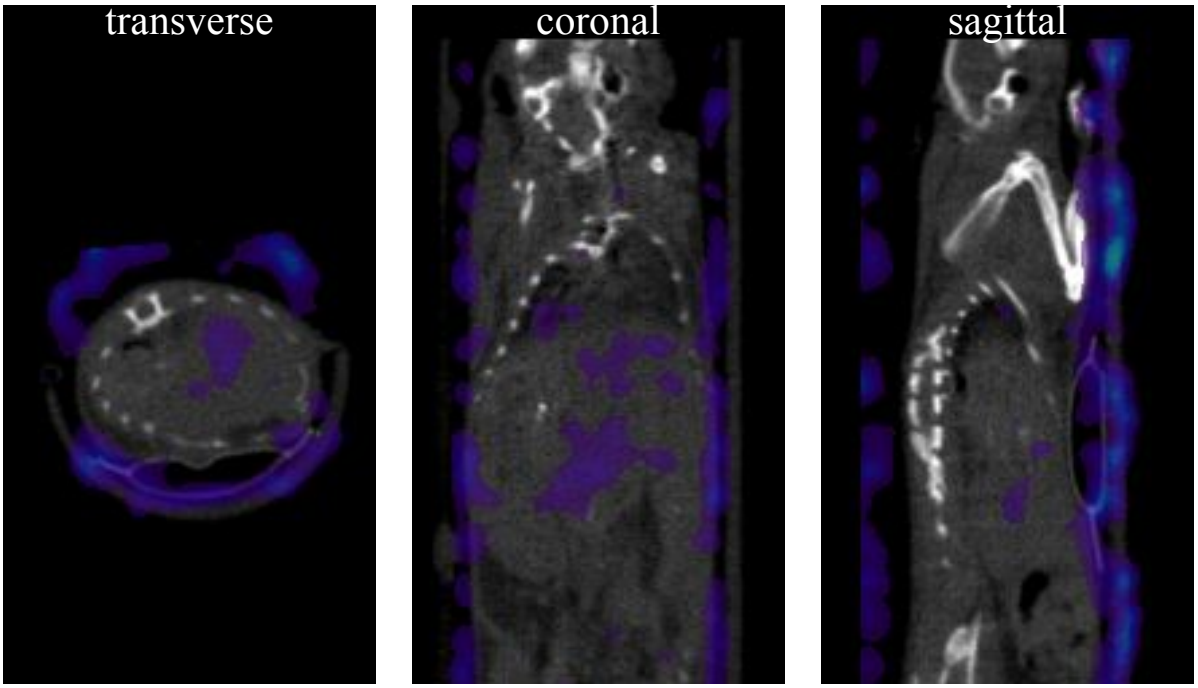

Figure 7.14: SPECT image resulting from the standard SPECT collimator (1.5 cm W), for free [^{209}At]astatide in a normal mouse. The SPECT image appeared not to contain spatial information, presumably the result of massive collimator penetration.

this biomolecule was rapidly cleared by the liver, without specific targeting of the organs where CD45 expression is high. As shown in Figure 7.15, images acquired 1 hour post-injection demonstrated rapid uptake of the ^{209}At-labelled protein by the liver. A significant fraction of the activity was still observable in the bloodstream; activity could be identified in areas of highest blood flow, including the heart, lungs, and major arteries (carotid arteries, abdominal aorta, and iliac arteries). One possible explanation for the rapid liver uptake was that the protein aggregated slightly, No uptake was observed in the kidneys (another blood filtering organ), which would be expected for smaller antibody fragments if the protein had been significantly degraded by radiolysis, or if the B10 moiety had become detached. Furthermore, purification of the labelled product size-exclusion columns (PD-10) ensured that the injected material consisted of proteins larger than 5 kDa, and iTLC demonstrated that the ^{209}At was labelled to protein. For these reasons, it was hypothesized that the injected material to which ^{209}At was bound was aggregated BC8 (non-functional). The rapid clearance of aggregated proteins by the liver was consistent with published findings [128]. Regardless, the ^{209}At-labelled BC8 (aggregated) provided an opportunity to evaluate ^{209}At-SPECT imaging for measuring ^{209}At activity distributions as coordinated by a biomolecule. This had never been done before and was considered a critical step towards future preclinical studies evaluating targeting efficacy with ^{209}At.

Another significant observation from these images was that uptake of ^{209}At activity

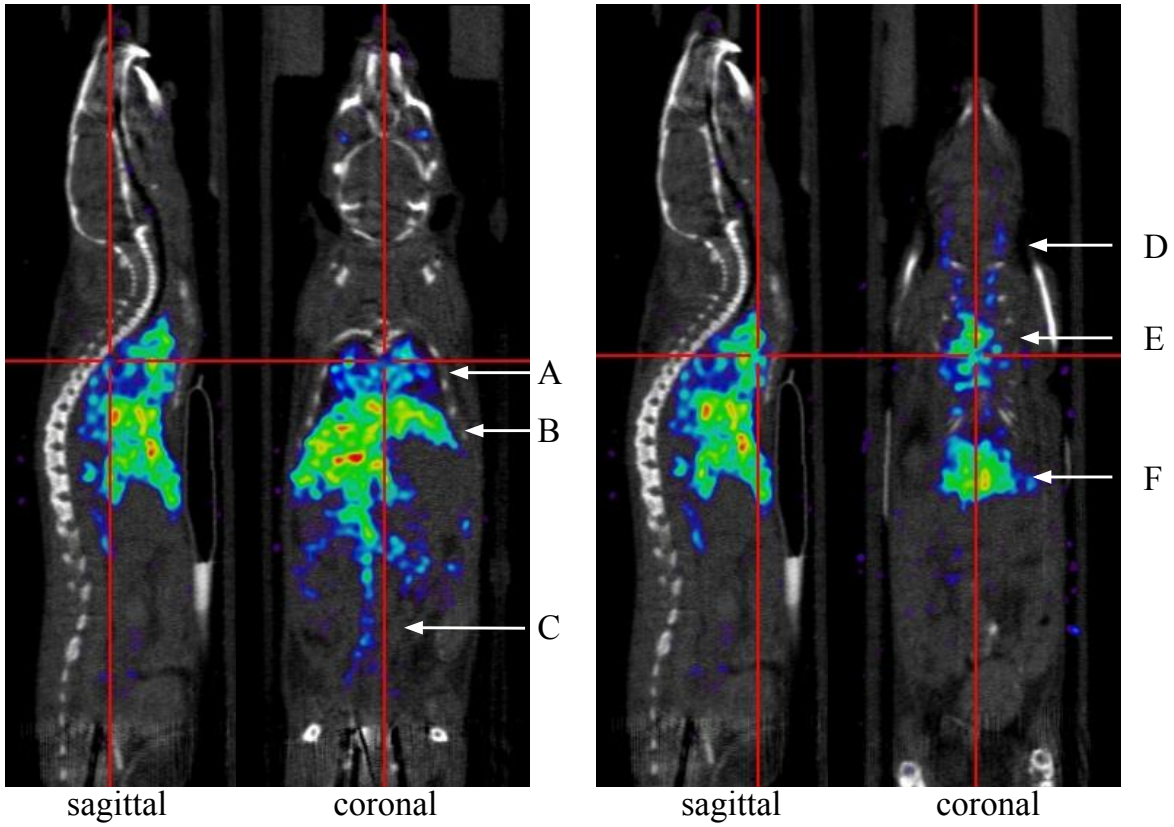

Figure 7.15: Fused SPECT/CT showing the activity distribution of ^{209}At-labelled protein (damaged BC8 mAb) in normal mouse (slice thickness = 0.4 mm), reconstructed with 77-90 keV X-ray photopeak. The reconstructed ^{209}At activity distribution, showing activity in thyroid glands, salivary glands, and stomach (imaged h hours post-injection by tail-vein. Anatomical structures with significant activity were identified: A = lungs, B (and F) = liver, C = abdominal aorta and iliac arteries, D = common carotid arteries, and E = heart.

was not seen in the thyroid or stomach, as would be expected if ^{209}At had become released from the peptide *in vivo*. This result was consistent for the 3 hour time point, as well. The absence of ^{209}At in the stomach and thyroid indicated that the ^{209}At-labelled protein was stable *in vivo*, and its distribution remained coordinated by the properties of the aggregated mAb. This is an important conclusion as it demonstrated the excellent *in vivo* stability of biomolecules astatinated with the boron-cage method. In contrast to the activity distribution shown in Figure 7.11, the stomach was identifiable as a void in the abdominal activity distribution of the ^{209}At-labelled protein.

Images reconstructed with either 77-90 keV X-rays or the 545 keV γ-ray were compared, examples of which are shown in Figure 7.16. X-ray images were always less noisy and more easily interpreted. Although still somewhat noisy, the summed image (X-rays + 545 keV) demonstrated increased contrast in liver hotspots which were believed to be physical, and not mere image artifacts. Overall, the X-ray image was still considered superior for studying the activity distribution, at least on a qualitative basis.

Image quality was observed to be much better for the mouse that received 6.2 MBq

of ^{209}At compared to the mouse that received 2.5 MBq. The striking difference in image quality for these two doses is shown in Figure 7.17, where X-ray images are compared for both doses and at two time points (1 hour and 3 hours post-injection). The resulting images illustrate how the 2.5 MBq injected dose was not sufficient for imaging, producing a noisy image that was difficult to interpret. Similar results were found for reconstructed images using the 545 keV photopeak. The lower dose (2.5 MBq) was 40% of the higher dose (6.2 MBq), representing 7.2 hours of ^{209}At decay (or 1.32 half-lives). This indicates that if imaging at later time points is required (e.g. 7.2 hours post-injection, also equal to 1 half-life of ^{211}At), even the higher dose (6.2 MBq) would not be sufficient. This late of a time point should actually be very significant for computing astatine dose distributions, because at one half-life of ^{211}At, the α-particle dose rate would still be significant and possible consequential to any observed therapeutic effect or endpoint. Since the image quality at 3 hrs appeared suitable for the higher injected activity of 6.2 MBq (or 4.2 MBq at 3 hours p.i.), an injected activity of 11 MBq (4.2 MBq $\times e^{7.2ln(2)/5.41}$) might be more suitable for imaging at 7.2 hours post-injection, all other factors being equal. This conclusion is only a guideline and in practice the optimal activity for injection will need to determined on a case-by-case basis.

Simultaneous imaging of ^{209}At-labelled BC8 and Free ^{123}I in normal mouse

Simultaneous dual-isotope imaging was performed using ^{209}At-labelled protein (4.1 MBq) and free [^{123}I^{-}]iodide (15.2 MBq), administered with adjuvent injections 10 minutes apart, into the blood stream via the tail vein. Scanning was performed 1 hour post-injection and proceeded for 40 minutes. Images were reconstructed separately with the 77-90 keV X-ray photopeak (associated with ^{209}At) and the 159 keV photopeak attributable to ^{123}I. The larger relative injected dose of ^{123}I was used in an attempt to overcome the background in the energy spetrum between 100-300 keV produced by the ^{209}At γ-rays. Cross-sections of the resulting image set are shown in Figure 7.18, including the fusion of both activity distributions. As expected, the ^{209}At-labelled protein sequestered to the liver, while the uptake of 123I was measured in the thyroid, stomach, and bladder. Importantantly these distributions did not interfere with each other, demonstrating, on the level of feasibility, dual-isotope imaging with ^{209}At and ^{123}I as a possible application of ^{209}At SPECT imaging. Doing so could be used as a new tool for making *in vivo* comparisons of biomolecules labelled with either iodine or astatine, in order to help validate the theranostic pairing of radioiodine and ^{211}At.

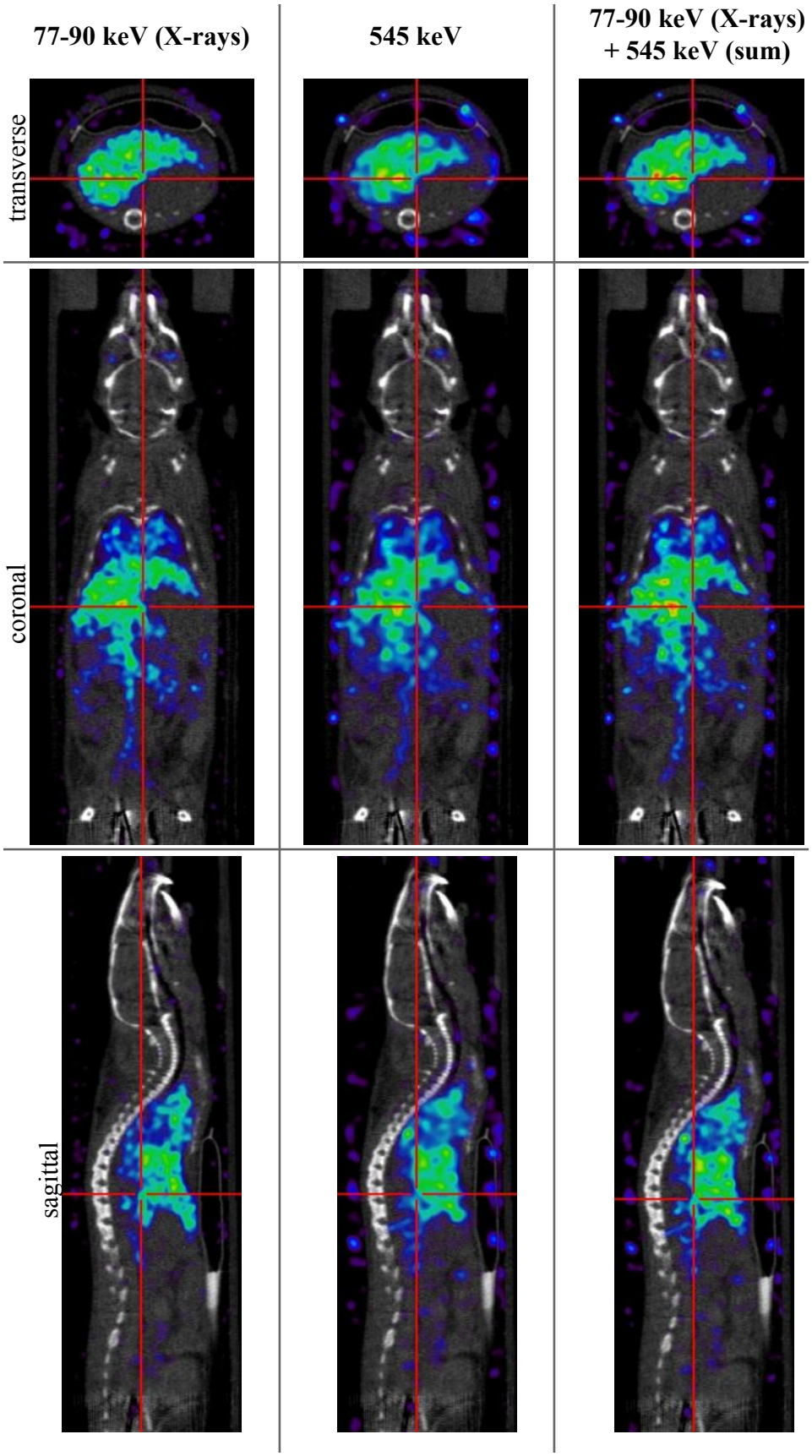

Figure 7.16: Fused SPECT/CT showing the activity distribution of ^{209}At-labelled BC8 (mAb) in a normal mouse, independently reconstructed with the 77-90 keV (X-rays) and 545 keV photopeaks, alone, as well as, in linear combination (summed single photopeak reconstructions).

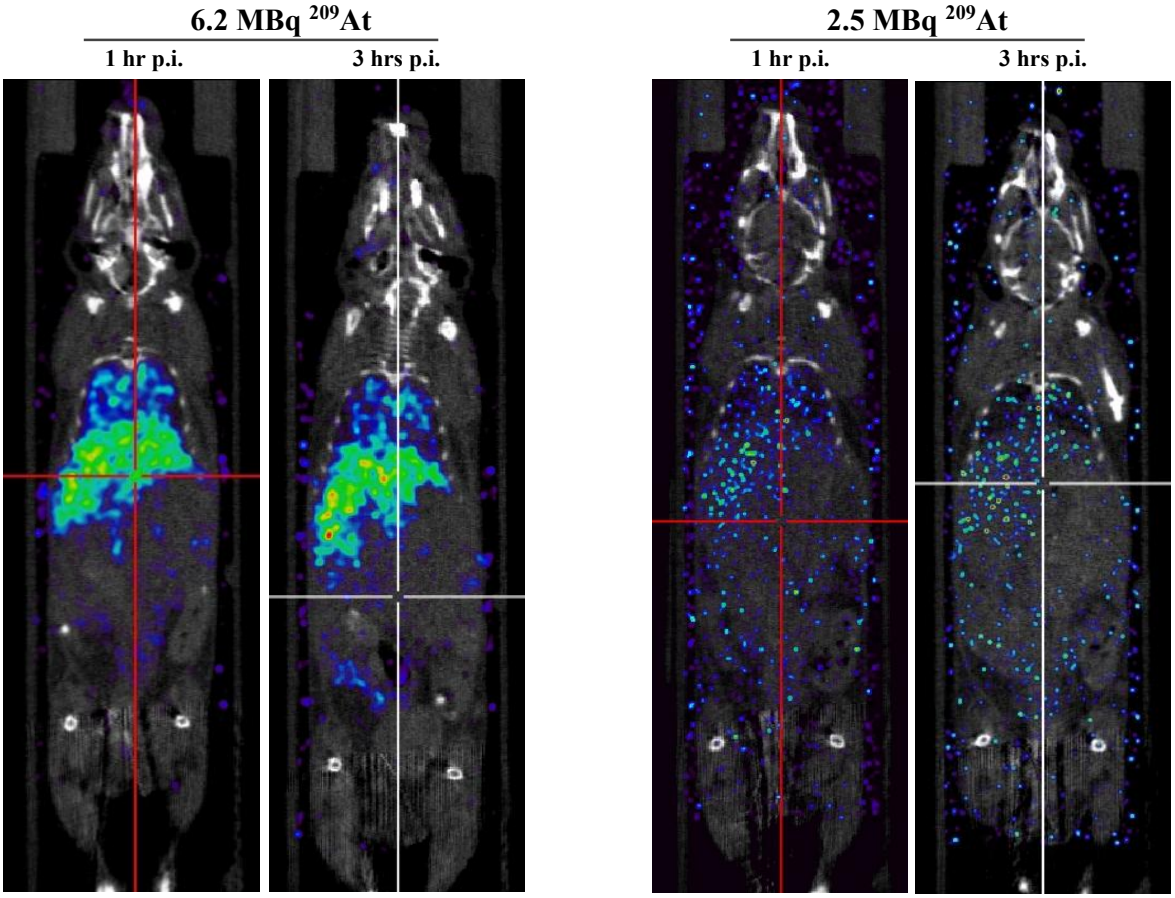

Figure 7.17: Comparison between SPECT image quality for high and low doses of injected ^{209}At activity. Fused SPECT/CT of the activity distribution of ^{209}At-labelled protein (damaged BC8) in normal mouse, reconstructed with the 77-90 keV X-ray photopeak, for two injected doses and measured at two time points (1 hr and 3 hrs, post-injection. The same animal was imaged for the same injected dose (n = 1 per dose).

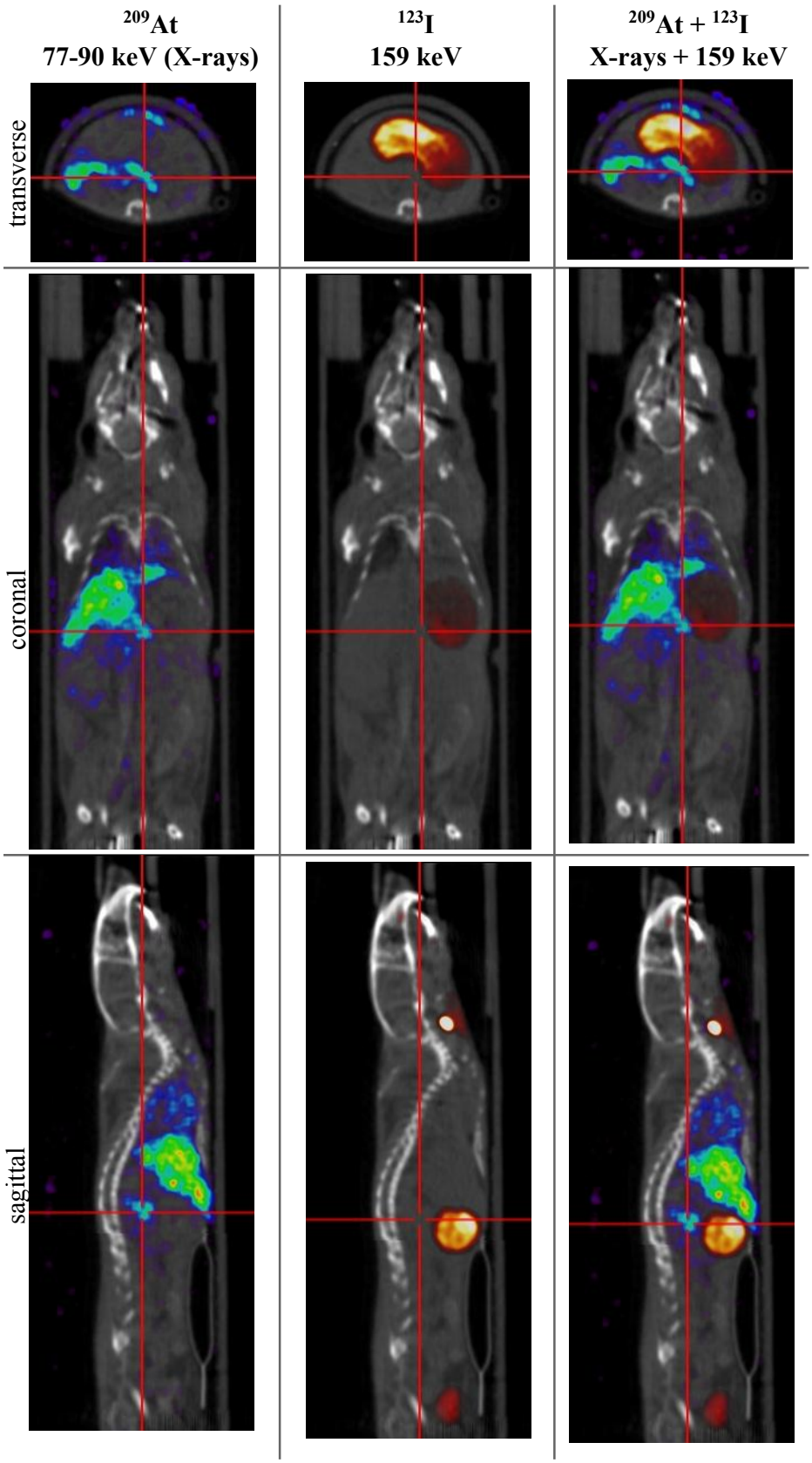

Figure 7.18: Simultaneously acquired, dual-isotope imaging of ^{209}At-labelled protein (damaged BC8) and free ^{123}I in a normal mouse. Fused SPECT/CT images are shown separately for the activity distributions of^{209}At-labelled BC8 (mAb) and free [^{123}I]iodide, separately and fused in combination. ^{209}At activity was reconstructed with 77-90 keV X-ray photopeak (colour = NIH = blue/green/yellow/red), ^{123}I was reconstructed with the 159 keV photopeak (colour = hot metal = black/red/orange/white).

Further discussion

These pilot studies have demonstrated the feasibility of small animal SPECT imaging with ^{209}At, a novel SPECT isotope for measuring astatine activity distributions, *in vivo*. Although still in active development, the novel, ISOL-based production methods for supplying ^{209}At demonstrated sufficient yields for enabling small animal SPECT imaging with this isotope. Beginning with natural uranium and ending with the measurement of ^{209}At activity distributions in a living organism, we demonstrated that the individual tasks of isotope production, purification, preparation, tracer shipment (from TRIUMF) and delivery (to CCM), and administration to the animal, could all be performed safely within a few hours (4-6 hours). This represented a great accomplishment in rapid tracer manufacturing and delivery by TRIUMF, with consideration to the time constraints for this process (posed by the 5.41 hour half-life of ^{209}At). Higher initial production yields should be expected in the future (up to 4 times higher[5]), which would enable more flexibility in the imaging studies, both for animal imaging and phantom imaging. With higher production yields, multiple tracers could be prepared and measured by SPECT imaging for a single production run. Cummulatively, these experiments suggest that injected activities of between 5-11 MBq ^{209}At will be optimal for whole-body imaging after administration to the venous bloodstream (in mice), for time points most significant to ^{211}At-based therapy research (up to 7.2 hours or one half-life of ^{211}At). At least 25 MBq would likely be required for imaging up to two half-lives of ^{211}At (14.4 hours). These are only guide lines for estimating the optimal injected dose; less activity may be required for SPECT scans of smaller volumes (e.g. activity leakage measurements following regional/local administration, etc). Ultimately, the optimum injected dose will depend on the specific animal model, tracer properties, desired timepoint(s), and scanning parameters (including the duration of scan (number of frames $\times$ frame time), the scanned volume (whole-body versus single organ or tumour, etc).

The *ex vivo* biodistribution measurements were a simple proof of principle experiment, and demonstrated how whole-organ astatine activity was measured quantitatively with ^{209}At. Compared to imaging, biodistribution studies could be performed with much less ^{209}At activity injected dose per animal. In turn, this means that larger scale biodistribution studies could be pursued with a single production run; biodistribution studies could likely be performed with as little as 0.5 MBq of ^{209}At per animal, permitting future biodistribution measurements of multiple animals and multiple time points, even with current production yields for ^{209}At at ISAC.

Small animal (mouse) imaging was performed using whole-body scans, and Static image reconstruction was used when assessing these images, without decay correction for

[5]The current production yields for ^{209}At at ISAC are only 25% of the theoretical maximum and further optimization will be pursued in the future.

individual acquisition frames. This was considered appropriate for evaluating the dependence of image quality on photopeak energy, but insufficient for image-based dosimetry. If the imaging volume were to be reduced (e.g. only the thorax and/or abdomen), the total number of detected counts in these regions could be still be sufficient for image reconstruction even for shorter frame duration, as each frame would require less bed positions. Even shorter-timed scans (lower number of bed positions) could be completed for single organs (e.g. stomach) or other small targets (e.g. solid tumours). Shortening scan duration would be useful for accurately approximating instantaneous activity distribution and dose rate for a given time point. In principle, the integral dose could be calculated by sequential measurements of dose rate over time, for which ^{209}At SPECT imaging would be a powerful quantitative tool for image-based dose calculation. Applications of dose calculation by ^{209}At SPECT imaging will require further assessment, to be pursued as future work.

For whole-body mouse SPECT scans, superior image quality was obtained by X-ray photopeak reconstructions, compared to images reconstructed with the 545 keV photopeak, in general. One exception to this was the image quality of the Jasczczak phantom, where the 545 keV photopeak was more representative of the physical ^{209}At distribution, at resolutions above 1.3-1.7 mm. Additionally, the quantification of voxel activity was shown to be more accurate for 545 keV reconstructed images (compared to X-ray reconstructed images), but only determined in one study. Based on these factors, the 545 keV photopeak might be better for small volume scans, such as single organs or tumours, where the results must be quantified better, and the distribution more representative of the real, physical activity distribution.

Unfortunately, no experimental comparison was made between ^{209}At and ^{211}At, due to the fact that ^{211}At was not available in suitable quantities at TRIUMF. The production yields for ^{211}At at TRIUMF were simply too low for imaging. Imaging studies with ^{211}At are planned for the future, for a similar set of SPECT imaging measurements. This will help determine if any advantages can be obtained from the distinct emission spectrum of ^{209}At, compared to ^{211}At. These experiments indicated that detection and image reconstruction with X-rays was meaningful for determining the activity distributions of ^{209}At. It is interesting to note that electron decay of both ^{209}At and ^{211}At leads to nearly the same set of promptly emitted Po X-rays (Table 5.1), which would present as the only imageable energy window for ^{211}At image reconstruction. In contrast to the high energy collimator required for ^{209}At imaging with VECTor/CT, optimal SPECT imaging of ^{211}At is expected to be achieved with the low energy, higher sensitivity collimators available for this system. For this reason, it is impossible (or misleading) to speculate on the imaging potential of ^{211}At with VECTor/CT, in the absence of experimental measurements. It can be expected that the sensitivity of the detector to X-rays will be increased, but not

known to what extent. The most important factor that remains to be determined is how much ^{211}At is required for producing image quality comparable to that obtained for ^{209}At, and if this amount will exceed therapeutic and/or lethal doses for ^{211}At in small animals.

Chapter 8

Peptide Labelling with I/^{123}I Surrogates for ^{211}At

This chapter summarizes a set of supplementary experiments geared toward developing a new method for astatinating octreotate, a peptide of interest in several targeted treatments of cancer. For this effort, isotopes of iodine were used as surrogates for ^{211}At for the purpose of developing the chemistry and performing an inital assessment.

Background

Peptides are also expected to play an important role in future clinical applications with ^{211}At; the short biological half-life and rapid organ uptake of most peptides is suitably matched to the physical half-life of ^{211}At (on the order of hours as oppose to minutes or days) [6]. Compared to large proteins such as mAb, peptides diffuse more readily and rapidly through cell clusters and are expected to provide more homogeneous dose distributions to tumour cell clusters and even large tumours [129]. Clinical pilot studies have already demonstrated the possibility of targeting α-particle radiation with peptides, in the cases of (i) ^{213}Bi-DOTA-substance P targeting neurokinin type 1 receptors for treating glioblastoma multiform (brain tumours) [130], and (ii) ^{213}Bi-DOTA-Octreotide (DOTA-TOC, somatostatin analogue derivative) targeting somatostatin receptors over-expressed by many neuroendocrine tumours [131]. With respect to the latter study, regional administration was used and induced tumour remission was observed, while therapy with beta emitters (i.e. ^{177}Lu) was ineffective (dose-limited) for these patients. Moreover, preclinical studies have reported that α-emissions from ^{213}Bi are more effective in treating human neuroendocrine tumour cells, compared to β-emissions of ^{177}Lu, when compared at the same absorbed dose [132].

Another somatostatin analogue with high specificity for Somatostatin receptor type 2a (sstr2a), octreotate (TATE), has been labelled with ^{211}At and evaluated in a preclinical study [133]. Labelling with either radioiodine or ^{211}At was performed with an indirect approach by first labelling an aryl carbon intermediate, followed by its conjugation with the N-terminus, analogous to the Zalutsky method (tin precurser). Radioiodinated octreotate

was shown to retain high binding affinity (Ki= 4.8 nM, see Equation 8.1). Although high tumour cell internalization was observed for these radiopeptides, high liver and kidney uptake have also been reported, suggesting that regional administration of treatment will be necessary [133].

BCCA is currently studying the use of octreotide derivatives (including octreotate) for diagnostic imaging with ^{68}Ga (positron emitter) and radionuclide therapy with ^{177}Lu (β-emitter). With these foundations at BCCA, this work hypothesized that the addition of a boron cage to octreotate would provide a direct method of labelling and result in high *in vivo* stability of the radiopeptide while sufficiently preserving binding affinity for cancer cell targeting. The novel approach to labelling octreotate was to conjugate octreotate with B10-NCS (the *closo*-decaborate moiety developed at UW for ^{211}At labelling, described in §2.3). Once prepared, modified peptides were labelled with iodine and evaluated with respect to binding affinity, tumour targeting efficacy, and *in vivo* stability.

Peptide modifications for labelling

In preparation for astatine and iodine labelling, a modified version of octreotate (TATE) was constructed by conjugating the B10-NCS moiety to the N-terminus of TATE (molecule of 8 amino acids: H-D-Phe-Cys-Phe-D-Trp-Lys-Thr-Cys-Thr-OH, MW = 1050 g/mol). To prevent conjugation of B10-NCS to the free NH_2 belonging to the lysine residue of TATE, Lys(Dde[1]) was used at the time of peptide synthesis, performed at BCCA using solid-phase peptide synthesis[2], producing TATE(Dde). In addition, an alternate PEGylated version of TATE(Dde) was prepared whereby PEG_2[3] (terminated by NH_2) was added to the N-terminus of TATE(Dde) at the time of solid phase synthesis, producing in PEG_2-TATE(Dde). The inclusion of PEG_2 was in order to reduce (or eliminate) possible steric effects between B10 and TATE. Synthesized peptide derivatives (shown in Figure 8.1) were cleaved from the resin with trifluoroacetic acid (TFA) and shipped to TRIUMF. The purity of starting materials, TATE(Dde) and PEG_2-TATE(Dde), were confirmed by reverse-phase High Performance Liquid Chromatography (HPLC), using a C18 Jupiter column (250x4.6 mm, Phenomenex, Torrance, CA) and 0.05 M triethylammonium acetate (TEAA) and methanol (MeOH); solvent gradient of 20% MeOH, 80% TEAA at t = 0 min, 100% MEOH at t = 15 min, with flow rate of 1 mL/min). HPLC was monitored by Ultra Violet (UV) light absorbance at 254 nm, shown in Figure 8.2.

B10-NCS, an phenethyl isothiocyanate, was not considered sufficiently stable to be supplied directly (from UW to TRIUMF). An aniline derivative with greater stability,

[1]Dde (N-(1-(4,4-dimethyl-2,6-dioxocyclohexylidene)ethyl) is a common *protecting group*, used to prevent undesired cross reactions with free NH_2 groups.

[2]In solid-phase peptide synthesis, peptides are synthetically manufactured by adding individual amino acids of a chain, in sequence, where the first amino acid remains continuously bound to a polystyrene resin.

[3]PEG_2 refers to the polyethylene glycol H−(O−CH_2−CH_2)n−OH) polymer chain, where n = 2.

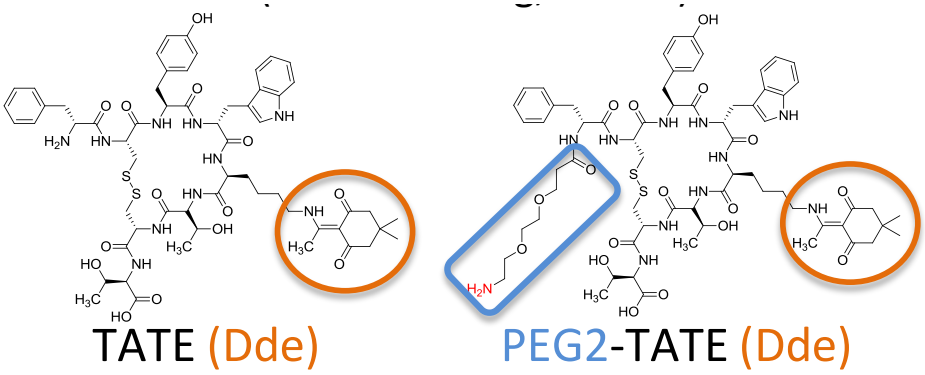

Figure 8.1: Molecular structures of TATE(DDe) and PEG_2-TATE(Dde), prepared at BCCA for conjugation to B10-NCS.

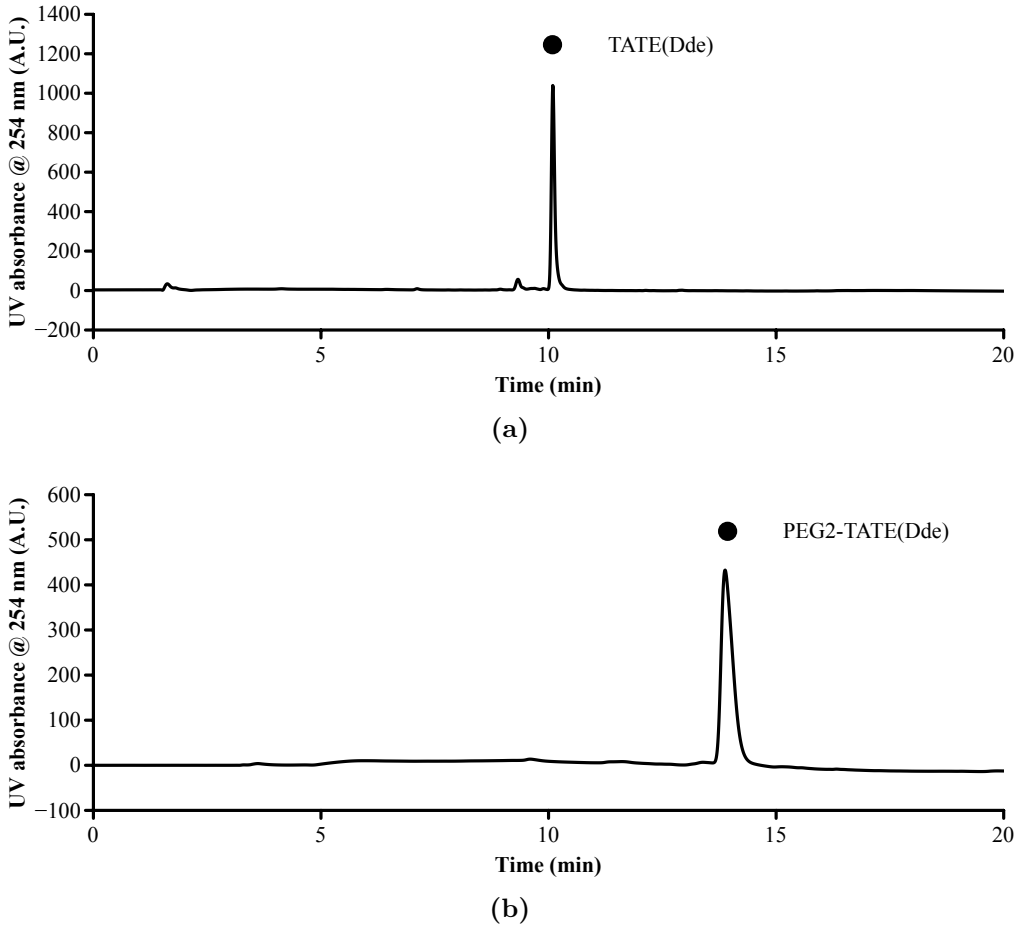

Figure 8.2: Reverse-phase HPLC (UV absorbance vs time) for (TATE(DDe)), used for conjugation reaction with B10-NCS.HPLC Conditions: C18 Jupiter column, 20% MeOH, 80% TEAA at t = 0 min, 100% MEOH at t = 15 min, 1 mL/min

B10-NH_2, was produced at the University of Washington and shipped to TRIUMF courtesey of Dr. Wilbur. Immediately before conjugation to TATE(Dde), B10-NH_2 was converted to B10-NCS by reaction with 1,1-thiocarbonyl-diimidazole, followed by washing with 10% EtOAc in hexanes. The conversion of B10-NH2 to B10-NCS is described in Figure 8.3. Conjugation of B10-NCS and TATE(Dde) (or PEG_2-TATE(Dde)) was com-

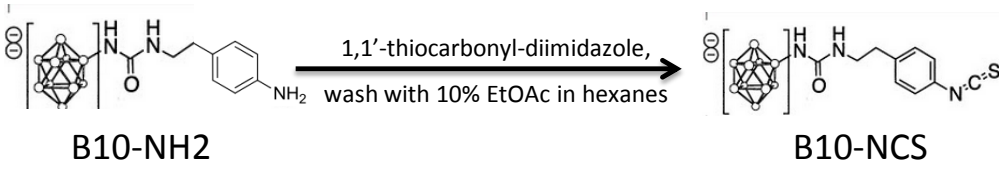

Figure 8.3: Preparation of closo-decaborate moiety from aniliine derivative (B10-NH2) to isothiocyanate derivative (B10-NCS), performed immediately before conjugation reaction with peptide.

pleted using a 3:1 (B10-NCS:peptide) molar equivalent ratio, with triethylamine in excess (in dimethylformamide (DMF)). The reaction proceeded for 24 hours, with constant stirring. HPLC elution time for the Dde protected product had changed significantly which indicated that the conversion of TATE(Dde) to B10-TATE had reached completion and was nearly quantitative. This was followed with deprotection of the peptide (removal of Dde) with hydrazine (2%) in DMF for 10 minutes.

The products of the conjugation reaction, either B10-TATE or B10-PEG_2-TATE, were evaluated with HPLC using the same solvent conditions and column as previously described for TATE(Dde) and PEG_2-TATE(Dde). The elution time was also slightly broader, as shown for B10-TATE(Dde) in Figure 8.4b. For purification, the Jupiter column was replaced with a monolithic column (100x4.6 mm, Phenomenex, Torrance, CA). The monolithic column provided a much sharper HPLC elution peak for collection/purification (Figure 8.4c). B10-TATE and B10-PEG_2-TATE were collected manually and HPLC solvent was removed by evaporation using centrifuge with vacuum until dried completely.

Non-radioactive (stable) iodinated versions of each peptide were produced, ^{nat}I-B10-TATE and ^{nat}I-B10-TATE, to function as surrogates for astatinated counterparts, to be evaluated for retention of binding affinity to sstr2a. Analogous to the antibody labelling reaction for astatine described in §4.5, B10-TATE and B10-PEG_2-TATE (Figure 8.5) were labelled with potassium iodide ($K^{nat}I$) by chloramine-T reaction (0.5 M phosphate buffer pH 6, 2 minute reaction quenched with $Na_2S_2O_5$), with KI supplied in excess (2 mol ^{nat}I per mol peptide). The labelled peptides were again purified with HPLC using the methods described above for unlabelled versions. Mass confirmation was performed by matrix-assisted laser desorption/ionization time of flight (MALDI/TOF) mass spectometry (at the Department of Chemistry, UBC), with measured masses of each molecule agreeing with within 0.1%of the expected (calculated) mass: B10-TATE (1386 g/mol), B10-PEG_2-

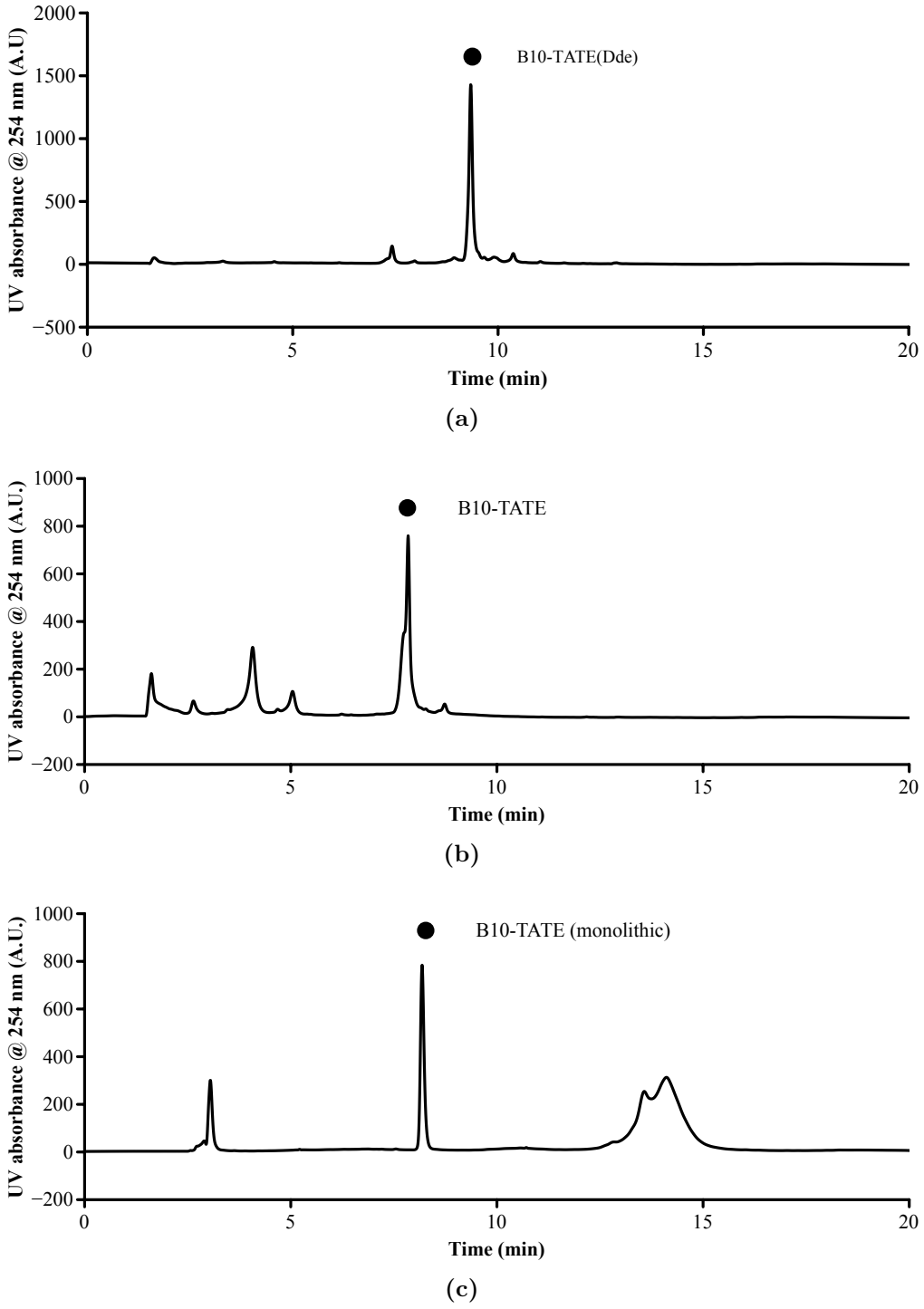

Figure 8.4: HPLC separation of B10-TATE conjugation reaction products for purification (UV absorbance @ 254 nm as a function of time). **(a)** B10-TATE(Dde), **(b)** B10-TATE on Jupiter column, and **(c)** B10-TATE on monolithic column. HPLC solvent gradient: 20% MeOH, 80% TEAA at t = 0 min, 100% MEOH at t = 15 min, 1 mL/min.

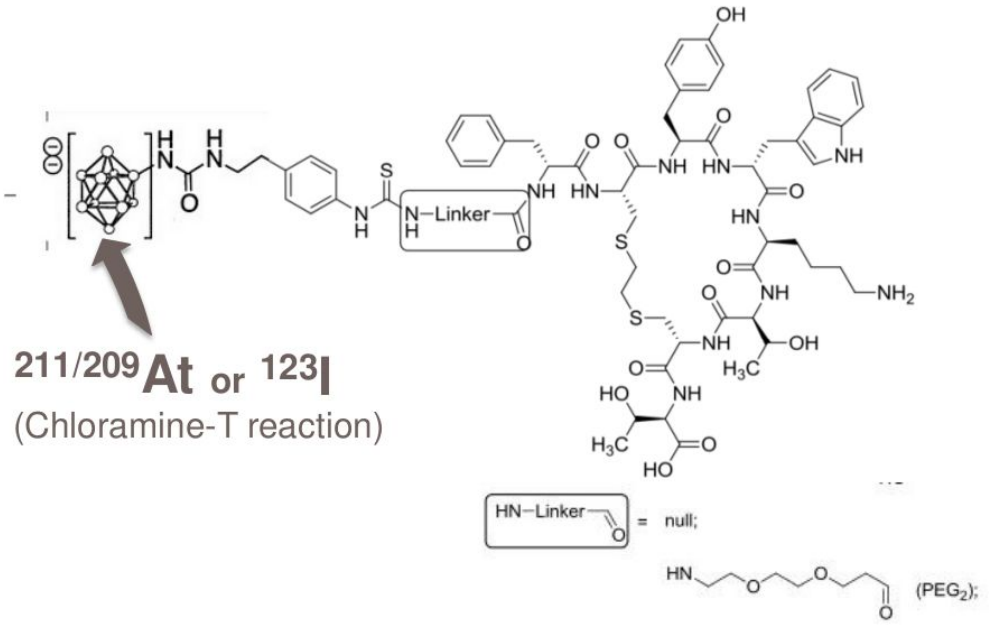

Figure 8.5: Octreotate derivatives with attached *closo*-decaborate moieties, prepared for astatine/iodine labelling.

TATE (1546 g/mol), I-B10-TATE (1513 g/mol), and I-B10-PEG$_2$-TATE (1673 g/mol).

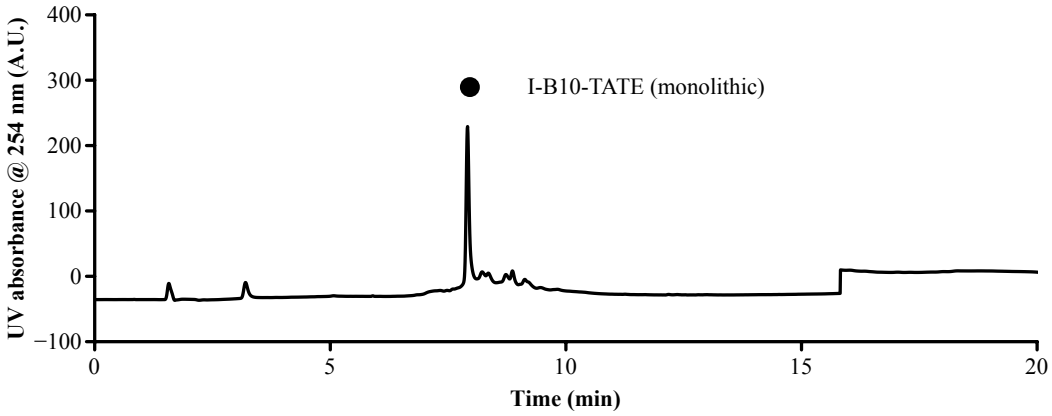

Figure 8.6: HPLC separation of I-B10-TATE iodine labelling reaction (UV absorbance @ 254 nm vs time).HPLC Conditions: monolithic column, 20% MeOH, 80% TEAA at t = 0 min, 100% MEOH at t = 15 min, 1 mL/min.

Competitive binding assays

For octreotate, the addition of the relatively large B10 moiety (with or without subsequent iodination) presented a significant change to the molecular structure and loss of binding affinity for the sstr2a receptor was certainly possible. To determine the binding affinity of the modified peptides, competitive binding assays were perform for both the modified octreotate derivatives (B10-TATE and B10-PEG2-TATE), as well as their respective

iodinated versions (I-B10-TATE and I-B10-PEG_2-TATE). The competitive binding assay was performed at BCCRC (In collaboration with Dr. Francois Benard), by Iulia Dude (UBC graduate student), for each peptide type individually. In this method, the binding affinity of each peptide was measured as its inhibitory effect on the binding of a radioactive standard sstr2a agonist; briefly, the sstr2a receptor, introduced as purified membrane from CHO-k1 cells overexpressing sstr2a (Perkin Elmer, Woodbridge, ON), was combined with a radioactive standard, ^{125}I-Tyr^{11}-somatostatin-14 (sstr2a agonist), as well as various concentrations of each tested peptide. Incubation was done at 27°C with moderate shaking. After 1 hour incubation, a vacuum manifold was used to condense the membranes onto filters, and then the amount of ^{125}I standard (as bound to the sstr2a receptors of the membrane) was measured by gamma counter to quantify the inhibitory effect of the tested peptide.

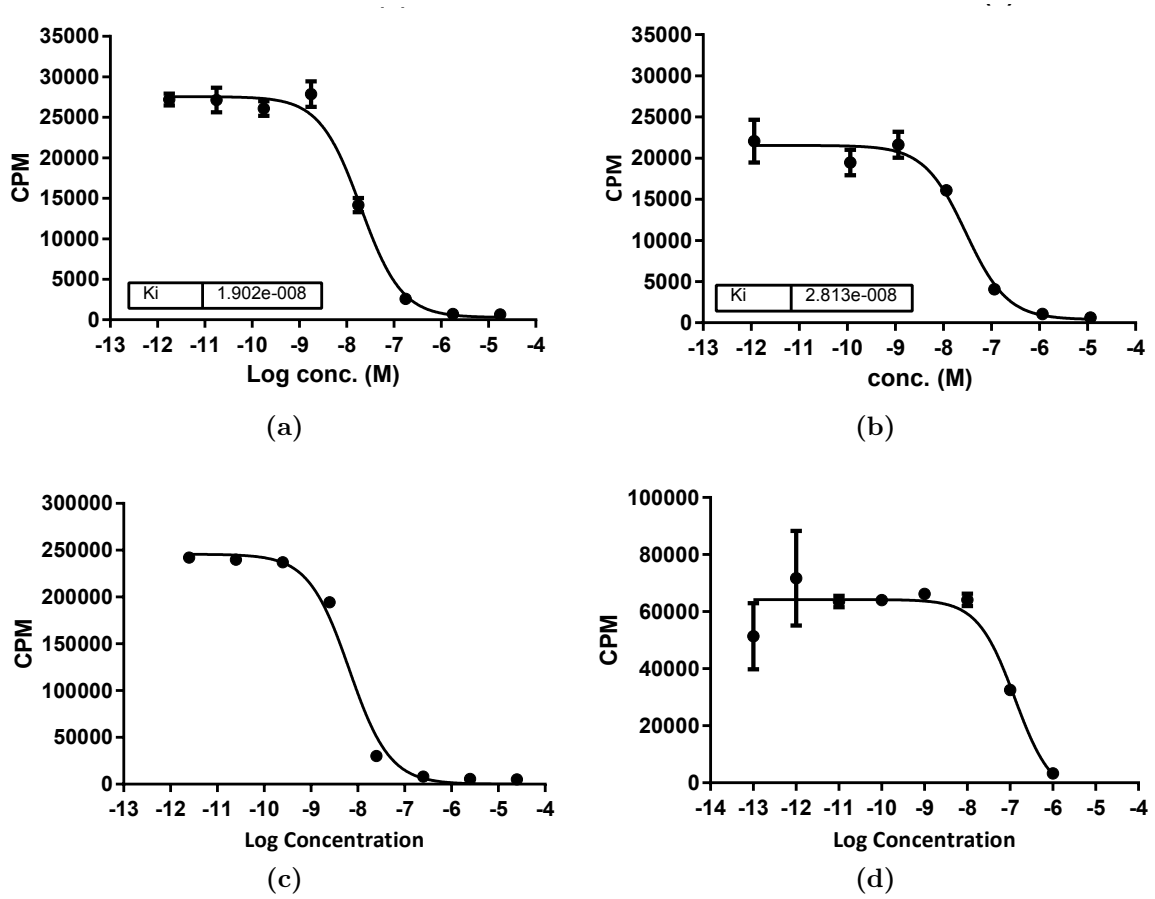

Figure 8.7: Competitive binding assays for octreotate derivatives prepared with attached **closo**-decaborate moieties: *(a)* B10-TATE, **(b)** I-B10-TATE, **(c)** B10-PEG_2-TATE, and **(d)** I-B10-PEG_2-TATE.

Based on counted ^{125}I activity on the to sstr2a receptors membrane, the binding affinity of each octreotate derivative was quantified in terms of the inhibitory constant,

K_i, as defined in Equation 8.1):

$$K_i = \frac{IC_{50}}{1 + F/K_d} \tag{8.1}$$

where IC_{50} was the concentration of each ligand required to inhibit the binding of the standard by 50% of its maximum value, F was the concentration of the standard, and K_d was the concentration of the standard at half-maximal binding. K_i values determined this way are tabulated in Table 8.1 for each of the evaluated octreotate derivatives. By definition, K_i values decreased as the binding affinity of the ligand increased. IC_{50} depended on the binding affinity of the radioactive standard, while K_i did not and thus provided a suitable metric for making comparisons in regards to absolute binding. The octreotate derivatives evaluated by this work were compared to others measured by BC-CRC, previously established for ^{nat}Ga-DOTA-TATE (K_i = 1.4 ± 0.3 nM, n=3) and somatotatin 1-28 (K_i = 3.7 ± 1.7 nM, n=5), both of which demonstrated high binding affinity (unpublished data).

Table 8.1: K_i values of the boron-cage containing octreotate derivatives (for sstr2a), with comparison to previously established values for other peptides with high affinity.

sstr2a agonist (ligand)	K_i
Previously measured (controls)	
^{nat}Ga-DOTA-TATE	1.4 ± 0.3 nM, n=3
Somatotatin 1-28	3.7 ± 1.7 nM, n=5
Derivatives without iodination	
B10-TATE	19 nM, n=1
B10-PEG2-TATE	4.6 nM, n=1
Derivatives with with iodination	
^{nat}I-B10-TATE	28 nM, n=1
^{nat}I-B10-PEG2-TATE	110 nM, n=1

Regarding the octreotate derivatives without iodination, it was found that the K_i of B10-TATE was roughly an order of magnitude higher compared to the controls, indicating a significant loss of binding affinity. In contrast, high binding affinity was preserved for B10-PEG_2-TATE, for which the measured K_i value was comparable to the controls. these results suggested that the PEG_2 reduced the amount of interference between the B10 moiety and octreotate observed for B10-TATE (possibly a steric effect). This may have simply been the result of the physical separation of B10 and TATE provided by the PEG_2 linker. Although it is possible that extending this linker with additional PEG groups (e.g. replacing PEG_2 with PEG_4), the PEG_2 appeared to provide at least sufficient retention of binding affinity.

The sstr2a binding affinity of I-B10-TATE and I-B10-PEG_2-TATE were both relatively low, compared to the controls. It was observed that I-B10-TATE binding affinity was only marginally lower than that of B10-TATE (also poor binding). In contrast, I-B10-PEG_2-TATE binding affinity was reduced by nearly two orders of magnitude. Such a significant difference between iodinated and non-iodinated versions of B10-PEG_2-TATE was unlikely to be caused by the addition of iodine, itself, which was a modest molecular change to relative to the addition of the B10 moiety. Product impurities in samples of I-B10-PEG_2-TATE was also a potential cause for the major loss of receptor binding affinity. The chloramine-T reaction used for iodination may have produced side reactions that may not have been removed during HPLC purification. Unintended, detrimental effects of the labelling reaction were not further evaluated by these experiments but may be a critical consideration for future work in this area.

Preparation of radiopeptides (^{123}I-B10-PEG_2-TATE)

Free [^{123}I]iodide was purchased from MDS Nordion (Vancouver, Canada), and used to label B10-PEG_2-TATE. Activity was measured with a Capintec dose calibrator (Capintec Inc, Ramsey, NJ, USA), using the designated setting for ^{123}I. Briefly, 320 MBq of ^{123}I in 30 μL aqueous solution[4] was added to a mixture of 0.5 M phosphate buffer (60 μL, pH 5.8) and B10-PEG_2-TATE (1600 ng in 20 μL). The labelling reaction was subsequently started with addition of chloramine-T (10 μL, 1 mg/mL) and proceeded for 2 minutes before stopping with addition of $Na_2S_2O_5$ (10 μL, 1 mg/mL). For product purification, the completed reaction solution was loaded to a disposable reverse-phase tC2 Sep-Pak© cartridge (Waters , Elstree, Hertfordshire, England), prewashed with 10 mL MeOH followed by 10 mL H_2O. The loaded cartridge was then washed with 1 mL H_2O, eluting any free ions. Elution of ^{123}I-B10-PEG_2-TATE was done in two 0.3 mL fractions of MeOH. The ^{123}I-B10-PEG_2-TATE in MeOH was then rapidly dried by vacuum pump at 80°C, with a gentle flow of N_2. ^{123}I-B10-PEG_2-TATE was reconstituted in 0.44 mL phosphate buffered saline (pH 7.4, 0.137 mol/L NaCl), and measured again by dose calibrator. Labelling efficiency was 50% (160 MBq ^{123}I, without decay correction), with the entire procedure taking less than 1 hour. Specific activity was not measured directly. Given the initial amount of B10-PEG_2-TATE (1600 ng), specific activity was at least 100 MBq/μg. This value of specific activity was considered consistent (and acceptable) with the specific activity required for SPECT evaluations of octreotide derivatives in mouse tumour models, without saturating somatostatin receptors (in accordance to ongoing imaging studies at BCCA).

[4] ^{123}I was initially supplied in 15 μL0.1 N NaOH and then brought to pH 7 with addition of 0.1 N HCl.

Small animal SPECT imaging study

^{123}I-B10-PEG$_2$-TATE was evaluated by SPECT imaging in a small animal tumour model with expression of the sstr2a receptor. Four NSIL2RKO (immune compromised) male mice were inoculated by subcutaneous injection at the shoulder with 5×10^6 HEK-293 cells transfected with the sstr2a receptor (HEK-293::sstr2a, positive for somatostatin receptor type 2a). Once tumours had grown approximately 250 cm^3 (measured by diameter of roughly spherical tumour), the mice were transferred from the BCCRC to the UBC CCM, in preparation for small animal SPECT.

Three mice were intravenously injected with 37 MBq of ^{123}I-B10-PEG$_2$-TATE (100 μL, over 95 MBq/μg) via tail-vein. One mouse was injected with 50 MBq of free [^{123}I]iodide, also 1 hour post-injection via tail-vein. SPECT scanning was performed for each mouse at 1 hour and 3.5 hours, with the MILabs VECTor/CT (microSPECT/PET/CT) small animal imaging system (located at CCM). See Chapter5, §5.1 for a description of this SPECT system. All scans were performed using the high resolution SPECT collimator (1.5 cm tungsten, focussed pinhole geometry, 75 pinholes, 1.5 mL central field of view.). All scans were completed with 7 frames, 5 minutes per frame). Images were reconstructed using the 159 keV photopeak of ^{123}I with 0.2x0.2x0.2 mm voxel size and triple energy scatter correction. Analogous to the image processing described in §5.1, SPECT image data sets were smoothed with a Guassian filter (1 mm FWHM, kernel size 7x7x7) and resampled to the CT voxel-size (0.16mmx0.16mmx0.16mm) by trilinear interpolation.

Based on SPECT imaging, uptake of free ^{123}I (iodide) was observed primarily in the thyroid, stomach, and bladder, as expected (Figure 8.8a). The representative activity distributions of ^{123}I-B10-PEG$_2$-TATE are shown in Figures 8.8b (1 hour post-injection) and 8.8c (3.5 hours post-injection). Unfortunately, significant tumour uptake of ^{123}I-B10-PEG$_2$-TATE was not observed at either time point, and this result was consistent for all 3 mice evaluated by SPECT. Multiple factors could have resulted in this lack of tumour uptake: The labelling of B10-PEG$_2$-TATE with ^{123}I may have strongly impacted its binding affinity for the sstr2a receptor. In addition, the reaction for radiolabelling could have resulted in side reactions involving other locations of the peptide (other than the boron-cage) that were important to binding affinity, essentially damaging the peptide to the degree that it lost its binding affinity.

At 1 hour post-injection, uptake was observed primarily liver, kidneys and bladder. At 3.5 hours, the majority of ^{123}I activity was easily identified in the kidneys. This bioditribution was consistent with nonspecific uptake for filtering organs by peptides, also observed for other radiolabelled somatostatin analogues. Importantly, mice injected with ^{123}I-B10-PEG$_2$-TATE did not show ^{123}I activity in the stomach or thyroid. Two important conclusions can be drawn from this result: First, the radiolabelling of ^{123}I-B10-PEG$_2$-TATE demonstrated high *in vivo* stability. With respect to binding affinity,

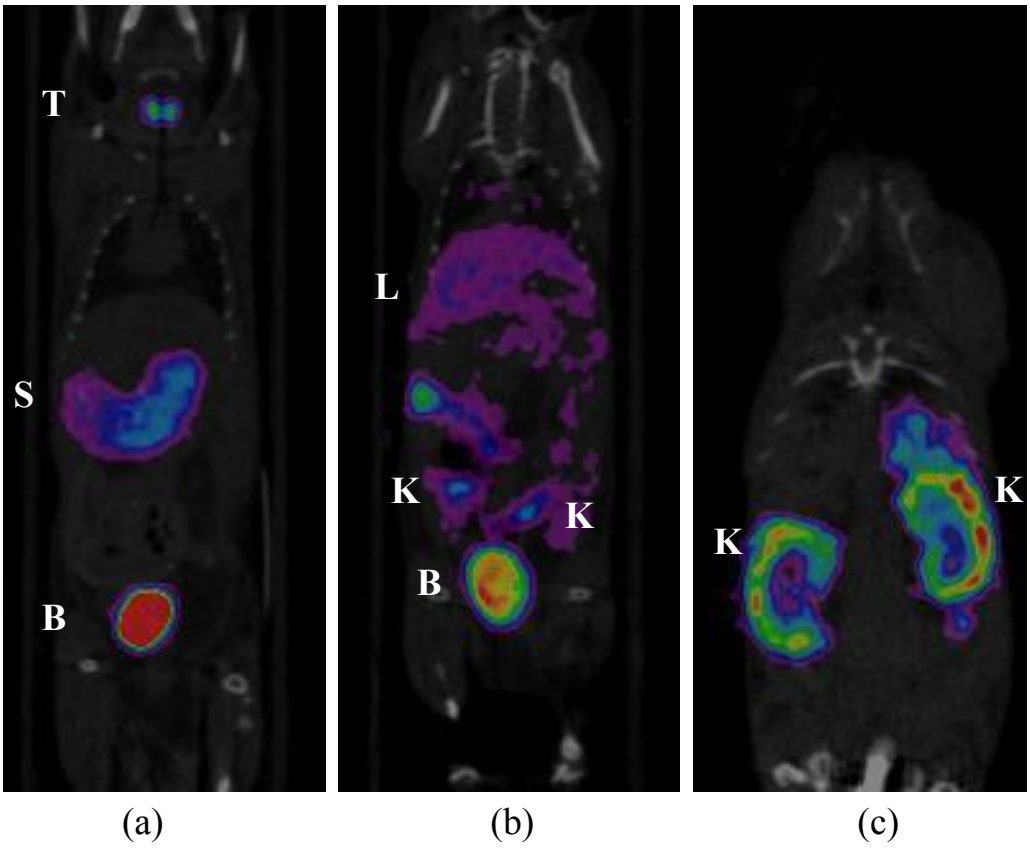

Figure 8.8: Fused SPECT/CT of ^{123}I activity distributions in a sstr2a positive mouse tumour model, following injection of (a) free ^{123}I (iodide), (b) ^{123}I-B10-PEG$_2$-TATE (1 hour p.i.), and (c) ^{123}I-B10-PEG$_2$-TATE (3.5 hour p.i.). Image reconstruction at 159 keV. Biodistribution labels: B=bladder, K=kidney, L=liver, S=stomach, T=thyroid.

this validated the use of B10 as a bifunctional synthon (linker) between the peptide and iodine. This result supported the hypothesis that high *in vivo* stability would also be achieved with $^{211/209}$At-B10-PEG$_2$-TATE, given the close similarity in biodistributions for other biomolecules labelled with either iodine or astatine using a *closo*-decaborate moiety [61]. Second, the lack of thyroid and stomach uptake normal for iodide provided confirmation that all (or nearly all) of the injected activity of ^{123}I was indeed bound, without a significant fraction of free ^{123}I present. This validated the use of the tC2 Sep-Pak© for purification of the labelled peptide. The ease of use of this purification will be highly advantageous for future translation of these methods to astatine labelling, where the methods can be easily and rapidly performed inside a hotcell or fumehood of the radiochemistry laboratory. This animal imaging study was repeated using ^{123}I-B10-TATE which produced very similar results with respect to the biodistribution, in general. Full analysis of this second animal study was not completed due primarily to time constraints for this work.

Discussion

Therapeutic developments with astatine are limited by the short half-lives of its isotopes and limited production resources. For the series of experiments presented in this chapter, iodine isotopes (radioactive and non-radioactive) were utilized as surrogates for astatine in pursuing preclinical experiments related to ^{211}At-based therapy. Although the properties of iodine surrogates do not fully describe their astatine counterparts, the use of iodine for this purpose is an accessible, relatively inexpensive method for evaluating several techniques that may have applications to ^{211}At. This is especially the case when assessing applications where radiolabelling is done with a boron-cage, given the high stability provided by this group to both iodine and astatine, alike.

The good *in vitro* binding affinity of B10-PEG$_2$-TATE indicated that the bioconjugate strategy worked, and that including the PEG$_2$ linker was important (in comparison to B10-TATE). The preparation of octreotate derivatives with *closo*-decaborate groups provided a method for direct labelling with iodine. The radiochemistry procedures were rapid and well-suited for use with astatine isotopes (^{211}At or ^{209}At), in general. However, low *in vitro* binding affinity and no *in vivo* tumour uptake may have been the result of factors related to the labelling reaction and purification.

Further development and validation of the labelling reaction conditions will be essential moving forward with this effort. One experiment would be to label B10-NCS with iodine before conjugation to PEG$_2$-TATE. This would eliminate TATE from the labeling reaction altogeher; however, this would not be effective for radiolabelling because of the long time (24 h) required for conjugation. Another choice may be to attempt labelling before Dde deprotection to determine if the order of these procedures is significant. It might also be possible to use a milder catalyst (e.g. N-iodosuccinimide), or avoid the use of an oxidizing agent altogether and rely on spontaneous binding of astatine to the boron-cage in the absence of a catalyst. These avenues for investigation offer some potential directions for future work.

Astatination of the ocreotate derivatives prepared by this work has not been attempted at this time. An important future experiment will be to evaluate the *in vivo* stability of ^{211}At-B10-PEG$_2$-TATE and determine if high stability is in fact achieved, as indicated by the radioiodinated surrogate. Similarly, yields for radiolabelling with ^{211}At still need to be evaluated. Although still in early development, these approaches to astatinating peptides are generalizable to other peptides having clinical potential for targeted α-therapy, further broadening the possibilities in treating cancer with ^{211}At.

Chapter 9

Conclusion

Thesis summary

The primary motivation for this doctoral research is that diffuse microscopic disease persists as the major medical problem for cancer treatment. This dissertation began by highlighting some of the therapeutic challenges for treating micrometastases with conventional forms of radiation therapy and chemotherapy, proposing TAT as having favourable properties for overcoming some of these challenges. Specifically, ^{211}At was identified as a strong candidate for many TAT applications, due primarily to its decay properties (compatible half-life with targeting vectors, high α-particle dose per decay), as well as the potential for curative therapies, shown to be possible in animal models of disseminated disease.

Fundamental strategies for harnessing the great potential for ^{211}At in medicine were presented: Chapter 2 discussed some of the methods that are used for targeting ^{211}At to cancer and how these have been successfully utilized in early clinical trials. Furthermore, concepts for ^{211}At dosimetry were introduced, emphasizing the important role theranostic imaging will have for patient-specific optimization of therapeutic efficacy with ^{211}At. Chapter 3 provided a summary of strategies for ^{211}At production, in which the ^{211}Rn/^{211}At generator system was described as an alternative to conventional methods, having benefits for wider distribution, while still being in early stages of development. The ISOL-based isotope production at ISAC was presented as a means for studying ^{211}Rn and At isotopes, with a description of the facility in relation to RIB production. The broad goal of this work was to develop new technologies for studying ^{211}At-based TAT, leveraging TRIUMF's powerful capabilities for producing rare isotopes. In addition to the aim of producing ^{211}Rn for ^{211}At production, this work also hypothesized and pursued the use of ^{209}At as an isotope-matched surrogate for theranostic imaging of ^{211}At.

Chapters 4 and 6 presented experiments designed to approach this task from the ground up, by designing an implantation and recovery strategy for producing ^{211}Rn and ^{209}At from mass separated beams of short-lived Ra and Fr ions, at ISAC. Dodecane

was found to be suitable for containing ^{211}Rn for later extraction of ^{211}At, presenting a practical approach to building a ^{211}Rn/^{211}At generator. ^{207}Po tracked with ^{211}At but was removed using a Te column for purifying the ^{211}At. Both the use of dodecane for trapping ^{211}Rn and Te columns for purifying At had been previously reported in the literature, but not in combination, and not with the radioactive inventory produced by ^{211}Fr and ^{211}Ra decay, as in these experiments. The ^{211}Rn/^{211}At generators were built out of syringes, which proved to be very practical (although possibly unorthodox) air-tight, isobaric vessels for manipulating, mixing, and extracting/sampling dodecane and aqueous solutions. Labelling experiments were performed for both the ^{211}At produced from the generator, as well as ^{209}At (recovered in solution directly from implantation targets).

Experiments presented in Chapters 5 and 7 were aimed to evaluate ^{209}At as a novel SPECT isotope for preclinical research with ^{211}At. Small animal SPECT with ^{209}At was shown to be feasible, using high energy collimation. Pilot studies in mice and phantoms demonstrated that the 77-90 keV photopeak provided the best signal for image reconstruction, showing good contrast for differentiating the uptake of different organs. Dual-isotope SPECT imaging with ^{209}At and ^{123}I was also successful, whereby the independent biodistributions of each isotope were indivdually reconstructed after simultaneous acquisition. Further theranostic approaches were taken in the experiments presented in Chapter 8. The labelling of TATE to I/^{123}I was performed with a boron-cage linking moiety (B10) specifically designed for attachment of ^{211}At. This study found that B10-PEG2-TATE showed retained good binding affinity for the target receptor (sstr2a), but that the labelling reaction significantly degraded this binding. This result was hypothesized to be due to the conditions of the labelling reaction, not the addition of iodine to the boron-cage. The experiments reported by this doctoral thesis make significant contributions to the knowledge base for ^{211}At-based TAT, in regards to ^{211}At production and theranostic imaging.

Future work

Progress in scientific research is incremental by nature and the results from these experiments present definite directions for future work. Discussion sections in Chapters 6-8 have already presented many suggestions for future work in some detail. Although the specific implantation/recovery methods to isotope production facilitated downstream experiments with ^{211}Rn and ^{209}At, it was found that the recovery efficiency for these measurements was low (approximately 25%). One hypothetical explanation that was offered was that the NaCl target was not an optimal material for ion beam implantation due to its electrical insulation during delivery. Potentially inaccurate RIB yield measurements (ions/s) were also suggested as a possible reason for lower than expected recovered yields. This work suggests to try electrically conducting target materials for implantation, such

as aluminum, to form a comparison with NaCl.

In regards to ^{211}At production by the ^{211}Rn/^{211}At generator at TRIUMF, the most immediate application is for preclinical scale ^{211}At production using direct implantations of mixed ^{211}Rn/^{211}At RIB. This will require demonstrating translation of the methods to this RIB and evaluating the implications to radiation safety, and could included considerations for shipping the generator. With respect to ^{209}At-SPECT imaging, this technology needs to be evaluated for its use in image-based dose calculations, as applied to preclinical evaluations of therapeutic efficacy with ^{211}At. Both of these planned future endeavours have been formally proposed in an application to Canadian Cancer Society Innovation to Impact Grant, currently in review. The eligibility for submitting an application to this competition for Phase 2 funding, in sequence with the initial Phase 1 funding from the CCS Innovation Grant, was based on the successful completion of the aims defined for Phase 1, as described by this work.

Final thoughts

For all experiments presented in this work, the collected data forming the basis of analysis was sparse; the difficulty in producing data was directly attributable to a reliance on the cutting-edge technologies offered by ISAC. The extremely powerful−exceptionally rare−isotope production capabilities of ISAC are a shared resource between experimenters, coming from many disciplines with a variety of scientific objectives, all of which are of high merit and high interest to humanity. This project was very fortunate that TRIUMF/ISAC was able to provide the radioactive ion beams on which the experiments critically depended. Throughout the course of this work, every effort was made to make the best use of the beam time that was allocated.

Personalized, patient-specific treatment of cancer is one of the major overarching goals of radiotherapy. This is true for both external beam radiation therapy and all internal radionuclide therapies, alike. With respect to personalized medicine, biomolecular targeting is known to be variable for patients, and represents an important degree of freedom for determining the suitability and planning of TAT treatments. In this regard, theranostic imaging offers noninvasive, patient-specific evaluation for pretreatment planning and dosimetric evaluations of delivered therapies. For therapeutic α-emitters, theranostic imaging will ultimately be extremely advantageous for understanding and thereby predicting therapeutic efficacy, when activity distributions are evaluated in the context of the underlying microdosimetry.

TAT is experimental at the present time, and some major developments are still required before its promising potential can be expanded and further utilized in the clinical setting. Although TAT is on the fringes of medical discovery, its potential is not a black or white issue. The medical possibilities with TAT fall into a grey area, for which the

limits of its clinical use will be continuously redefined. In this regard, TAT requires ongoing development from multiple experimenters who can address the subject from a variety of perspectives and resources. This is the hallmark of scientific discovery. The Canadian Cancer Society has recognized this, evidenced, in part, by providing funding for completion of the experiments presented in this work. The same can be said in regards to TRIUMF, BCCA, and the University of Victoria, who have also recognized the importance of TAT research and the important role that these institutions will have for its development, in Canada.

Bibliography

[1] Stabin, M. Nuclear medicine dosimetry. *Physics in Medicine and Biology* **51**, R187–202 (2006).

[2] Kircher, M. F., Hricak, H. & Larson, S. M. Molecular imaging for personalized cancer care. *Molecular Oncology* **6**, 182–195 (2012).

[3] Kramer-Marek, G. & Capala, J. The role of nuclear medicine in modern therapy of cancer. *Tumor Biology* **33**, 629–640 (2012).

[4] Bushberg, J. T., Seibert, J. A., Leidholdt, E. M. & Boone, J. M. *Essential Physics of Medical Imaging* (Lippincott Williams & Wilkins, Philadelphia, PA, 2012), third edn.

[5] Wallis, C. J., Saskin, R., Choo, R., Herschorn, S., Kodama, R. T., Satkunasivam, R., Shah, P. S., Danjoux, C. & Nam, R. K. Surgery versus radiotherapy for clinically-localized prostate cancer: a systematic review and meta-analysis. *European Urology* **70**, 21–30 (2016).

[6] Vaidyanathan, G. & Zalutsky, M. R. Astatine Radiopharmaceuticals: Prospects and Problems. *Current Radiopharmaceuticals.* **1**, 177–218 (2008).

[7] Kim, S. H., Karpeh, M. S., Klimstra, D. S., Leung, D. & Brennan, M. F. Effect of microscopic resection line disease on gastric cancer survival. *Journal of Gastrointestinal Surgery* **3**, 24–33 (1999).

[8] Young, M. E. J. *Radiological Physics* (H. K. Lewis Co. Ltd, London, England, 1983), third edn.

[9] Hall, E. J. *Radiobiology for the Radiologist* (Lippincott Williams and Wilkins, Philadelphia, PA, 2000), 5th edn.

[10] Sonntag, C. V. Free-Radical-Induced DNA Damage as Approached by Quantum-Mechanical and Monte Carlo Calculations : An Overview from the Standpoint of an Experimentalist. *Advances in Quantum Chemistry* **52**, 5–20 (2007).

[11] van der Kogel, A. & Joiner, M. *Basic Clinical Radiobiology* (Hodder Arnold, London, England, 2009), fourth edn.

[12] Nordsmark, M., Alsner, J., Busk, M., Overgaard, J. & Horsman, M. R. Hypoxia and radiation therapy. In *Hypoxia and Cancer*, 265–281 (Springer, 2014).

[13] Chambers, A. F., Groom, A. C. & MacDonald, I. C. Dissemination and growth of cancer cells in metastatic sites. *Nature Reviews Cancer* **2**, 563–572 (2002).

[14] Pantel, K., Cote, R. J. & Fodstad, Ø. Detection and clinical importance of micrometastatic disease. *Journal of the National Cancer Institute* **91**, 1113–1124 (1999).

[15] Szent-Györgyi, A. Cell-division and cancer. *Science* **149**, 34–37 (1965).

[16] Begg, A. C. Predicting response to radiotherapy: evolutions and revolutions. *International Journal of Radiation Biology* **85**, 825–836 (2009).

[17] Peters, L. J. Radiation therapy tolerance limits: For one or for all?-janeway lecture. *Cancer* **77**, 2379–2385 (1996).

[18] South, C., Partridge, M. & Evans, P. A theoretical framework for prescribing radiotherapy dose distributions using patient-specific biological information. *Medical Physics* **35**, 4599–4611 (2008).

[19] Schabel, F. Concepts for systemic treatment of micrometastases. *Cancer* **35**, 15–24 (1975).

[20] Marrett, L. D., De, P., Airia, P., Dryer, D., of Canadian Cancer Statistics 2008, S. C. *et al.* Cancer in canada in 2008. *Canadian Medical Association Journal* **179**, 1163–1170 (2008).

[21] Portenoy, R. K. & Lesage, P. Management of cancer pain. *The Lancet* **353**, 1695–1700 (1999).

[22] Mitchison, T. J. The proliferation rate paradox in antimitotic chemotherapy. *Molecular Biology of the Cell* **23**, 1–6 (2012).

[23] Currie, G. Eighty years of immunotherapy: a review of immunological methods used for the treatment of human cancer. *British Journal of Cancer* **26**, 141 (1972).

[24] Comparing antibody and small-molecule therapies for cancer. *Nature Reviews Cancer* **6**, 714–727 (2006).

[25] Brack, S. S., Dinkelborg, L. M. & Neri, D. Molecular targeting of angiogenesis for imaging and therapy. *European Journal of Nuclear Medicine and Molecular Imaging* 1327–1341.

[26] Strebhardt, K. & Ullrich, A. Paul Ehrlich's magic bullet concept: 100 years of progress. *Nature Reviews Cancer* **8**, 473–480 (2008).

[27] Williams, L. E., DeNardo, G. L. & Meredith, R. F. Targeted radionuclide therapy. *Medical Physics* **35**, 3062–3068 (2008).

[28] Volkert, W., Goeckeler, W., Ehrhardt, G. & Ketring, A. Therapeutic radionuclides: production and decay property considerations. *The Journal of Nuclear Medicine* **32**, 174–185 (1991).

[29] O'donoghue, J., Bardies, M. & Wheldon, T. Relationships between tumor size and curability for uniformly targeted therapy with beta-emitting radionuclides. *The Journal of Nuclear Medicine* **36**, 1902–1909 (1995).

[30] Reilly, R. M. *Monoclonal Antibody and Peptide-Targeted Radiotherapy of Cancer* (John Wiley and Sons, Inc., Hoboken, New Jersey, 2010).

[31] Raju, M., Eisen, Y., Carpenter, S. & Inkret, W. Radiobiology of α particles: III. cell inactivation by α-particle traversals of the cell nucleus. *Radiation Research* **128**, 204–209 (1991).

[32] Gudkov, S. V., Shilyagina, N. Y., Vodeneev, V. A. & Zvyagin, A. V. Targeted radionuclide therapy of human tumors. *International Journal of Molecular Sciences* **17**, 33 (2015).

[33] Siegel, J. A., Thomas, S. R., Stubbs, J. B., Stabin, M. G. *et al.* MIRD pamphlet no. 16: techniques for quantitative radiopharmaceutical biodistribution data acquisition and analysis for use in human radiation dose estimates. *The Journal of Nuclear Medicine* **40**, 37S (1999).

[34] Beylergil, V., Carrasquillo, J. A., Weber, W. A. & Larson, S. M. A historical perspective on the use of radionuclides for therapy. In *Therapeutic Nuclear Medicine*, 3–9 (Springer, 2013).

[35] Silberstein, E. B. Radioiodine: the classic theranostic agent. In *Seminars in Nuclear Medicine*, vol. 42, 164–170 (Elsevier, 2012).

[36] Allen, B. J., Raja, C., Rizvi, S., Li, Y., Tsui, W., Zhang, D., Song, E., Qu, C. F., Kearsley, J. & Graham, P. Targeted alpha therapy for cancer. *Physics in Medicine and Biology* **49**, 3703 (2004).

[37] Imam, S. K. Advancements in cancer therapy with alpha-emitters: a review. *International Journal of Radiation Oncology, Biology, Physics* **51**, 271–278 (2001).

[38] Zalutsky, M. R., Reardon, D. A., Pozzi, O. R., Vaidyanathan, G. & Bigner, D. D. Targeted alpha-particle radiotherapy with ^{211}At-labeled monoclonal antibodies. *Nuclear Medicine and Biology* **34**, 779–785 (2007).

[39] Vaidyanathan, G. & Zalutsky, M. R. Applications of ^{211}At and ^{223}Ra in targeted alpha-particle radiotherapy. *Current Radiopharmaceuticals.* **4**, 283–94 (2011).

[40] Schardt, D. & Elsässer, T. Heavy-ion tumor therapy: Physical and radiobiological benefits. *Reviews of Modern Physics* **82**, 383–425 (2010).

[41] Harvey, B. G. (Englewood Cliffs, New Jersey).

[42] Sgouros, G., Roeske, J. C., McDevitt, M. R., Palm, S., Allen, B. J., Fisher, D. R., Brill, a. B., Song, H., Howell, R. W., Akabani, G., Bolch, W. E., Meredith, R. F., Wessels, B. W. & Zanzonico, P. B. MIRD Pamphlet No. 22 (abridged): radiobiology and dosimetry of alpha-particle emitters for targeted radionuclide therapy. *The Journal of Nuclear Medicine* **51**, 311–328 (2010).

[43] Kassis, A. I., Harris, C. R., Adelstein, S. J., Ruth, T. J., Lambrecht, R. & Wolf, A. P. The in vitro radiobiology of astatine-211 decay. *Radiation Research* **105**, 27–36 (1986).

[44] Mirzadeh, S. Generator-produced Alpha-emitters. *Applied Radiation and Isotopes* **49**, 345–349 (1998).

[45] Zalutsky, M. R. & Pruszynski, M. Astatine-211: production and availability. *Current Radiopharmaceuticals.* **4**, 177–185 (2011).

[46] Beyer, G.-J., Miederer, M., Vranjes-Durić, S., Comor, J. J., Künzi, G., Hartley, O., Senekowitsch-Schmidtke, R., Soloviev, D. & Buchegger, F. Targeted alpha therapy *in vivo*: direct evidence for single cancer cell kill using ^{149}Tb-rituximab. *European Journal of Nuclear Medicine and Molecular Imaging* **31**, 547–554 (2004).

[47] Andersson, H., Cederkrantz, E., Bäck, T., Divgi, C., Elgqvist, J., Himmelman, J., Horvath, G., Jacobsson, L., Jensen, H., Lindegren, S., Palm, S. & Hultborn, R. Intraperitoneal alpha-particle radioimmunotherapy of ovarian cancer patients: pharmacokinetics and dosimetry of ^{211}At-MX35 F(ab')2–a phase I study. *The Journal of Nuclear Medicine* **50**, 1153–1160 (2009).

[48] Zalutsky, M. R., Reardon, D. A., Akabani, G., Coleman, R. E., Friedman, A. H., Friedman, H. S., McLendon, R. E., Wong, T. Z. & Bigner, D. D. Clinical experience with alpha-particle emitting ^{211}At: treatment of recurrent brain tumor patients with ^{211}At-labeled chimeric antitenascin monoclonal antibody 81C6. *The Journal of Nuclear Medicine* **49**, 30–38 (2008).

[49] Orozco, J. J., Bäck, T., Kenoyer, A., Balkin, E. R., Hamlin, D. K., Wilbur, D. S., Fisher, D. R., Frayo, S. L., Hylarides, M. D., Green, D. J., Gopal, A. K., Press, O. W. & Pagel, J. M. Anti-CD45 radioimmunotherapy using ^{211}At with bone marrow transplantation prolongs survival in a disseminated murine leukemia model. *Blood* **121**, 3759–3767 (2013).

[50] Turkington, T. G., Zalutsky, M. R., Jaszczak, R. J., Garg, P. K., Vaidyanathan, G. & Coleman, R. E. Measuring astatine-211 distributions with SPECT. *Physics in Medicine and Biology* **38**, 1121–1130 (1993).

[51] Johnson, E. L., Turkington, T. G., Jaszczak, R. J., Gilland, D. R., Vaidyanathan, G., Greer, K. L., Coleman, R. E. & Zalutsky, M. R. Quantitation of ^{211}At in small volumes for evaluation of targeted radiotherapy in animal models. *Nuclear Medicine and Biology* **22**, 45–54 (1995).

[52] Petrich, T., Helmeke, H.-J., Meyer, G., Knapp, W. & Potter, E. Establishment of radioactive astatine and iodine uptake in cancer cell lines expressing the human sodium/iodide symporter. *European Journal of Nuclear Medicine and Molecular Imaging* **29**, 842–854 (2002).

[53] Mirzadeh, S. & Lambrecht, R. Method for the simultaneous preparation of Radon-211, Xenon-125, Xenon-123, Astatine-211, Iodine-125 and Iodine-123 –*US Patent Publication* (1987).

[54] Ruth, T. J. The production of radionuclides for radiotracers in nuclear medicine. *Reviews of Accelerator Science and Technology* **2**, 17–33 (2009).

[55] Meyer, G. & Lambrechtg, R. M. Excitation function for the ^{209}Bi(7Li, 5n)^{211}Rn nuclear reaction. *The International Journal of Applied Radiation and Isotopes* **31**, 351–355 (1980).

[56] Ruth, T. J., Dombsky, M. & Dauria, J. M. Exploration of the production of Rn-211 as a source of At-211 via the TISOL facility. *Abstracts: Journal of the American Chemical Society* 205:69 (1993).

[57] Maeda, E., Yokoyama, A., Taniguchi, T., Washiyama, K. & Nishinaka, I. Extraction of astatine isotopes for development of radiopharmaceuticals using a ^{211}Rn-^{211}At generator. *Journal of Radioanalytical and Nuclear Chemistry* **303**, 1465–1468 (2014).

[58] Greene, J. P., Nolen, J. & Baker, S. Nickel-backed Bi targets for the production of ^{211}At. *Journal of Radioanalytical and Nuclear Chemistry* **305**, 943–946 (2015).

[59] Zalutsky, M. R. & Vaidyanathan, G. Astatine-211-labeled radiotherapeutics: an emerging approach to targeted alpha-particle radiotherapy. *Current Pharmaceutical Design* **6**, 1433–1455 (2000).

[60] Bloomer, W. D., Mclaughlin, W. H., Neirinckx, R. D., Adelstein, S. J., Gordon, P. R., Ruth, T. J., Wolf, A. P., Url, S. & Farber, J. L. Astatine-211–Tellurium radiocolloid cures experimental malignant ascites Astatine-211-Tellurium radiocolloid Cures experimental malignant ascites. *Advancement of Science* **212**, 340–341 (1981).

[61] Wilbur, D. S. [^{211}At]Astatine-labeled compond stability: issues with released [^{211}At]Astatide and development of labeling reagents to increase stability. *Current Radiopharmaceuticals.* **1**, 144–176 (2008).

[62] Petrich, T., Quintanilla-Martinez, L., Korkmaz, Z., Samson, E., Helmeke, H. J., Meyer, G. J., Knapp, W. H. & Pötter, E. Effective cancer therapy with the alpha-particle emitter [211At]astatine in a mouse model of genetically modified sodium/iodide symporter-expressing tumors. *Clinical Cancer Research* **12**, 1342–1348 (2006).

[63] Spetz, J., Rudqvist, N. & Forssell-Aronsson, E. Biodistribution and dosimetry of free 211At, 125I- and 131I- in rats. *Cancer Biotherapy and Radiopharmaceuticals* **28**, 657–664 (2013).

[64] Larsen, R. H., Slade, S. & Zalutsky, M. R. Blocking [211At]astatide accumulation in normal tissues: preliminary evaluation of seven potential compounds. *Nuclear Medicine and Biology* **25**, 351–357 (1998).

[65] Zalutsky, R. & Narula, A. S. Astatination of Proteins using an N-Succinimidyl Tri-n-Butylstannyl Benzoate Intermediate. *Applied Radiation and Isotopes* **39**, 227–232 (1988).

[66] Lindegren, S., Frost, S., Bäck, T., Haglund, E., Elgqvist, J. & Jensen, H. Direct procedure for the production of ^{211}At-labeled antibodies with an ϵ-lysyl-3-

(trimethylstannyl)benzamide immunoconjugate. *The Journal of Nuclear Medicine* 1537–1545.

[67] Aneheim, E., Jensen, H., Albertsson, P. & Lindegren, S. Astatine-211 labeling: a study towards automatic production of astatinated antibodies. *Journal of Radioanalytical and Nuclear Chemistry* **303**, 979–983 (2015). URL `http://link.springer.com/10.1007/s10967-014-3561-8`.

[68] Meyer, G. J., Walte, A., Sriyapureddy, S. R., Grote, M., Krull, D., Korkmaz, Z. & Knapp, W. H. Synthesis and analysis of 2-[211At]-L-phenylalanine and 4-[211At]-L-phenylalanine and their uptake in human glioma cell cultures in-vitro. *Applied Radiation and Isotopes* **68**, 1060–1065 (2010).

[69] Wilbur, D. S., Chyan, M.-K., Hamlin, D. K., Kegley, B. B., Risler, R., Pathare, P. M., Quinn, J., Vessella, R. L., Foulon, C., Zalutsky, M. *et al.* Reagents for astatination of biomolecules: comparison of the in vivo distribution and stability of some radioiodinated/astatinated benzamidyl and nido-carboranyl compounds. *Bioconjugate Chemistry* **15**, 203–223 (2004).

[70] Wilbur, D. S., Chyan, M.-K., Hamlin, D. K. & Perry, M. A. Preparation and in vivo evaluation of radioiodinated closo-decaborate(2-) derivatives to identify structural components that provide low retention in tissues. *Nuclear Medicine and Biology* **37**, 167–178 (2010).

[71] Wilbur, D. S., Chyan, M.-K., Hamlin, D. K., Nguyen, H. & Vessella, R. L. Reagents for astatination of biomolecules. 5. Evaluation of hydrazone linkers in ^{211}At- and ^{125}I-labeled closo-decaborate(2-) conjugates of Fab' as a means of decreasing kidney retention. *Bioconjugate Chemistry* **22**, 1089–1102 (2011).

[72] Pagel, J. M., Hedin, N., Subbiah, K., Meyer, D., Mallet, R., Axworthy, D., Theodore, L. J., Wilbur, D. S., Matthews, D. C. & Press, O. W. Comparison of anti-CD20 and anti-CD45 antibodies for conventional and pretargeted radioimmunotherapy of B-cell lymphomas. *Blood* **101**, 2340–2348 (2003).

[73] Jurcic, J. G. & Rosenblat, T. L. Targeted alpha-particle immunotherapy for acute myeloid leukemia. *American Society of Clinical Oncology educational book / ASCO. American Society of Clinical Oncology. Meeting* e126–e131 (2014).

[74] Bolch, W. E., Bouchet, L. G., Robertson, J. S. & Wessels, B. W. MIRD pamphlet No. 17: The dosimetry of nonuniform activity distributions–radionuclide S values at the voxel level. *The Journal of Nuclear Medicine* **40**, S11 (1999).

[75] Bolch, W. E., Eckerman, K. F., Sgouros, G. & Thomas, S. R. MIRD pamphlet No. 21: a generalized schema for radiopharmaceutical dosimetrystandardization of nomenclature. *The Journal of Nuclear Medicine* **50**, 477–484 (2009).

[76] Dewaraja, Y. K., Frey, E. C., Sgouros, G., Brill, A. B., Roberson, P., Zanzonico, P. B. & Ljungberg, M. MIRD pamphlet No. 23: quantitative SPECT for patient-specific 3-dimensional dosimetry in internal radionuclide therapy. *The Journal of Nuclear Medicine* **53**, 1310–1325 (2012).

[77] Stabin, M. G., Sparks, R. B. & Crowe, E. Olinda/exm: the second-generation personal computer software for internal dose assessment in nuclear medicine. *The Journal of Nuclear Medicine* **46**, 1023–1027 (2005).

[78] Grimes, J. *Patient-specific internal dose calculation techniques for clinical use in targeted radionuclide therapy.* Dissertation, Univeristy of British Columbia (2013).

[79] Bäck, T. & Jacobsson, L. The alpha-camera: a quantitative digital autoradiography technique using a charge-coupled device for ex vivo high-resolution bioimaging of alpha-particles. *The Journal of Nuclear Medicine* **51**, 1616–1623 (2010).

[80] Miller, B. W., Gregory, S. J., Fuller, E. S., Barrett, H. H., Bradford Barber, H. & Furenlid, L. R. The iQID camera: An ionizing-radiation quantum imaging detector. *Nuclear Instruments and Methods in Physics Research, Section A: Accelerators, Spectrometers, Detectors and Associated Equipment* 146–152.

[81] Branderhorst, W., Vastenhouw, B. & Beekman, F. J. Pixel-based subsets for rapid multi-pinhole SPECT reconstruction. *Physics in Medicine and Biology* **55**, 2023–2034 (2010).

[82] Shepp, L. A. & Vardi, Y. Maximum likelihood reconstruction for emission tomography. *IEEE Transactions on Medical Imaging* **1**, 113–122 (1982).

[83] Hutton, B. F., Hudson, H. M. & Beekman, F. J. A clinical perspective of accelerated statistical reconstruction. *Eur. The Journal of Nuclear Medicine* **24**, 797–808 (1997).

[84] Hudson, H. M. & Larkin, R. S. Accelerated image reconstruction using ordered subsets of projection data. *IEEE Transactions on Medical Imaging* **13**, 601–609 (1994).

[85] Corson, D., MacKenzie, K. & Segre, E. Artificially radioactive element 85. *Physical Review* **58**, 672 (1940).

[86] Hamilton, J. G. & Soley, M. H. A comparison of the metabolism of iodine and of element 85 (eka-iodine). *Proceedings of the National Academy of Sciences of the United States of America* **26**, 483–489 (1940).

[87] Wilbur, D. S., Vessella, R. L., Stray, J. E., Goffe, D. K., Blouke, K. A. & Atcher, R. W. Preparation and evaluation of para-[^{211}At]astatobenzoyl labeled anti-renal cell carcinoma antibody A6H F(ab)2; *in vivo* distribution comparison with para-[^{125}I]iodobenzoyl labeled A6H F(ab)2. *Nuclear Medicine and Biology* **20**, 917–927 (1993).

[88] Almqvist, Y. *Targeted Therapy in Colorectal Cancer. Preclinical Evaluation of a Radiolabelled Antibody.* Dissertation, Uppsala University (2008).

[89] Alfarano, A., Abbas, K., Holzwarth, U., Bonardi, M., Groppi, F., Alfassi, Z., Menapace, E. & Gibson, P. N. Thick target yield measurement of ^{211}At through the nuclear reaction ^{209}Bi(α, 2n). *Journal of Physics: Conference Series* **41**, 115–122 (2006).

[90] International Commission on Radiological Protection. *ICRP Publication 60: 1990 Recommendations of the International Commission on Radiological Protection.* 60 (Elsevier Health Sciences, 1991).

[91] Henriksen, G., Messelt, S., Olsen, E. & Larsen, R. H. Optimisation of cyclotron production parameters for the ^{209}Bi(α, 2n)^{211}At reaction related to biomedical use of ^{211}At. *Applied Radiation and Isotopes* **54**, 839–844 (2001).

[92] Larsen, R. H., Wieland, B. W. & Zalutsky, M. R. Evaluation of an internal cyclotron target for the production of ^{211}At via the ^{209}Bi(α,2n)^{211}At reaction. *Applied Radiation and Isotopes* **47**, 135–143 (1996).

[93] Zalutsky, M. R., Zhao, X. G., Alston, K. L. & Bigner, D. High-level production of α-particle-emitting ^{211}At and preparation of ^{211}At-labeled antibodies for clinical use. *The Journal of Nuclear Medicine* **42**, 1508–1515 (2001).

[94] Lindegren, S., Bäck, T. & Jensen, H. J. Dry-distillation of astatine-211 from irradiated bismuth targets: a time-saving procedure with high recovery yields. *Applied Radiation and Isotopes* **55**, 157–160 (2001).

[95] Schwarz, U. P., Plascjak, P., Beitzel, M. P., Gansow, O. a., Eckelman, W. C. & Waldmann, T. a. Preparation of ^{211}At-labeled humanized anti-Tac using ^{211}At produced in disposable internal and external bismuth targets. *Nuclear Medicine and Biology* **25**, 89–93 (1998).

[96] Yordanov, A., Pozzi, O., Carlin, S., Akabani, G., Wieland, B. & Zalutsky, M. Wet harvesting of no-carrier-added ^{211}At from an irradiated ^{209}Bi target for radiopharmaceutical applications. *Journal of Radioanalytical and Nuclear Chemistry* **262**, 593–599 (2004).

[97] Saha, G. B. *Physics and Radiobiology of Nuclear Medicine* (Springer Science & Business Media, 2012).

[98] Agostinelli, S., Allison, J., Amako, K. a., Apostolakis, J., Araujo, H., Arce, P., Asai, M., Axen, D., Banerjee, S., Barrand, G. *et al.* Geant4a simulation toolkit. *Nuclear Instruments and Methods in Physics Research Section A: Accelerators, Spectrometers, Detectors and Associated Equipment* **506**, 250–303 (2003).

[99] Lindroos, M. Review of ISOL-type radioactive beam facilities. *Proceedings of EPAC 2004, Lucerne, Switzerland* 45–49 (2004).

[100] Bricault, P., Baartman, R., Beveridge, J., Clark, G., Doornbos, J., Dutto, G., Hodges, T., Koscielniak, S., Root, L. & Schmor, P. ISAC-1: Radioactive ion beams facility at TRIUMF. In *Proceedings of the 1995 Particle Accelerator Conference*, vol. 1, 348–350 (IEEE, 1995).

[101] Dombsky, M., Bricault, P. & Hanemaayer, V. Increasing beam currents at the TRIUMF-ISAC Facility: techniques and experiences. *Nuclear Physics* **746**, 32c–39c (2004).

[102] Dombsky, M., D'Auria, J., Buchmann, L., Sprenger, H., Vincent, J., McNeely, P. & Roy, G. Target and ion source development at the TISOL facility at TRIUMF. *Nuclear Instruments and Methods in Physics Research Section A: Accelerators, Spectrometers, Detectors and Associated Equipment* **295**, 291–298 (1990).

[103] Bricault, P. Targets and ion sources development at ISAC-TRIUMF. In *Proceedings of LINAC 2006, Knoxville, Tennessee USA*, 823–827 (LINAC, 2006).

[104] Dombsky, M., Bishop, D., Bricault, P., Dale, D., Hurst, A., Jayamanna, K., Keitel, R., Olivo, M., Schmor, P. & Stanford, G. Commissioning and initial operation of a radioactive beam ion source at ISAC. *Review of Scientific Instruments* **71**, 978–980 (2000).

[105] Bricault, P. G., Dombsky, M., Lassen, J. & Ames, F. Progress in development of ISOL RIB ion sources and targets for high powder. *Cyclotrons and Their Applications 2007, Eighteenth International Conference* 500–506 (2007).

[106] Raeder, S., Heggen, H., Lassen, J., Ames, F., Bishop, D., Bricault, P., Kunz, P., Mjøs, A. & Teigelhöfer, A. An ion guide laser ion source for isobar-suppressed rare isotope beams. *Review of Scientific Instruments* **85**, 0333091–1–10 (2014).

[107] Kunz, P., Andreoiu, C., Bricault, P., Dombsky, M., Lassen, J., Teigelhöfer, A., Heggen, H. & Wong, F. Nuclear and in-source laser spectroscopy with the ISAC yield station. *Review of Scientific Instruments* **85**, 053305–1–9 (2014).

[108] Singh, B., Abriola, D., Baglin, C., Demetriou, V., Johnson, T., McCutchan, E., Mukherjee, G., Singh, S., Sonzogni, A. & Tuli, J. Nuclear Data Sheets for A= 211. *Nuclear Data Sheets* **114**, 661–749 (2013).

[109] Nucleonica GmbH, Decay Engine, Nuclear Science Portal (www.nucleonica.com), Version 3.0.49, Karlsruhe (2014).

[110] Kondev, F. & Lalkovski, S. Nuclear Data Sheets for A= 207. *Nuclear Data Sheets* **112**, 707–853 (2011).

[111] Kondev, F. Nuclear Data Sheets for A= 203. *Nuclear Data Sheets* **105**, 1–108 (2005).

[112] Basunia, M. Nuclear data sheets for A= 213. *Nuclear Data Sheets* **108**, 633–680 (2007).

[113] Chen, J. & Kondev, F. Nuclear Data Sheets for A= 209. *Nuclear Data Sheets* **126**, 373–546 (2015).

[114] Kondev, F. Nuclear Data Sheets for A= 205. *Nuclear Data Sheets* **101**, 521–662 (2004).

[115] Matzke, H. Inert gas diffusion and radiation damage in ionic crystals and sinters following ion bombardment. *Canadian Journal of Physics* **46**, 621–634 (1968).

[116] Burgess, J. *Metal Ions in Solution* (Ellis Horwood Chichester, Chichester, England, 1978).

[117] Ziegler, J. F., Ziegler, M. & Biersack, J. SRIM The stopping and range of ions in matter (2010). *Nuclear Instruments and Methods in Physics Research B* **268**, 1818–1823 (2010).

[118] Bochvarova, M., Tyung, D. K., Dudova, I., Norseev, Y. V. & Khalkin, V. A. Investigation of columns filled with crystalline tellurium for the production of radiochemically pure preparations of astatine. *Radiokhimiya* **14**, 889–895 (1972).

[119] Flux, G., Bardies, M., Monsieurs, M., Savolainen, S., Strands, S.-E. & Lassmann, M. The impact of PET and SPECT on dosimetry for targeted radionuclide therapy. *Zeitschrift für Medizinische Physik* **16**, 47–59 (2006).

[120] Harrison, J., Leggett, R., Lloyd, D., Phipps, A. & Scott, B. Polonium-210 as a poison. *Journal of Radiological Protection* **27**, 17 (2007).

[121] Jan, S., Santin, G., Strul, D., Staelens, S., Assie, K., Autret, D., Avner, S., Barbier, R., Bardies, M., Bloomfield, P. *et al.* GATE: a simulation toolkit for PET and SPECT. *Physics in Medicine and Biology* **49**, 4543 (2004).

[122] Goorden, M. C., van der Have, F., Kreuger, R., Ramakers, R. M., Vastenhouw, B., Burbach, J. P. H., Booij, J., Molthoff, C. F. M. & Beekman, F. J. VECTor: A Preclinical Imaging System for Simultaneous Submillimeter SPECT and PET. *The Journal of Nuclear Medicine* **54**, 306–313 (2013).

[123] Loening, A. M. & Gambhir, S. S. AMIDE: A Free Software Tool for Multimodality Medical Image Analysis. *Molecular Imaging* **2**, 131–137 (2003).

[124] Vollmar, S., Sue, R., Krais, R., Hohmann, C. & Hüsgen, A. Vinci 3 and experiences with multi-platform development. In *Abstracts of the XI Turku PET Symposium*, 104 (2008).

[125] Walker, M. D., Goorden, M. C., Dinelle, K., Ramakers, R. M., Blinder, S., Shirmohammad, M., van der Have, F., Beekman, F. J. & Sossi, V. Performance assessment of a preclinical PET Scanner with pinhole collimation by comparison to a coincidence-based small-animal PET scanner. *The Journal of Nuclear Medicine* **55**, 1368–1374 (2014).

[126] Graham, L. S., Fahey, F. H., Madsen, M. T., van Aswegen, A. & Yester, M. V. Quantitation of spect performance: report of task group 4, nuclear medicine committee. *Medical Physics* **22**, 401–409 (1995).

[127] Walker, M. D., Ramakers, R. M., Blinder, S., Dinelle, K., Shirmohammad, M., Van Der Have, F., Goorden, M. C., Beekman, F. J. & Sossi, V. Comparison of two small animal PET scanners: pinhole collimation vs. electronic collimation. *IEEE Nuclear Science Symposium Conference Record* **120**, 2191–2195 (2012).

[128] Ilium, L., Davis, S., Wilson, C., Thomas, N., Frier, M. & Hardy, J. Blood clearance and organ deposition of intravenously administered colloidal particles. the effects of particle size, nature and shape. *International Journal of Pharmaceutics* **12**, 135–146 (1982).

[129] Thundimadathil, J. Cancer treatment using peptides: current therapies and future prospects. *Journal of Amino Acids* **1**, 13 pages (2012).

[130] Cordier, D., Forrer, F., Bruchertseifer, F., Morgenstern, a., Apostolidis, C., Good, S., Müller-Brand, J., Mäcke, H., Reubi, J. C. & Merlo, a. Targeted alpha-radionuclide therapy of functionally critically located gliomas with 213Bi-DOTA-[Thi8,Met(O2)11]-substance P: a pilot trial. *European Journal of Nuclear Medicine and Molecular Imaging* **37**, 1335–1344 (2010).

[131] Kratochwil, C., Giesel, F., Morgenstern, A., Bruchertseifer, F., Mier, W., Zechmann, C., Apostolidis, C. & Haberkorn, U. Regional ^{213}Bi-DOTATOC peptide receptor alpha-therapy in patients with neuroendocrine liver metastases refractory to beta-radiation. *The Journal of Nuclear Medicine* **52**, 29 (2011).

[132] Nayak, T. K., Norenberg, J. P., Anderson, T. L., Prossnitz, E. R., Stabin, M. G. & Atcher, R. W. Somatostatin-receptor-targeted alpha-emitting 213Bi is therapeutically more effective than beta(-)-emitting 177Lu in human pancreatic adenocarcinoma cells. *Nuclear Medicine and Biology* **34**, 185–193 (2007).

[133] Vaidyanathan, G., Boskovitz, A., Shankar, S. & Zalutsky, M. R. Radioiodine and ^{211}At-labeled guanidinomethyl halobenzoyl octreotate conjugates: potential peptide radiotherapeutics for somatostatin receptor-positive cancers. *Peptides* **25**, 2087–2097 (2004).